# Cooper pairs and fermion trimers in solids and cold-atom systems

Kumulative Dissertation

zur Erlangung des Doktorgrades
an der Fakultät für Mathematik, Informatik und Naturwissenschaften
Fachbereich Physik
der Universität Hamburg

vorgelegt von

Ali Sanayei

geboren am 20. Dezember 1987 in Teheran

Hamburg

2020

for
*Bushra*

in memory of

*Prof. Dr. Maryam Mirzakhani*
(1977-2017)

# Abstract

In this work, we study Cooper pairs and fermion trimers in solid-state and cold-atom systems in three main projects. In a first project, we solve the Cooper problem in a cuprate lattice *a priori.* The cuprate lattice is a Lieb lattice with a sufficiently large charge-transfer energy. It provides a useful platform to study a $CuO_2$ plane, which is a main unit of the high-temperature cuprate superconductors. We consider a square unit cell with three sites including a $d_{x^2-y^2}$ orbital configuration representing a Cu atom, and two $p_x$ and $p_y$ orbital configurations representing the oxygens. We demonstrate that the next-nearest-neighbor hopping changes the curvature of the dispersive bands, and provides a better agreement of the Fermi-surface geometry compared to experimental data. This implies that we can increase the hole doping while the desired geometry of the Fermi surface is preserved. We constitute the Fermi-Hubbard Hamiltonian on a submanifold of a dispersive band, where the total momentum of a pair vanishes. While the Cooper problem is usually considered as a weak-coupling limit of an electron pair, here we present an example that includes a strong-coupling limit of the repulsive on-site interactions. We do not impose any constraints on the orbital symmetry of a Cooper pair *a posteriori.* Our results demonstrate that the ground-state solution of the Cooper problem in a cuprate lattice supports the orbital symmetry of $d_{x^2-y^2}$. We find a largest absolute value of the ground-state energy corresponding to a critical temperature of the order of 100 K. Further, and going beyond high-temperature cuprate superconductors, we propose an experimental signature of the *d*-wave Cooper pairs for a cold-atom system in a cuprate lattice using the techniques of time-of-flight image and noise correlations.

We are also interested in the formation of three-electron bound states in a solid-state system. In a second project, we consider two spin-up and spin-down electrons that are subject to an inert Fermi sea in a lower band with a quadratic dispersion relation, forming a Cooper pair. We expand the Cooper problem by including an additional electron in an otherwise empty band with a quadratic dispersion relation that interacts attractively with the other electrons. We constitute a system of two coupled integral equations in momentum space describing the three-electron system. Our analytical and numerical solutions demonstrate that beyond a critical interband interaction, three electrons can form a bound state at interaction strengths that are not yet sufficient to form a Cooper pair. We refer to that three-electron bound state as an electron trimer state. Our analytical estimate of the critical interband interaction strength shows that it is the lowest for large effective masses of the additional electron, small Fermi velocities, and a large Debye energy. As we increase the intraband interaction strength in absolute magnitude, the trimer state competes with the formation of a Cooper pair. Our results imply that three electrons can also form a bound state for noninteracting intraband electrons. From the perspective of the electrons in a lower band, this trimer state can be interpreted as a particle-induced bound state. Moreover, when the effective mass of the electrons in a lower band is

much larger than the effective mass of the electron in a higher band and also for a Debye energy comparable to the Fermi energy, we observe the formation of more than one trimer state. As an experimental signature of the electron trimers in conventional superconductors, we propose two scenarios using the modern technology of pump-probe experiments. A first scenario is to detect an electron trimer as an excited state revealed as an in-gap resonance peak by optically probing this state or by optically pumping electrons to a higher band. A second scenario is to detect a trimer state as the ground state of the system which destabilizes the BCS state.

As another example of trimers we mention Efimov states, that are the three-body bound states of particles interacting in short ranges. In contrast to a Cooper pair, an Efimov state is formed in vacuum. Unlike the electron trimers, the number of the Efimov states is in principle infinite, obeying a geometric scaling law. In a third project, we study the effect of Fermi seas on the Efimov spectrum. We constitute a system of two coupled integral equations in momentum space, and determine the three-body bound states of an atom in a Fermi mixture for contact interactions. We demonstrate that the Fermi seas deform the corresponding Efimov spectrum systematically, and push the overall spectrum towards positive values of the $s$-wave scattering lengths due to the Pauli blocking of states. We show that this effect is more pronounced near unitarity, for which we find an analytical estimate. We note that the deformation of the Efimov spectrum breaks the translational symmetry, implying that the Efimov scaling law does not hold anymore. We obtain a generalized scaling law that governs three-body bound states in the presence of Fermi seas. Finally, our results enable us to propose three scenarios to observe the experimental signature of the three-body bound states in an ultracold fermionic mixture of Yb isotopes. We estimate the onset of a three-body bound state and the binding energy.

# Zusammenfassung

In dieser Arbeit untersuchen wir in drei Projekte die Cooper-Paare und die Fermion-Trimere in Festkörper- und Kaltatomsystemen. Im ersten Projekt lösen wir das Cooper-Problem *a priori* in einem Cuprat-Gitter. Das Cuprat-Gitter ist ein Lieb-Gitter mit einer ausreichend großen Ladungstransferenergie. Es bietet eine nützliche Plattform für die Untersuchung einer $CuO_2$-Ebene, die eine Hauptkomponente der Hochtemperatur-Cuprat-Supraleiter darstellt. Wir betrachten eine quadratische Einheitszelle mit drei Gitterplätze inklusive einer $d_{x^2-y^2}$-Orbitalkonfiguration, die ein Cu-Atom darstellt, und zwei $p_x$- und $p_y$-Orbitalkonfigurationen, die die Sauerstoffatome darstellen. Wir zeigen, dass das Hüpfen zum übernächsten Nachbarn die Krümmung der dispersiven Bänder ändert und so eine bessere Übereinstimmung der Fermi-Oberflächengeometrie mit experimentellen Daten liefert. Auf diese Weise können wir die Lochdotierung erhöhen, während die gewünschte Geometrie der Fermi-Oberfläche erhalten bleibt. Wir bilden den Fermi-Hubbard-Hamilton-Operator auf einer Untermannigfaltigkeit eines dispersiven Einzelbandes ab, in der der Gesamtimpuls eines Paares verschwindet. Während das Cooper-Problem normalerweise als die schwache Kopplungsgrenze eines Elektronpaars betrachtet wird, präsentieren wir hier ein Beispiel, das eine starke Kopplungsgrenze der abstoßenden Wechselwirkung enthält. Wir erlegen der Orbitalsymmetrie eines Cooper-Paares *a posteriori* keine Einschränkungen auf. Unsere Ergebnisse zeigen, dass die Grundzustandslösung des Cooper-Problems in einem Cuprat-Gitter die Orbitalsymmetrie von $d_{x^2-y^2}$ unterstützt. Wir finden einen höchsten absoluten Wert der Grundzustandsenergie, der einer kritischen Temperatur in der Größenordnung von 100 K entspricht. Über die Hochtemperatur-Cuprat-Supraleiter hinausgehend schlagen wir eine experimentelle Signatur der $d$-Wellen-Cooper-Paare für ein Kaltatomsystem in einem Cuprat-Gitter unter Verwendung der Techniken der time-of-flight-image- und noise-correlations vor.

Wir sind zugleich auch an der Bildung von drei elektronengebundenen Zuständen in einem Festkörpersystem interessiert. Im zweiten Projekt betrachten wir dann zwei Spin-up- und Spin-down-Elektronen, die einem inerten Fermi-See in einem unteren Band mit einer quadratischen Dispersionsrelation ausgesetzt sind und ein Cooper-Paar bilden. Wir erweitern dabei das Cooper-Problem, indem wir ein zusätzliches Elektron in ein ansonsten leeres Band mit einer quadratischen Dispersionsrelation aufnehmen, das attraktiv mit anderen Elektronen interagiert. Wir bilden dazu ein System aus der zwei gekoppelten Integralgleichungen im Impulsraum, das das Drei-Elektronen-System beschreibt. Unsere analytischen und numerischen Lösungen zeigen, dass drei Elektronen über eine kritische Interband-Wechselwirkung hinaus einen gebundenen Zustand bilden können bei Wechselwirkungsstärken, die noch nicht ausreichen, um ein Cooper-Paar zu bilden. Wir bezeichnen diesen gebundenen Drei-Elektronen-Zustand als Elektronen-Trimer. Unsere analytische Abschätzung der kritischen Interband-Wechselwirkungsstärke zeigt, dass sie für große effek-

tive Massen des zusätzlichen Elektrons, sowie kleine Fermi-Geschwindigkeiten und eine große Debye-Energie am niedrigsten ist. Wenn wir die Stärke der Intraband-Wechselwirkung in ihrer absoluten Größenordnung erhöhen, konkurriert der Trimer-Zustand mit der Bildung eines Cooper-Paares. Unsere Ergebnisse besagen, dass drei Elektronen einen gebundenen Zustand für nicht wechselwirkende Intraband-Elektronen bilden können. Aus der Sicht der Elektronen in einem unteren Band kann dieser Trimer-Zustand als ein Teilchen-induzierter gebundener Zustand interpretiert werden. Wenn darüber hinaus die effektive Masse der Elektronen in einem tieferen Band sehr viel schwerer ist als die effektive Masse des Elektrons in einem höheren Band und dies für eine Debye-Energie, die mit der Fermi-Energie vergleichbar ist, dann beobachten wir die Bildung von mehr als einem Trimer-Zustand. Als experimentelle Signatur für Elektronen-Trimere in herkömmlichen Supraleitern schlagen wir zwei Szenarien vor, die die moderne Technologie von sogenannten Pump-Probe-Experimenten verwenden. Das erste Szenario fasst das Elektrontrimer als einen angeregten Zustand auf, der als ein In-Gap-Resonanz-Peak sichtbar wird, wobei dieser Zustand entweder optisch untersucht wird oder elektronenoptisch in ein höheres Band gepumpt wird. Das zweite Szenario besteht darin, den Trimeren-Zustand als einen Grundzustand des Systems aufzufassen, der den BCS-Zustand destabilisiert.

Als ein weiteres Beispiel für Trimere erwähnen wir Efimov-Zustände, d.h. die Dreikörper-gebundenen Zustände von Teilchen, die über kurze Entfernungen interagieren. Im Gegensatz zu einem Cooper-Paar kann im Vakuum ein Efimov-Zustand gebildet werden. Und im Unterschied zu den Elektronentrimeren ist die Anzahl der Efimov-Zustände im Prinzip unendlich, wobei ein geometrisches Skalierungsgesetz gilt. Im dritten Projekt schließlich untersuchen wir die Auswirkung der Fermi-Seen auf das Efimov-Spektrum. Wir bilden dazu ein System aus zwei gekoppelten Integralgleichungen im Impulsraum und bestimmen die Dreikörper-Bindungszustände eines Atoms in einer Fermi-Mischung für Kontaktwechselwirkungen. Wir zeigen, dass die Fermi-Seen das entsprechende Efimov-Spektrum systematisch deformieren und dabei das Gesamtspektrum aufgrund der Pauli-Blockierung von Zuständen in Richtung positiver Werte der $s$-Wellen-Streulängen verschieben. Wir finden, dass dieser Effekt in der Nähe der Unitarität stärker ausgeprägt ist, wofür wir eine analytische Schätzung angeben können. Wir stellen darüberhinaus fest, dass die Verformung des Efimov-Spektrums die Translationssymmetrie bricht. Dies impliziert, dass das Efimov-Skalierungsgesetz dann nicht mehr gilt. Wir erhalten so ein verallgemeinertes Skalierungsgesetz, das die gebundenen Drei-Körper-Zustände in Gegenwart von Fermi-Seen beschreibt. Schließlich ermöglichen es unsere Ergebnisse, drei experimentelle Szenarien vorzuschlagen, um Drei-Körper-Bindungszustände in einer ultrakalten fermionischen Mischung von Yb-Isotopen beobachten zu können. Wir können dazu den Beginn eines Drei-Körper-Bindungszustands abschätzen inklusive der zugehörigen Bindungsenergie.

# Acknowledgments

First of all, I would like to thank my supervisor, Prof. Dr. Ludwig Mathey, for creating a friendly atmosphere with many inspiring discussions which made this work possible. I would also thank my co-supervisor, Prof. Dr. Henning Moritz, for many useful hints and points. This work could not have been accomplished without the fruitful discussions and the collaborations with Dr. Pascal Naidon at the RIKEN Nishina Centre.

I thank all my friends and colleagues in Ludwig's group, in particular Marlon Nuske and Lukas Broers, for very useful discussions. I am thankful of all colleagues in the SFB-925 graduate school. I would also like to express my gratitude to my experimental colleagues in the group of Dr. Christoph Becker, in particular Koen Sponselee, Benjamin Abeln, and Marcel Diem, for useful discussions.

Last but not least, my special thanks go to my family, in particular my wife Bushra, for their unlimited supports. I am very much indebted to my teachers and professors during this journey.

# Publications and statement of contributions

The following manuscripts constitute the main basis of this cumulative Thesis.

- **[S1]** <u>Ali Sanayei</u>, Pascal Naidon, and Ludwig Mathey, *Electron trimer states in conventional superconductors*, Phys. Rev. Research **2**, 013341 (2020)

  The main project and model discussed in this paper was proposed by Ludwig Mathey and Pascal Naidon, at the RIKEN Nishina Centre, and was supervised by Ludwig Mathey. Theoretical results including the analytical derivations and numerical calculations were mostly accomplished by the author of this Thesis. A more concise method to implement the Gauss-Legendre quadrature rule in our numerical code was proposed by Pascal Naidon. The manuscript was written by the author of this Thesis, and it was then revised and edited by Ludwig Mathey and Pascal Naidon. All figures were obtained and designed by the author of this Thesis. This paper is enclosed to the last chapter of the Thesis.

- **[S2]** <u>Ali Sanayei</u> and Ludwig Mathey, *Three-body bound states of an atom in a Fermi mixture*, arXiv:2007.13511v2 [submitted]

  The main project discussed in this paper was proposed and supervised by Ludwig Mathey. All theoretical results including the mathematical model, analytical derivations and calculations, and also the numerical analysis were accomplished by the author of this Thesis. The manuscript was written by the author of this Thesis, and it was then revised and edited by Ludwig Mathey. All figures were obtained and designed by the author of this Thesis. This manuscript is enclosed to the last chapter of the Thesis.

- **[S3]** <u>Ali Sanayei</u> and Ludwig Mathey, *Cooper problem in a cuprate lattice* [manuscript is ready for submission]

  The main project discussed in this paper was proposed and supervised by Ludwig Mathey. All theoretical results including the analytical derivations and calculations as well as the numerical analysis were accomplished by the author of this Thesis. The manuscript was written by the author of this Thesis, and it will be revised and edited by Ludwig Mathey. All figures were obtained and designed by the author of this Thesis. This manuscript is going to be submitted very soon. The corresponding draft is enclosed to the last chapter of the Thesis.

# Contents

# Chapter 1

# Introduction

In a seminal paper, Ref. [1], L. N. Cooper showed that two electrons immersed in an inert Fermi sea form a bound state for arbitrarily weak attractive interactions. The attractive interaction between two electrons in a metal seems to be counterintuitive, as the Coulomb force between two negatively charged particles is repulsive. To realize that, we note that in a metal the ionic background forms a lattice. The effective attraction between two electrons is realized via the lattice vibrations [2, 3, 4, 5, 6], confirmed by isotope effect [5, 6, 7, 8]. This phenomenon is well described in quantum mechanics by introducing a quasiparticle, phonon. It is also legitimate to ask how an effectively weak attraction between two electrons leads to a bound state. The key point to realize the formation of a bound state is the Fermi seas, i.e., the background effect of the other electrons in a metal. If there were no Fermi seas, the two interacting electrons would be isolated. In this case the density of states would not be constant, and the weak attractive interaction between two electrons would not necessarily lead to a bound state [3, 6]. The Cooper problem assumes the dominance of the effective interaction induced by the electron-phonon interaction over the screened Coulomb potential. It is modeled as constant in momentum space within a narrow energy range of the order of the Debye energy for the relative kinetic energy of the electrons. The solution of the Cooper problem results in an isotropic order parameter, not depending on the orientation of the momenta. The order parameter is also static, not depending on the phonon frequency. However, a dynamic order parameter was later taken into account by Migdal and Eliashberg, using an electron-phonon propagator [9, 10, 11, 12, 13, 14, 15].

The existence of this bound state indicates that the noninteracting Fermi sea is unstable against pair formation, implying the emergence of a superconducting state. A more extensive theory of this state was provided by Bardeen-Cooper-Schrieffer (BCS) theory, which elaborated on the essential ingredients that are necessary for the formation of conventional superconductors, pointed out by the Cooper problem and its solution [S1], [2, 5, 6, 16, 17, 18, 19, 20, 21, 22]. Furthermore, and going beyond superconductivity, a Cooper problem can be formulated for any order parameter composed of two fermionic operators. For example, the weak-coupling

limit of charge-density-wave and spin-density-wave orders can be formulated as the formation of an electron-hole pair. Here the electron is restricted to occupy states outside the Fermi sea, and the hole is restricted to states inside the Fermi sea; see, e.g., Ref. [23, 24]. Given this broad applicability of the Cooper problem, it is of fundamental importance for solid-state physics [S1].

The solution of the Cooper problem in a lattice is also crucial. Here we are primarily interested in a Lieb lattice, a two-dimensional lattice constituted by a square unit cell with three sites [25, 26]. The electronic band structure of the lattice exhibits two dispersive bands and one flat band in between. When the charge-transfer energy tends to vanishing, the low-energy spectrum of the lattice reveals a Dirac cone at $\Gamma$-point. The Lieb lattice has been engineered artificially via the optical lattices [27, 28, 29], photonics [30], and cold atoms [31, 32]. There have been also several attempts to realize it in materials like covalent organics [33, 34]. These realizations provide useful platforms to investigate and examine the physical phenomena predicted to occur in a flat band or in a three-band system; see, e.g., Refs. [35, 36, 37, 38, 39, 40, 41, 42]. A very important application of a Lieb lattice is the copper-oxide, $CuO_2$, plane. The structure of a $CuO_2$ plane can be realized by a Lieb lattice geometry with a sufficiently large charge-transfer energy, which is referred to as a cuprate lattice [43, 44]. A $CuO_2$ plane is considered as the basic structural unit of the high-temperate cuprate superconductors. Here, the three sites of the square unit cell includes one $d_{x^2-y^2}$ orbital configuration representing the Cu atom, and two $p_x$ and $p_y$ orbital configurations representing the oxygens [45, 46, 47, 48]. It is accepted that superconductivity in cuprates is due to the Cooper pairs that occur independently in different $CuO_2$ planes. The order parameter is spin singlet and supports a $d$-wave symmetry [44]. Nevertheless, the mechanism of the Cooper pairing is still under debates. There are arguments in favor of the electron-phonon interactions as the main pairing mechanism [49, 50, 51, 52, 53]. On the other hand, an orbital $d$-wave symmetry of the order parameter originates mostly from the strong electron-electron repulsive interactions. Accordingly, there are counterarguments in favor of the antiferromagnetic magnons [54, 55] or plasmons [56, 57, 58, 59].

The ground-state solution of a Cooper pair in a $CuO_2$ plane has been considered theoretically by different approaches. The ground-state solutions of the Fermi-Hubbard model or the $t$-$J$ and $t$-$J$-$U$ models were found by variational calculations using a diagrammatic expansion of the Gutzwiller wave functions [60, 61, 62]. A variational calculation was also applied to Hatsugai-Kohmoto model [63], which is considered as a simplification of the Fermi-Hubbard model, to determine the ground-state solution of a Cooper pair [64]. The other approaches are, for example, based on the density matrix embedding theory (DMET) [65, 66], constrained path auxiliary field Monte Carlo (AFQMC) [67], the tensor network wave function ansatz (iPEPS) [68], density matrix renormalization group method (DMRG) [69], and dynamical mean-field theory combined with the fluctuation exchange approximation (FLEX+DMFT) [70]. We notice that in many calculations, an orbital $d$-wave sym-

metry of the order parameter has been considered *a posteriori* to follow the experiments. A main question to be addressed here is whether the solution of the Cooper problem in a cuprate lattice can reveal *a priori* a ground state supporting a *d*-wave symmetry. We note that the Cooper problem and its solution is usually considered as a weak-coupling limit of an electron pair. Our objective is thus to show an example of the Cooper problem that includes the strong-coupling limit of the repulsive on-site interactions.

While the solution of the Cooper problem is a two-particle bound state, we are also interested in the formation of three-particle bound states in a solid. As an example for three-body bound states, we mention Efimov states demonstrated by V. Efimov for short-range interactions [71]. In contrast to Cooper pairs, Efimov states are formed in vacuum. Efimov showed that three bosons that interact attractively in vacuum via short-range interactions form three-body bound states at interaction strengths that are not yet sufficient to support two-body bound states. The number of the Efimov states is in principle infinite, and there is a geometric scaling law that governs the bound states [71, 72, 73, 74, 75]. These states have been observed in ultracold atomic gases [76, 77, 78, 79] and helium beams experiments [80, 81]. The Efimov effect motivates us to expand the Cooper problem, and to investigate whether there is an electron trimer state in a solid-state system. And if so, we are also interested in finding out how an electron trimer competes with the formation of a Cooper pair.

As discussed above, the Efimov effect considers three-body bound states for short-range interactions in vacuum. An important problem that arises here is to find how the Efimov spectrum is deformed in the presence of Fermi seas. This results in determining the three-body bound states of cold fermionic mixtures and estimating the corresponding binding energy. Moreover, the deformation of the Efimov spectrum implies that the geometric scaling law that governs three-body bound states in vacuum will not be valid anymore. Another problem is to find a generalized scaling law governing the three-body bound states in the presence of Fermi seas. The answer enables us to predict the onset of the excited three-body bound states for different densities of Fermi mixtures.

The main aim of this work is threefold. First, we solve the Cooper problem in a cuprate lattice. We do not impose any orbital symmetry on a Cooper pair *a posteriori* to follow the experiment. We consider a cuprate lattice with a square unit cell containing three sites. The A-site includes a $d_{x^2-y^2}$ orbital configuration representing a Cu atom. The B- and C-site includes a $p_x$ and $p_y$ orbital configuration, respectively, representing the oxygens. We take into account the nearest-neighbor hopping $t_{pd}$, and show the effect of the next-nearest-neighbor hopping, $t_{pp}$, on the Fermi surface. Our argument is in favor of including $t_{pp}$ in the formalism, implying a better agreement of the Fermi-surface geometry compared to experimental data extracted mostly from the angle-resolved photoemission spectroscopy (ARPES). Next, we take into account the repulsive on-site interactions in the strong-coupling regime,

and constitute the Fermi-Hubbard Hamiltonian on a submanifold of a dispersive band where the total momentum of a pair vanishes. We assume a singlet-state wave function of the Cooper pair, and solve the Cooper problem numerically. Our result demonstrates that the ground-state solution supports the orbital $d_{x^2-y^2}$ symmetry. Further, and going beyond high-temperature cuprate superconductors, we propose an experimental signature of the $d$-wave Cooper pairs for a cold-atom system in a cuprate lattice using the techniques of time-of-flight image and noise correlations.

In a second project, we expand the original Cooper problem by including a third electron in an otherwise empty band with a quadratic dispersion relation. The other two electrons are restricted to be outside of an inert Fermi sea in a lower band with a quadratic dispersion relation. We assume that the effective interaction between the electrons is attractive, following the reasoning of the Cooper problem. We constitute a system of two coupled integral equations describing the three electrons in momentum space. We provide an analytical estimate of the solution, and calculate the full spectrum numerically. Our results demonstrate the formation of electron trimers in the presence of a Fermi sea. These trimers are formed for sufficiently strong interband attractive interactions. The trimer state is formed at interaction strengths that are not yet sufficient to form a Cooper pair. We show that an electron trimer is also formed for vanishing intraband interactions. From the perspective of the electrons in a lower band, this can be interpreted as a bound-state formation that is induced by a third electron in a higher band. We find that the trimer state competes with the formation of the two-electron Cooper pair. Our results shed light on the general problem of Efimov effect in a solid-state system. Unlike the Efimov states, we show that the number of the electron trimers is in principle finite, and that there is no scaling law governing the trimer states. We also discuss two experimental scenarios to realize the signatures of the trimer states in conventional superconductors.

Finally, in a third project we determine the three-body bound states of an atom in a Fermi mixture, where all species interact via contact interactions. We assume a density of the species, labeled "2", that interacts attractively via contact interactions with the same density of another species, labeled "3". We assume that the two species are in different internal states. We include an additional atom, labeled "1", that interacts attractively with the other atoms via contact interactions. The species "2" and "3" constitute the Fermi mixture and define the Fermi seas with the Fermi momentum $k_F$. We derive a system of two coupled integral equations in momentum space, and solve the full spectrum numerically. We also obtain analytical solutions of limiting cases. Our results show that the Fermi seas deform the corresponding Efimov spectrum systematically, and push the solution towards positive values of the $s$-wave scattering lengths. We demonstrate that this effect is more pronounced near unitarity, for which we find an analytical estimate. We show that in the presence of Fermi seas, the Efimov scaling law in vacuum does not hold anymore. We find a generalized discrete scaling law that governs the three-body bound states. For an

experimental confirmation of our prediction, we propose three signatures of three-body bound states of an ultracold Fermi mixture of Yb isotopes, and provide an estimate for the onset of the bound state and the binding energy.

## Outline

This Thesis is organized as follows. After Introduction, Chap. 1, we consider the following chapters:

- Chapter 2 includes three sections to provide the most important physical concepts that we need in the Thesis. The three sections are devoted to:

  - (i) Cooper pairs in conventional superconductors, where we discuss how two electrons in a solid can attract each other and form a bound state. We also represent a formalism in momentum space to solve the Cooper problem. We will expand this formalism in Chap. 4.
  - (ii) cuprate lattice, where we discuss the lattice geometry and its applications. We constitute the tight-binding model, and derive the electronic band structure. We also review the Fermi-Hubbard model briefly.
  - (iii) Efimov effect, where we start out from Thomas collapse and discuss the Efimov attraction. We discuss the Efimov scaling law governing three-body bound states in vacuum. We also review the experimental signatures of the Efimov effect in ultracold atoms.

- Chapter 3 elaborates on the first project, and discusses the Cooper problem in a cuprate lattice.

- Chapter 4 is devoted to the second project, and investigates the electron trimer states in conventional superconductors.

- Chapter 5 covers the third project, and investigates the three-body bound states of an atom in a Fermi mixture for contact interactions.

- Chapter 6 represents the concluding remarks and future studies.

- Chapter 7 is the supplemental material, which explains the details of some calculations and derivations, and also includes our appended publications and manuscripts.

# Chapter 2

# From Cooper pairs to Efimov trimers

In this Chapter, we discuss and review the most important concepts that we need in this Thesis. We start out with the Cooper problem and its solution, and go to the cuprate lattice and Fermi-Hubbard model. We end this Chapter by discussing the Efimov effect and its signatures in cold-atom systems.

## 2.1 Cooper problem

### 2.1.1 How two electrons attract each other

The solution of the Cooper problem shows that two electrons that are subject to an inert Fermi sea form a bound state for arbitrarily weak attractive interactions [1]. This finding turned out to be a cornerstone of the BSC theory of superconductivity, developed by Bardeen, Schrieffer, and Cooper [16], and independently by Bogoliubov [82]. The BCS theory describes the low-temperature superconducting state in materials mostly discovered before 1975, and usually called classical or conventional superconductors [2]. There are two crucial phenomena that seem to be counterintuitive. First, two electrons repel each other by the electrostatic Coulomb force. How can then the effective interaction of two electrons become attractive? Second, a weak attractive interaction does not necessarily provide a bound state. For example, an attractive interaction between helium atoms lead to a condensation, and do not form a bound state [3, 4]. It is therefore legitimate to ask how a weak attractive interaction between two electrons leads to a bound state.

To address the first question, recall that the direct interaction between two electrons is governed by the repulsive Coulomb potential. In a solid, the ionic background forms a lattice and the Coulomb potential is screened by the dielectric function of the medium [5, 6]. The electrons in a metal move through the lattice [2, 3]. An ion is attracted to an electron and moves slowly, as it is much heavier than

the electron. This results in polarizing the medium and distorting the lattice. The moving ion provides a path for another electron to be attracted. From a different perspective, we can imagine that the lattice distortion mediates an attractive interaction between the two electrons. If lattice distortions are modeled by harmonic oscillators, this can be formulated more rigorously by a generic theorem pointed out by Leggett: "If two systems $S_1$ and $S_2$ interact in the same way with a harmonic oscillator of natural frequency $\omega_0$, then the result is to produce an effective attraction between $S_1$ and $S_2$ at frequencies $\omega < \omega_0$ and a repulsion for $\omega > \omega_0$"; see Ref. [2].

The importance of the interaction of electrons with lattice vibrations was first realized by Fröhlich [83]. His finding that the ions do not have merely a static contribution to the superconductivity was confirmed by the isotope effect [5, 6], showing that the critical temperature varies systematically for different isotopes of a given metallic element [7, 8]. The Fröhlich's discovery was developed further by Bardeen and Pines [84], Migdal [9], and eventually improved by Eliashberg who took into account the effect of phonons' dynamics on the electron pairings [11, 12].

In quantum mechanics, the lattice distortion is described by a quasiparticle called phonon. The dispersion relation for a diatomic linear chain reveals two branches for phonons. The acoustic branch with linear dispersion for small values of momentum, and the optical branch which has a maximum dispersion at zero momentum and decreases by increasing the absolute values of the momentum. The minimum dispersion of an optical phonon is larger than the maximum dispersion of an acoustic phonon; see Ref. [85]. From here we can expect that mostly optical phonons contribute to the electron pairing. The largest electron-phonon interaction is provided by the highest-frequency phonon in the lattice, determined by the Debye frequency $\omega_D$. The corresponding energy that determines the largest energy available by the lattice distortion is the Debye energy $E_D = \hbar\omega_D$, where $\hbar$ is the reduced Planck's constant.

The Cooper problem assumes the dominance of the effective interaction induced by the electron-phonon interaction over the screened Coulomb potential [5, 16, 17, 18]. It is modeled as constant in momentum space within a narrow energy range of the order of the Debye energy for the relative kinetic energy of the electrons [1, 5, 19]. Since the interaction strength is constant in this region and does not depend on the rotational angle of the electrons' momenta, the Cooper model of interaction supports an *s*-wave symmetry of states. This implies that the total wave function of the interacting electrons is symmetric with respect to the interchange of coordinates. On the other hand, electrons obey Fermi-Dirac statistics whose total wave function is antisymmetric. As a result, the spin orientation of two interacting electrons has to be in the opposite directions [4]. This simplified model distills the key features and energy scales of the full interaction induced by electron-phonon coupling that are relevant for the formation of the bound state and its properties.

A first experimental evidence of the Cooper-pairing mechanism in low-temperature superconductors was realized in the 1960s and 70s at the Bell Telephone Laborato-
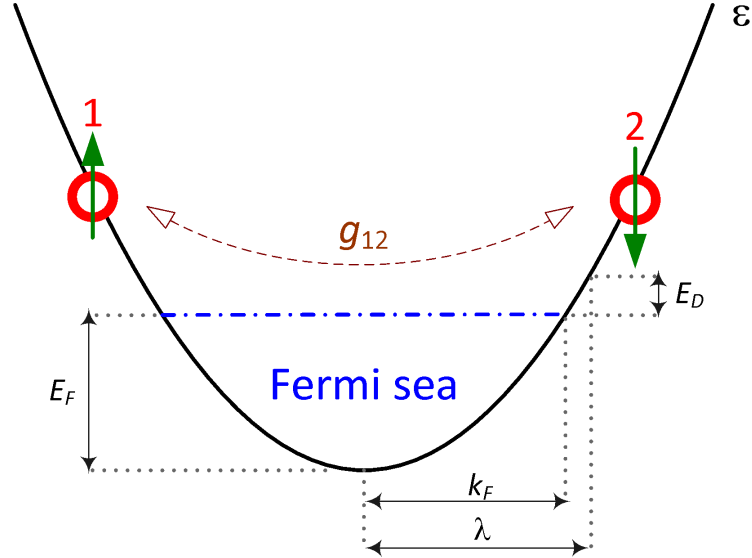
Figure 2.1: Visualization of the Cooper problem. Two spin-up and spin-down electrons, labeled "1" and "2", with the same mass $m$ are in a band with quadratic dispersion relation $\varepsilon$. The electrons are outside an inert Fermi sea, where the Fermi momentum is $k_F$ and the Fermi energy is $E_F$. They interact attractively with the interaction strength $g_{12} < 0$, following the reasoning of the Cooper problem. The momentum cutoff $\lambda$ is chosen such that $\varepsilon(\lambda) - E_F = E_D$, where $E_D$ is the Debye energy.

ries, where the boson generation-detection spectroscopy was employed [86, 87, 88]. The main idea of those experiments is based on an inelastic process where injected quasiparticles into a superconductor relax to the ground state and recombine into Cooper pairs. Here, the emission of phonons are detected, showing the electron pairing is mediated by phonons. This experiment has also been generalized to investigate the Cooper-pairing mechanism in high-temperature superconductors [55].

## 2.1.2 Solution of the Cooper problem

To address the second question on the bound-state formation of two electrons, we need to solve the Cooper problem. In this Section, we formulate the problem in a way which is slightly different from a typical formalism usually presented in textbooks. We will expand this formulation in Chap. 4, where we discuss the electron trimer states.

We construct an equation in momentum space describing two spin-up and spin-down electrons, labeled "1" and "2", that interact attractively following the Cooper model. The electrons are restricted to be in a spin-singlet state and outside an inert Fermi sea with the Fermi momentum $k_F$ and the Fermi energy $E_F$. We consider the

interaction between the two electrons to be a negative constant $g_{12}$, for the incoming and outgoing momentum of a particle smaller than a cutoff $\lambda$ and zero otherwise; see Fig. 2.1. We fix the value of the cutoff such that

$$E_D = \frac{\hbar^2}{2m}(\lambda^2 - k_F^2) = \frac{\hbar^2}{2m}\lambda^2 - E_F, \tag{2.1}$$

where $E_D$ is the Debye energy, $m$ is the mass of each electron, and $E_F = \hbar^2 k_F^2 / 2m$ is the Fermi energy.

The Schrödinger equation governing the two electrons in momentum space consists of the kinetic energy of each electron and the Cooper interaction:

$$\left(\frac{\hbar^2 k_1^2}{2m} + \frac{\hbar^2 k_2^2}{2m} + \hat{U}_{12}\right)\psi(\mathbf{k}_1, \mathbf{k}_2) = E_{12}\psi(\mathbf{k}_1, \mathbf{k}_2), \tag{2.2}$$

where $\mathbf{k}_1$ and $\mathbf{k}_2$ are electrons' momenta, $\psi(\mathbf{k}_1, \mathbf{k}_2)$ is the wave function, and $E_{12}$ is energy. The interaction $\hat{U}_{12}$ between the electrons "1" and "2" is

$$\hat{U}_{12}\psi(\mathbf{k}_1, \mathbf{k}_2) = g_{12}\theta_{k_F,\lambda}(\mathbf{k}_1)\theta_{k_F,\lambda}(\mathbf{k}_2) \int \frac{d^3\mathbf{q}}{(2\pi)^3}\theta_\lambda(\mathbf{k}_1 - \mathbf{q})\theta_\lambda(\mathbf{k}_2 + \mathbf{q})\psi(\mathbf{k}_1 - \mathbf{q}, \mathbf{k}_2 + \mathbf{q}), \tag{2.3}$$

where $\mathbf{q}$ is the momentum transfer, defined as the difference of the in-state and out-state momenta of a particle [89]. The cutoff function $\theta_{a,b}(\mathbf{k})$, for $a, b \in \mathbb{R}$ and $0 \leqslant a < b$, is defined as

$$\theta_{a,b}(\mathbf{k}) = \begin{cases} 1 & \text{for } a \leqslant \mathbf{k} \leqslant b, \\ 0 & \text{otherwise}, \end{cases} \tag{2.4}$$

and $\theta_b(\mathbf{k}) \equiv \theta_{0,b}(\mathbf{k})$. The physical interpretation of Eq. (2.3) is as follows: electrons "1" and "2", restricted to be outside an inert Fermi sea, are interacting attractively with a constant interaction strength in momentum space, if the corresponding relative kinetic energy does not exceed the Debye energy. There is another assumption in the original Cooper problem, that the total momentum of the two-electron system is vanishing, i.e., $\mathbf{k}_1 = -\mathbf{k}_2$. This implies that the interaction between the two electrons possesses its highest value [3]. With this assumption, Eq. (2.2) provides an ansatz for the wave function $\psi(-\mathbf{k}_2, \mathbf{k}_2)$ as

$$\psi(-\mathbf{k}_2, \mathbf{k}_2) = -\frac{\theta_{k_F,\lambda}(\mathbf{k}_2)\mathcal{F}_{12}}{\frac{\hbar^2}{m}k_2^2 - E_{12}}, \tag{2.5}$$

where

$$\mathcal{F}_{12} \equiv g_{12} \int \frac{d^3\mathbf{p}}{(2\pi)^3}\,\theta_\lambda(\mathbf{p})\psi(-\mathbf{p}, \mathbf{p}). \tag{2.6}$$

We insert the anstaz (2.6) into Eq. (2.5), resulting in

$$\frac{1}{g_{12}} + \int \frac{d^3\mathbf{p}}{(2\pi)^3} \frac{\theta_{k_F,\lambda}(\mathbf{p})}{\frac{\hbar^2}{m}\mathbf{p}^2 - E_{12}} = 0. \tag{2.7}$$

Equation (2.7) describes the two electrons with a vanishing total momentum that are outside an inert Fermi sea and interact attractively through the interaction model (2.3).

Next, we define an interaction parameter

$$\xi_{12} = \frac{2\mu}{4\pi\hbar^2} g_{12}, \tag{2.8}$$

where $\mu = 2/m$ is a reduced mass. If the electrons form a bound state near the Fermi surface, we can define a corresponding binding energy as[1] $|\Delta| \equiv \hbar^2\kappa^2/2m$, where $0 < \kappa/k_F \ll 1$. This implies that the bound-state energy can be written as $|\mathcal{E}_{12}| \equiv 2\mu|E_{12}|/\hbar^2 = k_F^2 - \kappa^2$. We assume that within the narrow energy range of $E_D$, the interaction is isotropic and does not depend on the momentum orientation. The isotropic assumption implies that there is no restriction on the direction of $\mathbf{p}$. Without loss of generality, we assume that $\mathbf{p} = p\mathbf{e}_z$, where $\mathbf{e}_z$ is the unit vector in the direction of the $z$-axis. We insert the new expressions for the interaction strength and for the bound-state energy into Eq. (2.7), and solve it analytically to obtain:

$$\frac{-\pi}{2\xi_{12}} = \lambda - k_F + \frac{1}{2}\sqrt{k_F^2 - \kappa^2}\ln\left(\frac{\kappa^2 + (\lambda - k_F)(k_F + \sqrt{k_F^2 - \kappa^2})}{\kappa^2 + (\lambda - k_F)(k_F - \sqrt{k_F^2 - \kappa^2})}\right). \tag{2.9}$$

To find an expression for the binding energy, we employ two approximations based on the physical and mathematical grounds. First, the binding energy is much smaller than the Fermi energy, $\kappa/k_F \ll 1$, which leads to a simplification of each square-root in Eq. (2.9). Second, recall that we have fixed the cutoff $\lambda$ using the relation (2.1). For a typical conventional superconductor the Debye energy is much smaller than the Fermi energy, $E_D \ll E_F$ [3, 19], implying that $\lambda - k_F \ll k_F$. With these assumptions, we solve Eq. (2.9) for $\kappa^2$ and arrive at the following expression for the binding energy:

$$|\Delta| \approx 2E_D \exp\left(\frac{-\pi}{k_F|\xi_{12}|}\right); \tag{2.10}$$

see Appendix A in Sec. 7.1 for more details. Figure 2.2 shows the binding energy as a function of the interaction parameter. We note that the binding energy is not an analytic function as we approach the origin, implying that the two-electron bound state cannot be described by perturbation theory.

---

[1]Some authors prefer to define the binding energy as $2|\Delta| \equiv \hbar^2\kappa^2/2m$. In this way, the factor 2 for the Debye energy $E_D$, appeared in Eqs. (2.10) and (2.12), shall be dropped.
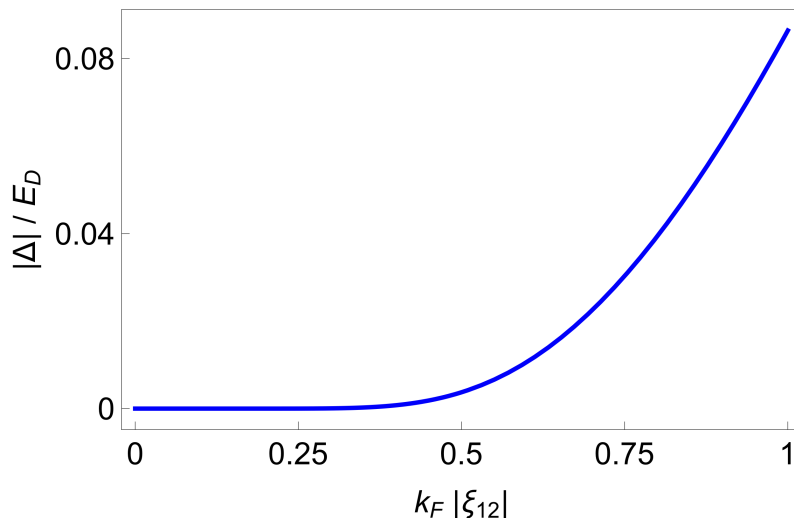
Figure 2.2: Cooper-pair binding energy $|\Delta|/E_D$ as a function of the interaction parameter $k_F|\xi_{12}|$, where $E_D$ is the Debye energy and $k_F$ is the Fermi momentum.

In order to prove that the relation (2.10) is equivalent to a typical textbook expression, we notice that the density of states at the Fermi surface, $N_0$, is the number of states that are occupied up to the Fermi energy; i.e.,

$$N_0 = \int \frac{d^3\mathbf{k}}{(2\pi)^3}\delta(E_F - E_{\mathbf{k}}) = \frac{mk_F}{2\pi^2\hbar^2}, \tag{2.11}$$

where $\mathbf{k}$ denotes the momentum, $\delta$ is the Dirac delta function, $E_F = \hbar^2k_F^2/2m$ is the Fermi energy, and $k_F$ is the Fermi momentum. Now we can rewrite the binding energy (2.10) in terms of $N_0$:

$$|\Delta| \approx 2E_D \exp\left(\frac{-2}{N_0|g_{12}|}\right). \tag{2.12}$$

Equation (2.10) or (2.12) implies that the two electrons form a bound state for any weak interaction strength. As the density of states $N_0$ increases, the number of the states that are available to contribute to the wave function of a pair increases, implying that the weak interaction $g_{12}$ is strengthened as $N_0|g_{12}|$. Moreover, Eq. (2.11) shows that the density of states at the Fermi surface is constant. We note that if there were no Fermi seas and the two interacting electrons were isolated, the density of states would not be constant. In this case, the weak attractive interaction between the two electrons would not necessarily lead to a bound state [3, 6]. This explains the physical ingredients of how a weak attractive interaction implies an electron pair, and answers the second question that we posed in the beginning of this Chapter.

A singlet-state wave function of a Cooper pair with a vanishing total momentum is obtained by introducing a set of creation operators $c_{\mathbf{k}\sigma}^\dagger$ [90], for a spin-up and

spin-down electron, $\sigma \in \{\uparrow, \downarrow\}$, with momentum $\mathbf{k}$ and $-\mathbf{k}$:

$$|\Phi\rangle = \sum_{|\mathbf{k}|>k_F} \phi(\mathbf{k})c^\dagger_{\mathbf{k}\uparrow}c^\dagger_{-\mathbf{k}\downarrow} |FS\rangle, \tag{2.13}$$

where $\phi(\mathbf{k})$ represents the wave function of a Cooper pair and $|FS\rangle$ denotes the Fermi-sea state with all states occupied up to the Fermi momentum $k_F$; see, e.g., Refs. [4, 5, 6, 16, 17, 91].

### 2.1.3   Eliashberg's idea in a nutshell

We recall that the binding energy in Eq. (2.10) or (2.12) is static, not depending on the phonon frequency. The phonon dynamics results in a retardation, affecting the electron pairing [15]. This effect was taken into account by Eliashberg using an electron-phonon propagator [11, 12]. The electron-phonon interaction in Eliashberg theory follows the Migdal approximation [9], assuming that the electronic and ionic degrees of freedom can be separated [10, 14, 92]. Recently, it was shown that the dependency of the binding energy to the phonon frequency is a feature of the Eliashberg theory that also holds for the weak-coupling regime [13]. That is why some authors avoid considering the BCS theory of superconductivity as a weak-coupling limit of the Eliashberg theory; see, e.g., Ref. [14]. Finally, the validity of the Eliashberg theory is a broad subject in the literature, which is beyond the scope of our work. For this, we refer to the recent review [15] and references therein.

## 2.2   Cuprate lattice and Fermi-Hubbard model

### 2.2.1   Geometry and applications

A cuprate lattice is a two-dimensional Lieb lattice that is characterized by a square unit cell with three sites and a sufficiently large charge-transfer energy [25, 26, 43, 44]. Two sites of the unit cell have only two sites in their neighbors, however, the other site is in neighborhood of four sites; see Fig. 2.3. In general, one of the main characteristics of the Lieb lattice is the one-particle energy spectrum that exhibits two dispersive bands and one flat band in between [26, 35]; see Fig. 2.4. There are other lattices supporting a flat band, however, the Lieb lattice is more intriguing for several reasons. For example, unlike the kagome lattice [93, 94], the flat band in a Lieb lattice is surrounded by dispersive bands and does not possess the highest energy in the spectrum. The flat band is robust against the magnetic field and spin-orbit coupling, and does not develop dispersions [26]. Because of that, a Lieb lattice provides an ideal platform to examine the physical predictions occurring in a flat band [36]. With technical advances in the trapping and cooling of atoms in the last decade [95, 96], there are realizations of a Lieb lattice using the optical lattices [27, 28, 29], photonics [30], and cold atoms [31, 32], that are generally considered
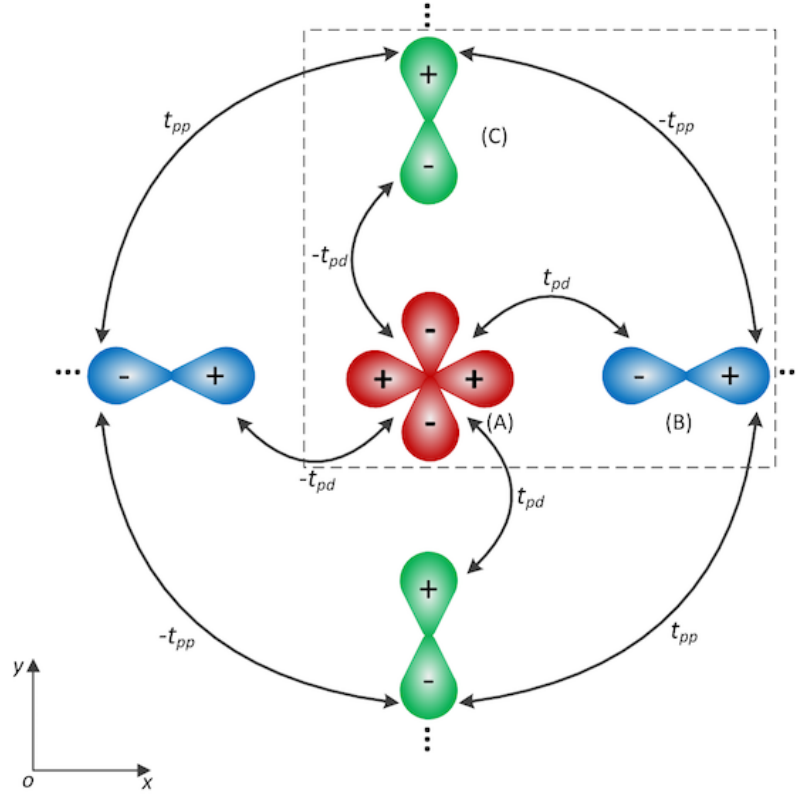
Figure 2.3: Sketch of the two-dimensional cuprate lattice in real space. The unit cell is shown by a dashed square, including a $d_{x^2-y^2}$ orbital configuration on A-site, a $p_x$ on B-site, and a $p_y$ on C-site. The nearest-neighbor hopping is $t_{pd}$ and the next-nearest-neighbor hopping is $t_{pp}$.

as artificial realizations of the Lieb lattice. Recently, the material realization of the Lieb lattice has also been proposed in a covalent-organic framework [33, 34].

In solid-state physics, a copper-oxide, $CuO_2$, plane is the basic structural unit of the high-temperate cuprate superconductors [43, 44]. A $CuO_2$ plane is layers of Cu and O that are arranged as a square lattice with the lattice side of around 4 Å; see, e.g. Refs. [43, 44, 45, 46, 47, 48, 97]. Cuprates are synthesized materials which exhibit superconductivity above the critical temperatures 50 K. The crystal structure of cuprates includes the copper oxide, an alkaline earth or a rare earth element, and an arbitrary collection of elements, which can be in general in nonrational stoichiometric proportions [44]. The $CuO_2$ planes are separated by layers of the so-called charge reservoir units. These units are responsible for neutralizing $CuO_2$ planes [43, 44]. The chemistry of $CuO_2$ at stoichiometry includes copper and oxygen atoms with the valence state of 2- for both atoms [44]. The electronic configuration of Cu atoms is a singly occupied $3d_{x^2-y^2}$ orbital. It forms a single band by hybridization between this orbital and the $O2p_x$ and $O2p_y$ orbitals [43, 44, 60]; see Fig. 2.3.
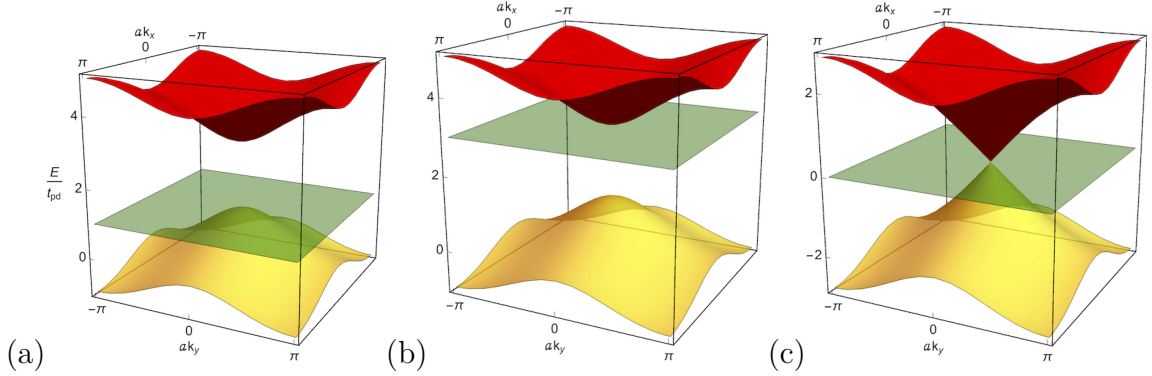
Figure 2.4: Electronic band structure of the Lieb lattice for vanishing next-nearest-neighbor hopping, $t_{pp} = 0$, in the first Brillouin zone: (a) $V_{dp} > 0$, (b) $V_{dp} < 0$, (c) $V_{dp} = 0$. The lattice constant is denoted by $a$. Panel (a) corresponds to the cuprate lattice. In panel (c) the low-energy spectrum shows a Dirac cone at the point $\Gamma = (0,0)$.

## 2.2.2 Electronic band structure

To analyze the electronic band structure of the cuprate lattice, we utilize the tight-binding approximation and calculate the so-called tight-binding Hamiltonian. The tight-binding approximation is based on Bloch's theorem, and provides a linear combination of the atomic orbitals [98]. Here we consider Fig. 2.3, showing a unit cell of the cuprate lattice to describe a $CuO_2$ plane. The unit cell includes three sites: A-site for the $d_{x^2-y^2}$ orbital, B-site for the $p_x$ orbital, and C-site for the $p_y$ orbital. We use the integer numbers $n$ and $m$, as the unit-cell indices for the $x$- and $y$ direction in real space, respectively.

In this Section, we only take into account the nearest-neighbor hopping, $t_{pd}$, and assume that the next-nearest-neighbor hopping, $t_{pp}$, vanishes. We will discuss the effect of $t_{pp}$ further in Chap. 3. For each site we can consider an on-site energy as $V_A \equiv V_d$ and $V_B = V_C \equiv V_p$. For each unit cell we consider three localized states $|A_{mn}\rangle$, $|B_{mn}\rangle$, and $|C_{mn}\rangle$; cf. Ref. [26]. Accordingly, we introduce three sets of creation and annihilation operators $\{a^\dagger_{nm}, a_{nm}\}$, $\{b^\dagger_{nm}, b_{nm}\}$, and $\{c^\dagger_{nm}, c_{nm}\}$ fulfilling the fermionic algebra [90]. We refer to them further as the site operators. The spinless tight-binding Hamiltonian for $t_{pp} = 0$ in real space reads:

$$\hat{H}_{\text{tb}}^{(t_{pp}=0)} = \sum_{nm} \Big[ V_d a^\dagger_{nm} a_{nm} + V_p b^\dagger_{nm} b_{nm} + V_d c^\dagger_{nm} c_{nm} + t_{pd} a^\dagger_{nm} b_{nm} + t_{pd} b^\dagger_{nm} a_{nm}$$

$$- t_{pd} a^\dagger_{nm} c_{nm} - t_{pd} c^\dagger_{nm} a_{nm} - t_{pd} a^\dagger_{nm} b_{n-1,m} - t_{pd} b^\dagger_{n-1,m} a_{nm}$$

$$+ t_{pd} a^\dagger_{nm} c_{n,m-1} + t_{pd} c^\dagger_{n,m-1} a_{nm} \Big]. \tag{2.14}$$

In general, the number of the cells in the $x$- and $y$ direction is $N$ and $M$, respectively. Here we are primarily interested in the case $M = N$. We take the Fourier transform

$$a_{\mathbf{k}} \equiv a_{k_x,k_y} = \frac{1}{\sqrt{NM}} \sum_{nm} a_{nm} e^{i(nk_x + mk_y)} \tag{2.15}$$

for each creation and annihilation operator, see, e.g., Ref. [26], where $\mathbf{k} = (k_x, k_y)$. We write the tight-binding Hamiltonian (2.14) in momentum space as

$$\begin{aligned}
\hat{H}_{\mathrm{tb}}^{(t_{pp}=0)} = \sum_{\mathbf{k} \in 1.\mathrm{BZ}} & \Big[ V_d a_{\mathbf{k}}^\dagger a_{\mathbf{k}} + V_p b_{\mathbf{k}}^\dagger b_{\mathbf{k}} + V_d c_{\mathbf{k}}^\dagger c_{\mathbf{k}} + t_{pd} a_{\mathbf{k}}^\dagger b_{\mathbf{k}} + t_{pd} b_{\mathbf{k}}^\dagger a_{\mathbf{k}} \\
& - t_{pd} a_{\mathbf{k}}^\dagger c_{\mathbf{k}} - t_{pd} c_{\mathbf{k}}^\dagger a_{\mathbf{k}} - t_{pd} e^{-ik_x} a_{\mathbf{k}}^\dagger b_{\mathbf{k}} - t_{pd} e^{ik_x} b_{\mathbf{k}}^\dagger a_{\mathbf{k}} \\
& + t_{pd} e^{-ik_y} a_{\mathbf{k}}^\dagger c_{\mathbf{k}} + t_{pd} e^{ik_y} c_{\mathbf{k}}^\dagger a_{\mathbf{k}} \Big],
\end{aligned} \tag{2.16}$$

for $k_x, k_y \in [-\pi/a, \pi/a)$, defining the first Brillouin zone (1.BZ), where $a$ denotes the lattice constant. Next, we define two functions $f(k_x) = t_{pd}(1 - e^{-ik_x})$ and $g(k_y) = t_{pd}(1 - e^{-ik_y})$, and write Eq. (2.16) as

$$\hat{H}_{\mathrm{tb}}^{(t_{pp}=0)} = \sum_{\mathbf{k} \in 1.\mathrm{BZ}} \begin{pmatrix} a_{\mathbf{k}}^\dagger & b_{\mathbf{k}}^\dagger & c_{\mathbf{k}}^\dagger \end{pmatrix} \begin{pmatrix} V_d & f(k_x) & -g(k_y) \\ f^*(k_x) & V_p & 0 \\ -g^*(k_y) & 0 & V_p \end{pmatrix} \begin{pmatrix} a_{\mathbf{k}} \\ b_{\mathbf{k}} \\ c_{\mathbf{k}} \end{pmatrix}, \tag{2.17}$$

where $f^*$ and $g^*$ denote the complex conjugate of $f$ and $g$, respectively.

The eigenvalues of the tight-binding Hamiltonian (2.17) exhibit the electronic band structure of the cuprate lattice for $t_{pp} = 0$:

$$E_{\mathbf{k}}^{(\mathrm{U})} = \frac{1}{2}(V_d + V_p) + \sqrt{|f(k_x)|^2 + |g(k_y)|^2 + \frac{1}{4} V_{dp}^2}, \tag{2.18}$$

$$E_{\mathbf{k}}^{(\mathrm{F})} = V_p, \tag{2.19}$$

$$E_{\mathbf{k}}^{(\mathrm{L})} = \frac{1}{2}(V_d + V_p) - \sqrt{|f(k_x)|^2 + |g(k_y)|^2 + \frac{1}{4} V_{dp}^2}, \tag{2.20}$$

where $V_{dp} \equiv V_d - V_p$ is the charge-transfer energy, $|f(k_x)|^2 = 4 t_{pd}^2 \sin^2(k_x/2)$, and $|g(k_y)|^2 = 4 t_{pd}^2 \sin^2(k_y/2)$. The indices U, F, and L stand for the upper-, flat-, and lower band, respectively. The solution (2.19) reveals a completely flat band with an energy level that is determined by the on-site energy of the $p$ orbitals, $V_p$. Figure 2.4 shows the band structures (2.18)-(2.20) in the first Brillouin zone. For $V_{dp} > 0$ the flat band is tangent to the maximum of the lower band, and both are separated from the upper band; cf. Fig. 2.4(a). This is the relevant structure for the cuprate lattice. However, for $V_{dp} < 0$ the flat band is tangent to the upper band, and both are separated from the lower band; cf. Fig. 2.4(b). Finally, for $V_{dp} = 0$ the three bands intersect each other at the point $\Gamma = (0,0)$. Here the low-energy spectrum reveals a Dirac cone at $\Gamma$-point; see Fig. 2.4(c).

## 2.2.3 Fermi-Hubbard model in a nutshell

A very simplified model to describe simple metals considers a number of electrons that interact via the Coulomb potential in a volume subject to a periodic boundary condition. The ions are assumed to be singly positively charged that form a homogenous distribution. Here, the Bloch functions reduce to plane waves and the electrons are limited in broad energy bands. This is the so-called jellium model where the crystal structure is neglected; see, e.g., Refs. [5, 90]. However, in a lattice, the crystal structure and the Brillouin-zone effects are crucial. Electrons near the Fermi surface with low mobility are subject to narrow energy bands [90, 99]. As a result, it would be inappropriate to use the plane waves to describe the energy structures. Instead, the tight-binding picture provides a better approximation to describe the electronic band structure by introducing the tunneling (hopping) of particles between different orbitals on a lattice site. This approximation together with taking into account the on-site Coulomb interactions result in an effective low-energy Hamiltonian that contains an interplay of the Pauli exclusion principle, kinetic energy, Coulomb interactions, and the lattice structure [44, 90, 99, 100, 101, 102, 103]:

$$\hat{H} = \sum_{\substack{\langle i,j \rangle \\ \sigma \in \{\uparrow,\downarrow\}}} t_{ij} c_{i,\sigma}^\dagger c_{j,\sigma} + U_{\mathrm{C}} \sum_i \hat{n}_{i\uparrow} \hat{n}_{i\downarrow}. \tag{2.21}$$

This is the two-dimensional Fermi-Hubbard model, first introduced in the 1960s [104, 105, 106, 107, 108]. Here, $c^\dagger$ and $c$ are the fermionic creation and annihilation operators, respectively, $t_{ij}$ is the hopping parameter, $\sigma \in \{\uparrow,\downarrow\}$ is a spin index, $\langle i,j \rangle$ denotes the nearest neighbors, and $U_{\mathrm{C}}$ is the on-site Coulomb interaction strength which can be attractive, $U_{\mathrm{C}} < 0$, or repulsive, $U_{\mathrm{C}} > 0$. Moreover, $\hat{n}_{i\uparrow} = c_{i\uparrow}^\dagger c_{i\uparrow}$ and $\hat{n}_{i\downarrow} = c_{i\downarrow}^\dagger c_{i\downarrow}$ are the particle number operators.

The Hamiltonian (2.21) can be extended further to include the next-nearest-neighbor hopping terms, $t_{ij}'$, or to include the off-site interactions, $V_{\mathrm{C}}$, referring to the interactions between fermions on nearest neighboring sites; see, e.g. Refs. [101, 103, 109, 110, 111, 112, 113, 114]. In addition, when the ratio $t_{ij}/U_{\mathrm{C}}$ is very small, the hopping effect can be taken into account as a perturbation. This leads to the so-called *t-J* model, where *J* is the antiferromagnetic exchange coupling strength [44, 61]. If the *t-J* model allows a small number of double occupancies, this results in the *t-J-U* or *t-J-U-V* models; see, e.g., Ref. [62].

Finally, it is worth mentioning that the effective single-band Hamiltonian (2.21) has various applications in solids and cold-atom systems. It can be utilized to describe transition metals, band magnetism, Mott transitions, and high-temperature superconductivity; see, e.g., Refs. [99, 101, 115]. Moreover, as discussed above, the copper-oxide plane is a main unit of the high-temperature cuprate superconductors possessing a square lattice structure. Following P. W. Anderson, see, e.g. Refs. [47, 116], it has been accepted by many physicists[2] that the Fermi-Hubbard Hamiltonian

---

[2]However, this idea has not yet been accepted by the whole community, and it is still under

or the *t-J* model of the $CuO_2$ plane provides a qualitatively adequate description of the cuprate superconductors [43, 47, 60, 117, 118, 119, 120]. Going beyond the high-temperature cuprate superconductors, we also mentioned that the square lattice can be engineered via optical lattices. This provides a platform to realize the Cooper-pairing mechanism for a cold-atom system in a cuprate lattice. However, we note that for cold atoms in an optical lattice, the single-band Hubbard model suffers a limitation, that for the scattering lengths comparative to the size of the Wannier functions it cannot describe the two-particle physics adequately. Here one needs to introduce the multi-band notion [102]. Also, the Hubbard model is incapable of describing the maximum time scale of an experiment where inelastic scatterings play roles [102].

## 2.3 Efimov physics

### 2.3.1 Thomas collapse and Efimov effect

In 1935, L. H. Thomas showed that two neutrons and one proton with a symmetric wave function that interact attractively through a sufficiently short-range force can form a bound state with arbitrarily large binding energy [121]. With this, he could estimate the range of the nuclear forces. This finding, which does not hold for two particles, is referred to as Thomas collapse or fall of the particles to the center [73]. Two decades later, Skorniakov and Ter-Martirosian considered the three-body problem with short-range interactions and calculated the neutron-deuteron scattering cross section by constituting an integral equation in momentum space [122]. Afterwards, in a seminal paper of 1970, Ref. [71], V. Efimov showed that three bosons that interact attractively via short-range interactions in vacuum form three-body bound states at interaction strengths that are not yet sufficient to support two-body bound states; see Fig. 2.5. These three-body bound states are referred to as Efimov states, and this unexpected phenomenon is referred to as Effimov effect. This result enabled Efimov to explain the tritium nucleus as a bound state of two neutrons and one proton, and also the Hoyle state of $^{12}C$ as a bound state of three helium nuclei [73]. In what follows we aim to give a short overview of the Efimov effect.

We recall that there exist many short-range forces governing physical systems. By "short range" we mean an interaction decaying faster than $1/r^3$, where $r$ denotes the distance of two particles in real space [73]. For example, in atomic systems, the van der Waals interaction between two neutral atoms separated with distance $r$ has a short range [95]. This potential decays as $1/r^6$ and has a range of the interaction within the order of nanometer. In nuclear physics, the Coulomb potential between two nucleons separated with distance $r$ is screened as $e^{-r}/r$, referred to as Yukawa

---

serious debates; see, e.g., Ref. [44].
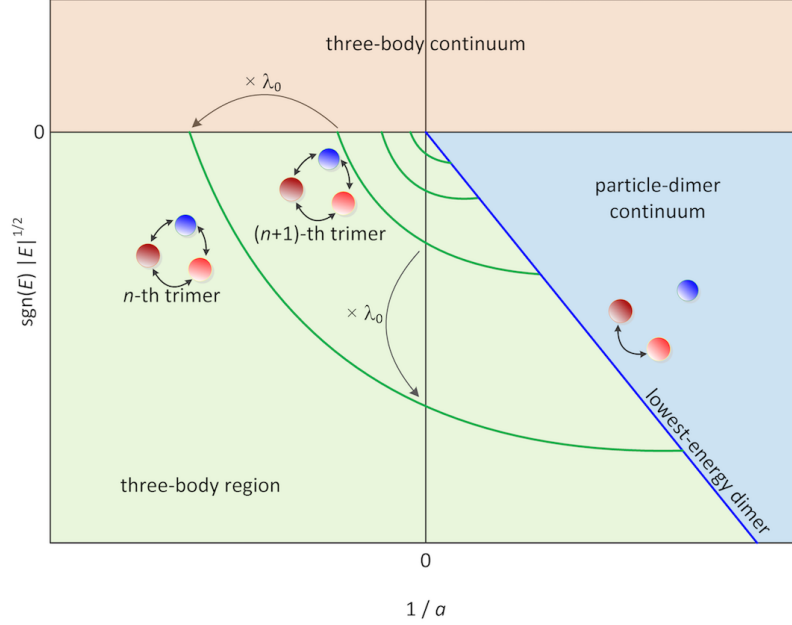
Figure 2.5: Illustration of the so-called Efimov plot for three bosons in vacuum that interact attractively via short-range interactions: $\mathrm{sgn}(E)\sqrt{|E|}$ vs $1/a$, where $E$ is energy, $a$ is an $s$-wave scattering length, and $\mathrm{sgn}(E) = E/|E|$. The single blue line is the lowest-energy two-body bound state. The blue region shows the two-body bound-state continuum. The discrete green curves show the three-body bound states, obeying the Efimov scaling law. The parameter $\lambda_0$ denotes the Efimov scaling factor. In principle, there are an infinite number of Efimov states forming in the green three-body region. The red region shows the three-body continuum.

potential [123]. This has a short range within the order of femtometer. In quantum mechanics, the quantum fluctuations of the kinetic energy, referred to as zero-point energy, are against the attractive forces and tends to overcome the short-range interactions which can bind the particles. If the attractive interactions are strong enough, the two particles can form a bound state over a long distance much larger than the range of the interactions. Such interactions which tend to form weakly bound states are referred to as nearly-resonant [73].

## 2.3.2 Efimov attraction

Efimov considered three equal-mass particles in vacuum obeying Bose-Einstein statistics and interacting attractively near resonant via short-range interactions. To find out the nature of the effective three-body potential, he assumed the vanishing total momentum and the $s$-wave symmetry of states. He employed a result of Bethe and Peierls [124], and simplified the problem to three noninteracting particles with a wave function $\psi$, that is subject to a boundary condition for very small relative dis-
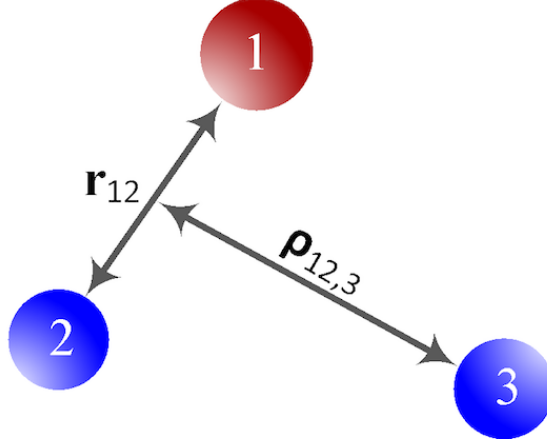
Figure 2.6: Visualization of the Jacobi coordinates $\mathbf{r}_{12}$ and $\boldsymbol{\rho}_{12,3}$ for three particles in real space. Here, $\mathbf{r}_{12} = \mathbf{r}_2 - \mathbf{r}_1$ and $\boldsymbol{\rho}_{12,3} = \mathbf{r}_3 - (m_1\mathbf{r}_1 + m_2\mathbf{r}_2)/(m_1 + m_2)$, where $\mathbf{r}_1$, $\mathbf{r}_2$, and $\mathbf{r}_3$ denote the position of the particles with masses $m_1$, $m_2$, and $m_3$, respectively. The other Jacobi variables are obtained by cyclic permutations.

tances. The noninteracting approximation is justified in the region much larger than the range of the interactions, where the relative motion of two particles is assumed to be free. The boundary condition that is imposed on the corresponding Schrödinger equation is referred to as Bethe-Peierls boundary condition, which fixes the phase of the wave function as a definite value for small distances [124]. Efimov constituted the Schrödinger equation in real space and in terms of the Jacobi coordinates; i.e., in terms of the relative distance of a pair, $\mathbf{r}_{12}$, and the distance of the third particle to the center-of-mass of that pair, $\boldsymbol{\rho}_{12,3}$; see Fig. 2.6. He imposed the Bethe-Peierls boundary condition

$$\lim_{r_{12} \to 0^+} \frac{\partial}{\partial r_{12}} \ln[r_{12}\psi(r_{12}, \rho_{12,3})] = \frac{1}{a}, \tag{2.22}$$

where $a$ denotes an $s$-wave scattering length.

Next, Efimov utilized the bosonic exchange symmetry of $\psi$, and decomposed it into three Faddeev components [125]:

$$\psi = \chi(\mathbf{r}_{12}, \boldsymbol{\rho}_{12,3}) + \chi(\mathbf{r}_{23}, \boldsymbol{\rho}_{23,1}) + \chi(\mathbf{r}_{31}, \boldsymbol{\rho}_{31,2}), \tag{2.23}$$

subject to the Bethe-Peierls boundary condition for each component, where the function $\chi$ satisfies the Schrödinger equation. He expanded the function $\chi$ in partial $s$-waves and rewrote the Schrödinger equation in hyper-spherical coordinates $(R, \alpha)$, subject to the boundary conditions for $\alpha = 0$ and $\alpha = \pi/2$. Here, $R$ is the hyper-radius, $R^2 = r_{12}^2 + \rho_{12,3}^2$, and $\alpha$ is the hyper-angle, $\tan\alpha = r_{12}/\rho_{12,3}$ [75, 126]. Efimov found that the Schrödinger equation in hyper-spherical coordinates is separable in terms of the variables $R$ and $\alpha$. He solved the corresponding equations,

imposed the boundary conditions, and finally found that the effective three-body potential behaves as $-1/mR^2$, where $m$ is the mass of the particles and $R$ can be interpreted as the average distance of the three particles. In Appendix B of Sec. 7.1 we have sketched the details of the Efimov's derivation. This attractive potential that constitutes the basis of the Efimov effect is referred to as Efimov attraction.

We note that Efimov investigated the three-body problem in a three-dimensional space. In 2001, Nielsen *et al.* proved that the Efimov effect can occur in a $d$-dimensional space, where $2.3 < d < 3.8$ [72]. The only integer dimension in this interval is $d = 3$, implying that there is no Efimov effect for one- and two-dimensional space. Studying the fractal dimensions and their physical interpretations are still interesting and ongoing topics [127]. Although there is no Effimov attraction for one- and two-dimensional systems, there exist some universal states in these dimensions. This is beyond the scope of this Thesis, and we refer the reader to Ref. [73] for a detailed discussion.

### 2.3.3 Efimov scaling law

Not only is the Efimov attraction determined universally by the mass of the particles, $m$, but also it is scale invariant. This implies that a three-body bound state can be excited to another state which is described by a universal scaling law. More concretely speaking, if we apply the scaling transformation $R \mapsto \lambda_0 R$, where $\lambda_0$ is a scaling factor, the Schrödinger equation governing the Efimov attraction with eigenenergy $E < 0$ also admits the scaled energy $\lambda_0^2 E$; see Appendix B in Sec. 7.1. This implies that there exists in principle an infinite number of three-body bound states [71]. As a result, the spectrum is not bounded from below, retrieving Thomas collapse. This problem has been resolved in several ways. For example, one can impose a new boundary condition on the three-body solutions [128], or define a momentum cutoff on the Schrödinger equation governing the three particles in momentum space [129]. All these solutions introduce a new length scale to the problem, which is referred to as three-body parameter. This parameter fixes the range of the three-body interactions and prevents the three-body system collapsing on itself [73, 130, 131].

Efimov also found that there is a geometric scaling law governing the three-body bound states [71]. To show that, he approximated the solution of the hyper-radial equation for a very small hyper-radius $R_0$ with eigenenergy $E_1$ by power-law functions of the hyper-radius $R$. As a result, the three-particle wave function reveals log-periodic oscillations, which are scale invariant if the scaling factor $\lambda_0$ is chosen to be $\exp(\pi/|s_0|) \approx 22.7$, where $|s_0| \approx 1.00624$; see Appendix B of Sec. 7.1. This implies that the three-body bound states form a geometric series of energy as $E_{n+1} = E_1/\lambda_0^{2n}$, where $n \in \mathbb{N}$ is an index labeling the discrete spectrum. In general, the Efimov discrete scaling law reads as

$$\frac{E_{n+1}}{E_n} = \frac{1}{\lambda_0^2}, \tag{2.24}$$

$$\frac{a_{n+1}}{a_n} = \lambda_0, \tag{2.25}$$

where $a$ denotes an $s$-wave scattering length; see Fig. 2.5.

The value of the parameter $s_0$ depends on the mass of the three particles. It is also sensitive whether all three pairs interact resonantly, or only two pairs are interacting. For the $s$-wave symmetry of states, if we have a system of three species with two-resonantly interacting pairs, then $s_0$ is the purely imaginary root of the transcendental equation

$$\cos\left(\frac{\pi}{2}s_0\right) = \frac{2}{\sin 2\vartheta}\frac{\sin(\vartheta s_0)}{s_0}, \tag{2.26}$$

where $\vartheta = \arcsin[(m_2/m_1)/(1 + m_2/m_1)]$, $\vartheta \in [0, \pi/2]$. If all three species are resonantly interacting, we obtain $s_0$ as the purely imaginary root of the equation

$$\left[\cos\left(\frac{\pi}{2}s_0\right) - \frac{2}{\sin 2\vartheta}\frac{\sin(\vartheta s_0)}{s_0}\right]\cos\left(\frac{\pi}{2}s_0\right) = \frac{8}{\sin^2 2\gamma}\frac{\sin^2(\gamma s_0)}{s_0^2}, \tag{2.27}$$

where $\gamma = \arcsin\{\sqrt{(m_1/m_2)/[2(1 + m_2/m_1)]}\}$, $\gamma \in [0, \pi/4]$. For a proof, see Ref. [73].

### 2.3.4 Experimental signatures

For almost thirty years it was thought that observing an experimental signature of the Efimov effect is not feasible, as the nearly-resonant interactions between particles could not be satisfied. However, in the beginning of the twenty-first century, technical advances in the trapping and cooling of atoms [95, 96] as well as in the Feshbach resonances [132, 133] led to the observation of the Efimov effect in ultracold atomic gases. The first convincing evidence of an Efimov state was confirmed in 2006 by Innsbruck group [76]. They considered a gas of cesium atoms evaporatively cooled to temperature of about 10 nK. An Efimov state was observed as a giant three-body loss resonance [134]. In 2014, the Innsbruck group observed an excited Efimov state by increasing the magnetic field, and confirmed the Efimov scaling factor [134, 135]. Afterwards, the Efimov effect was also observed in ultracold atomic mixtures [77, 78, 79] and in helium beams experiments [80, 81]. In 2016, two excited Efimov states were observed in an ultracold mixture of $^6$Li and $^{133}$Cs [136], confirming the Efimov scaling factor. Recently, the Efimov states of three interacting photons were also observed in cold gases of Rydberg atoms [137, 138]. This observation can be considered as a realization of the control of quantum many-body states of light whose interactions are mediated by Rydberg states of atoms.

In solid-state and condensed-matter physics we can mention two efforts, investigating the Efimov effect in quantum spin systems [139, 140] as well as in excitons [141]. In 2013, Nishida *et al.* considered the Heisenberg model in three spatial dimensions and investigated the three-body bound states of magnons in a ferromagnetic quantum spin system [142, 143]. They utilized the quadratic dispersion relation of magnons in a ferromagnet system [140, 144], and assumed the anisotropic exchange coupling and single-ion anisotropy [73]. With this, they fulfilled the near-resonant interactions, and obtained a spectrum in agreement with the Efimov scaling law. Another attempt to study the Efimov effect in solid-state physics is Ref. [145], where the authors considered the excitonic $N$-body bound states, called poly-excitons. Here, the binding energy of ploy-excitons normalized to the exciton Rydberg energy in a diamond crystal up to $N = 6$ was measured and a well-agreement compared to silicon was found, suggesting a universal behavior of ploy-excitons. However, the comparison to Efimov effect is not clear, as the excitonic interactions are typically non-resonant [73].

Finally, the Efimov effect has been generalized to more than three particles [73, 146]. It was shown that for a critical mass ratio, three fermions and a lighter particle form a four-body bound state [147]. The four-body bound states of two heavy and two light bosons for different mass ratios was also investigated in Ref. [148]. The formation of a five-body bound state in fermionic mixtures was discussed in Ref. [149]. The whole physical discussions and generalizations of the Efimov effect is usually referred to as Efimov physics [73, 74, 75].

## 2.4   Summary

In this Chapter, we have presented the most important concepts and phenomena that wee need in the Thesis. We have reviewed the original Cooper problem, and have discussed how a weak attractive interaction between two electrons leads to a bound state. We have presented a formalism in momentum space to solve the Cooper problem. Moreover, we have discussed the cuprate lattice, its geometry and electronic band structure, and have reviewed the Fermi-Hubbard model briefly. Finally, we have discussed the Efimov effect, and have shown how three bosons that interact attractively in vacuum via short-range interactions form an infinite number of three-body bound states. We have also reviewed the experimental signatures of the Efimov effect in ultracold atomic gases.

# Chapter 3

# Cooper problem in a cuprate lattice

The main aim of this Chapter is to solve the Cooper problem in a two-dimensional cuprate lattice. We are primarily interested in a copper-oxide, $CuO_2$, plane which is a main structural unit of the high-temperature cuprate superconductors. We calculate the ground-state energy of a Cooper pair for strongly repulsive on-site interactions, and demonstrate *a priori* that the corresponding wave function supports an orbital symmetry of $d_{x^2-y^2}$. We also show that the next-nearest-neighbor hopping changes the curvature of the dispersive bands, resulting in a Fermi-surface geometry that is in better agreement with experiments. Finally, we propose a scenario to observe the experimental signature of the $d$-wave Cooper pairs for a cold-atom system in a cuprate lattice using the techniques of time-of-flight image and noise correlations[1].

## 3.1 Next-nearest-neighbor hopping and electronic band structure

For the cuprate lattice, see Fig. 2.3, the next-nearest-neighbor hopping, $t_{pp}$, leads to eight new tunneling terms between the $p_x$ and $p_y$ orbitals in the spinless tight-binding Hamiltonian (2.17):

$$\hat{H}_{\text{tb}} = \sum_{\mathbf{k} \in 1.\text{BZ}} \begin{pmatrix} a_{\mathbf{k}}^{\dagger} & b_{\mathbf{k}}^{\dagger} & c_{\mathbf{k}}^{\dagger} \end{pmatrix} \begin{pmatrix} V_d & f(k_x) & -g(k_y) \\ f^*(k_x) & V_p & -\tau f^*(k_x)g(k_y) \\ -g^*(k_y) & -\tau f(k_x)g^*(k_y) & V_p \end{pmatrix} \begin{pmatrix} a_{\mathbf{k}} \\ b_{\mathbf{k}} \\ c_{\mathbf{k}} \end{pmatrix},$$

$$(3.1)$$

where $f(k_x) = t_{pd}(1 - e^{-ik_x})$, $g(k_y) = t_{pd}(1 - e^{-ik_y})$, and $\tau = t_{pp}/t_{pd}^2$; see Appendix C in Sec. 7.1 for derivation. The characteristic equation associated with the tight-binding Hamiltonian is a cubic equation whose solutions exhibit the electronic band

---

[1] Parts of this Chapter will be published in [S3].
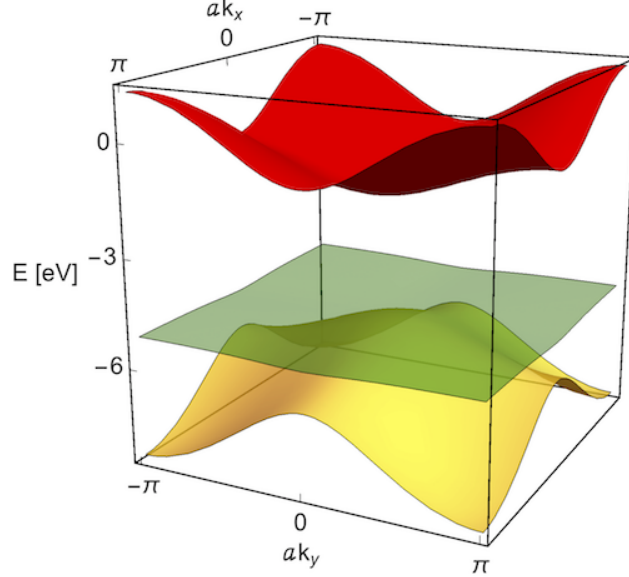
Figure 3.1: Electronic band structure of the cuprate lattice for the lattice parameters $V_{dp} = 3.45$ eV, $t_{pd} = 1.13$ eV, and $t_{pp} = 0.8$ eV in the first Brillouin zone. The lattice constant is denoted by $a$.

structure. These solutions are not as straightforward as of the tight-binding Hamiltonian for $t_{pp} = 0$. Following the mathematical formalism discussed in Ref. [150], we find the three solutions analytically as

$$E_{\mathbf{k}}^{(\mathrm{U})} = 2\sqrt{-p(k_x, k_y)} \cos\left(\frac{\theta(k_x, k_y)}{3}\right) - \frac{c(k_x, k_y)}{3}, \tag{3.2}$$

$$E_{\mathbf{k}}^{(\mathrm{F})} = 2\sqrt{-p(k_x, k_y)} \cos\left(\frac{\theta(k_x, k_y) + 4\pi}{3}\right) - \frac{c(k_x, k_y)}{3}, \tag{3.3}$$

$$E_{\mathbf{k}}^{(\mathrm{L})} = 2\sqrt{-p(k_x, k_y)} \cos\left(\frac{\theta(k_x, k_y) + 2\pi}{3}\right) - \frac{c(k_x, k_y)}{3}, \tag{3.4}$$

where the indices U, F, L stand for the upper-, flat-, and lower band, respectively, and the functions $c(k_x, k_y)$, $p(k_x, k_y)$, and $\theta(k_x, k_y)$ are represented in Appendix C of Sec. 7.1.

Figure 3.1 shows the electronic band structure for the lattice parameters $V_{dp} = 3.45$ eV, $t_{pd} = 1.13$ eV, and $t_{pp} = 0.8$ eV. By comparing Eqs. (2.18)-(2.20) with Eqs. (3.2)-(3.4) we find that $t_{pp} \neq 0$ deforms the flat band, and changes the curvature of the dispersive upper- and lower band. In Sec. 3.3, we demonstrate how the Fermi surface is affected by including a nonvanishing $t_{pp}$.

## 3.2 Fermi-Hubbard model in a cuprate lattice

Following the Anderson's proposal, see, e.g. Refs. [47, 116], the single-band Fermi-Hubbard model of a $CuO_2$ plane has been considered widely to provide a qualitatively adequate description of the cuprate superconductors [43, 47, 60, 117, 119, 120]. In this Section we take this proposal, and solve the Cooper problem for repulsive on-site interactions in the upper band of the cuprate lattice. Our main objective is to take the singlet-state wave function of a Cooper pair, and find the ground-state solution *a priori*. To do this, in what follows we establish the general formulation of the Fermi-Hubbard model for three bands, and reduce it to a submanifold of the upper band, where the total momentum of a pair vanishes.

### 3.2.1 General formulation

To constitute the Fermi-Hubbard model of a $CuO_2$ plane, we note that for each eigenvalue of the tight-binding Hamiltonian there exists a corresponding normalized eigenvector $\mathbf{v}_\mathbf{k}^{(U)} = (v_\mathbf{k}^{(1;U)}, v_\mathbf{k}^{(2;U)}, v_\mathbf{k}^{(3;U)})$, $\mathbf{v}_\mathbf{k}^{(F)} = (v_\mathbf{k}^{(1;F)}, v_\mathbf{k}^{(2;F)}, v_\mathbf{k}^{(3;F)})$, and $\mathbf{v}_\mathbf{k}^{(L)} = (v_\mathbf{k}^{(1;L)}, v_\mathbf{k}^{(2;L)}, v_\mathbf{k}^{(3;L)})$ associated with the upper-, flat-, and lower band, respectively. We define three sets of fermionic creation and annihilation operators $\{\psi_{U,\mathbf{k}\sigma}^\dagger, \psi_{U,\mathbf{k}\sigma}\}$, $\{\psi_{F,\mathbf{k}\sigma}^\dagger, \psi_{F,\mathbf{k}\sigma}\}$, and $\{\psi_{L,\mathbf{k}\sigma}^\dagger, \psi_{L,\mathbf{k}\sigma}\}$, where $\sigma \in \{\uparrow, \downarrow\}$ is a spin index. These operators create or annihilate an electron in the upper-, flat-, or lower band, respectively. We refer to them as band operators. We note that the tight-binding Hamiltonian (3.1) in the basis spanned by the band operators is diagonal:

$$\hat{H}_{\text{tb}} = \sum_{\substack{\mathbf{k} \in 1.\text{BZ} \\ \sigma \in \{\uparrow, \downarrow\}}} \begin{pmatrix} \psi_{U,\mathbf{k}\sigma}^\dagger & \psi_{F,\mathbf{k}\sigma}^\dagger & \psi_{L,\mathbf{k}\sigma}^\dagger \end{pmatrix} \begin{pmatrix} E_\mathbf{k}^{(U)} & 0 & 0 \\ 0 & E_\mathbf{k}^{(F)} & 0 \\ 0 & 0 & E_\mathbf{k}^{(L)} \end{pmatrix} \begin{pmatrix} \psi_{U,\mathbf{k}\sigma} \\ \psi_{F,\mathbf{k}\sigma} \\ \psi_{L,\mathbf{k}\sigma} \end{pmatrix}. \quad (3.5)$$

Recall that in Sec. 2.2.2 we defined three sets of site operators $\{a_{\mathbf{k},\sigma}^\dagger, a_{\mathbf{k},\sigma}\}$, $\{b_{\mathbf{k},\sigma}^\dagger, b_{\mathbf{k},\sigma}\}$, and $\{c_{\mathbf{k},\sigma}^\dagger, c_{\mathbf{k},\sigma}\}$ corresponding to lattice sites A, B, and C, respectively. We can write the site operators in terms of the band operators using the following relation:

$$\begin{pmatrix} a_{\mathbf{k}\sigma}^\dagger \\ b_{\mathbf{k}\sigma}^\dagger \\ c_{\mathbf{k}\sigma}^\dagger \end{pmatrix} = \begin{pmatrix} v_\mathbf{k}^{(1;U)} & v_\mathbf{k}^{(2;U)} & v_\mathbf{k}^{(3;U)} \\ v_\mathbf{k}^{(1;F)} & v_\mathbf{k}^{(2;F)} & v_\mathbf{k}^{(3;F)} \\ v_\mathbf{k}^{(1;L)} & v_\mathbf{k}^{(2;L)} & v_\mathbf{k}^{(3;L)} \end{pmatrix}^{-1} \begin{pmatrix} \psi_{U,\mathbf{k}\sigma}^\dagger \\ \psi_{F,\mathbf{k}\sigma}^\dagger \\ \psi_{L,\mathbf{k}\sigma}^\dagger \end{pmatrix}$$

$$\equiv \begin{pmatrix} v_{11}(\mathbf{k}) & v_{12}(\mathbf{k}) & v_{13}(\mathbf{k}) \\ v_{21}(\mathbf{k}) & v_{22}(\mathbf{k}) & v_{23}(\mathbf{k}) \\ v_{31}(\mathbf{k}) & v_{32}(\mathbf{k}) & v_{33}(\mathbf{k}) \end{pmatrix} \begin{pmatrix} \psi_{U,\mathbf{k}\sigma}^\dagger \\ \psi_{F,\mathbf{k}\sigma}^\dagger \\ \psi_{L,\mathbf{k}\sigma}^\dagger \end{pmatrix}. \quad (3.6)$$

Next, the interaction part of the Fermi-Hubbard Hamiltonian (2.21) in momentum space reads in general as

$$\hat{\tilde{H}}_{\text{int}} = \frac{U_{\text{C}}}{\mathcal{A}} \sum_{\mathbf{k},\mathbf{p},\mathbf{q}\in 1.\text{BZ}} \alpha^\dagger_{\mathbf{k}+\mathbf{q},\downarrow} \alpha^\dagger_{\mathbf{p}-\mathbf{q},\uparrow} \alpha_{\mathbf{p},\uparrow} \alpha_{\mathbf{k}\downarrow}, \tag{3.7}$$

where $\alpha^\dagger \in \{a^\dagger, b^\dagger, c^\dagger\}$ and $\alpha \in \{a, b, c\}$ denote the creation and annihilation site operators, respectively, $\mathbf{q}$ is the momentum transfer[2], $\mathcal{A}$ is the area of the first Brillouin zone, and $U_{\text{C}}$ is the on-site interaction strength representing the local Coulomb correlation on the rare-earth sites; see, e.g., Refs. [90, 99, 101, 151, 152]. For the cuprate lattice we have three interaction Hamiltonians corresponding to three sites. The A-site includes a $d_{x^2-y^2}$ orbital configuration, where the on-site interaction strength is assumed to be $U_d$. The B- and C-site includes a $p_x$ and $p_y$ orbital configuration, respectively. We assume that the on-site interaction strength for both is $U_p$.

## 3.2.2 Fermi-Hubbard model on a submanifold of the upper band

To constitute the Fermi-Hubbard model on the upper band of the cuprate lattice, we note that we are primarily interested in a submanifold $\mathcal{S}$, where the total momentum of a Cooper pair vanishes. This assumption implies that in Eq. (3.7) we have $\mathbf{p} = -\mathbf{k}$. We define $\mathbf{k}' = \mathbf{k} + \mathbf{q}$, resulting in $\mathbf{p} - \mathbf{q} = -\mathbf{k} - \mathbf{q} = -\mathbf{k}'$. Therefore, in this submanifold the interaction Hamiltonian (3.7) reduces to

$$\hat{H}_{\text{int}} = \frac{U_{\text{C}}}{\mathcal{A}} \sum_{\mathbf{k},\mathbf{k}'\in 1.\text{BZ}} \alpha^\dagger_{\mathbf{k}'\downarrow} \alpha^\dagger_{-\mathbf{k}'\uparrow} \alpha_{-\mathbf{k}\uparrow} \alpha_{\mathbf{k}\downarrow}. \tag{3.8}$$

To investigate the problem in the upper band, we should prevent pairings in the flat- and lower band and also neglect the interband pairings. For that, we assume that the charge-transfer energy, $V_{dp} \equiv V_d - V_p$, is sufficiently large so that there is a relatively large gap between the upper band and the other two bands; see Fig. 3.1. We write the three interaction Hamiltonians associated with $d_{x^2-y^2}$, $p_x$, and $p_y$ orbital configurations in the submanifold $\mathcal{S}$ of the upper band in terms of the band operators:

$$\hat{H}^{(d)}_{\text{int}} = \frac{1}{\mathcal{A}} \sum_{\mathbf{k},\mathbf{k}'\in 1.\text{BZ}} \mathcal{V}^{(d)}_{\mathbf{k},\mathbf{k}'} \psi^\dagger_{\text{U},\mathbf{k}'\downarrow} \psi^\dagger_{\text{U},-\mathbf{k}'\uparrow} \psi_{\text{U},-\mathbf{k}\uparrow} \psi_{\text{U},\mathbf{k}\downarrow}, \tag{3.9}$$

$$\hat{H}^{(p_x)}_{\text{int}} = \frac{1}{\mathcal{A}} \sum_{\mathbf{k},\mathbf{k}'\in 1.\text{BZ}} \mathcal{V}^{(p_x)}_{\mathbf{k},\mathbf{k}'} \psi^\dagger_{\text{U},\mathbf{k}'\downarrow} \psi^\dagger_{\text{U},-\mathbf{k}'\uparrow} \psi_{\text{U},-\mathbf{k}\uparrow} \psi_{\text{U},\mathbf{k}\downarrow}, \tag{3.10}$$

---

[2] By "momentum transfer" we mean the difference of the in-state and out-state momenta of a particle; see, e.g., Ref. [89].

$$\hat{H}_{\text{int}}^{(p_y)} = \frac{1}{\mathcal{A}} \sum_{\mathbf{k},\mathbf{k}'\in 1.\text{BZ}} \mathcal{V}_{\mathbf{k},\mathbf{k}'}^{(p_y)} \psi_{\text{U},\mathbf{k}'\downarrow}^{\dagger} \psi_{\text{U},-\mathbf{k}'\uparrow}^{\dagger} \psi_{\text{U},-\mathbf{k}\uparrow} \psi_{\text{U},\mathbf{k}\downarrow}. \tag{3.11}$$

The interaction functions are

$$\mathcal{V}_{\mathbf{k},\mathbf{k}'}^{(d)} = U_d v_{11}(\mathbf{k}')v_{11}(-\mathbf{k}')v_{11}^{*}(-\mathbf{k})v_{11}^{*}(\mathbf{k}), \tag{3.12}$$

$$\mathcal{V}_{\mathbf{k},\mathbf{k}'}^{(p_x)} = U_p v_{21}(\mathbf{k}')v_{21}(-\mathbf{k}')v_{21}^{*}(-\mathbf{k})v_{21}^{*}(\mathbf{k}), \tag{3.13}$$

$$\mathcal{V}_{\mathbf{k},\mathbf{k}'}^{(p_y)} = U_p v_{31}(\mathbf{k}')v_{31}(-\mathbf{k}')v_{31}^{*}(-\mathbf{k})v_{31}^{*}(\mathbf{k}), \tag{3.14}$$

where the functions $v_{ij}$ have been introduced in Eq. (3.6), and $v_{ij}^{*}$ denotes the complex conjugate of $v_{ij}$; see Appendix D in Sec. 7.1 for derivations.

The total interaction Hamiltonian is obtained to be

$$\begin{aligned}\hat{H}_{\text{int}} &= \hat{H}_{\text{int}}^{(d)} + \hat{H}_{\text{int}}^{(p_x)} + \hat{H}_{\text{int}}^{(p_y)} \\ &= \frac{1}{\mathcal{A}} \sum_{\mathbf{k},\mathbf{k}'\in 1.\text{BZ}} \mathcal{V}_{\mathbf{k},\mathbf{k}'} \psi_{\text{U},\mathbf{k}'\downarrow}^{\dagger} \psi_{\text{U},-\mathbf{k}'\uparrow}^{\dagger} \psi_{\text{U},-\mathbf{k}\uparrow} \psi_{\text{U},\mathbf{k}\downarrow},\end{aligned} \tag{3.15}$$

where

$$\mathcal{V}_{\mathbf{k},\mathbf{k}'} = \mathcal{V}_{\mathbf{k},\mathbf{k}'}^{(d)} + \mathcal{V}_{\mathbf{k},\mathbf{k}'}^{(p_x)} + \mathcal{V}_{\mathbf{k},\mathbf{k}'}^{(p_y)}. \tag{3.16}$$

For the submanifold $\mathcal{S}$ of the upper band, the tight-binding Hamiltonian (3.5) represents the corresponding kinetic energy as

$$\hat{H}_{\text{kin}} = \sum_{\substack{\mathbf{k}\in 1.\text{BZ} \\ \sigma\in\{\uparrow,\downarrow\}}} E_{\mathbf{k}}^{(\text{U})} \psi_{\text{U},\mathbf{k}\sigma}^{\dagger} \psi_{\text{U},\mathbf{k}\sigma}, \tag{3.17}$$

where the dispersion relation $E_{\mathbf{k}}^{(\text{U})}$ is given by Eq. (3.2).

Finally, the total Fermi-Hubbard Hamiltonian constituted on the submanifold $\mathcal{S}$ of the upper band reads as

$$\begin{aligned}\hat{H}_{\text{tot}} &= \hat{H}_{\text{kin}} + \hat{H}_{\text{int}} \\ &= \sum_{\substack{\mathbf{k}\in 1.\text{BZ} \\ \sigma\in\{\uparrow,\downarrow\}}} E_{\mathbf{k}}^{(\text{U})} \psi_{\text{U},\mathbf{k}\sigma}^{\dagger} \psi_{\text{U},\mathbf{k}\sigma} + \frac{1}{\mathcal{A}} \sum_{\mathbf{k},\mathbf{k}'\in 1.\text{BZ}} \mathcal{V}_{\mathbf{k},\mathbf{k}'} \psi_{\text{U},\mathbf{k}'\downarrow}^{\dagger} \psi_{\text{U},-\mathbf{k}'\uparrow}^{\dagger} \psi_{\text{U},-\mathbf{k}\uparrow} \psi_{\text{U},\mathbf{k}\downarrow},\end{aligned} \tag{3.18}$$

where $\mathcal{V}_{\mathbf{k},\mathbf{k}'}$ is given by Eq. (3.16). Note that we have not yet introduced the Fermi sea. In the next Section, we construct the Fermi sea by introducing a chemical potential, $\mu$, and arrive at the final version of the total Hamiltonian.

## 3.3 ARPES and Fermi surface

Knowledge on the structure and geometry of the Fermi sea is crucial, as many physical properties of metals can be extracted from the low-energy electron excitations near the Fermi surface [152]. Many important data on the Fermi surface of a copper-oxide plane have been extracted from the angle-resolved photoemission spectroscopy (ARPES); see, e.g., Refs. [152, 153, 154, 155, 156, 157, 158]. A photoemission spectroscopy is a technique based on the photoelectric effect, that was originally observed by Hertz [159] and later described by Einstein [160]. To have an intuitive picture, we consider a photon that is ejected from a photon source and incident on a sample. An electron from the sample can absorb the photon and escape with the maximum kinetic energy of the photon subtracted by an amount which is responsible for keeping the electron on the valence band of the sample. The photon source can be, for example, a beam of monochromatized radiation supplied by a gas-charge lamp or a synchrotron beamline [154]. The emitted electron, which is referred to as photo-electron, is collected by an electron energy analyzer located in a finite acceptance angle. With this angle and with the kinetic energy of the photoelectron in question, one can estimate the momenta of the crystal and photoelectron. For different angles one can find the dispersion relation of the crystal by tracking the peaks detected in the ARPES spectra [154].

Experimental data reveal that cuprates at exact stoichiometry is almost not a superconductor [44]. To dope the system, i.e., to inject holes into a $CuO_2$ plane, the properties of one or more of the charge-reservoir element should be adjusted [44]. Moreover, extracted results from ARPES show that the geometry of the Fermi surface for a $CuO_2$ plane is dependent on the doping; see, e.g., Refs. [61, 120, 152, 161, 162, 163]. By changing the doping, the Fermi surface can be deformed from being quite rounded to the form of a square near the half-filling with vanishing hole doping. The desired geometry of the Fermi surface in the high-temperature cuprate superconductors consists of four Fermi arcs, and reveals nodal and antinodal regions [44, 120, 152, 154, 158, 163, 164, 165]; see Figs. 3.2(b) and 3.2(d). Following P. W. Anderson, this can be realized to a first approximation by the single-band two-dimensional Fermi-Hubbard model; see, e.g., Refs. [47, 60, 116, 120, 152]. This implies that the Fermi surface not only depends on the hole doping, but it also varies if the on-site Coulomb interaction strength, $U_C$, changes. Accordingly, the notion of the interacting- and noninteracting Fermi sea corresponds to $U_C = 0$ and $U_C \neq 0$, respectively.

As discussed in Sec. 3.1, the next-nearest-neighbor hopping, $t_{pp}$, deforms the flat band and changes the curvature of the dispersive bands, influencing the geometry of the Fermi surface constructed in a single dispersive band. It is known that the Fermi surface of the Hubbard model for the weak- and intermediate-coupling regimes is in agreement with experiments when one takes into account the next-nearest-neighbor hopping; see, e.g. Ref. [166] and references therein. Also, it has been shown that

these terms affect the superfluid to Mott-insulator transition [167, 168], and slightly change the renormalization of the quasiparticle mass [169]. To visualize the effect of the next-nearest-neighbor hopping on the Fermi surface of the cuprate lattice, we construct the Fermi surface in the upper band with dispersion relation $E_{\mathbf{k}}^{(\mathrm{U})}$ by introducing a chemical potential, $\mu$. For the noninteracting Fermi sea, the on-site Coulomb interactions are assumed to be vanishing, $U_d = U_p = 0$. The intersection of $E_{\mathbf{k}}^{(\mathrm{U})}$ and $\mu$ results in the corresponding Fermi surface. We define the noninteracting Fermi sea, $\mathrm{FS_{nonint}}$, as the momentum space occupied by electrons:

$$\mathrm{FS_{nonint}} = \left\{ \mathbf{k} \in 1.\mathrm{BZ} : \ E_{\mathbf{k}}^{(\mathrm{U})} < \mu \right\}, \tag{3.19}$$

implying that $E_{\mathbf{k}}^{(\mathrm{U})} > \mu$ shows the unoccupied region. The interacting Fermi sea is constructed when the effect of the on-site interactions is taken into account. For an interacting pair, we take into account the on-site interactions at each point in momentum space, and define the interacting Fermi sea, $\mathrm{FS_{int}}$, as

$$\mathrm{FS_{int}} = \left\{ \mathbf{k} \in 1.\mathrm{BZ} : \ 2E_{\mathbf{k}}^{(\mathrm{U})} + \frac{1}{\mathcal{A}} \mathcal{V}_{\mathbf{k},\mathbf{k}} < 2\mu \right\}, \tag{3.20}$$

where $\mathcal{A}$ is the area of the first Brillouin zone and the interaction function $\mathcal{V}_{\mathbf{k},\mathbf{k}}$ is given by Eq. (3.16) for $\mathbf{k}' = \mathbf{k}$. The unoccupied region where a pair can form is thus defined as the $\mathbf{k}$-points subject to $2E_{\mathbf{k}}^{(\mathrm{U})} + \mathcal{V}_{\mathbf{k},\mathbf{k}}/\mathcal{A} > 2\mu$.

Figure 3.2 shows the interacting Fermi surface for vanishing and nonvanishing $t_{pp}$. We find that the existence of the next-nearest-neighbor hopping has a significant effect on the curvature of the Fermi arcs. Moreover, Fig. 3.3 shows the electron density, $n_e$, as a function of the chemical potential, $\mu$. For a given value of $\mu$, we find that $n_e(t_{pp} \neq 0) \leqslant n_e(t_{pp} = 0)$, implying that we can still increase the hole doping[3] for $t_{pp} \neq 0$ while preserving the desired geometry of the Fermi surface. Therefore, our arguments are in favor of including $t_{pp} \neq 0$, leading to a geometry of the Fermi surface that is in better agreement with experimental data extracted from ARPES; cf. e.g., Refs. [152, 154, 155, 156, 157, 158].

Finally, we take into account the interacting Fermi sea, and arrive at the total Fermi-Hubbard Hamiltonian (3.18) as

$$\hat{H}_{\mathrm{tot}} = \sum_{\substack{\mathbf{k} \in 1.\mathrm{BZ} \backslash \mathrm{FS_{int}} \\ \sigma \in \{\uparrow,\downarrow\}}} \xi_{\mathbf{k}}^{(\mathrm{U})} \psi_{\mathrm{U},\mathbf{k}\sigma}^{\dagger} \psi_{\mathrm{U},\mathbf{k}\sigma} + \frac{1}{\mathcal{A}} \sum_{\mathbf{k},\mathbf{k}' \in 1.\mathrm{BZ} \backslash \mathrm{FS_{int}}} \mathcal{V}_{\mathbf{k},\mathbf{k}'} \psi_{\mathrm{U},\mathbf{k}'\downarrow}^{\dagger} \psi_{\mathrm{U},-\mathbf{k}'\uparrow}^{\dagger} \psi_{\mathrm{U},-\mathbf{k}\uparrow} \psi_{\mathrm{U},\mathbf{k}\downarrow},$$

$$\tag{3.21}$$

---

[3]To define the hole doping, $\delta_h$, here we follow this convention: For the half-filling, the electron density $n_e = 1/2$ and the hole doping is defined to be vanishing, $\delta_h = 0$. As we decrease $n_e$, we inject more holes into the desired momentum space, and increase $\delta_h$. Here the hole doping is obtained as $\delta_h = 1/2 - n_e$, for $0 \leqslant n_e \leqslant 1/2$.
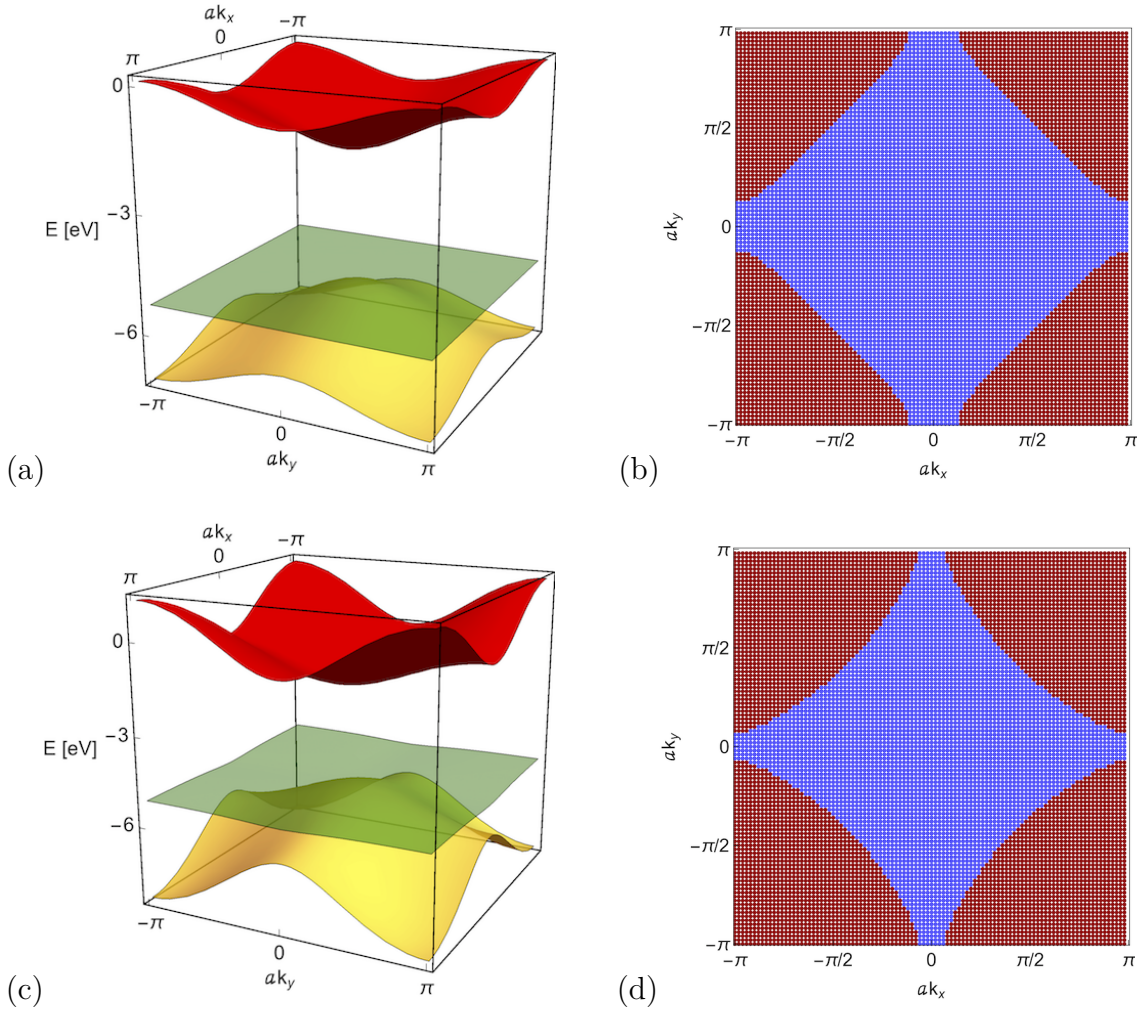
Figure 3.2: Electronic band structure and interacting Fermi surface of a cuprate lattice in the first Brillouin zone for $V_{dp} = 3.45$ eV and $t_{pd} = 1.13$ eV: (a) Band structure for $t_{pp} = 0$; (b) the corresponding Fermi surface for $\mu \approx -0.679$ eV; (c) band structure for $t_{pp} = 0.8$ eV; and (d) the corresponding Fermi surface for $\mu \approx -0.679$ eV. For $t_{pp} \neq 0$ the flat band is deformed, and the curvature of the dispersive bands is changed. Blue and red dots in panels (b) and (d) show the occupied and unoccupied states, respectively.
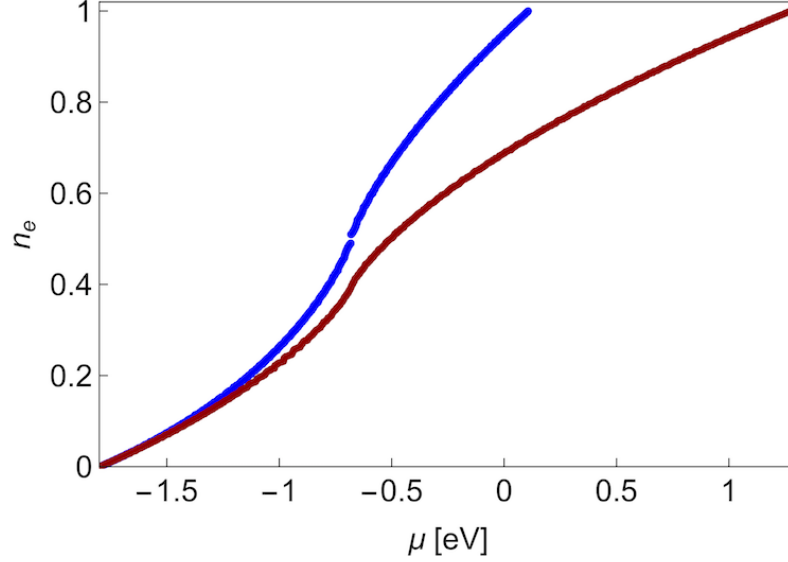
Figure 3.3: Electron density, $n_e$, vs chemical potential, $\mu$, in units of eV, for a single upper band of the cuprate lattice, where $V_{dp} = 3.45$ eV and $t_{pd} = 1.13$ eV. The blue curve corresponds to $t_{pp} = 0$, and the red curve corresponds to $t_{pp} = 0.8$ eV.

where $\xi_{\mathbf{k}}^{(\mathrm{U})} \equiv E_{\mathbf{k}}^{(\mathrm{U})} - \mu$, and the symbol $1.\mathrm{BZ} \setminus \mathrm{FS_{int}}$ denotes the first Brillouin zone where the interacting Fermi sea has been excluded.

## 3.4 Cooper problem and pairing equation

As discussed in Chap. 2, the Cooper problem and its solution show that for an arbitrarily weak attractive interaction, two electrons that are immersed in an inert Fermi sea form a bound state that supports an orbital *s*-wave symmetry. The effective attraction is due to the electron-phonon interaction that is dominant over the screened Coulomb repulsion. The Cooper problem is usually considered as a weak-coupling limit of the electron pairing. On the other hand, experimental data as well as different theoretical approaches reveal that the Cooper pairing in a cuprate lattice is mainly due to the strongly repulsive electron-electron interaction; see, e.g. Refs. [60, 115, 172, 173, 174, 175]. Our objective is to show an example of the Cooper problem that includes the strong-coupling limit of the repulsive on-site interactions for the single-band Fermi-Hubbard model (3.21). To this end, we follow the Cooper problem and consider the singlet-state ansatz as

$$|\Phi\rangle = \sum_{\boldsymbol{\kappa} \in 1.\mathrm{BZ} \setminus \mathrm{FS_{int}}} \phi(\boldsymbol{\kappa}) \psi_{\mathrm{U}, \boldsymbol{\kappa} \uparrow}^{\dagger} \psi_{\mathrm{U}, -\boldsymbol{\kappa} \downarrow}^{\dagger} |\mathrm{FS_{int}}\rangle, \tag{3.22}$$

where $\phi(\boldsymbol{\kappa})$ denotes the wave function of a Cooper pair in momentum space and $|\mathrm{FS_{int}}\rangle$ denotes the interacting Fermi-sea state defined by (3.20); cf. Eq. (2.13).

To find an equation describing a Cooper pair in the upper band of the cuprate lattice subject to the Fermi sea, first we should calculate the effect of the total Hamiltonian (3.21) on the ansatz (3.22). Applying the kinetic energy (3.17) on $|\Phi\rangle$ results in

$$
\begin{aligned}
\hat{H}_{\mathrm{kin}} |\Phi\rangle &= \sum_{\substack{\mathbf{k}\in 1.\mathrm{BZ}\backslash \mathrm{FS}_{\mathrm{int}} \\ \sigma\in\{\uparrow,\downarrow\}}} \xi_{\mathbf{k}}^{(\mathrm{U})} \psi_{\mathrm{U},\mathbf{k}\sigma}^{\dagger}\psi_{\mathrm{U},\mathbf{k}\sigma} |\Phi\rangle \\
&= \sum_{\mathbf{k}\in 1.\mathrm{BZ}\backslash \mathrm{FS}_{\mathrm{int}}} \left(\xi_{\mathbf{k}}^{(\mathrm{U})} + \xi_{-\mathbf{k}}^{(\mathrm{U})}\right) |\Phi\rangle ;
\end{aligned}
\tag{3.23}
$$

see Appendix E of Sec. 7.1 for derivation. Next, we apply the interaction Hamiltonian (3.15) on $|\Phi\rangle$:

$$
\begin{aligned}
\hat{H}_{\mathrm{int}} |\Phi\rangle &= \frac{1}{\mathcal{A}} \sum_{\mathbf{k},\mathbf{k}'\in 1.\mathrm{BZ}\backslash \mathrm{FS}_{\mathrm{int}}} \mathcal{V}_{\mathbf{k},\mathbf{k}'} \psi_{\mathrm{U},\mathbf{k}'\downarrow}^{\dagger}\psi_{\mathrm{U},-\mathbf{k}'\uparrow}^{\dagger}\psi_{\mathrm{U},-\mathbf{k}\uparrow}\psi_{\mathrm{U},\mathbf{k}\downarrow} |\Phi\rangle \\
&= \frac{1}{\mathcal{A}} \sum_{\mathbf{k},\mathbf{k}'\in 1.\mathrm{BZ}\backslash \mathrm{FS}_{\mathrm{int}}} \mathcal{V}_{\mathbf{k},\mathbf{k}'} |\Phi\rangle ,
\end{aligned}
\tag{3.24}
$$

where $\mathcal{V}_{\mathbf{k},\mathbf{k}'}$ is given by Eq. (3.16); see Appendix E of Sec. 7.1 for derivation.

The equation describing a Cooper pair in the upper band of the cuprate lattice subject to the interacting Fermi sea is obtained as

$$
\begin{aligned}
\hat{H}_{\mathrm{tot}} |\Phi\rangle &= \hat{H}_{\mathrm{kin}} |\Phi\rangle + \hat{H}_{\mathrm{int}} |\Phi\rangle \\
&= \mathcal{E} |\Phi\rangle ,
\end{aligned}
\tag{3.25}
$$

where $\mathcal{E}$ is the eigenenrgy. We insert Eqs. (3.23) and (3.24) into Eq. (3.25), and arrive at

$$
\left(\xi_{\mathbf{k}}^{(\mathrm{U})} + \xi_{-\mathbf{k}}^{(\mathrm{U})} + \frac{1}{\mathcal{A}}\mathcal{V}_{\mathbf{k},\mathbf{k}}\right)\phi(\mathbf{k}) + \frac{1}{\mathcal{A}} \sum_{\substack{\mathbf{k},\mathbf{k}'\in 1.\mathrm{BZ}\backslash \mathrm{FS}_{\mathrm{int}} \\ \mathbf{k}'\neq\mathbf{k}}} \mathcal{V}_{\mathbf{k},\mathbf{k}'}\phi(\mathbf{k}') = \mathcal{E}\phi(\mathbf{k});
\tag{3.26}
$$

see Appendix E of Sec. 7.1 for derivation. To calculate the ground-state energy, $E_{\mathrm{G}} < 0$, and the wave function, we solve Eq. (3.26) numerically.

## 3.5 Ground-state solution and wave function

### 3.5.1 Numerical algorithm

To find the ground-state solution, we solve Eq. (3.26) numerically. To do this, first we discretize the first Brillouin zone as $\mathbf{k}_j = (k_x^{(j)}, k_y^{(j)})$, where
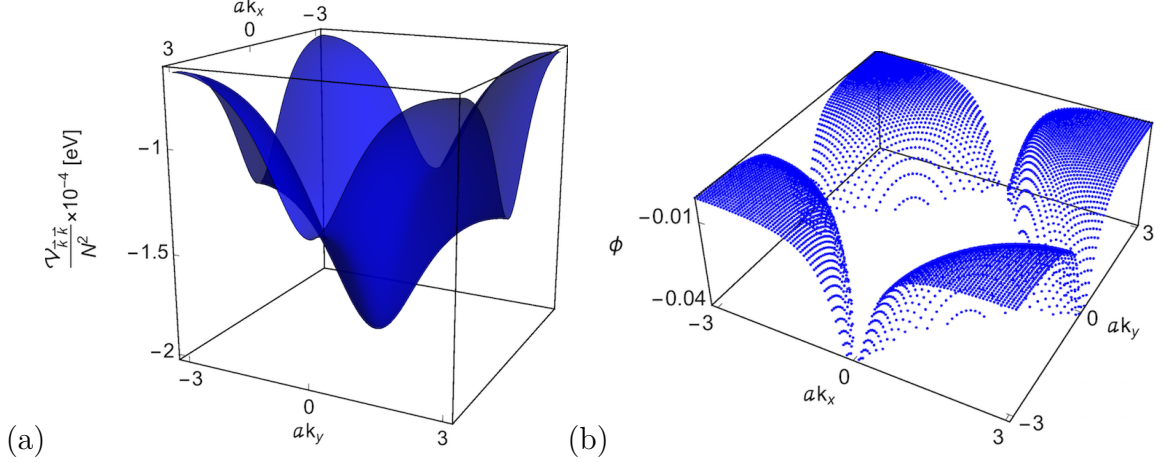
Figure 3.4: (a) Interaction function $\mathcal{V}_{\mathbf{k},\mathbf{k}}/N^2$ in units of eV for the attractive regime of the Fermi-Hubbard model (3.21), (b) ground-state wave function of the Cooper pair, supporting an *s*-wave orbital symmetry. In both panels, $N = 100$, $V_{dp} = 3.45$ eV, $t_{pd} = 1.13$ eV, $t_{pp} = 0.8$ eV, $\mu \approx -0.679$ eV, $U_d = -2$ eV, and $U_p = -1$ eV. The lattice constant is denoted by $a$.

$$k_x^{(j)}, k_y^{(j)} = \frac{1}{a}\left[-\pi + \frac{2\pi}{N}(j-1)\right] \quad \text{for } j = 1, 2, \ldots, N. \tag{3.27}$$

Here, $a$ denotes the lattice constant and $N \in \mathbb{N}$ is the number of the grid points in $x$- and $y$ direction; i.e., $N_x = N_y = N$. We calculate the functions $f(k_x^{(j)}) = t_{pd}[1 - e^{-ik_x^{(j)}}]$ and $g(k_y^{(j)}) = t_{pd}[1 - e^{-ik_y^{(j)}}]$, and constitute the tight-binding Hamiltonian (3.1) at each grid point. With this, we find the electronic band structure numerically, and follow the relation (3.6) to calculate the interaction coefficients $\mathcal{V}_{\mathbf{k},\mathbf{k}'}$ at each grid point; cf. Eq. (3.16).

We note that the number of the grid points within the first Brillouin zone is $N_x N_y = N^2$. The size of the matrix associated with $\hat{H}_{\text{tot}}$ is $N^4$, cf. Eq. (3.21), which increases drastically by increasing the number of the grid points. In order to stabilize the numerical calculation, the number of the grid points should be sufficiently large. For that, we calculate the Fermi sea numerically using the relation

$$\text{FS}_{\text{int}} = \left\{\mathbf{k}^{(j)} \in 1.\text{BZ} : 2E_{\mathbf{k}^{(j)}}^{(\text{U})} + \frac{1}{N^2}\mathcal{V}_{\mathbf{k}^{(j)},\mathbf{k}^{(j)}} < 2\mu\right\}, \tag{3.28}$$

and exclude it from the first Brillouin zone; see Fig. 3.2(d). Next, we constitute the pairing equation (3.26) on the reduced momentum space as

$$\left(\xi_{\mathbf{k}_j}^{(\text{U})} + \xi_{-\mathbf{k}_j}^{(\text{U})} + \frac{1}{N^2}\mathcal{V}_{\mathbf{k}_j,\mathbf{k}_j}\right)\phi(\mathbf{k}_j) + \frac{1}{N^2}\sum_{\substack{\mathbf{k}_j,\mathbf{k}_j' \in 1.\text{BZ}\backslash\text{FS}_{\text{int}} \\ \mathbf{k}_j' \neq \mathbf{k}_j}}\mathcal{V}_{\mathbf{k}_j,\mathbf{k}_j'}\phi(\mathbf{k}_j') = \mathcal{E}_j\phi(\mathbf{k}_j), \tag{3.29}$$
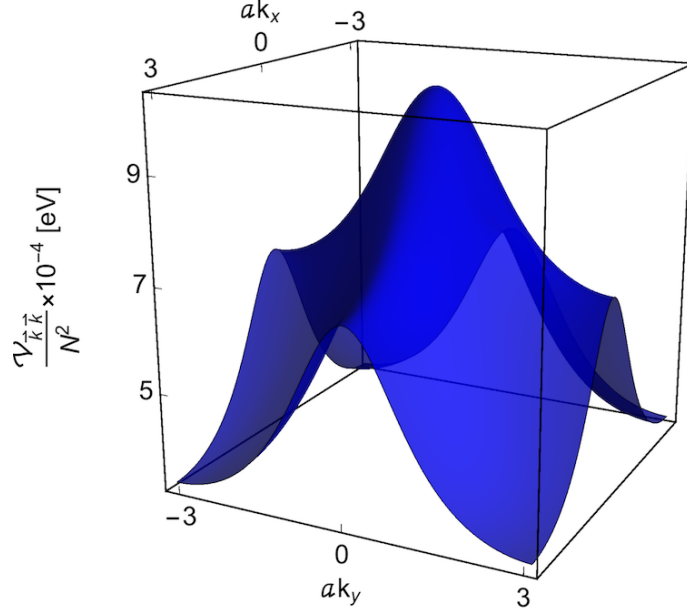
Figure 3.5: Interaction function $\mathcal{V}_{\mathbf{k},\mathbf{k}}/N^2$ in units of eV for the strong-coupling limit of the Fermi-Hubbard model (3.21) and repulsive on-site interactions, where $N = 100$, $V_{dp} = 3.45$ eV, $t_{pd} = 1.13$ eV, $t_{pp} = 0.8$ eV, $U_d = 10.3$ eV, and $U_p = 4.1$ eV. The lattice constant is denoted by $a$.

for $j = 1, 2, \ldots, N$. Finally, we diagonalize Eq. (3.29), and obtain the eigenenergies $\mathcal{E}_j$. Among the eigenenergies $\mathcal{E}_j$, the desired ground-state energy, $E_{\mathrm{G}}$, is the one which is negative and has the largest absolute value.

Finally, we note that the behavior of the desired eigenvalues as a function of the chemical potential might display a zigzag effect due to the finite-size discretization of the momentum space. To prevent this effect, for the noninteracting regime we calculate the smallest eigenenergy, $E_0$, corresponding to Eq. (3.29) in the occupied space. We add $E_0$ to the first bracket of Eq. (3.29) for the interacting regime, and calculate the ground-state energy in the unoccupied space[4].

## 3.5.2   Results

For the attractive Fermi-Hubbard model (3.21) where $U_d, U_p < 0$, the interaction function $\mathcal{V}_{\mathbf{k},\mathbf{k}}$, cf. Eq. (3.16), reveals an overall convex structure; see Fig. 3.4(a). Here the kinetic energy of a Cooper pair is minimized. We find that the ground-state solution of Eq. (3.26) reveals that the two electrons have a tendency to an *s*-wave pairing. Figure 3.4(b) shows the wave function for $U_d = -2$ eV and $U_p = -1$ eV, demonstrating the orbital *s*-wave symmetry of the Cooper pair. This result is in agreement with other approaches, where the renormalized perturbation expansion

---

[4]Private communication with Ludwig Mathey.
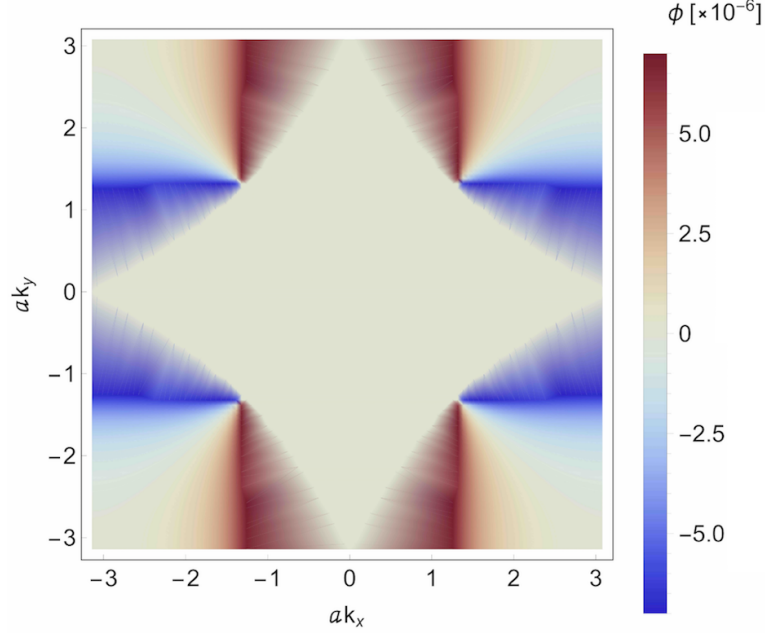
Figure 3.6: Ground-state wave function, $\phi(ak_x, ak_y)$, of a Cooper pair for $N = 100$, $V_{dp} = 3.45$ eV, $t_{pd} = 1.13$ eV, $t_{pp} = 0.8$ eV, $U_d = 10.3$ eV, $U_p = 4.1$ eV, and hole doing $\delta_h \approx 0.104$. The nodal points are visible along the Fermi arcs. The Blue color corresponds to the points with zero phase, and the red color corresponds to the points with the phase $\pi$. The orbital symmetry of the wave function is $d_{x^2-y^2}$. The lattice constant is denoted by $a$.

for $U_d, U_p < 0$ gives rise to $s$-wave superconductivity at first order; see, e.g. Refs. [170, 171].

For the repulsive on-site interactions, $U_d, U_p > 0$, we are primarily interested in the strong-coupling limit $U_d/t_{pd} \gg 1$; cf. Ref [172]. Here the interaction function $\mathcal{V}_{\mathbf{k},\mathbf{k}}$ has a concave structure; see Fig. 3.5. The two electrons repel each other strongly, and there is no tendency for the kinetic energy of the pair to be minimized. If the two electrons form a bound state, the geometry of the Fermi surface and the strong repulsion do not support an isotropic ground-state solution, preventing an orbital $s$-wave symmetry of the wave function. For the lattice parameters $V_{dp} = 3.45$ eV, $t_{pd} = 1.13$ eV, and $t_{pp} = 0.8$ eV that follow approximately the values given by Ref. [60], Fig. 3.6 shows the ground-state wave function for the strongly repulsive regime. We find that the wave function of the Cooper pair reveals nodal points along the Fermi arcs. Here, a nodal point partitions a Fermi arc into two regions with a phase shift of $\pi$. As a result, the wave function supports an orbital symmetry of $d_{x^2-y^2}$.

We also vary the hole doping, $\delta_h$, by changing the chemical potential, $\mu$, and calculate the ground-state solution. Figure 3.7 shows the ground-state energy, $|E_{\mathrm{G}}|$,
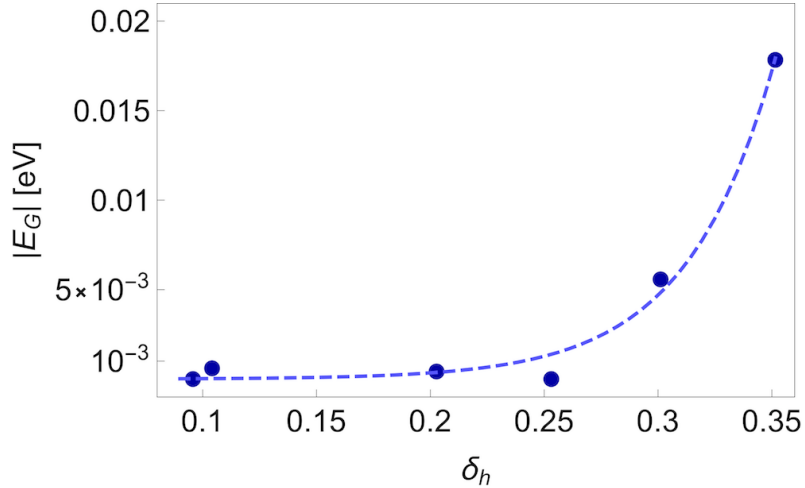
Figure 3.7: Ground-state energy $|E_{\mathrm{G}}|$ of a Cooper pair in units of eV vs hole doping, $\delta_h$, where $N = 100$, $V_{dp} = 3.45$ eV, $t_{pd} = 1.13$ eV, $t_{pp} = 0.8$ eV, $U_d = 10.3$ eV, and $U_p = 4.1$ eV. A largest value of $|E_{\mathrm{G}}|$ that corresponds to a critical temperature of the order of 100 K is obtained near the hole doping of 0.35.

as a function of $\delta_h$. It reveals a largest absolute value of the ground-state energy, $|E_{\mathrm{G}}^{(\mathrm{max})}| \sim 0.01$ eV, occurring near the hole doping $\delta_h \sim 0.35$. Interestingly, the behavior of the ground-state energy captures Ref. [60] qualitatively. We also find that the corresponding critical temperature is within the order of 100 K [5].

## 3.6 Experimental signature in a cold-atom system

Going beyond the hight-temperature cuprate superconductors, we propose an experimental signature of the *d*-wave Cooper pairs for a cold-atom system of fermionic species that are in different internal states in a cuprate lattice. A first step here is to engineer the cuprate lattice by providing an appropriate optical lattice. Next, the desired Fermi-surface geometry that includes Fermi arcs should be constructed. To do this, recall that in a solid, finding the desired momentum distribution and the Fermi-surface geometry is usually performed by ARPES. In a cold-atom system, a useful technique to find the desired Fermi surface can be the time-of-flight image and the noise correlations; see, e.g., Refs. [176, 177, 178].

We note that following the reasoning of the Cooper problem, for an atom with the momentum **k** and spin $\sigma$ in the ground state, there is another atom with the momentum $-\mathbf{k}$ and spin $-\sigma$ , for which we consider the density operators $\hat{n}(\mathbf{k}, \sigma)$ and $\hat{n}(-\mathbf{k}, -\sigma)$, respectively. The time-of-flight image of a cold-atom system is performed when the optical trap is turned off and the atoms fall freely in gravity for a

---

[5]To convert eV to K, recall that the quantity $k_{\mathrm{B}}T$, where $k_{\mathrm{B}}$ is the Boltzmann constant and $T$ is temperature, has a unit of energy. With this, we obtain that 1 eV $\sim 1.160 \times 10^4$ K.

certain time, if they are dilute and the interactions are far from the resonance. After a sufficiently long time of flight $t$, this provides a single realization of the momentum density $\langle \hat{n}(\mathbf{k}, \sigma) \rangle$ and $\langle \hat{n}(-\mathbf{k}, -\sigma) \rangle$ [6]. As a result, to construct the interacting Fermi sea and to determine the orbital symmetry of a Cooper pair, a time-of-flight image is not merely adequate. For that, the density-density correlation

$$\mathcal{G} = \langle \hat{n}(\mathbf{k}, \sigma) \hat{n}(-\mathbf{k}, -\sigma) \rangle \tag{3.30}$$

can be measured at $T > 0$ around the Fermi surface using the technique of noise correlations [179, 180, 181], resulting in an enhanced correlation for a Cooper pair. The behavior of the enhanced correlation can be considered as a probe of the regime where a Cooper pair is formed [179], leading to an estimate of the binding energy. Detecting higher angular harmonics in the correlation data will be a signature of the higher angular symmetry of a Cooper pair. We realize that this measurement is quite delicate, as the atomic noises and correlated fluctuations should be detectable [179]. Keeping a fixed Fermi momentum might also be challenging, as the density in a trap can change.

## 3.7   Summary

In this Chapter, we have solved the Cooper problem in a cuprate lattice for strongly repulsive Coulomb interactions. We have derived an eigenequation describing a Cooper pair in a single-band Fermi-Hubbard model, and have calculated the ground-state solution *a priori*. We have demonstrated that the ground-state wave function reveals nodal points along the Fermi arcs, supporting an orbital symmetry of $d_{x^2-y^2}$. We have shown that the next-nearest-neighbor hopping, $t_{pp}$, deforms the flat band and changes the curvature of the dispersive bands. As a result, we have found that the geometry of the Fermi surface for $t_{pp} \neq 0$ is in better agreement with the experimental data extracted from ARPES. This implies that we can achieve a larger hole doping while the desired Fermi-surface geometry is preserved. We have also calculated the ground-state energy for different values of the hole doping, and have found that a largest absolute magnitude of the energy corresponding to a critical temperature of the order of 100 K. We have also proposed to realize the *d*-wave Cooper pairings in a cuprate lattice for a cold-atom system of fermionic species using the techniques of time-of-flight image and noise correlations.

---

[6]Note that after a sufficiently long time of flight $t$, the position, $\mathbf{r}$, and momentum, $\mathbf{k}$, of an atom with the mass $m$ can be related by $\mathbf{k} = m\mathbf{r}/\hbar t$.

# Chapter 4

# Electron trimer states in conventional superconductors

The main aim of this Chapter is to investigate the three-body bound states of electrons in a solid-state system. We expand the Cooper problem by including a third electron in an otherwise empty band. We constitute a system of two coupled integral equations in momentum space describing the three electrons. We demonstrate the formation of a trimer state of two electrons above the Fermi sea and the third electron, for sufficiently strong interband attractive interactions. We show that the critical interaction strength is the lowest for small Fermi velocities, large masses of the additional electron, and large Debye energy. We also show a regime where more than one trimer state can be formed. Finally, we propose two scenarios to realize the experimental signatures of the electron trimers[1].

## 4.1 Expansion of the Cooper problem

In Sec. 2.1 we discussed the original Cooper problem in detail. We mentioned that the Cooper problem and its solution show that two electrons immersed in an inert Fermi sea form a bound state for arbitrarily weak attractive interactions. The effective attraction originates from the dominance of the electron-phonon interaction over the screened Coulomb potential, and the existence of the Fermi seas results in a bound state. Moreover, in Sec. 2.3 we discussed the Efimov effect as an example of three-body bound states for short-range interactions. This motivates us to investigate the formation of three-body bound states in a solid-state system.

We assume two electrons, labeled "2" and "3", that are restricted to be outside an inert Fermi sea in a lower band with a quadratic dispersion relation $\varepsilon_2$; see Fig. 4.1. The Fermi momentum is $k_F$ and the Fermi energy is $E_F$. Following the reasoning of the Cooper problem, discussed in Sec. 2.1, the interaction between the electrons

---

[1]Parts of this Chapter are adapted from the publication [S1].
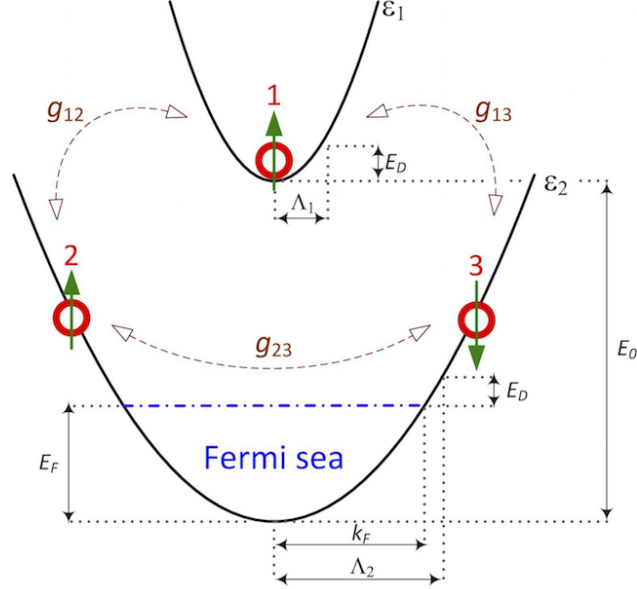
Figure 4.1: Sketch of the expanded Cooper problem. Electrons "2" and "3" are subject to an inert Fermi sea in a lower band with quadratic dispersion $\varepsilon_2$, and form a Cooper pair. The Fermi energy is $E_F$ and the Fermi momentum is $k_F$. The additional electron "1" is in an otherwise empty band with quadratic dispersion $\varepsilon_1$. The energy difference of the two bands is $E_0$. The three electrons interact attractively via the two-body interaction strengths $g_{12}$, $g_{13}$, and $g_{23}$. The interactions are cut off in momentum space by the cutoffs $\Lambda_1$ and $\Lambda_2$ through the relation $\varepsilon_1(\Lambda_1) = \varepsilon_2(\Lambda_2) - E_F = E_D$, where $E_D$ is the Debye energy.

"2" and "3" is considered to be a negative constant $g_{23}$ in momentum space, for the incoming and outgoing momentum of the electron "2" (or "3") smaller than a cutoff $\Lambda_2$ (or $\Lambda_3$) and zero otherwise. Here we assume that $\Lambda_3 = \Lambda_2$. The electrons "2" and "3" form a Cooper pair with the binding energy that is given by Eq. (2.10); cf. Sec. 2.1.2. Next, we expand the Cooper problem by including a third electron, labeled "1", in an otherwise empty band with a quadratic dispersion relation $\varepsilon_1$; see Fig. 4.1. Its spin state is arbitrarily depicted as spin-up. We also consider the interactions between the additional electron and the other two electrons to be a negative constant $g_{12}$ and $g_{13}$, for the incoming and outgoing momentum of the electron "1" smaller than a cutoff $\Lambda_1$ and zero otherwise. We fix the value of the cutoffs such that

$$E_D = \frac{\hbar^2}{2m_1}\Lambda_1^2 = \frac{\hbar^2}{2m_2}(\Lambda_2^2 - k_F^2), \tag{4.1}$$

where $m_i$ is the effective mass of the electron "$i$" and $E_D$ denotes the Debye energy. In general, the effective masses $m_1$, $m_2$, and $m_3$ can be different, but we are pri-

marily interested in the case $m_3 = m_2$. We also assume a similar restriction on the interaction strengths that $g_{13} = g_{12}$. In this Chapter, we define a length scale $r_D$ as

$$r_D = \frac{1}{\Lambda_2 - k_F} \approx \hbar \frac{v_F}{E_D}, \tag{4.2}$$

where $v_F = \hbar k_F / m_2$ is the Fermi velocity. We also define the interaction parameters

$$\xi_{12} = \frac{2\mu}{4\pi\hbar^2} g_{12}, \tag{4.3}$$

$$\xi_{23} = \frac{2\tilde{\mu}}{4\pi\hbar^2} g_{23}, \tag{4.4}$$

where $\mu$ and $\tilde{\mu}$ are reduced masses defined as $1/\mu = 1/m_1 + 1/m_2$ and $1/\tilde{\mu} = 1/m_2 + 1/m_3 = 2/m_2$, respectively. In the following, we assume that the electrons "2" and "3" are in a spin-singlet state, and the total momentum of the three-body bound states of three electrons is vanishing, i.e., $\mathbf{k}_1 + \mathbf{k}_2 + \mathbf{k}_3 = \mathbf{0}$.

## 4.2 Formulation of the problem

In this Section, we expand the formalism that we have already introduced in Sec. 2.1.1. The Schrödinger equation governing the three electrons in momentum space reads as

$$\left( \frac{\hbar^2 k_1^2}{2m_1} + E_0 + \frac{\hbar^2 k_2^2}{2m_2} + \frac{\hbar^2 k_3^2}{2m_3} + \hat{U}_{12} + \hat{U}_{13} + \hat{U}_{23} - \mathcal{E} \right) \psi = 0, \tag{4.5}$$

where $\hbar$ is the reduced Planck's constant, $\mathbf{k}_i$ is the electron momentum, and $\psi = \psi(\mathbf{k}_1, \mathbf{k}_2, \mathbf{k}_3)$ is the wave function. The total energy of the electron "1" is $\hbar^2 k_1^2 / 2m_1 + E_0$, where $E_0$ is the energy difference of the two bands; see Fig. 4.1. We define a shifted energy $E = \mathcal{E} - E_0$, where $\mathcal{E}$ is the eigenenergy[2]. The interaction $\hat{U}_{ij}$ between the electrons "$i$" and "$j$" is

$$\hat{U}_{ij}\psi = g_{ij}\theta_{\Lambda_i}(\mathbf{k}_i)\theta_{\Lambda_i}(\mathbf{k}_i) \int \frac{d^3\mathbf{q}}{(2\pi)^3} \theta_{\Lambda_i}(\mathbf{k}_i - \mathbf{q})\theta_{\Lambda_j}(\mathbf{k}_j + \mathbf{q})\psi, \tag{4.6}$$

where $g_{ij} < 0$, $i,j = 1,2,3$, $i \neq j$, and $\mathbf{q}$ is the momentum transfer[3]. Recall that the cutoff function $\theta_{a,b}(\mathbf{k})$ is defined as

$$\theta_{a,b}(\mathbf{k}) = \begin{cases} 1 & \text{for } a \leqslant |\mathbf{k}| \leqslant b, \\ 0 & \text{otherwise,} \end{cases} \tag{4.7}$$

---

[2]In this Chapter, momentum is measured in units of the Fermi momentum, $k_F$, and energy is measured in units of the Fermi energy, $E_F = \hbar^2 k_F^2 / 2m_2$.

[3]By "momentum transfer" we mean the difference of the in-state and out-state momenta of a particle; see, e.g., Ref. [89].

for $a, b \in \mathbb{R}$, $0 \leqslant a < b$, and $\theta_b(\mathbf{k}) \equiv \theta_{0,b}(\mathbf{k})$. We obtain that

$$\hat{U}_{12}\psi = g_{12}\theta_{\Lambda_1}(\mathbf{k}_1)\theta_{\Lambda_2}(\mathbf{k}_2) \int \frac{d^3\mathbf{q}}{(2\pi)^3} \theta_{\Lambda_1}(\mathbf{k}_1 - \mathbf{q})\theta_{\Lambda_2}(\mathbf{k}_2 + \mathbf{q})\psi(\mathbf{k}_1 - \mathbf{q}, \mathbf{k}_2 + \mathbf{q}, \mathbf{k}_3),$$
(4.8)

$$\hat{U}_{13}\psi = g_{13}\theta_{\Lambda_1}(\mathbf{k}_1)\theta_{\Lambda_3}(\mathbf{k}_3) \int \frac{d^3\mathbf{q}}{(2\pi)^3} \theta_{\Lambda_1}(\mathbf{k}_1 - \mathbf{q})\theta_{\Lambda_3}(\mathbf{k}_3 + \mathbf{q})\psi(\mathbf{k}_1 - \mathbf{q}, \mathbf{k}_2, \mathbf{k}_3 + \mathbf{q}),$$
(4.9)

$$\hat{U}_{23}\psi = g_{23}\theta_{\Lambda_2}(\mathbf{k}_2)\theta_{\Lambda_3}(\mathbf{k}_3) \int \frac{d^3\mathbf{q}}{(2\pi)^3} \theta_{\Lambda_1}(\mathbf{k}_2 - \mathbf{q})\theta_{\Lambda_3}(\mathbf{k}_3 + \mathbf{q})\psi(\mathbf{k}_1, \mathbf{k}_2 - \mathbf{q}, \mathbf{k}_3 + \mathbf{q}).$$
(4.10)

In general, an interaction operator $\hat{U}$ which is a projector onto a state $|\varphi\rangle$ is called separable, and can be represented as $\hat{U} = g\,|\varphi\rangle\,\langle\varphi|$, where $g$ is the strength of the interaction; see, e.g., Refs. [73, 182, 183, 184]. Accordingly, the resulting operators (4.8)-(4.10) imply that the interaction model (4.6) is separable.

Next, we introduce three variables $\tilde{\mathbf{p}}_i \equiv \mathbf{q} + \mathbf{k}_i$, $i = 1, 2, 3$, and assume the zero total momentum of the system, $\psi(\mathbf{k}_1, \mathbf{k}_2, \mathbf{k}_3) = \psi(\mathbf{k}_2, \mathbf{k}_3)\delta^{(3)}(\mathbf{k}_1 + \mathbf{k}_2 + \mathbf{k}_3)$, where $\delta^{(3)}$ is the three-dimensional Dirac delta function. We rewrite the Schrödinger Eq. (4.5) as

$$\left(\frac{\hbar^2(\mathbf{k}_2 + \mathbf{k}_3)^2}{2m_1} + \frac{\hbar^2 k_2^2}{2m_2} + \frac{\hbar^2 k_3^2}{2m_3} - E\right)\psi(\mathbf{k}_2, \mathbf{k}_3) = -\theta_{\Lambda_2}(\mathbf{k}_2)\theta_{\Lambda_3}(\mathbf{k}_3)F_1(-\mathbf{k}_2 - \mathbf{k}_3)$$
$$-\theta_{\Lambda_1}(-\mathbf{k}_2 - \mathbf{k}_3)\theta_{\Lambda_3}(\mathbf{k}_3)F_2(\mathbf{k}_2)$$
$$-\theta_{\Lambda_1}(-\mathbf{k}_2 - \mathbf{k}_3)\theta_{\Lambda_2}(\mathbf{k}_2)F_3(\mathbf{k}_3),$$
(4.11)

where the functions $F_1$, $F_2$, and $F_3$ are defined as

$$F_1(\mathbf{k}_1) = g_{23} \int \frac{d^3\tilde{\mathbf{p}}_3}{(2\pi)^3} \theta_{\Lambda_2}(-\mathbf{k}_1 - \tilde{\mathbf{p}}_3)\theta_{\Lambda_3}(\tilde{\mathbf{p}}_3)\psi(-\mathbf{k}_1 - \tilde{\mathbf{p}}_3, \tilde{\mathbf{p}}_3), \qquad (4.12)$$

$$F_2(\mathbf{k}_2) = g_{13} \int \frac{d^3\tilde{\mathbf{p}}_3}{(2\pi)^3} \theta_{\Lambda_1}(-\mathbf{k}_2 - \tilde{\mathbf{p}}_3)\theta_{\Lambda_3}(\tilde{\mathbf{p}}_3)\psi(\mathbf{k}_2, \tilde{\mathbf{p}}_3), \qquad (4.13)$$

$$F_3(\mathbf{k}_3) = g_{12} \int \frac{d^3\tilde{\mathbf{p}}_2}{(2\pi)^3} \theta_{\Lambda_1}(-\mathbf{k}_3 - \tilde{\mathbf{p}}_2)\theta_{\Lambda_2}(\tilde{\mathbf{p}}_2)\psi(\tilde{\mathbf{p}}_2, \mathbf{k}_3). \qquad (4.14)$$

Equation (4.11) provides now an ansatz for the wave function $\psi(\mathbf{k}_2, \mathbf{k}_3)$ in terms of the unknown functions $F_i$:

$$\psi(\mathbf{k}_2, \mathbf{k}_3) = -\frac{1}{\frac{\hbar^2(\mathbf{k}_2+\mathbf{k}_3)^2}{2m_1} + \frac{\hbar^2 k_2^2}{2m_2} + \frac{\hbar^2 k_3^2}{2m_3} - E}\Big[\theta_{\Lambda_2}(\mathbf{k}_2)\theta_{\Lambda_3}(\mathbf{k}_3)F_1(-\mathbf{k}_2-\mathbf{k}_3)$$

$$+ \theta_{\Lambda_1}(-\mathbf{k}_2-\mathbf{k}_3)\theta_{\Lambda_3}(\mathbf{k}_3)F_2(\mathbf{k}_2) + \theta_{\Lambda_1}(-\mathbf{k}_2-\mathbf{k}_3)\theta_{\Lambda_2}(\mathbf{k}_2)F_3(\mathbf{k}_3)\Big]. \quad (4.15)$$

We note that the Fermi sea demands two constraints $k_2 > k_F$ and $k_3 > k_F$ on the momentum of the electron "2" and "3", respectively. Also, recall that we have assumed $m_3 = m_2$ and $\Lambda_3 = \Lambda_2$. If electrons "2" and "3" are in a spin-singlet state and $g_{12} = g_{13}$, then $F_3 = F_2$. We introduce the variables $\mathbf{p}_1 \equiv -\mathbf{k}_2 - \tilde{\mathbf{p}}_3$ and $\mathbf{p}_2 \equiv -\mathbf{k}_1 - \tilde{\mathbf{p}}_3$, with $\mathbf{p}_3 \equiv \tilde{\mathbf{p}}_3$, and write the functions $F_1$ and $F_2$ as

$$F_1(\mathbf{k}_1) = g_{23}\int \frac{d^3\mathbf{p}_3}{(2\pi)^3}\theta_{k_F,\Lambda_2}(-\mathbf{k}_1-\mathbf{p}_3)\theta_{k_F,\Lambda_2}(\mathbf{p}_3)\psi(-\mathbf{k}_1-\mathbf{p}_3, \mathbf{p}_3), \quad (4.16)$$

$$F_2(\mathbf{k}_2) = g_{12}\int \frac{d^3\mathbf{p}_3}{(2\pi)^3}\theta_{\Lambda_1}(-\mathbf{k}_2-\mathbf{p}_3)\theta_{k_F,\Lambda_2}(\mathbf{p}_3)\psi(\mathbf{k}_2, \mathbf{p}_3), \quad (4.17)$$

where we have included the Fermi-sea constraints through the cutoff functions. We assume that $F_i(\mathbf{k}) = F_i(k)$, implying $s$-wave symmetry of the states.

Finally, we insert the ansatz (4.15) into Eqs. (4.16) and (4.17), and arrive at a system of two coupled integral equations

$$\left[\frac{1}{g_{12}} + \int \frac{d^3\mathbf{p}_3}{(2\pi)^3}K_1(\mathbf{k}_2, \mathbf{p}_3; E)\right] F_2(\mathbf{k}_2) = -\theta_{k_F,\Lambda_2}(\mathbf{k}_2)\left[\int \frac{d^3\mathbf{p}_3}{(2\pi)^3}K_1(\mathbf{k}_2, \mathbf{p}_3; E)F_2(\mathbf{p}_3)\right.$$

$$\left. + \int \frac{d^3\mathbf{p}_1}{(2\pi)^3}K_2(\mathbf{k}_2, \mathbf{p}_1; E)F_1(\mathbf{p}_1)\right], \quad (4.18)$$

$$\left[\frac{1}{g_{23}} + \int \frac{d^3\mathbf{p}_3}{(2\pi)^3}K_3(\mathbf{k}_1, \mathbf{p}_3; E)\right] F_1(\mathbf{k}_1) = -2\theta_{\Lambda_1}(\mathbf{k}_1)\int \frac{d^3\mathbf{p}_3}{(2\pi)^3}K_3(\mathbf{k}_1, \mathbf{p}_3; E)F_2(\mathbf{p}_3), \quad (4.19)$$

where the three integral kernels $K_1$, $K_2$, and $K_3$ are:

$$K_1(\mathbf{k}_2, \mathbf{p}_3; E) = \frac{\theta_{\Lambda_1}(-\mathbf{k}_2-\mathbf{p}_3)\theta_{k_F,\Lambda_2}(\mathbf{p}_3)}{\frac{\hbar^2(\mathbf{k}_2+\mathbf{p}_3)^2}{2m_1} + \frac{\hbar^2 k_2^2}{2m_2} + \frac{\hbar^2 p_3^2}{2m_2} - E}, \quad (4.20)$$

$$K_2(\mathbf{k}_2, \mathbf{p}_1; E) = \frac{\theta_{\Lambda_1}(\mathbf{p}_1)\theta_{k_F,\Lambda_2}(-\mathbf{p}_1-\mathbf{k}_2)}{\frac{\hbar^2 p_1^2}{2m_1} + \frac{\hbar^2 k_2^2}{2m_2} + \frac{\hbar^2(\mathbf{p}_1+\mathbf{k}_2)^2}{2m_2} - E}, \quad (4.21)$$

$$K_3(\mathbf{k}_1, \mathbf{p}_3; E) = \frac{\theta_{k_F,\Lambda_2}(-\mathbf{k}_1-\mathbf{p}_3)\theta_{k_F,\Lambda_2}(\mathbf{p}_3)}{\frac{\hbar^2 k_1^2}{2m_1} + \frac{\hbar^2(\mathbf{k}_1+\mathbf{p}_3)^2}{2m_2} + \frac{\hbar^2 p_3^2}{2m_2} - E}. \quad (4.22)$$
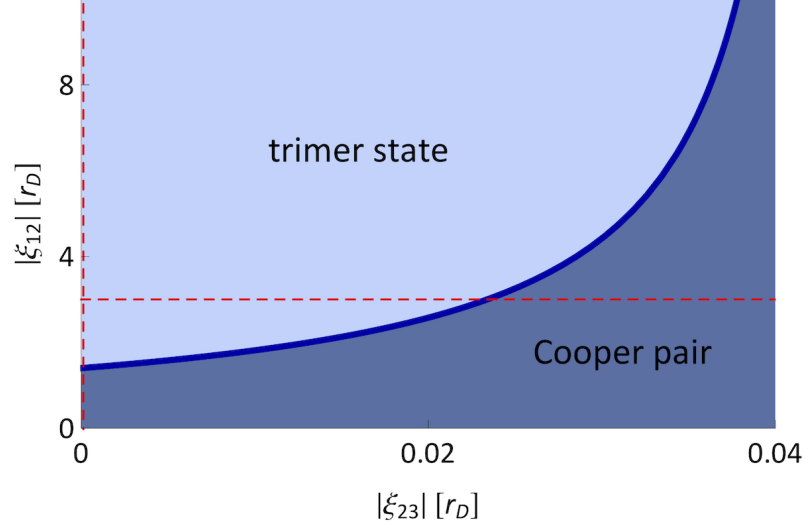
Figure 4.2: Lowest energy state as a function of the interaction strengths $|\xi_{12}|$ and $|\xi_{23}|$, in units of $r_D$, for $m_2 = m_1$ and $E_D/E_F = 0.02$. The cutoffs $\Lambda_1$ and $\Lambda_2$ are chosen according to relation (4.1). The vertical red dashed line is a cut at $\xi_{23} = 0$ and the horizontal red dashed line is a cut at $\xi_{12} = -3r_D$. For any attractive interaction $\xi_{23}$ the electrons "2" and "3" form a Cooper pair. Beyond a critical interband interaction, the trimer state has a lower energy than the Cooper pair. As we increase $|\xi_{23}|$, the trimer state and the Cooper pair compete with each other.

## 4.3 Electron trimer states

To determine whether the lowest energy state is a two-body or a three-body bound state, we solve the system of integral Eqs. (4.18) and (4.19). In this Section we provide both analytical and numerical solutions, and discuss the results.

### 4.3.1 Overview of the main result

Recall that we choose the values of the cutoffs $\Lambda_1$ and $\Lambda_2$ according to relation (4.1). We note that for a typical conventional superconductor $E_D \ll E_F$, see, e.g., Ref. [19], implying that $\Lambda_1 \ll k_F$ and $\Lambda_2 - k_F \ll k_F$. We also recall that $0 < k_1 < \Lambda_1$ and $k_F < k_2 < \Lambda_2$. We make a first approximation such that $k_1 \sim 0$ and $k_2 \sim k_F$. In addition, because the integral variable $p_3$ is varying within the interval $(k_F, \Lambda_2)$ and also $\Lambda_2 - k_F \ll k_F$, we make a second approximation in this interval and assume that the two functions $F_2(k_2)$ and $F_2(p_3)$ remain as the constant value $F_2(k_F)$. With these approximations, we rewrite the system of integral Eqs. (4.18) and (4.19) as

$$\begin{cases} \Gamma_1(E, g_{12}; \tau)F_2(k_F) + \Gamma_2(E)F_1(0) \approx 0, \\ \Gamma_3(E)F_2(k_F) + \Gamma_4(E, g_{23})F_1(0) \approx 0, \end{cases} \tag{4.23}$$

where $\tau = 1$ describes the system of three electrons and $\tau = 1/2$ corresponds to a system of two electrons "1" and "2" (or "3"). The function $\Gamma_1$ reads as

$$\Gamma_1(E, g_{12}; \tau) = \frac{4\pi\hbar^2}{2\mu g_{12}} + \tilde{\Gamma}_1(E; \tau), \tag{4.24}$$

where

$$
\begin{aligned}
\tilde{\Gamma}_1(E; \tau) =& \frac{\tau}{\frac{\mu}{m_1}\pi k_F} \int_{k_F}^{\Lambda_2} dp_3\, p_3 \ln\left(\frac{(1 - \frac{\mu}{m_1})p_3^2 + (1 - \frac{\mu}{m_1})k_F^2 + \frac{\mu}{m_1}\Lambda_1^2 - \frac{2\mu}{\hbar^2}E}{p_3^2 - \frac{2\mu}{m_1}k_F p_3 + k_F^2 - \frac{2\mu}{\hbar^2}E}\right) \\
=& \frac{\tau}{\pi}(\Lambda_2 - k_F) + \frac{2\tau}{\pi}\sqrt{\eta(E)}\left[\arctan\left(\frac{\frac{\mu}{m_1}k_F - \Lambda_2}{\sqrt{\eta(E)}}\right)\right. \\
& \left. - \arctan\left(\frac{(\frac{\mu}{m_1} - 1)k_F}{\sqrt{\eta(E)}}\right)\right] + \frac{\tau\Lambda_2^2}{\frac{2\mu}{m_1}\pi k_F} \ln\left(\frac{-\rho(E) + (1 - \frac{\mu}{m_1})\Lambda_2^2}{\chi(E)}\right) \\
& - \frac{\tau k_F}{\frac{2\mu}{m_1}\pi} \ln\left(\frac{\rho(E) + (\frac{\mu}{m_1} - 1)k_F^2}{\rho(E) + (\frac{\mu}{m_1} - 1)k_F^2 + \frac{\mu}{m_1}\Lambda_1^2}\right) + \frac{\tau\rho(E)}{\frac{2\mu}{m_1}(\frac{\mu}{m_1} - 1)\pi k_F} \\
& \times \ln\left(\frac{\rho(E) + (\frac{\mu}{m_1} - 1)\Lambda_2^2}{\rho(E) + (\frac{\mu}{m_1} - 1)k_F^2}\right) - \frac{\tau}{\frac{2\mu}{m_1}\pi k_F}\left(\eta(E) - (\frac{\mu}{m_1})^2 k_F^2\right) \\
& \times \ln\left(\frac{\chi(E)}{-\rho(E) + (1 - \frac{\mu}{m_1})k_F^2 - \frac{\mu}{m_1}\Lambda_1^2}\right). \tag{4.25}
\end{aligned}
$$

Here, $\eta(E) = [1 - (\frac{\mu}{m_1})^2]k_F^2 - \frac{2\mu}{\hbar^2}E$, $\rho(E) = (\frac{\mu}{m_1} - 1)k_F^2 - \frac{\mu}{m_1}\Lambda_1^2 + \frac{2\mu}{\hbar^2}E$, $\chi(E) = k_F^2 - \frac{2\mu}{m_1}k_F\Lambda_2 + \Lambda_2^2 - \frac{2\mu}{\hbar^2}E$, and $1/\mu = 1/m_1 + 1/m_2$. For $\Lambda_1 \ll k_F$ and $\Lambda_2 - k_F \ll k_F$ we also obtain:

$$
\begin{aligned}
\Gamma_2(E) =& \frac{1}{\frac{2\mu}{m_2}\pi k_F} \int_0^{\Lambda_1} dp_1\, p_1 \ln\left(\frac{p_1^2 + \frac{2\mu}{m_2}k_F p_1 + k_F^2 - \frac{2\mu}{\hbar^2}E}{p_1^2 - \frac{2\mu}{m_2}k_F p_1 + k_F^2 - \frac{2\mu}{\hbar^2}E}\right) \\
\approx& \frac{2}{3\pi}\frac{\Lambda_1^3}{k_F^2 - \frac{2\mu}{\hbar^2}E}, \tag{4.26}
\end{aligned}
$$

$$
\begin{aligned}
\Gamma_3(E) =& \frac{2}{\frac{2\tilde{\mu}}{m_2}\pi k_F} \int_{k_F}^{\Lambda_2} dp_3\, \frac{p_3}{k_1} \ln\left(\frac{\frac{2\tilde{\mu}}{m_2}p_3^2 + \frac{2\tilde{\mu}}{m_2}k_1 p_3 + \frac{\tilde{\mu}}{\mu}k_1^2 - \frac{\tilde{\mu}}{\mu}\frac{2\mu}{\hbar^2}E}{\frac{2\tilde{\mu}}{m_2}p_3^2 - \frac{2\tilde{\mu}}{m_2}k_1 p_3 + \frac{\tilde{\mu}}{\mu}k_1^2 - \frac{\tilde{\mu}}{\mu}\frac{2\mu}{\hbar^2}E}\right) \\
\sim& \frac{4}{\pi} \int_{k_F}^{\Lambda_2} dp_3\, \frac{p_3^2}{p_3^2 - \frac{\tilde{\mu}}{\mu}\frac{2\mu}{\hbar^2}E} \\
\approx& \frac{4}{\pi}\left[\Lambda_2 - k_F + \frac{k_F}{2}\ln\left(\frac{2k_F(\Lambda_2 - k_F)}{k_F^2 - \frac{\tilde{\mu}}{\mu}\frac{2\mu}{\hbar^2}E}\right)\right], \tag{4.27}
\end{aligned}
$$

$$\Gamma_4(E, g_{23}) = \frac{4\pi\hbar^2}{2\tilde{\mu}g_{23}} + \frac{1}{2}\Gamma_3(E), \tag{4.28}$$

where $1/\tilde{\mu} = 1/m_2 + 1/m_3 = 2/m_2$.

To ensure that Eq. (4.23) possesses nontrivial solutions, it is required that

$$\Gamma_1(E, g_{12}; \tau = 1)\Gamma_4(E, g_{23}) - \Gamma_2(E)\Gamma_3(E) = 0, \tag{4.29}$$

leading to a relation between $g_{12}$ and $g_{23}$ through $E$. Figure 4.2 shows the result near the threshold energy

$$E_{\text{thr}} = 2E_F + E_0, \tag{4.30}$$

where $E_F = \hbar^2 k_F^2/2m_2$ is the Fermi energy and $k_F$ is the Fermi momentum. We find a region where electrons "2" and "3" form a Cooper pair, and a second region where the three electrons form a three-body bound state. We refer to a three-body bound state of electrons as a trimer state[4]. We notice that for any value of $g_{23} < 0$, the intraband electrons "2" and "3" form a Cooper pair. As $g_{12}$ is set to a nonzero value, the three electrons form a trimer state beyond a critical value of $g_{12}$. We will provide an analytical estimate of this critical value in Sec. 4.3.4. As we increase $|g_{23}|$, there is a competition of a trimer state and the Cooper pair. The horizontal cut depicted in Fig. 4.2 corresponds to three interacting pairs where $\xi_{23} = -3r_D$, which we discuss further in Sec. 4.3.3.

Interestingly, the trimer state is also formed for vanishing $g_{23}$. The vertical cut depicted in Fig. 4.2 corresponds to this case that we discuss further in Sec. 4.3.4. From the perspective of the electrons in the lower band, this can be considered as a bound-state formation that is induced by a third electron in a higher band, i.e., a particle-induced bound state.

### 4.3.2 Numerical calculation of the spectrum

To find the full spectrum and also to validate the analytical estimates, we solve the system of integral Eqs. (4.18) and (4.19) numerically. To do this, first recall that we have assumed $F_i(\mathbf{k}) = F_i(k)$, implying that we only consider the isotropic solutions of Eqs. (4.18) and (4.19). Accordingly, we replace the three-dimensional integrals over momentum by one-dimensional integrals over absolute values of each momentum. Next, we discretize each integral range such that the grid points $\{k_j\}$, $j = 1, 2, \ldots, N$, are the set of zeros of the Legendre polynomials $P_N(k)$. We approximate the integrals by a truncated sum weighted by $w_j$:

---

[4]In general, we refer to a two-body bound state of electrons "1" and "2" (or "3") as dimer-12 (or dimer-13), and to a three-body bound state of the electrons as trimer-123. We also refer to a two-body bound state of electrons "2" and "3" as Cooper pair or Cooper pair-23.
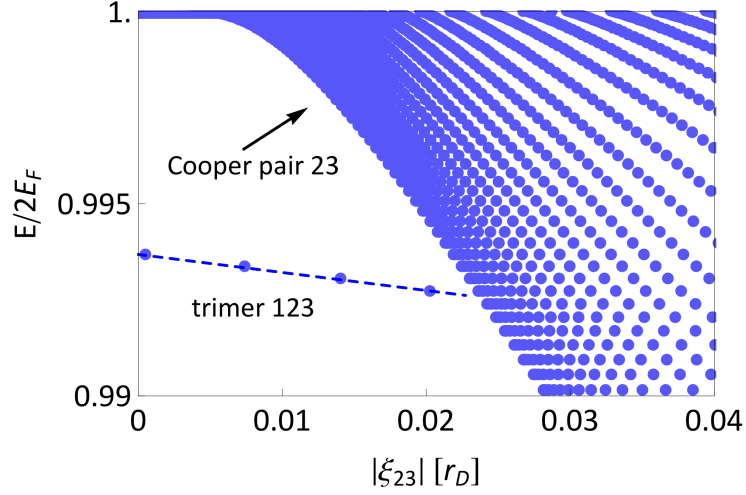
Figure 4.3: Shifted energy $E = \mathcal{E} - E_0$ normalized by $2E_F$ as a function of the interaction parameter $|\xi_{23}|$, in units of $r_D$, for $m_2 = m_1$, $E_D/E_F = 0.02$, and $\xi_{23} = -3r_D$, corresponding to the horizontal cut depicted in Fig. 4.2. The lowest energy state is a trimer state that is shown by a single blue curve. For sufficiently large $|\xi_{23}|$, the formation of Cooper pairs is dominant over a trimer state. Notice that, due to the truncation on each sum described in Sec. 4.3.2, the two-body continuum appears with finite range.

$$w_j = \frac{2}{(1 - k_j^2)[P_N'(k_j)]^2}, \tag{4.31}$$

where $P_N'(k) = dP_N(k)/dk$ [185, 186, 187]. This choice, which is the so-called Gauss-Legendre quadrature rule, scales the range of the integration from a given real interval $(a, b)$ to $(-1, 1)$, and has order of accuracy exactly $2N - 1$, which is the highest accuracy among the other quadrature choices [185]. Finally, we apply the Gauss-Legendre quadrature rule on each integral and construct a matrix equation corresponding to each integral equation. For given values of $\mathcal{E} \lesssim E_{\text{thr}}$ we calculate the eigenvalues, providing the corresponding values of the interaction parameter. The functions $F_1$ and $F_2$ are also obtained as the eigenvectors of the matrix equations[5]. We note that trimer states of zero total momentum appear as discrete energy levels, whereas two-body bound states appear as continuum of states.

### 4.3.3 Trimer states of three interacting pairs

For three interacting pairs we fix the intraband interactions, and calculate the spectrum as a function of the interband interaction parameter. Here, we consider

---

[5]Thanks to Pascal Naidon for proposing a concise method of implementation of this algorithm in our numerical code.

$\xi_{12} = -3r_D$ that corresponds to the horizontal cut depicted in Fig. 4.2. We also assume a typical value of the Debye energy as $E_D/E_F = 0.02$. Figure 4.3 shows the shifted energy $E = \mathcal{E} - E_0$ normalized by $2E_F$ as a function of $|\xi_{23}|$. The lowest energy state is a trimer state appearing as a single curve of solution. An intuitive explanation of forming a trimer state as the lowest energy state is as follows. A three-body bound state possesses three interaction parameters and supports two degrees of freedom; however, a two-body bound state has only one interaction parameter and supports one degree of freedom. We notice that in quantum mechanics, a bound state with more degrees of freedom costs more kinetic energy against the gain from the attractive interactions. Therefore, compared to a Cooper pair, an electron trimer is formed as the lowest energy state[6]. As we increase $|\xi_{23}|$, the Cooper pair is dominant over the trimer state, and appears as a two-body bound-state continuum.

### 4.3.4 Critical interband interaction and the trimer state for noninteracting intraband electrons

Recall that for noninteracting intraband electrons, $g_{23} = 0$, an electron trimer is formed if the interband interaction $g_{12}$ is larger than a critical value; see Fig. 4.2. To find the critical value, we note that for $g_{23} = 0$ we have $F_1 = 0$, and Eq. (4.19) will have no effect anymore. Next, we use similar approximations $k_1 \sim 0$ and $k_2 \sim k_F$ described in Sec. 4.3.1. With these approximations, the system of the integral Eqs. (4.18) and (4.19) reduce to $\Gamma_1(E, g_{12}; \tau) = 0$, where $\Gamma_1$ is given by Eq. (4.24) and $\tau \in \{1/2, 1\}$.

For $\tau = 1$, referring to a system of three interacting electrons, we should solve

$$\Gamma_1(E, g_{12}; \tau = 1) = 0. \tag{4.32}$$

To this end, we expand Eq. (4.32) for $\Lambda_2 - k_F \ll k_F$ and $\Lambda_1 \ll k_F$ at the shifted energy $E \approx 2E_F = \hbar^2 k_F^2/m_2$, and solve the leading order for the interaction parameter $g_{12}^{(c)} \equiv g_{12}(E = 2E_F)$. This results in the critical interband interaction to be

$$|g_{12}^{(c)}| \sim \frac{2\pi^2\hbar^2}{m_1}r_D \approx \frac{2\pi^2\hbar^3}{m_1}\frac{v_F}{E_D}, \tag{4.33}$$

where $E_D$ is the Debye energy, cf. Eq. (4.1), and $v_F = \hbar k_F/m_2$ is the Fermi velocity. Equation (4.33) shows that the magnitude of the critical value of $g_{12}$ for trimer formation is controlled by the ratio of the Fermi velocity, and the mass of the electron in the upper band and the Debye energy. If the mass of the electrons in the upper band is heavier, the critical value is reduced. Similarly, a smaller Fermi velocity and a larger Debye energy reduces the critical value; cf. Fig. 4.4.

---

[6]Private communication with Pascal Naidon.
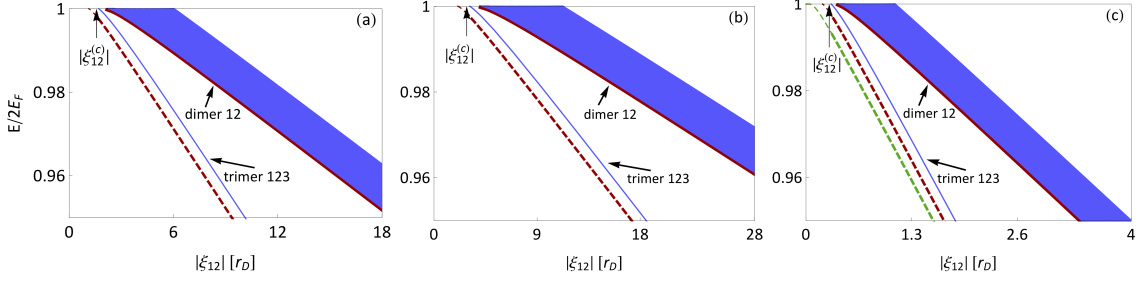
Figure 4.4: Shifted energy $E = \mathcal{E} - E_0$ as a function of the interaction parameter $|\xi_{12}|$, in units of $r_D$, where $E_D/E_F = 0.02$ and $g_{23} = 0$: (a) $m_2/m_1 = 1$, corresponding to the vertical cut depicted in Fig. 4.2, (b) $m_2/m_1 = 10$, and (c) $m_2/m_1 = 1/10$. The single blue curve is the numerical solution of the lowest-energy trimer state, and the red dashed curve is the analytical approximation for the trimer state; cf. Eq. (4.32). As $|\xi_{12}|$ increases, the first two-body bound state (dimer-12) appears as the lowest energy state of a two-body bound-state continuum (blue dense curves). The red solid curve is the analytical approximation for the lowest-energy dimer-12 given by Eq. (4.34). The vertical arrow locates the critical value of the interband interaction parameter given by Eq. (4.33). In panel (c), the green dashed curve is the second analytical approximation (4.35). Notice that, due to the truncation on each sum described in Sec. 4.3.2, the two-body continuum appears with finite range.

We note that Eq. (4.32) provides a relation between the interaction parameter $g_{12}$ and the shifted energy $E$, leading to an analytical estimate for the lowest-energy trimer state with $g_{23} = 0$; see red dashed curves in Fig. 4.4. For a system of two electrons "1" and "2" (or "3") we set $\tau = 1/2$, and calculate the integral by the same argument. The lowest-energy two-body bound state is obtained analytically by solving

$$\Gamma_1(E, g_{12}; \tau = 1/2) = 0; \tag{4.34}$$

see red solid curves Fig. 4.4.

We notice that the onset of the trimer state for $m_1 \gg m_2$ leads to the origin, $|\xi_{12}^{(c)}| = 2\mu|g_{12}^{(c)}|/4\pi\hbar^2 \to 0^+$. For a conventional superconductor, the upper bound of the integral (4.25), $\Lambda_2/k_F$, is very close to the lower bound, 1. Therefore, we calculate the integration (4.25) by making the leading order of the integrand as $p_3/k_F \to 1$. We solve the result for $E$ and arrive at

$$E \approx 2E_F + \frac{E_D}{1 - \exp\left(\pi \frac{\mu}{m_1} \frac{r_D}{|\xi_{12}|}\right)} \qquad \text{for } m_1 \gg m_2; \tag{4.35}$$

see green dashed line in Fig. 4.4(c).

We also calculate the spectrum numerically, following the algorithm described in Sec. 4.3.2, and compare the result with these analytical estimates for different
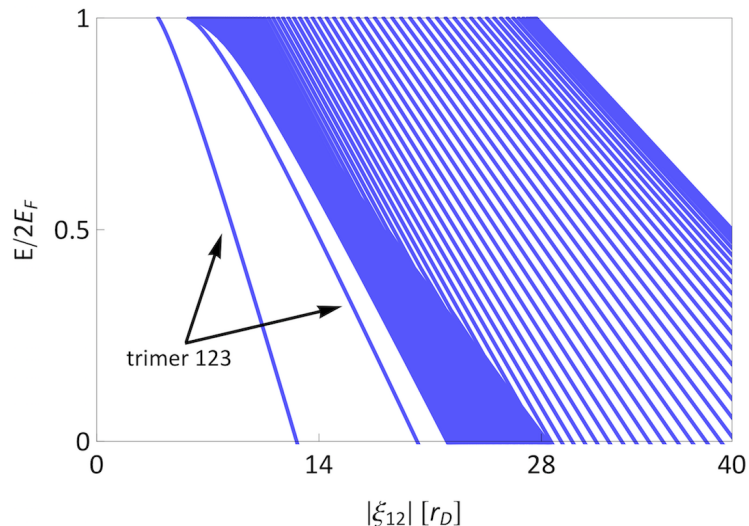
Figure 4.5: Shifted energy $E = \mathcal{E} - E_0$ normalized by $2E_F$ as a function of the interaction parameter $|\xi_{12}|$, in units of $r_D$, for $m_2/m_1 = 10$, $E_D \sim E_F$, and $g_{23} = 0$. We observe the emergence of two trimer states as the lowest energy state that are shown by single blue curves. The dense curves show the two-body bound-state continuum. Notice that, due to the truncation on each sum described in Sec. 4.3.2, the two-body continuum appears with finite range.

parameter sets. In Fig. 4.4(a) we use $m_1 = m_2$ that corresponds to the vertical cut depicting in Fig. 4.2. In Figs. 4.4(b) and 4.4(c) we use $m_2/m_1 = 10$ and $m_2/m_1 = 1/10$, respectively. In all three cases we have used a typical value of the Debye energy, $E_D/E_F = 0.02$. We observe the formation of a trimer state that is well approximated by the analytical approximation. In contrast to the Cooper problem where a two-body bound state originates at a vanishing coupling constant, cf. Fig. 2.2, here a trimer state emerges at the critical value $g_{12}^{(c)}$.

Finally, we find a regime where more than one electron trimer can be formed. For $m_2 \gg m_1$ and large values of the Debye energy comparable to the Fermi energy, $E_D \sim E_F$, we observe the formation of more than one trimer state. This is reminiscent of the Efimov effect discussed in Sec. 2.3, however, here the number of the trimers remains finite. As a result, in contrast to Efimov states, there is no scaling law governing the electron trimer states. Figure 4.5 shows the formation of two trimer states for $m_2/m_1 = 10$. Physical systems in this regime are BCS-like superconductors, e.g., fullerides [188] or magnesium diboride [189].

## 4.4 Experimental signatures

In this Section, we provide two scenarios to realize the electron trimer states in conventional superconductors. As a first scenario, we assume that the electrons in
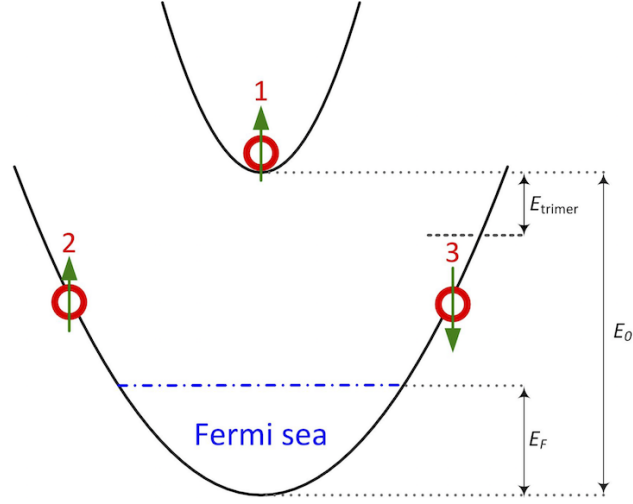
Figure 4.6: Visualization fo the first scenario for the experimental signature of the trimer state. Here, the trimer binding energy, $E_{\text{trimer}}$, is larger than the energy difference of the two bands, $E_0$. We predict that by optically probing the state or pumping electrons from the lower band, the trimer state can be detected as an excited state, revealing as an in-gap resonance peak.

the lower band are either in a superconducting, $g_{23} < 0$, or in a metallic state, $g_{23} = 0$. We also assume that the energy difference of the two bands is larger than the Fermi energy, $E_0 > E_F$. We predict that a trimer state can be detected as an excited state by applying a probe or a pump pulse [190, 191]. By optically probing this state, one can observe a trimer state as an in-gap resonance peak at the trimer binding energy, $E_{\text{trimer}}$, below the empty band; see Fig. 4.6. We predict that the three-body bound state broadens the resonance peak. Also, by optically pumping electrons from the lower band to the upper empty band [192], we predict that a trimer state can be formed in the region indicated in Fig. 4.2, provided that the time scales do not exceed the relaxation rate from the upper band; see Fig. 4.6. Our studies here applies to a long-lived metastable state that is created by optically pumping electrons to a higher band.

As a second scenario, we assume that the electrons in the lower band are in a superconducting state and the trimer binding energy is larger than the energy difference of the bands, $E_{\text{trimer}} > E_0$. We predict that the trimer state destabilizes the BCS state and can be detected as the ground state of the system. Further, the upper band is lowered, $E_0 \gtrsim E_F$, see Fig. 4.7(a), and touches the Fermi surface, $E_0 \sim E_F$, see Fig. 4.7(b). In both cases the electrons in the lower band are localized around the Fermi surface. The upper band can also be lowered into the Fermi sea of the lower band, $E_0 \lesssim E_F$, see Fig. 4.7(c), giving rise to new electron pockets. Here we assume that the upper band is very dilute and the Fermi sea is tuned to formation of the electron pockets. In this case we also predict that the trimer state
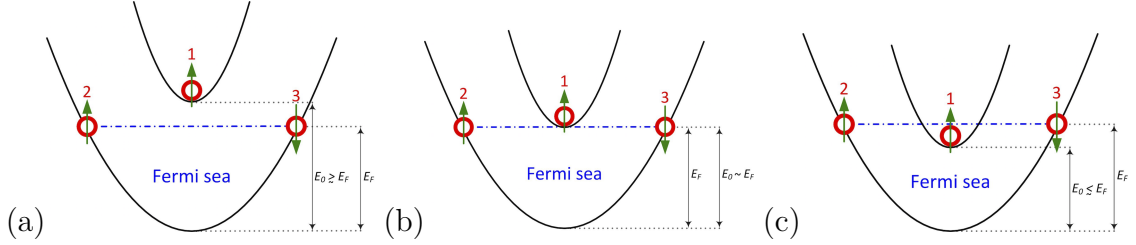
Figure 4.7: Visualization fo the second scenario for the experimental signature of the trimer state: (a) the upper band is lowered, $E_0 \gtrsim E_F$, (b) it touches the Fermi surface in the lower band, $E_0 \sim E_F$, (c) it is lowered into the Fermi sea, $E_0 \lesssim E_F$. In all cases we have assumed that the upper band is very dilute. Here we predict that the trimer state is observed as the ground state.

can be formed as the ground state of the system. We notice that for noninteracting intraband electrons, $g_{23} = 0$, the formation of a trimer liquid is achieved for any density of fermions in the upper band, provided that $g_{12}, g_{13} > g_{12}^{(c)}$. Finally, for interacting intraband electrons, $g_{23} \neq 0$, a BCS state in the lower band is induced. As a result, the energy of the formation of a trimer liquid is reduced. If the electron density in the upper band is sufficiently high, the trimer state competes with the BCS order.

## 4.5 Summary

In this Chapter, we have expanded the Cooper problem by including a third electron in an otherwise empty band. We have demonstrated that for sufficiently strong interband interactions, the lowest energy spectrum is an electron trimer state. We have shown that as we increase the intraband interactions in absolute value, the Cooper pair competes with the formation of a trimer state. We have also shown that for noninteracting intraband electrons, a trimer state can be formed if the interband interaction is beyond a critical value, for which we have provided an analytical estimate. From the perspective of the electrons in the lower band, this can be interpreted as a particle-induced bound state. We have found that for a high mass ratio $m_2/m_1$ and for the values of the Debye energy that are comparable with the Fermi energy, we can observe more than one trimer state. Finally, we have proposed two scenarios as experimental signatures of the trimer states. We recall that in the beginning of this Chapter, we have mentioned the Efimov effect as a motivation to investigate three-body bound states in solid-state physics. In this regard, our study shows that the formation of more than one trimer state for a high mass ratio $m_2/m_1$ and $E_D \sim E_F$ is reminiscent of the Efimov trimers; however, unlike the Efimov states, here the number of the trimer states is finite and there is no discrete scaling law governing the states.

# Chapter 5

# Three-body bound states of an atom in a Fermi mixture

In the previous chapter we discussed the electron three-body bound states in a solid-state system. In this Chapter, we determine the three-body bound states of an atom in a Fermi mixture. Compared to the Efimov spectrum of three atoms in vacuum, discussed in Sec. 2.3, here we show that the Fermi seas deform the Efimov spectrum systematically, and push the three-body bound-state solution towards positive values of the $s$-wave scattering lengths. We demonstrate that this effect is more pronounced near unitarity, for which we obtain an analytical estimate. We show that in the presence of Fermi seas, the Efimov scaling law does not hold anymore. We find a generalized discrete scaling law that governs the three-body bound states. We also propose three signatures of three-body bound states of an ultracold Fermi mixture of Yb isotopes, and provide an estimate for the onset of the bound state and the binding energy[1].

## 5.1   An atom in a Fermi mixture

We consider a cold-atom system of Fermi mixtures. We assume a density, $n_{\text{tot}}/2$, of the species, labeled "2", that interacts attractively via contact interactions with the same density of other species, labeled "3". We assume that the two species "2" and "3" are in different internal states. Next, we include an additional atom, labeled "1", that interacts attractively with the other atoms via contact interactions; see Fig. 5.1. The three masses $m_1$, $m_2$, and $m_3$ can be different in general, but we are primarily interested in the case $m_3 = m_2$. We note that the atom "1" can be generally a fermion or a boson. Here we assume that it is a fermion[2]. The species "2" and "3" define the Fermi seas with the Fermi momentum $k_F = (3\pi^2 n_{\text{tot}})^{1/3}$; see, e.g., Ref. [95]. The Fermi seas demand the constraints $k_2 > k_F$ and $k_3 > k_F$ on

---

[1]Parts of this Chapter are adapted from the publication [S2].

[2]We note that a similar analysis can be applied when it is a boson.
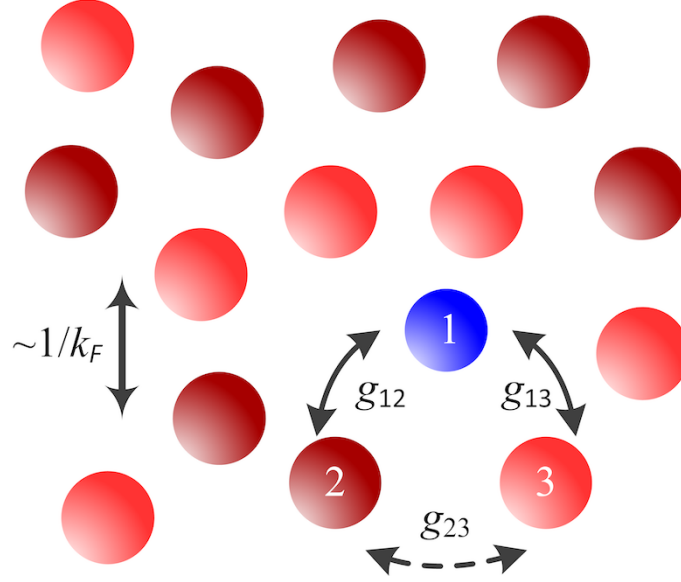
Figure 5.1: Sketch of an atom in a Fermi mixture interacting attractively via contact interactions. Species "2" and "3" are a Fermi mixture, and atom "1" can be in general a boson or a fermion. The interaction strengths in momentum space are shown by three negative constants $g_{12}$, $g_{13}$, and $g_{23}$. The species "2" and "3" are assumed to be in different internal states and $m_3 = m_2$. The interatomic distances are proportional to $1/k_F$, where $k_F$ is the Fermi momentum.

the momentum of the atoms "2" and "3", respectively. The threshold energy of the bound states is

$$E_{\text{thr}} = \frac{\hbar^2}{m_2} k_F^2 = 2E_F, \tag{5.1}$$

where $E_F$ denotes the Fermi energy. Here we consider three-body bound states with the vanishing total momentum. We also consider a singlet state for the species "2" and "3" in the following. In this Chapter we use the following terminology: we refer to a two-body bound state of atoms "$i$" and "$j$" as a dimer-$ij$, and to a three-body bound state of atoms "$i$", "$j$", and "$l$" as a trimer-$ijl$. We also refer to a two-body bound state of species "2" and "3" as a Cooper pair for $k_F \neq 0$, and as a dimer-23 for $k_F = 0$.

The interatomic distances are proportional to $1/k_F$. We assume that the range of the atomic interactions are much smaller than $1/k_F$, by which we neglect the many-body effects on the formation of a three-body bound state within the interatomic distances. We also assume that the range of the interactions are much larger than the Compton wave length of the particles, implying that relativistic corrections to the three-body bound-state spectrum can be neglected.

## 5.2 Formulation of the problem

### 5.2.1 Schrödinger equation

The Schrödinger equation governing three atoms in momentum space is

$$\left( \frac{\hbar^2 k_1^2}{2m_1} + \frac{\hbar^2 k_2^2}{2m_2} + \frac{\hbar^2 k_3^2}{2m_3} + \hat{U}_{12} + \hat{U}_{13} + \hat{U}_{23} - E \right) \psi = 0, \tag{5.2}$$

where $\hbar$ is the reduced Planck's constant, $m_i$ and $\mathbf{k}_i$ is an atom mass and momentum, respectively, $E$ is the energy, and $\psi = \psi(\mathbf{k}_1, \mathbf{k}_2, \mathbf{k}_3)$ is the wave function. We consider the interaction $\hat{U}_{ij}$ between the atom "$i$" and "$j$", $i, j = 1, 2, 3$ and $i \neq j$, as

$$\hat{U}_{ij}\psi = g_{ij}\theta_{\Lambda_i}(\mathbf{k}_i)\theta_{\Lambda_j}(\mathbf{k}_j) \int \frac{d^3\mathbf{q}}{(2\pi)^3}\theta_{\Lambda_i}(\mathbf{k}_i - \mathbf{q})\theta_{\Lambda_j}(\mathbf{k}_j + \mathbf{q})\psi, \tag{5.3}$$

where $\mathbf{q}$ is the momentum transfer[3] and $g_{ij} < 0$ is the interaction strength; cf. Eq. (4.6). The resulting operators $\hat{U}_{ij}\psi$ are given by Eqs. (4.8)-(4.10), implying that $\hat{U}_{ij}$ is separable. The cutoff function $\theta_{a,b}(\mathbf{k})$ for $a, b \in \mathbb{R}$ and $0 \leqslant a < b$ is defined as Eq. (4.7). In Chap. 4, we fixed the values of the cutoffs $\Lambda_i$ and $\Lambda_j$ by the Debye energy. Here, to describe contact interactions we take the limit of the cutoffs to infinity. We note that this leads to some ultraviolet divergences. To resolve that, in the following we derive a regularization relation, by which we introduce the $s$-wave scattering lengths.

### 5.2.2 Regularization relation

Let us consider the Schrödinger Eq. (5.2) for two interacting atoms, labeled "A" and "B", with the vanishing total momentum in vacuum:

$$\left( \frac{\hbar^2 k_A^2}{2m_A} + \frac{\hbar^2 k_B^2}{2m_B} + \hat{U}_{AB} - E_{AB} \right) \phi = 0, \tag{5.4}$$

where $E_{AB}$ is the energy, $\phi = \phi(\mathbf{k}_A, \mathbf{k}_B)$ is the wave function, and the interaction $\hat{U}_{AB}$ follows the relation (5.3):

$$\hat{U}_{AB}\phi = g_{AB}\theta_{\Lambda_A}(\mathbf{k}_A)\theta_{\Lambda_B}(\mathbf{k}_B) \int \frac{d^3\mathbf{q}}{(2\pi)^3} \theta_{\Lambda_A}(\mathbf{k}_A - \mathbf{q})\theta_{\Lambda_B}(\mathbf{k}_B + \mathbf{q})\phi(\mathbf{k}_A - \mathbf{q}, \mathbf{k}_B + \mathbf{q}), \tag{5.5}$$

where $g_{AB} < 0$, $\mathbf{k}_A + \mathbf{k}_B = \mathbf{0}$, and $\Lambda_B = \Lambda_A$. Next, we define the variables $\boldsymbol{\kappa}_i = \mathbf{q} + \mathbf{k}_i$, $i \in \{A, B\}$, and write the Schrödinger Eq. (5.4) as

---

[3]By "momentum transfer" we mean the difference of the in-state and out-state momenta of a particle; see, e.g., Ref. [89].

$$\left(\frac{\hbar^2 k_{\mathrm{A}}^2}{2\mu_{\mathrm{AB}}} - E_{\mathrm{AB}}\right)\phi(\mathbf{k}_{\mathrm{A}}) = -\,g_{\mathrm{AB}}\theta_{\Lambda_{\mathrm{A}}}(\mathbf{k}_{\mathrm{A}})\int\frac{d^3\boldsymbol{\kappa}_{\mathrm{B}}}{(2\pi)^3}\,\theta_{\Lambda_{\mathrm{A}}}(\boldsymbol{\kappa}_{\mathrm{B}})\phi(\boldsymbol{\kappa}_{\mathrm{B}}), \qquad (5.6)$$

where $\mu_{\mathrm{AB}}$ is a reduced mass, $1/\mu_{\mathrm{AB}} = 1/m_{\mathrm{A}} + 1/m_{\mathrm{B}}$. We define

$$\mathcal{F} = -4\pi\left(\frac{2\mu_{\mathrm{AB}}}{4\pi\hbar^2}g_{\mathrm{AB}}\right)\theta_{\Lambda_{\mathrm{A}}}(\mathbf{k}_{\mathrm{A}})\int\frac{d^3\mathbf{k}_{\mathrm{A}}}{(2\pi)^3}\,\theta_{\Lambda_{\mathrm{A}}}(\mathbf{k}_{\mathrm{A}})\phi(\mathbf{k}_{\mathrm{A}}), \qquad (5.7)$$

and rewrite Eq. (5.6) as

$$(k_{\mathrm{A}}^2 - \mathcal{E}_{\mathrm{AB}})\phi(\mathbf{k}_{\mathrm{A}}) = \mathcal{F}, \qquad (5.8)$$

where $\mathcal{E}_{\mathrm{AB}} = 2\mu_{\mathrm{AB}}E_{\mathrm{AB}}/\hbar^2$. We assume $s$-wave symmetry of the states in the following.

For $\mathcal{E}_{\mathrm{AB}} > 0$ the solution of Eq. (5.8) is

$$\phi(\mathbf{k}_{\mathrm{A}}) = (2\pi)^3\delta^{(3)}(\mathbf{k}_{\mathrm{A}} - \mathbf{K}) + \frac{\mathcal{F}}{k_{\mathrm{A}}^2 - \mathcal{E}_{\mathrm{AB}} + i\varepsilon}, \qquad (5.9)$$

where $|\mathbf{K}|^2 = \mathcal{E}_{\mathrm{AB}}$, $\delta^{(3)}$ denotes the three-dimensional Dirac delta function, and $0 < \varepsilon \ll 1$. We insert the ansazt (5.9) into Eq. (5.7) to obtain

$$\frac{\mathcal{F}}{4\pi\left(\frac{2\mu_{\mathrm{AB}}}{4\pi\hbar^2}g_{\mathrm{AB}}\right)} = -\,\theta_{\Lambda_{\mathrm{A}}}(\mathbf{k}_{\mathrm{A}})\int\frac{d^3\mathbf{k}_{\mathrm{A}}}{(2\pi)^3}\theta_{\Lambda_{\mathrm{A}}}(\mathbf{k}_{\mathrm{A}})\left[(2\pi)^3\delta^{(3)}(\mathbf{k}_{\mathrm{A}} - \mathbf{K}) + \frac{\mathcal{F}}{k_{\mathrm{A}}^2 - \mathcal{E}_{\mathrm{AB}} + i\varepsilon}\right].$$
$$(5.10)$$

We note that in the zero-energy limit, $\mathcal{E}_{\mathrm{AB}} \to 0^+$, we have $\mathcal{F} = -4\pi a_{\mathrm{AB}}$, where $a_{\mathrm{AB}}$ is the corresponding $s$-wave scattering length; see, e.g., Ref. [89]. For contact interactions we evaluate Eq. (5.10) by taking the limit of $\Lambda_{\mathrm{A}}$ to infinity, yielding[4]

$$\frac{2\pi\hbar^2}{\mu_{\mathrm{AB}}}\frac{1}{g_{\mathrm{AB}}} + \frac{2}{\pi}\Lambda_{\mathrm{A}} = \frac{1}{a_{\mathrm{AB}}} \quad \text{as } \Lambda_{\mathrm{A}} \to \infty. \qquad (5.11)$$

In this Chapter, we use Eq. (5.11) as a regularization relation to introduce the $s$-wave scattering lengths, and also to eliminate the ultraviolet divergences occurring due to contact interactions.

## 5.2.3   A system of integral equations

To avoid Thomas collapse, described in Secs. 2.3.1 and 2.3.2, here we define $\Lambda$ as the three-body cutoff that fixes the range of the atomic interactions and regularizes

---

[4]Without loss of generality, we can assume that $\mathbf{k}_{\mathrm{A}} = k_{\mathrm{A}}\mathbf{e}_z$, where $\mathbf{e}_z$ is the unit vector in the direction of the $z$-axis.

the three-body bound states [73, 130, 131]. In this Chapter, we define a length scale, $r_D$, as

$$r_D = \frac{1}{\Lambda}. \tag{5.12}$$

The value of $\Lambda$ is chosen such that $\Lambda \gg k_F$, implying that $r_D \ll 1/k_F$ [5]. We determine $r_D$ as the range of the atomic interactions, which we take proportional the van der Waals length

$$\ell_{ij}^{(\mathrm{vdW})} = \frac{1}{2}\left(\frac{2\mu_{ij}C_6}{\hbar^2}\right)^{\frac{1}{4}}, \tag{5.13}$$

where $C_6$ is a dispersive coefficient associated with the polarizability of the electronic cloud of the atoms; see, e.g., Refs. [73, 133, 193, 194, 195].

Recall that in Sec. 4.2 we showed that the interaction model (5.3) is separable, resulting in a system of two coupled integral equations of the functions $F_1$ and $F_2$, defined as Eqs. (4.16) and (4.17), respectively. We follow the same procedure described in Sec. 4.2, and arrive at the system of coupled integral equations

$$\Omega_{12}(g_{12}, \mathbf{k}_2; k_F, E)F_2(\mathbf{k}_2) = \xi_1(\mathbf{k}_2; F_2) + \xi_2(\mathbf{k}_2; F_1), \tag{5.14}$$

$$\Omega_{23}(g_{23}, \mathbf{k}_1; k_F, E)F_1(\mathbf{k}_1) = \xi_3(\mathbf{k}_1; F_2), \tag{5.15}$$

where we assume $F_i(\mathbf{k}) = F_i(k)$, implying $s$-wave symmetry of the states. The functions $\Omega_{12}$ and $\Omega_{23}$ describe the two-body bound state continuum, dimers-12 and dimers-23, respectively:

$$\Omega_{12}(g_{12}, \mathbf{k}_2; k_F, E) = \frac{1}{g_{12}} + \int \frac{d^3\mathbf{p}_3}{(2\pi)^3} \, K_1(\mathbf{k}_2, \mathbf{p}_3; E), \tag{5.16}$$

$$\Omega_{23}(g_{23}, \mathbf{k}_1; k_F, E) = \frac{1}{g_{23}} + \int \frac{d^3\mathbf{p}_3}{(2\pi)^3} \, K_3(\mathbf{k}_1, \mathbf{p}_3; E). \tag{5.17}$$

Note that for contact interactions we use the regularization relation (5.11) to introduce the $s$-wave scattering lengths. Within the range of $r_D$, the coupling of a pair to the third atom is described by three functions $\xi_1$, $\xi_2$, and $\xi_3$:

$$\xi_1(\mathbf{k}_2; F_2) = -\int \frac{d^3\tilde{\mathbf{p}}_3}{(2\pi)^3} \, \tilde{K}_1(\mathbf{k}_2, \tilde{\mathbf{p}}_3; E)F_2(\tilde{\mathbf{p}}_3), \tag{5.18}$$

$$\xi_2(\mathbf{k}_2; F_1) = -\int \frac{d^3\tilde{\mathbf{p}}_1}{(2\pi)^3} \, \tilde{K}_2(\mathbf{k}_2, \tilde{\mathbf{p}}_1; E)F_1(\tilde{\mathbf{p}}_1), \tag{5.19}$$

---

[5]This is consistent with our first assumption that the range of the atomic interactions are much smaller than $1/k_F$

$$\xi_3(\mathbf{k}_1; F_2) = -2 \int \frac{d^3\tilde{\mathbf{p}}_3}{(2\pi)^3} \tilde{K}_3(\mathbf{k}_1, \tilde{\mathbf{p}}_3; E) F_2(\tilde{\mathbf{p}}_3), \tag{5.20}$$

where the integral kernels $K_i$ and $\tilde{K}_i$, $i = 1, 2, 3$, are

$$K_1(\mathbf{k}_2, \mathbf{p}_3; E) = \frac{\theta_{\Lambda_1}(-\mathbf{k}_2 - \mathbf{p}_3)\theta_{k_F,\Lambda_2}(\mathbf{p}_3)}{\frac{\hbar^2(\mathbf{k}_2+\mathbf{p}_3)^2}{2m_1} + \frac{\hbar^2 k_2^2}{2m_2} + \frac{\hbar^2 p_3^2}{2m_2} - E}, \tag{5.21}$$

$$K_2(\mathbf{k}_2, \mathbf{p}_1; E) = \frac{\theta_{\Lambda_1}(\mathbf{p}_1)\theta_{k_F,\Lambda_2}(-\mathbf{p}_1 - \mathbf{k}_2)}{\frac{\hbar^2 p_1^2}{2m_1} + \frac{\hbar^2 k_2^2}{2m_2} + \frac{\hbar^2(\mathbf{p}_1+\mathbf{k}_2)^2}{2m_2} - E}, \tag{5.22}$$

$$K_3(\mathbf{k}_1, \mathbf{p}_3; E) = \frac{\theta_{k_F,\Lambda_2}(-\mathbf{k}_1 - \mathbf{p}_3)\theta_{k_F,\Lambda_2}(\mathbf{p}_3)}{\frac{\hbar^2 k_1^2}{2m_1} + \frac{\hbar^2(\mathbf{k}_1+\mathbf{p}_3)^2}{2m_2} + \frac{\hbar^2 p_3^2}{2m_2} - E}, \tag{5.23}$$

$$\tilde{K}_1(\mathbf{k}_2, \tilde{\mathbf{p}}_3; E) = \frac{\theta_{\Lambda}(-\mathbf{k}_2 - \tilde{\mathbf{p}}_3)\theta_{k_F,\Lambda}(\mathbf{k}_2)\theta_{k_F,\Lambda}(\tilde{\mathbf{p}}_3)}{\frac{\hbar^2(\mathbf{k}_2+\tilde{\mathbf{p}}_3)^2}{2m_1} + \frac{\hbar^2 k_2^2}{2m_2} + \frac{\hbar^2 \tilde{p}_3^2}{2m_2} - E}, \tag{5.24}$$

$$\tilde{K}_2(\mathbf{k}_2, \tilde{\mathbf{p}}_1; E) = \frac{\theta_{\Lambda}(\tilde{\mathbf{p}}_1)\theta_{k_F,\Lambda}(\mathbf{k}_2)\theta_{k_F,\Lambda}(-\tilde{\mathbf{p}}_1 - \mathbf{k}_2)}{\frac{\hbar^2 \tilde{p}_1^2}{2m_1} + \frac{\hbar^2 k_2^2}{2m_2} + \frac{\hbar^2(\tilde{\mathbf{p}}_1+\mathbf{k}_2)^2}{2m_2} - E}, \tag{5.25}$$

$$\tilde{K}_3(\mathbf{k}_1, \tilde{\mathbf{p}}_3; E) = \frac{\theta_{k_F,\Lambda}(-\mathbf{k}_1 - \tilde{\mathbf{p}}_3)\theta_{\Lambda}(\mathbf{k}_1)\theta_{k_F,\Lambda}(\tilde{\mathbf{p}}_3)}{\frac{\hbar^2 k_1^2}{2m_1} + \frac{\hbar^2(\mathbf{k}_1+\tilde{\mathbf{p}}_3)^2}{2m_2} + \frac{\hbar^2 \tilde{p}_3^2}{2m_2} - E}. \tag{5.26}$$

## 5.3 Three-body bound states of three interacting pairs

### 5.3.1 Analytical description of dimers-23 and dimers-12

The system of Eqs. (5.14) and (5.15) describe the three interacting pairs. To find the solutions, first we note that the dimers-23 and dimers-12 can be described analytically. To find the lowest-energy two-body bound states of atoms "2" and "3", dimers-23, we calculate the function $\Omega_{23}$ analytically. We notice that the cutoff function $\theta_{k_F,\Lambda_2}(-\mathbf{k}_1 - \mathbf{p}_3)$ appearing in $K_3$ imposes a lower bound, $v_{\min}$, and an upper bound, $v_{\max}$, on the angle between the momenta $\mathbf{p}_3$ and $\mathbf{k}_1$, $v \equiv \cos\vartheta_{\mathbf{p}_3,\mathbf{k}_1}$:

$$v_{\min} = \max_{p_3} \left(-1, \frac{k_F^2 - k_1^2 - p_3^2}{2k_1 p_3}\right) = \begin{cases} -1, & \text{for } k_F < p_3 < k_1 - k_F \\ & \text{or } p_3 > k_1 + k_F, \\[2mm] \frac{k_F^2 - k_1^2 - p_3^2}{2k_1 p_3}, & \text{for } k_1 - k_F < p_3 < k_1 + k_F, \end{cases}$$

(5.27)

$$v_{\max} = \min_{p_3}\left(1, \frac{\Lambda_2^2 - k_1^2 - p_3^2}{2k_1 p_3}\right) \to 1 \text{ as } \Lambda_2 \to \infty,$$ (5.28)

where the limit $\Lambda_2 \to \infty$ in Eq. (5.28) is due to contact interactions. Next, without loss of generality we assume that $\mathbf{p_3} = p_3 \mathbf{e}_z$, where $\mathbf{e}_z$ is the unit vector in the direction of the $z$-axis. For $s$-wave symmetry of the states, we calculate the function $\Omega_{23}$, cf. Eq. (5.17), analytically:

$$\Omega_{23} = \frac{4\pi\hbar^2}{2\mu_{23}g_{23}} + \frac{1}{\frac{2\mu_{23}}{m_2}\pi k_1} \lim_{\Lambda_2 \to \infty} \int_{k_F}^{\Lambda_2} dp_3\, p_3 \ln\left(\frac{p_3^2 + k_1 p_3 v_{\max} + \frac{\mu_{23}}{\mu_{12}}k_1^2 - \frac{\mu_{23}}{\mu_{12}}\mathcal{E}}{p_3^2 + k_1 p_3 v_{\min} + \frac{\mu_{23}}{\mu_{12}}k_1^2 - \frac{\mu_{23}}{\mu_{12}}\mathcal{E}}\right).$$

(5.29)

To calculate the integration (5.29) we consider two cases. For $0 < k_1 \leqslant 2k_F$ we have:

$$\Omega_{23} = \frac{4\pi\hbar^2}{2\mu_{23}g_{23}} + \frac{1}{\pi k_1}\int_{k_F}^{k_1+k_F} dp_3\, p_3 \ln\left(\frac{p_3^2 + k_1 p_3 + \frac{\mu_{23}}{\mu_{12}}k_1^2 - \frac{\mu_{23}}{\mu_{12}}\mathcal{E}}{\frac{1}{2}p_3^2 + (\frac{\mu_{23}}{\mu_{12}} - \frac{1}{2})k_1^2 + \frac{1}{2}k_F^2 - \frac{\mu_{23}}{\mu_{12}}\mathcal{E}}\right)$$

$$+ \frac{1}{\pi k_1}\lim_{\Lambda_2 \to \infty}\int_{k_1+k_F}^{\Lambda_2} dp_3\, p_3 \ln\left(\frac{p_3^2 + k_1 p_3 + \frac{\mu_{23}}{\mu_{12}}k_1^2 - \frac{\mu_{23}}{\mu_{12}}\mathcal{E}}{p_3^2 - k_1 p_3 + \frac{\mu_{23}}{\mu_{12}}k_1^2 - \frac{\mu_{23}}{\mu_{12}}\mathcal{E}}\right).$$ (5.30)

We calculate each integral, see Appendix F in Sec. 7.1, and use the regularization relation (5.11) to obtain

$$\Omega_{23} \equiv \Omega_{23}(a_{23}, k_1; k_F, \mathcal{E})$$
$$= \frac{1}{a_{23}} - \frac{k_1}{2\pi} - \frac{k_F}{\pi} + \frac{2\sqrt{\kappa}}{\pi}\left[\arctan\left(\frac{\frac{1}{2}k_1 + k_F}{\sqrt{\kappa}}\right) - \frac{\pi}{2}\right] + \frac{1}{\pi k_1}$$
$$\times \left((\frac{\mu_{23}}{\mu_{12}} - \frac{1}{2})k_1^2 + k_F^2 - \frac{\mu_{23}}{\mu_{12}}\mathcal{E}\right)\ln\left(\frac{(\frac{\mu_{23}}{\mu_{12}} - \frac{1}{2})k_1^2 + k_F^2 - \frac{\mu_{23}}{\mu_{12}}\mathcal{E}}{\frac{\mu_{23}}{\mu_{12}}k_1^2 + k_F k_1 + k_F^2 - \frac{\mu_{23}}{\mu_{12}}\mathcal{E}}\right),$$ (5.31)

where $a_{23}$ is the $s$-wave scattering lengths of species "2" and "3" and $\kappa \equiv (\frac{\mu_{23}}{\mu_{12}} - \frac{1}{4})k_1^2 - \frac{\mu_{23}}{\mu_{12}}\mathcal{E}$. We note that the lowest-energy two-body bound state, Cooper pair-23, is described by

$$\Omega_{23}(a_{23}, k_1 \to 0; k_F, \mathcal{E} \to \mathcal{E}_{23}) = 0, \tag{5.32}$$

leading to

$$\frac{1}{a_{23}} = \frac{2}{\pi} k_F + \frac{2}{\pi} \sqrt{-\mathcal{E}_{23}} \arctan\left(\frac{\sqrt{-\mathcal{E}_{23}}}{k_F}\right), \tag{5.33}$$

where $\mathcal{E}_{23} = 2\mu_{23}E_{23}/\hbar^2$ and $E_{23}$ is the energy of the Cooper pair; see gray dashed curves in Fig. 5.2 and also see Fig. 5.6. The lowest-energy two-body bound state in vacuum is described by Eq. (5.33) as $k_F \to 0$, resulting in

$$\frac{1}{a_{23}} = \sqrt{-\mathcal{E}_{23}}; \tag{5.34}$$

see Figs. 5.2 and 5.6. We find that far from the resonance, the Cooper-pair solution for $k_F \neq 0$ converges asymptotically to the lowest-energy dimer-23 for $k_F = 0$.

For the second case, where $k_1 \geqslant 2k_F$, we have:

$$\begin{aligned}
\Omega_{23} =& \frac{4\pi\hbar^2}{2\mu_{23}g_{23}} + \frac{1}{\pi k_1} \int_{k_F}^{k_1-k_F} dp_3\, p_3 \ln\left(\frac{p_3^2 + k_1 p_3 + \frac{\mu_{23}}{\mu_{12}}k_1^2 - \frac{\mu_{23}}{\mu_{12}}\mathcal{E}}{p_3^2 - k_1 p_3 + \frac{\mu_{23}}{\mu_{12}}k_1^2 - \frac{\mu_{23}}{\mu_{12}}\mathcal{E}}\right) \\
&+ \frac{1}{\pi k_1} \int_{k_1-k_F}^{k_1+k_F} dp_3\, p_3 \ln\left(\frac{p_3^2 + k_1 p_3 + \frac{\mu_{23}}{\mu_{12}}k_1^2 - \frac{\mu_{23}}{\mu_{12}}\mathcal{E}}{\frac{1}{2}p_3^2 + (\frac{\mu_{23}}{\mu_{12}} - \frac{1}{2})k_1^2 + \frac{1}{2}k_F^2 - \frac{\mu_{23}}{\mu_{12}}\mathcal{E}}\right) \\
&+ \frac{1}{\pi k_1} \lim_{\Lambda_2 \to \infty} \int_{k_1+k_F}^{\Lambda_2} dp_3\, p_3 \ln\left(\frac{p_3^2 + k_1 p_3 + \frac{\mu_{23}}{\mu_{12}}k_1^2 - \frac{\mu_{23}}{\mu_{12}}\mathcal{E}}{p_3^2 - k_1 p_3 + \frac{\mu_{23}}{\mu_{12}}k_1^2 - \frac{\mu_{23}}{\mu_{12}}\mathcal{E}}\right). \tag{5.35}
\end{aligned}$$

Similar to the previous case, we calculate each integral and use the relation (5.11) to obtain

$$\begin{aligned}
\Omega_{23} =& \frac{1}{a_{23}} - \frac{2k_F}{\pi} - \frac{2\sqrt{\kappa}}{\pi}\left[\arctan\left(\frac{\frac{1}{2}k_1 - k_F}{\sqrt{\kappa}}\right) - \arctan\left(\frac{\frac{1}{2}k_1 + k_F}{\sqrt{\kappa}}\right) + \frac{\pi}{2}\right] \\
&+ \frac{1}{\pi k_1}\left((\frac{\mu_{23}}{\mu_{12}} - \frac{1}{2})k_1^2 + k_F^2 - \frac{\mu_{23}}{\mu_{12}}\mathcal{E}\right) \ln\left(\frac{\frac{\mu_{23}}{\mu_{12}}k_1^2 + k_F k_1 + k_F^2 - \frac{\mu_{23}}{\mu_{12}}\mathcal{E}}{\frac{\mu_{23}}{\mu_{12}}k_1^2 - k_F k_1 + k_F^2 - \frac{\mu_{23}}{\mu_{12}}\mathcal{E}}\right). \tag{5.36}
\end{aligned}$$

The function $\Omega_{23}$ describes the lowest-energy two-body bound states and the two-body continuum, dimers-23.

Next, to find the lowest-energy two-body bound states of atoms "1" and "2" (or "3"), dimers-12, we calculate the function $\Omega_{12}$ analytically. To do this, we note that the cutoff function $\theta_{\Lambda_1}(-\mathbf{k}_2 - \mathbf{p}_3)$ appearing in $K_1$, imposes an upper bound, $u_{\max}$, on the angle between two momenta $\mathbf{k}_2$ and $\mathbf{p}_3$. However, for contact interactions we find that

$$u_{\max} = \min_{p_3} \left( 1, \frac{\Lambda_1^2 - k_2^2 - p_3^2}{2k_2 p_3} \right) \to 1 \text{ as } \Lambda_1 \to \infty, \tag{5.37}$$

where $u \equiv \cos \vartheta_{\mathbf{p}_3, \mathbf{k}_2}$. Next, without loss of generality we assume that $\mathbf{p}_3 = p_3 \mathbf{e}_z$, where $\mathbf{e}_z$ is the unit vector in the direction of the $z$-axis. For $s$-wave symmetry of the states, the function $\Omega_{12}$, cf. Eq. (5.16), reads

$$\Omega_{12} = \frac{4\pi\hbar^2}{2\mu_{12} g_{12}} + \frac{1}{2\pi \frac{\mu_{12}}{m_1} k_2} \lim_{\Lambda_2 \to \infty} \int_{k_F}^{\Lambda_2} dp_3 \, p_3 \ln \left( \frac{p_3^2 + \frac{2\mu_{12}}{m_1} k_2 p_3 + k_2^2 - \mathcal{E}}{p_3^2 - \frac{2\mu_{12}}{m_1} k_2 p_3 + k_2^2 - \mathcal{E}} \right). \tag{5.38}$$

We calculate the integral (5.38), see Appendix F in Sec. 7.1, and use the regularization relation (5.11) to obtain

$$\begin{aligned}
\Omega_{12} \equiv & \Omega_{12}(a_{12}, k_2; k_F, \mathcal{E}) \\
= & \frac{1}{a_{12}} - \frac{k_F}{\pi} + \frac{\sqrt{\eta}}{\pi} \left[ \arctan \left( \frac{\frac{\mu_{12}}{m_1} k_2 + k_F}{\sqrt{\eta}} \right) - \arctan \left( \frac{\frac{\mu_{12}}{m_1} k_2 - k_F}{\sqrt{\eta}} \right) - \pi \right] \\
& + \frac{1}{4\pi \frac{\mu_{12}}{m_1} k_2} \left[ \left( 2(\frac{\mu_{12}}{m_1})^2 - 1 \right) k_2^2 - k_F^2 + \mathcal{E} \right] \ln \left( \frac{k_2^2 + \frac{2\mu_{12}}{m_1} k_F k_2 + k_F^2 - \mathcal{E}}{k_2^2 - \frac{2\mu_{12}}{m_1} k_F k_2 + k_F^2 - \mathcal{E}} \right),
\end{aligned} \tag{5.39}$$

where $a_{12}$ is the $s$-wave scattering lengths of species "1" and "2" (or "3") and $\eta \equiv [1 - (\mu/m_1)^2]k_2^2 - \mathcal{E}$. We note that the two-body bound-states, dimers-12, are described by solving

$$\Omega_{12}(a_{12}, k_2; k_F, \mathcal{E}_{12}) = 0, \tag{5.40}$$

where $\mathcal{E}_{12} = 2\mu_{12} E_{12}/\hbar^2$ and $E_{12}$ is the energy of the dimers-12. For the lowest-energy dimer-12, we solve Eq. (5.40) as $k_2 \to k_F$. We find that the solution converges asymptotically to the lowest-energy two-body bound state in vacuum; see gray dashed curves in Fig. 5.3.

## 5.3.2   Three-body bound-state solution for three interacting pairs

So far, we have evaluated the left-hand side of Eqs. (5.14) and (5.15) analytically. Further, we solve the coupled integral Eqs. (5.14) and (5.15) numerically by choosing a three-body cutoff $\Lambda \gg k_F$. To this end, we follow the numerical algorithm described in Sec. 4.3.2, and evaluate the functions $\xi_1$, $\xi_2$, and $\xi_3$ numerically. We
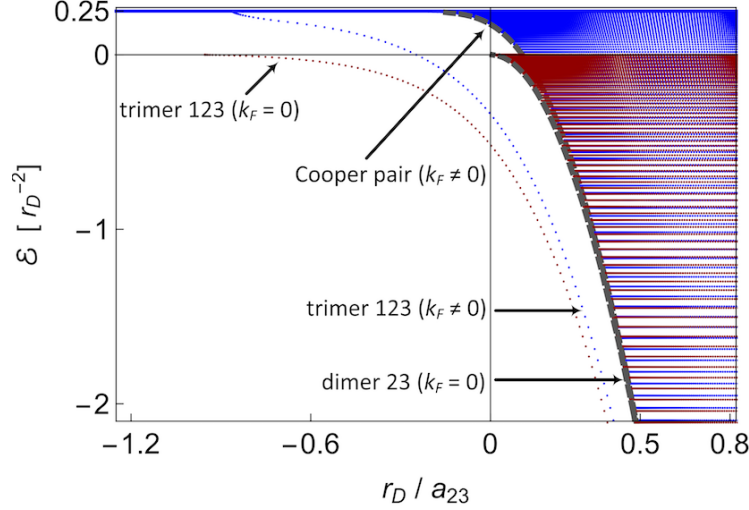
Figure 5.2: Three-body spectrum for three interacting pairs: Energy $\mathcal{E} = 2\mu_{12}E/\hbar^2$ in units of $r_D^{-2}$ vs $r_D/a_{23}$ for $m_2/m_1 = 1$ and $a_{12} \approx -36r_D$. Red curves show the Efimov spectrum, $k_F = 0$. Blue curves show the result in the presence of Fermi seas, $k_F r_D \approx 0.17$. The single blue curve is the three-body bound-state solution for $k_F \neq 0$, which asymptotically converges to the single red curve corresponding to $k_F = 0$. Gray dashed curves are the lowest-energy two-body bound-state solutions of the two-body continuum in vacuum, cf. Eq. (5.34), and in the presence of Fermi seas described by Eq. (5.33). The onset of the three-body bound state in the presence of Fermi seas undergoes a shift towards positive values of $a_{23}$. The onset of the Cooper pair is shifted towards negative values of $a_{23}$.

construct the corresponding matrix equation and calculate the eigenvalues for different values of energy $E \leqslant E_{\text{thr}}$, resulting in the $s$-wave scattering lengths $a_{23}$ and $a_{12}$ [6].

For three interacting pairs and for a fixed value of $a_{12}$, we calculate the three-body spectrum and compare the result with the corresponding Efimov spectrum in vacuum, $k_F = 0$. We find that for vanishing $k_F$ the two-body bound states emerge at unitarity, $a_{23} \to \pm\infty$, however, the Fermi seas expands the region of the two-body bound states to negative values of $a_{23}$; see Fig. 5.2. The three-body bound-state solution for $k_F \neq 0$ emerges at an $s$-wave scattering length with a larger value of $|a_{23}|$ at threshold energy $E_{\text{thr}}$, and converges asymptotically to the corresponding Efimov state; see Fig. 5.2. This implies that the Pauli blocking of states demands stronger attractive interactions between the pairs to forming a three-body bound state. Moreover, it implies that the effect of the Fermi seas is more pronounced near unitarity. As a result, the translational symmetry is broken and the Efimov

---

[6]As described in Chap. 4, recall that the two-body bound states appear as continuum states, and the three-body bound states appear at discrete energy levels. Moreover, due to the truncation on each sum, the two-body continuum appears with finite range; see Sec. 4.3.2 for more details.
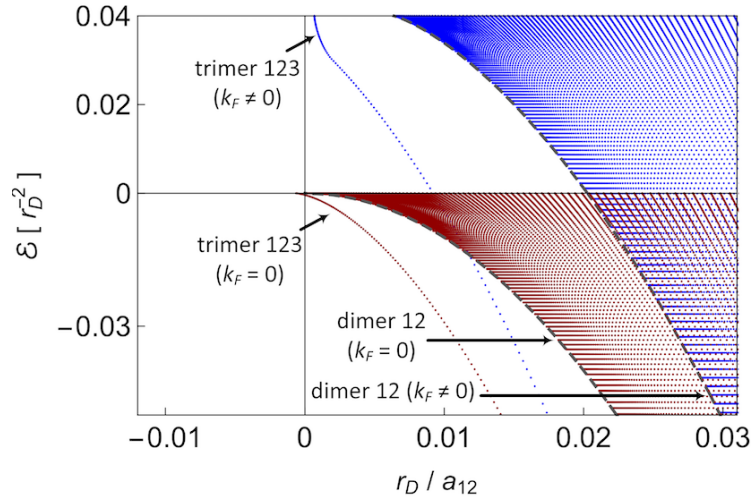
Figure 5.3: Three-body spectrum for a noninteracting Fermi mixture, $g_{23} = 0$: Energy $\mathcal{E} = 2\mu_{12}E/\hbar^2$ in units of $r_D^{-2}$ vs $r_D/a_{12}$ for $m_2/m_1 = 1$. Red curves show the Efimov spectrum in vacuum, $k_F = 0$. Blue curves show the three-body spectrum for $k_F r_D \approx 0.02$. Gray dashed curves are the lowest-energy two-body bound states of the two-body continuum in vacuum, cf. Eq. (5.34), and in the presence of Fermi seas; cf. Eq. (5.40). The Fermi seas push the onset of the two-body bound-state continuum as well as the onset of the three-body bound state to positive values of $a_{12}$. Far from unitarity, the three-body bound-state solution (single blue curve) converges asymptotically to the corresponding Efimov state (single red curve).

scaling law governing three-body bound states in vacuum, cf. Sec. 2.3.3, does not hold anymore. We find our results consistent with Refs. [196, 197], where in the former one light fermion immersed in a Fermi sea interacts resonantly with two heavy bosons, and in the latter, three distinguishable particles with equal masses are subject to Fermi seas and interact resonantly. Our results are also in agreement with Refs. [198, 199], where a system of three identical masses with one particle immersed in a Fermi sea was considered in the zero-range limit. Here the two-body bound-state continuum was derived using the dressed dimer propagator, and the three-body bound state was calculated using the three-body on-shell $T$-matrix [125, 200]. Moreover, our results are consistent with Ref. [201], where a QCD-like phase diagram was discussed for Efimov trimers and Cooper pairs in a Fermi gas.

## 5.4   Three-body bound states for a noninteracting Fermi mixture

For a noninteracting mixture, $g_{23} = 0$, we have $F_1 = 0$; cf. Eq. (4.16). As a result, $\xi_2(\mathbf{k}_2; F_1) = 0$ and Eq. (5.15) has no effect anymore. The resulting integral equation
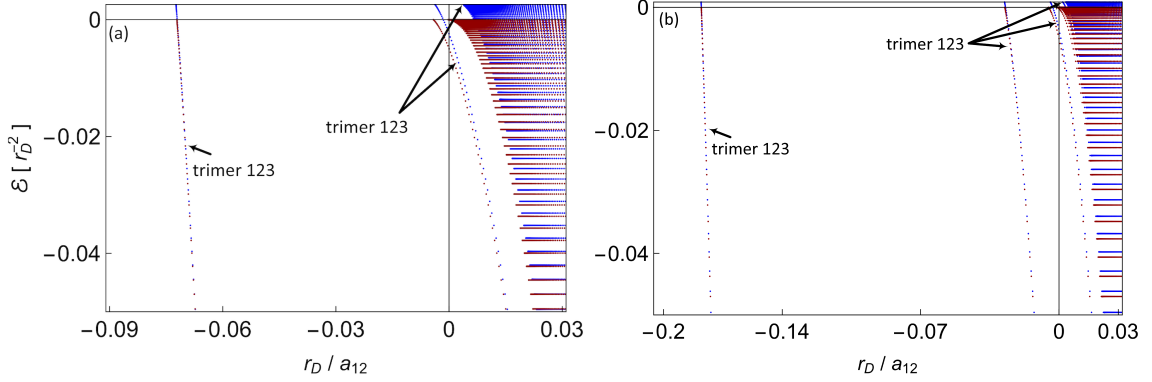
Figure 5.4: Three-body spectrum for noninteracting Fermi mixture, $g_{23} = 0$: Energy $\mathcal{E} = 2\mu_{12}E/\hbar^2$ in units of $r_D^{-2}$ vs $r_D/a_{12}$. Red curves correspond to Efimov spectrum, $k_F = 0$, and blue curves are the result for $k_F r_D \approx 0.01$: (a) $m_2/m_1 \approx 6.64$, (b) $m_2/m_1 \approx 22.26$. By increasing the mass ratio $m_2/m_1$, we find more excited three-body bound states. The effect of the Fermi seas is more pronounced near unitarity. Far from unitarity and for low energies, the three-body bound states for $k_F \neq 0$ converge asymptotically to the corresponding Efimov states. A zoom on the region where a highest-energy excited three-body bound state emerges is represented in Fig. 5.5.

for $s$-wave symmetry of the states and for a given three-body parameter $\Lambda$ reads as

$$\Omega_{12}(a_{12}, k_2; k_F, \mathcal{E})F_2(k_2) = -\frac{1}{2\pi\frac{\mu_{12}}{m_1}k_2} \int_{k_F}^{\Lambda} d\tilde{p}_3\, \tilde{p}_3 \ln\left(\frac{\tilde{p}_3^2 + \frac{2\mu_{12}}{m_1}k_2\tilde{p}_3 + k_2^2 - \mathcal{E}}{\tilde{p}_3^2 - \frac{2\mu_{12}}{m_1}k_2\tilde{p}_3 + k_2^2 - \mathcal{E}}\right) F_2(\tilde{p}_3),$$

$$(5.41)$$

where the function $\Omega_{12}$ is given by Eq. (5.39).

For the three-body bound states, we solve Eq. (5.41) numerically, following the algorithm described in Sec. 4.3.2. The resulting spectrum for $m_2/m_1 = 1$ is shown in Fig. 5.3. Compared to the corresponding Efimov spectrum of three atoms in vacuum, we find that in the presence of Fermi seas, the onset of the lowest-energy two-body bound state as well as the onset of the three-body bound state are pushed to positive values of $a_{12}$. The three-body bound-state solution converges asymptotically to the corresponding Efimov state in vacuum.

We note that for a given value of the three-body cutoff $\Lambda$, increasing the mass ratio $m_2/m_1$ for three atoms in vacuum decreases the Efimov scaling factor; see Sec. 2.3.3. This results in emerging excited Efimov states. We also find that for $k_F \neq 0$, as we increase the mass ratio $m_2/m_1$, we observe the emergence of the excited three-body bound states. For a given value of $k_F$ we increase the mass ratio $m_2/m_1$, resulting in Fig. 5.4. In Fig. 5.4(a) we have $m_2/m_1 \approx 6.64$, where we find two excited additional three-body bound states. In Fig. 5.4(b) we increase the mass
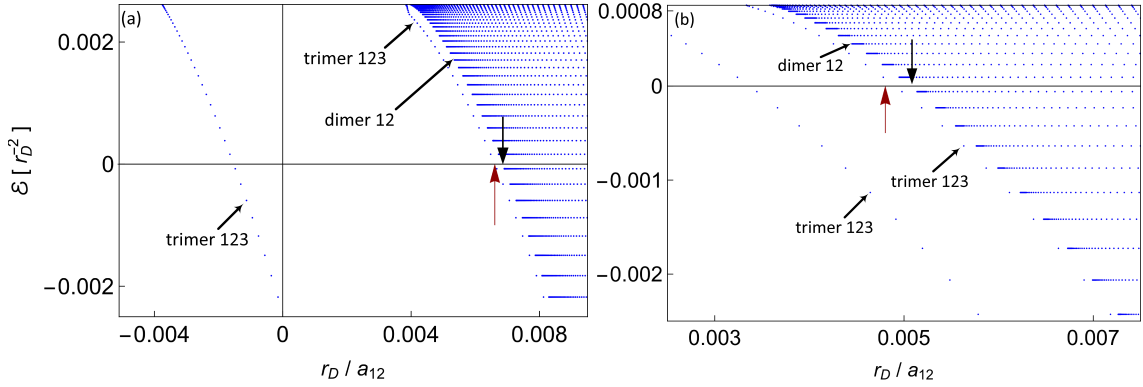
Figure 5.5: A zoom on the plot of energy $\mathcal{E} = 2\mu_{12}E/\hbar^2$ in units of $r_D^{-2}$ vs $r_D/a_{12}$ for (a) $m_2/m_1 \approx 6.64$ corresponding to Fig. 5.4(a), and (b) $m_2/m_1 \approx 22.26$ corresponding to Fig. 5.4(b). Both panels show the region where a highest-energy excited three-body bound state emerges. Black vertical arrow locates the onset of the lowest-energy two-body bound state at zero energy, given by Eq. (5.43). Red vertical arrow locates the onset of a highest-energy excited three-body bound state at zero energy, given by Eq. (5.51).

ratio to $m_2/m_1 \approx 22.26$, and obtain three excited three-body bound states. The red curves in both figures show the result in vacuum, which are the Efimov states, and the blue curves show the result in the presence of Fermi seas. We find that as we approach unitarity, the effect of the Fermi seas on the spectrum is more pronounced, and the spectrum is shifted towards positive values of the $s$-wave scattering length. Far from unitarity and for low energies, the effect of the Fermi seas is negligible, and the spectrum converges asymptotically to the corresponding Efimov spectrum.

## 5.5 Quantitative description of the spectrum near unitarity for a noninteracting Fermi mixture

We have shown that near unitarity, $a_{12} \to \pm\infty$, the effect of the Fermi seas is more pronounced, and the spectrum is pushed towards positive values of the $s$-wave scattering lengths. In this Section, we provide a quantitative description of the spectrum near unitarity for a noninteracting Fermi mixture, $g_{23} = 0$. To do this, we calculate the onset of the $s$-wave scattering length for the lowest-energy two-body bound state at zero energy. Moreover, for a large mass ratio $m_2/m_1$, we estimate the onset of a highest-energy excited three-body bound state at zero energy. With these two values, we obtain an estimate for the amount of the shift that the spectrum undergoes near unitarity.

## 5.5.1 Onset of the lowest-energy two-body bound state at zero energy

We find the onset of the lowest-energy two-body bound state at zero energy by solving

$$\Omega_{12}(a_{12}, k_2 \to k_F; k_F, \mathcal{E}_{12} \to 0) = 0, \tag{5.42}$$

where the function $\Omega_{12}$ is given by Eq. (5.39), $\mathcal{E}_{12} = 2\mu_{12}E_{12}/\hbar^2$, and $E_{12}$ is the energy of the dimer-12. This results in a critical $s$-wave scattering length, $a_{12,\text{dimer}}^{(c)} \equiv a_{12}(E_{12} = 0)$ as

$$\frac{1}{a_{12,\text{dimer}}^{(c)}} = \frac{k_F}{\pi} \left[ 1 + \frac{1 + \frac{2m_2}{m_1}}{\frac{2m_2}{m_1}(1 + \frac{m_2}{m_1})} \ln\left(1 + \frac{2m_2}{m_1}\right) + \frac{\pi}{2} \frac{1}{1 + \frac{m_2}{m_1}} \sqrt{1 + \frac{2m_2}{m_1}} \right]. \tag{5.43}$$

Equation (5.43) gives an estimate of the shift towards positive values of $a_{12}$ that the lowest-energy two-body bound-state solution undergoes at zero energy in the presence of Fermi seas; see black vertical arrows in Fig. 5.5(a) and 5.5(b). This critical value varies as we change the Fermi momentum $k_F$ or the mass ratio $m_2/m_1$. Figure 5.7 shows the dependence of the critical value on the mass ratio. For very large mass ratios $m_2/m_1$, this amount approaches $k_F/\pi$.

## 5.5.2 Onset of a highest-energy excited three-body bound state for a large mass ratio $m_2/m_1$ at zero energy

To find the onset of a highest-energy excited three-body bound state for a large mass ratio $m_2/m_1$ at zero energy, first we note that near the Fermi surface we can approximate the momentum of the species "2" and "3" to be around $k_F$ but in opposite directions, $\mathbf{k}_2 \sim -\mathbf{k}_3$. Also, recall that we have assumed a vanishing total momentum of the three-body bound state. As a result, in this regime, the momentum of the atom "1" can be approximated to be vanishing, $\mathbf{k}_1 \sim \mathbf{0}$.

Next, we define the relative momentum of the pair-12, $\mathbf{p}_{12}$, as

$$\mathbf{p}_{12} = \frac{m_2}{m_1 + m_2}\mathbf{k}_1 - \frac{m_1}{m_1 + m_2}\mathbf{k}_2. \tag{5.44}$$

We note that for $m_2/m_1 \gg 1$ and $\mathbf{k}_1 \sim \mathbf{0}$, Eq. (5.44) implies that $\mathbf{p}_{12} \sim \mathbf{0}$. The Fermi surface, that is characterized by $k_2 \sim k_F$, can be described in terms of the relative and total momenta of the pair-12 as

$$\left| \frac{\mu_{12}}{m_1}\mathbf{P}_{12} - \mathbf{p}_{12} \right| \sim k_F, \tag{5.45}$$

where $\mathbf{P}_{12} = \mathbf{k}_1 + \mathbf{k}_2$ is the total momentum of the pair-12. Near the Fermi surface and for $m_2/m_1 \gg 1$, Eq. (5.45) implies that $P_{12} \sim (\mu_{12}/m_1)^{-1}k_F$. We note that as

the mass ratio $m_2/m_1$ becomes very large, the threshold energy of the three-body bound state, i.e., $\mathcal{E}_{\text{thr}} = 2\mu_{12}E_{\text{thr}}/\hbar^2 = 2(1 - \mu_{12}/m_1)k_F^2$, approaches the threshold energy of the pair-12, $\mathcal{E}_{\text{thr}}^{(12)} = \mathcal{E}_{\text{thr}}/2$. Therefore, we can estimate the onset of a highest-energy excited three-body bound state at zero energy by calculating the onset of the lowest-energy pair-12 for the total momentum $P_{12} \sim (\mu_{12}/m_1)^{-1}k_F$ at $E_{12} \sim 0$. To do this, first we calculate the spectrum of two atoms "1" and "2" interacting attractively via the contact interaction (5.3), and estimate the onset of the $s$-wave scattering length at zero energy near the Fermi surface.

The Schrödinger equation describing the pair-12 for a contact interaction in terms of the relative and total momenta can be represented as[7]

$$\frac{4\pi\hbar^2}{2\mu_{12}g_{12}} = -4\pi \int \frac{d^3\mathbf{p}_{12}}{(2\pi)^3} \frac{1}{p_{12}^2 + \frac{\mu_{12}}{m_1}(1 - \frac{\mu_{12}}{m_1})P_{12}^2 - \mathcal{E}_{12}}, \tag{5.46}$$

where $\mu_{12}$ is a reduced mass, $1/\mu_{12} = 1/m_1 + 1/m_2$. In general, the Fermi sea demands a constraint on the momentum of the atom "2", $k_2 > k_F$, which in terms of the relative and total momenta reads as $|\frac{\mu_{12}}{m_1}\mathbf{P}_{12} - \mathbf{p}_{12}| > k_F$. This constraint imposes an upper bound on the angle between $\mathbf{p}_{12}$ and $\mathbf{P}_{12}$. Without loss of generality we assume that $\mathbf{P}_{12} = P_{12}\mathbf{e}_z$, where $\mathbf{e}_z$ is the unit vector in the direction of the $z$-axis. We also assume $s$-wave symmetry of the states. We solve Eq. (5.46) analytically. To do this, we consider two cases. For $P_{12} \leqslant (\mu_{12}/m_1)^{-1}k_F$ we have:

$$\begin{aligned}\frac{4\pi\hbar^2}{2\mu_{12}g_{12}} =& \frac{-1}{\frac{2\mu_{12}}{m_1}\pi P_{12}} \int_{k_F - \frac{\mu_{12}}{m_1}P_{12}}^{k_F + \frac{\mu_{12}}{m_1}P_{12}} dp_{12}\, p_{12} \frac{p_{12}^2 + (\frac{\mu_{12}}{m_1})^2 P_{12}^2 - k_F^2}{p_{12}^2 + \frac{\mu_{12}}{m_1}(1 - \frac{\mu_{12}}{m_1})P_{12}^2 - \mathcal{E}_{12}} \\ & - \frac{1}{\pi}\int_{k_F - \frac{\mu_{12}}{m_1}P_{12}}^{k_F + \frac{\mu_{12}}{m_1}P_{12}} dp_{12}\, p_{12}^2 \frac{1}{p_{12}^2 + \frac{\mu_{12}}{m_1}(1 - \frac{\mu_{12}}{m_1})P_{12}^2 - \mathcal{E}_{12}} \\ & - \frac{2}{\pi}\lim_{\Lambda_2 \to \infty}\int_{k_F + \frac{\mu_{12}}{m_1}P_{12}}^{\Lambda_2} dp_{12}\, p_{12}^2 \frac{1}{p_{12}^2 + \frac{\mu_{12}}{m_1}(1 - \frac{\mu_{12}}{m_1})P_{12}^2 - \mathcal{E}_{12}}. \end{aligned} \tag{5.47}$$

We calculate each integral, see Appendix F in Sec. 7.1, and use the regularization relation (5.11). We obtain

$$\begin{aligned}\frac{1}{a_{12}} =& \frac{k_F}{\pi} - \frac{\sqrt{\varrho}}{\pi}\left[\arctan\left(\frac{k_F - \frac{\mu_{12}}{m_1}P_{12}}{\sqrt{\varrho}}\right) + \arctan\left(\frac{k_F + \frac{\mu_{12}}{m_1}P_{12}}{\sqrt{\varrho}}\right) - \pi\right] + \frac{1}{4\pi\frac{\mu_{12}}{m_1}P_{12}} \\ & \times \left(\frac{\mu_{12}}{m_1}(\frac{2\mu_{12}}{m_1} - 1)P_{12}^2 - k_F^2 + \mathcal{E}_{12}\right)\ln\left(\frac{\frac{\mu_{12}}{m_1}P_{12}^2 - \frac{2\mu_{12}}{m_1}k_F P_{12} + k_F^2 - \mathcal{E}_{12}}{\frac{\mu_{12}}{m_1}P_{12}^2 + \frac{2\mu_{12}}{m_1}k_F P_{12} + k_F^2 - \mathcal{E}_{12}}\right),\end{aligned} \tag{5.48}$$

---

[7]To arrive at Eq. (5.46), we note that the kinetic energy of the pair-12 can be written in terms of $\mathbf{p}_{12}$ and $\mathbf{P}_{12}$, i.e., we have $\frac{\mu_{12}}{m_1}k_1^2 + \frac{\mu_{12}}{m_2}k_2^2 = p_{12}^2 + \frac{\mu_{12}}{m_1}(1 - \frac{\mu_{12}}{m_1})P_{12}^2$. Next, we follow the procedure described in Sec. 5.2.2 for the pair-12 with a nonvanishing total momentum.
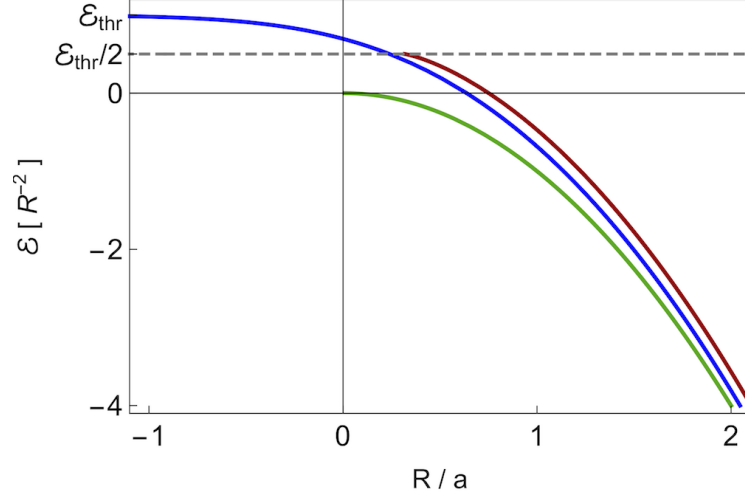
Figure 5.6: Energy $\mathcal{E} = 2\mu E/\hbar^2$ in units of $R^{-2}$ vs $R/a$, for two equal-mass atoms with a reduced mass $\mu$ and an $s$-wave scattering length $a$, where $R$ is an arbitrary length scale. Green curve is the result in vacuum, $k_F = 0$, given by Eq. (5.34), emerging at unitarity. Blue curve shows the result of a Cooper pair with vanishing total momentum described by Eq. (5.33), where both atoms are immersed in an inert Fermi sea with the Fermi momentum $k_F R = 1$. Here the result is expanded to $a < 0$. Red curve is the result for a pair with the total momentum $P_{12} = k_F$, where only one atom is subject to an inert Fermi sea with the Fermi momentum $k_F R = 1$; cf. Eqs. (5.48) and (5.50). Here the result emerges at a finite value of $a$. Gray dashed lines show the threshold energy $\mathcal{E}_{\text{thr}}$ and $\mathcal{E}_{\text{thr}}/2$, where $\mathcal{E}_{\text{thr}} = 2\mu E_{\text{thr}}/\hbar^2 = k_F^2$.

where $\varrho \equiv \frac{\mu_{12}}{m_1}(1 - \frac{\mu_{12}}{m_1})P_{12}^2 - \mathcal{E}_{12}$ .

For $P_{12} \geqslant (\mu_{12}/m_1)^{-1}k_F$ we have:

$$
\begin{aligned}
\frac{4\pi\hbar^2}{2\mu_{12}g_{12}} = & -\frac{2}{\pi}\int_0^{\frac{\mu_{12}}{m_1}P_{12}-k_F} dp_{12}\, p_{12}^2 \frac{1}{p_{12}^2 + \frac{\mu_{12}}{m_1}(1-\frac{\mu_{12}}{m_1})P_{12}^2 - \mathcal{E}_{12}} \\
& -\frac{1}{\frac{2\mu_{12}}{m_1}\pi P_{12}}\int_{\frac{\mu_{12}}{m_1}P_{12}-k_F}^{\frac{\mu_{12}}{m_1}P_{12}+k_F} dp_{12}\, p_{12}\frac{p_{12}^2 + (\frac{\mu_{12}}{m_1})^2 P_{12}^2 - k_F^2}{p_{12}^2 + \frac{\mu}{m_1}(1-\frac{\mu}{m_1})P_{12}^2 - \mathcal{E}_{12}} \\
& -\frac{1}{\pi}\int_{\frac{\mu_{12}}{m_1}P_{12}-k_F}^{\frac{\mu_{12}}{m_1}P_{12}+k_F} dp_{12}\, p_{12}^2 \frac{1}{p_{12}^2 + \frac{\mu_{12}}{m_1}(1-\frac{\mu_{12}}{m_1})P_{12}^2 - \mathcal{E}_{12}} \\
& -\frac{2}{\pi}\lim_{\Lambda_2\to\infty}\int_{\frac{\mu_{12}}{m_1}P_{12}+k_F}^{\Lambda_2} dp_{12}\, p_{12}^2 \frac{1}{p_{12}^2 + \frac{\mu_{12}}{m_1}(1-\frac{\mu_{12}}{m_1})P_{12}^2 - \mathcal{E}_{12}}.
\end{aligned} \qquad (5.49)
$$

Similar to previous case, we calculate each integral individually and use the regularization relation (5.11). We obtain

$$\frac{1}{a_{12}} = \frac{k_F}{\pi} + \frac{\sqrt{\varrho}}{\pi} \left[ \arctan\left( \frac{\frac{\mu_{12}}{m_1}P_{12} - k_F}{\sqrt{\varrho}} \right) - \arctan\left( \frac{\frac{\mu_{12}}{m_1}P_{12} + k_F}{\sqrt{\varrho}} \right) + \pi \right] + \frac{1}{4\pi\frac{\mu_{12}}{m_1}P_{12}}$$

$$\times \left( \frac{\mu_{12}}{m_1}(\frac{2\mu_{12}}{m_1} - 1)P_{12}^2 - k_F^2 + \mathcal{E}_{12} \right) \ln\left( \frac{\frac{\mu_{12}}{m_1}P_{12}^2 - \frac{2\mu_{12}}{m_1}k_F P_{12} + k_F^2 - \mathcal{E}_{12}}{\frac{\mu_{12}}{m_1}P_{12}^2 + \frac{2\mu_{12}}{m_1}k_F P_{12} + k_F^2 - \mathcal{E}_{12}} \right).$$

$$(5.50)$$

Figure 5.6 compares the lowest-energy two-body bound-state solution in vacuum with a Cooper pair, and also with a pair for a nonvanishing total momentum where only one species is subject to a Fermi sea.

Finally, we expand Eq. (5.48) or Eq. (5.50) for $m_2/m_1 \gg 1$, and take the limits $\mathcal{E}_{12} \to 0$ and $P_{12} \to (\frac{\mu_{12}}{m_1})^{-1}k_F$. This provides an estimate for the critical $s$-wave scattering length, $a_{12,\text{trimer}}^{(c)} \equiv a_{12}(E \approx 0)$:

$$\frac{1}{a_{12,\text{trimer}}^{(c)}} \approx \frac{k_F}{\pi} \left[ 1 + \frac{1}{4}\frac{1}{1 + \frac{m_2}{m_1}} \ln\left( 4(1 + \frac{m_2}{m_1}) \right) - \frac{\pi}{2}\frac{1}{\sqrt{1 + \frac{m_2}{m_1}}} + \frac{1}{2}\frac{1}{1 + \frac{m_2}{m_1}} \right] \quad (5.51)$$

for $m_2/m_1 \gg 1$. Equation (5.51) gives an estimate for the amount of the shift towards positive values of $a_{12}$ that a highest-energy excited three-body bound state in the presence of Fermi seas undergoes at zero energy; see Fig. 5.5. Figure 5.7 shows the dependence of this critical value on the mass ratio $m_2/m_1$. For very large values of $m_2/m_1$, this critical value eventually approaches $k_F/\pi$, converging to the onset of the lowest-energy two-body bound state at zero energy.

Figure 5.5 shows a zoom on the region where a highest-energy excited three-body bound state emerges for $m_2/m_1 = 6.64$ and $m_2/m_1 \approx 22.26$. The black and red vertical arrows locate the critical values (5.43) and (5.51), respectively. With these two values, we can estimate the amount of the shift that the spectrum undergoes near unitarity.

## 5.6 Generalized scaling law

Our results in Secs. 5.3 and 5.4 imply that in the presence of the Fermi seas, the translational invariance is broken and the Efimov scaling law in vacuum, see Eqs. (2.24) and (2.25), is not valid. In this Section, we show that a scaling transformation $k_F \mapsto \lambda_0 k_F$, where $\lambda_0$ is the Efimov scaling factor, cf. Sec. 2.3.3, results in a generalized scaling law governing the three-body bound states in the presence of Fermi seas.

We note that $k_F \mapsto \lambda_0 k_F$ implies a scaling transformation of all momenta as $k_i \mapsto \lambda_0 k_i$, for $i = 1, 2, 3$. It also rescales the threshold energy as $E_{\text{thr}} \mapsto \lambda_0^2 E_{\text{thr}}$, cf. Eq. (5.1), implying a general scaling transformation of the energy as $E \mapsto \lambda_0^2 E$.
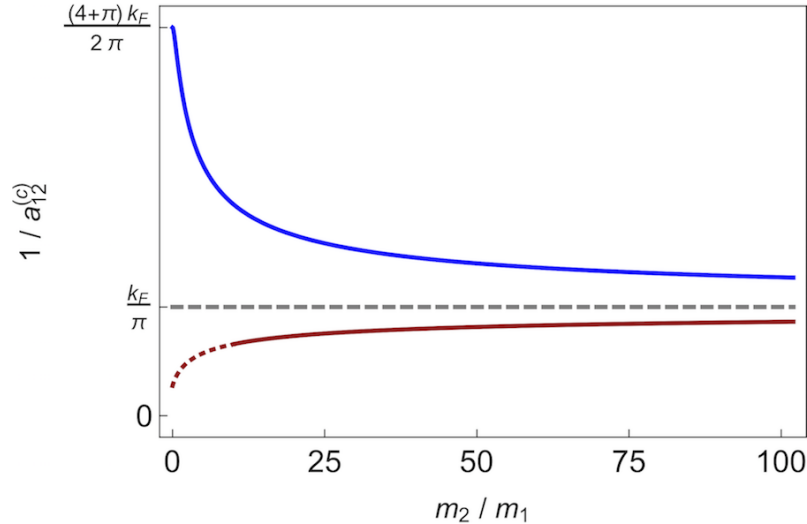
Figure 5.7: Critical *s*-wave scattering length $1/a_{12}^{(c)}$ as a function of the mass ratio $m_2/m_1$ at zero energy. Blue curve corresponds to the lowest-energy two-body bound state, cf. Eq. (5.43), and red curve corresponds to a highest-energy excited three-body bound state that holds for $m_2/m_1 \gg 1$; cf. Eq. (5.51). Both curves converge asymptotically to $k_F/\pi$ for very large mass ratios.

In order that the system of the coupled integral Eqs. (5.14) and (5.15) remains valid, Eqs. (5.31), (5.36), and (5.39) demand a scaling transformation of the *s*-wave scattering length as $a \mapsto a/\lambda_0$. This results in a discrete scaling law for the three-body bound states in the presence of Fermi seas as:

$$\frac{\lambda_0}{a_{n+1}(k_F)} = \frac{1}{a_n(\lambda_0 k_F)}, \tag{5.52}$$

$$\lambda_0^2 E_{n+1}(k_F, 1/a) = E_n(\lambda_0 k_F, \lambda_0/a), \tag{5.53}$$

where $n \in \mathbb{N}$ is an index labeling a three-body bound state; cf. Eqs. (2.24) and (2.25). This result is in agreement with Ref. [202], where the interactions between the species were modeled by an effective potential in real space. Figure 5.8 demonstrates the generalized scaling law (5.52) and (5.53) for an atomic system of three fermions with $g_{23} = 0$ and $m_2/m_1 \approx 22.26$.

## 5.7 Experimental signatures in fermionic mixtures of Yb isotopes

Ytterbium, Yb, is an element in the lanthanide series with various bosonic and fermionc isotopes. It provides one of the most flexible cold-atom systems for quantum-gas experiments. Many experiments with different Yb isotopes have been performed
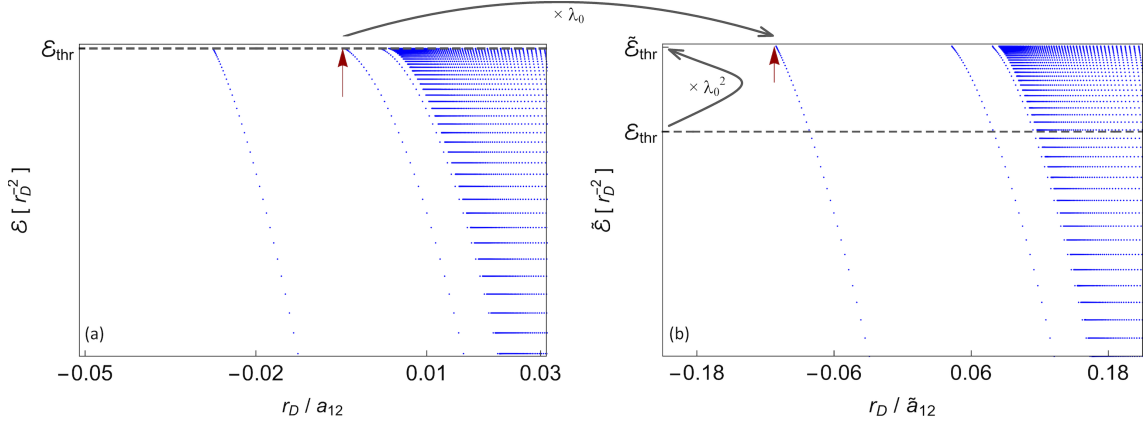
Figure 5.8: Demonstration of the generalized scaling law (5.52) and (5.53) for $g_{23} = 0$ and $m_2/m_1 \approx 22.26$: (a) energy $\mathcal{E} = 2\mu_{12}E/\hbar^2$ in units of $r_D^{-2}$ vs $r_D/a_{12}$ for $k_F r_D \approx 0.01$, (b) rescaled energy $\tilde{\mathcal{E}} = 2\mu_{12}\tilde{E}/\hbar^2$ in units of $r_D^{-2}$ vs rescaled $r_D/\tilde{a}_{12}$, for the scaling transformation $k_i \mapsto \lambda_0 k_i$, $i = 1, 2, 3$, $k_F \mapsto \lambda_0 k_F$, $a_{12} \mapsto a_{12}/\lambda_0$, $E \mapsto \lambda_0^2 E$, where $\lambda_0 = \exp(\pi/|s_0|) \approx 4.84998$ is the corresponding Efimov scaling factor. Red vertical arrow in panel (a) locates the onset of the $(n+1)$-th excited three-body bound state emerging at threshold energy $\mathcal{E}_{\text{thr}} = (2\mu_{12}/\hbar^2)E_{\text{thr}}$. Red vertical arrow in panel (b) locates the onset of the $n$-th excited three-body bound state of the rescaled spectrum emerging at $\tilde{\mathcal{E}}_{\text{thr}} = \lambda_0^2 \mathcal{E}_{\text{thr}}$. Gray dashed lines in both panels show the value of $\mathcal{E}_{\text{thr}}$.

in recent years; see, e.g., Refs. [203, 204, 205, 206, 207, 208, 209]. In this Section, we propose three scenarios as experimental signatures of the three-body bound states in an ultracold Fermi mixture of Yb isotopes.

We note that the two isotopes $^{171}$Yb and $^{173}$Yb are fermion. We consider two densities, $n_{\text{tot}}/2$, of $^{171}$Yb species that are in different internal sates, and include one $^{173}$Yb; see Fig. 5.1, where species "2" and "3" are replaced by $^{171}$Yb, and "1" is replaced by $^{173}$Yb. We denote the $s$-wave scattering lengths of $^{171}$Yb and $^{173}$Yb by $a_{12}$ and $a_{13}$, and the $s$-wave scattering length of two $^{171}$Yb by $a_{23}$. In the following we also assume that $a_{13} = a_{12}$.

The two-color photoassociation spectroscopy (PAS) of Yb atoms, see Ref. [194], shows that two $^{171}$Yb isotopes are almost noninteracting; however, two $^{171}$Yb and $^{173}$Yb interact attractively with the $s$-wave scattering length

$$a_{12}^{(\text{PAS})} \approx -30.6 \text{ nm} \approx -578.23a_0, \tag{5.54}$$

where $a_0$ denotes the Bohr radius[8]. Two isotopes $^{171}$Yb and $^{173}$Yb have almost the same atomic mass with a reduced mass of $\mu_{12} \approx 85.9657$ u [210]. The reduced mass of the Fermi mixture of $^{171}$Yb is $\mu_{23} \approx 85.4682$ u [210].

---

[8]The Bohr radius is $a_0 = \frac{\hbar^2}{m_e}\frac{4\pi\varepsilon_0}{|e|} \approx 0.05292$ nm.
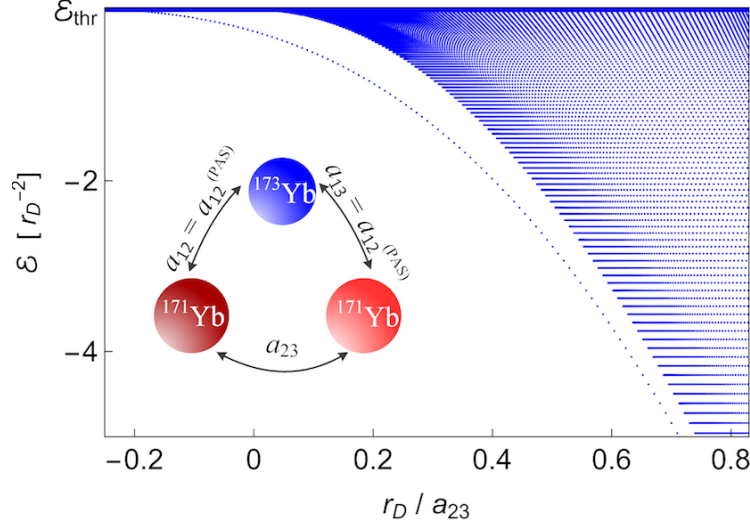
Figure 5.9: Signature of a three-body bound state for the first scenario in an ultracold fermionic mixture of Yb isotopes: Energy $\mathcal{E} = 2\mu_{12}E/\hbar^2$ in units of $r_D^{-2}$ vs $r_D/a_{23}$, where $r_D = \ell_{23}^{(\mathrm{vdW})} \approx 4.145$ nm. The $s$-wave scattering length of $^{171}$Yb and $^{173}$Yb is fixed as the value measured by the photoassociation spectroscopy, $a_{12} = a_{13} = a_{12}^{(\mathrm{PAS})} \approx -30.6$ nm. The three-body bound state emerges at $a_{23} \approx -20.7$ nm at threshold energy $E_{\mathrm{thr}}/h \approx 1.10$ kHz.

The van der Waals dispersive coefficient, $C_6^{(\mathrm{Yb})}$, that determines the atomic interaction in a Yb$_2$ molecule is given by Refs. [194, 211]. We use Eq. (5.13), and calculate the corresponding van der Waals lengths as

$$\ell_{12}^{(\mathrm{vdW})} = \frac{1}{2}\left(\frac{2\mu_{12}C_6^{(\mathrm{Yb})}}{\hbar^2}\right)^{\frac{1}{4}} \approx 4.151 \text{ nm} \approx 78.44a_0, \tag{5.55}$$

$$\ell_{23}^{(\mathrm{vdW})} = \frac{1}{2}\left(\frac{2\mu_{23}C_6^{(\mathrm{Yb})}}{\hbar^2}\right)^{\frac{1}{4}} \approx 4.145 \text{ nm} \approx 78.33a_0. \tag{5.56}$$

These values fix the corresponding length scales $r_D$ defined as Eq. (5.12) [9]. Next, for each internal state we assume that the density of $^{171}$Yb species is $n_{\mathrm{tot}}/2 \approx \frac{1}{2} \times 10^{17}$ m$^{-3}$. We calculate the value of the Fermi momentum as $k_F = (3\pi^2 n_{\mathrm{tot}})^{1/3}$; cf. Ref. [95]. We note that in all following scenarios we assume that the interatomic distances are much larger than the range of the atomic interactions, $1/k_F \gg r_D$. The onset of the three-body bound states might slightly deviate if this criterion

---

[9]We note that here we fix the range of the interaction to be the corresponding van der Waals length. This can be modified by tuning the proportionality coefficient, once a precise measurement of the range of the interaction is provided.
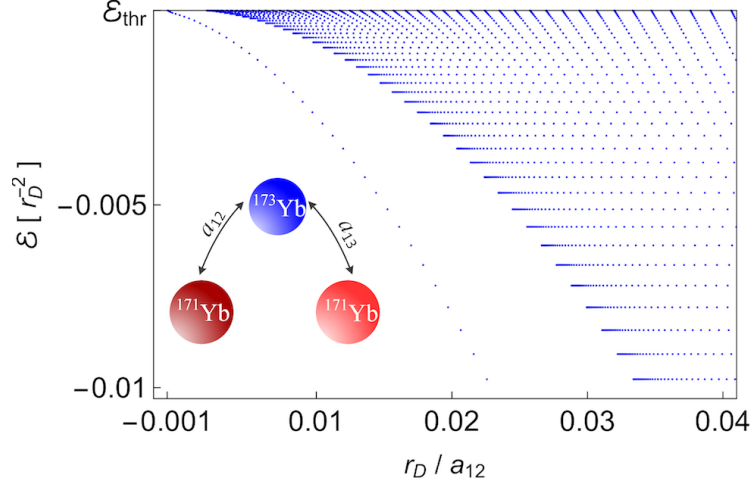
Figure 5.10: Signature of a three-body bound state for the second scenario in an ultracold fermionic mixture of Yb isotopes with a noninteracting Fermi mixture: Energy $\mathcal{E} = 2\mu_{12}E/\hbar^2$ in units of $r_D^{-2}$ vs $r_D/a_{12}$, where $r_D = \ell_{12}^{(\text{vdW})} \approx 4.151$ nm and $a_{13} = a_{12}$. The onset of the three-body bound state is $a_{12} \approx -3193$ nm emerging at threshold energy $E_{\text{thr}}/h \approx 1.09$ kHz.

is not met. As a result, there will be a competition of $^{171}$Yb isotopes to form a three-body bound state with $^{173}$Yb.

## 5.7.1 First scenario

A first scenario is to fix the *s*-wave scattering length of $^{171}$Yb and $^{173}$Yb as the value reported by the photoassociation spectroscopy [194], i.e., $a_{12} = a_{12}^{(\text{PAS})}$; see Eq. (5.54). With this, we calculate the three-body spectrum for three interacting pairs, resulting in Fig. 5.9. We find that a three-body bound state emerges at $a_{23} \approx -20.7$ nm $\approx -391.16a_0$ at threshold energy $E_{\text{thr}}/h \approx 1.10$ kHz. This implies that to observe a three-body bound state, the Fermi mixture should be interacting. As a result, a three-body bound state is observed, if the interaction between two $^{171}$Yb isotopes is tuned via orbital Feshbach resonances [212, 213]. The binding energy is increased in amplitude, provided that the interaction between $^{171}$Yb and $^{173}$Yb is tuned to a more attractive strength.

## 5.7.2 Second scenario

A second scenario is to consider the noninteracting Fermi mixture, i.e., two noninteracting $^{171}$Yb isotopes. We calculate the three-body spectrum for two interacting pairs $^{171}$Yb-$^{173}$Yb. Figure 5.10 shows the result, revealing that a three-body bound state emerges at $a_{12} \approx -3193$ nm $\approx -60336.40a_0$ at threshold energy $E_{\text{thr}}/h \approx 1.09$ kHz. The resulting *s*-wave scattering length $a_{12}$ is much larger in
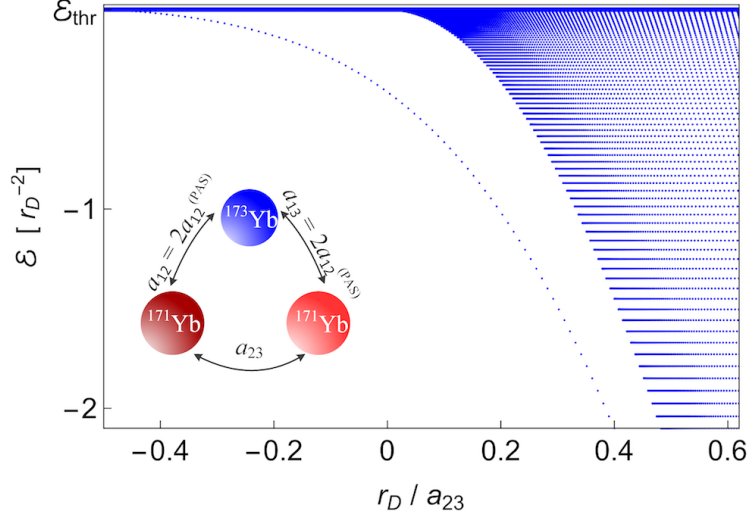
Figure 5.11: Signature of a three-body bound state for the third scenario in an ultracold fermionic mixture of Yb isotopes: Energy $\mathcal{E} = 2\mu_{12}E/\hbar^2$ in units of $r_D^{-2}$ vs $r_D/a_{23}$, where $r_D = \ell_{23}^{(\mathrm{vdW})} \approx 4.145$ nm. The $s$-wave scattering length of $^{171}$Yb and $^{173}$Yb is fixed to be $a_{12} = a_{13} = 2a_{12}^{(\mathrm{PAS})} \approx -2 \times 30.6$ nm, where $a_{12}^{(\mathrm{PAS})}$ is given by Eq. (5.54). The three-body bound state emerges at $a_{23} \approx -10.4$ nm at threshold energy $E_{\mathrm{thr}}/h \approx 1.10$ kHz.

amplitude than $a_{12}^{(\mathrm{PAS})}$, and the threshold energy is slightly smaller than the value obtained in the first scenario. Here a three-body bound state is observed, if the interaction between two $^{171}$Yb and $^{173}$Yb is tuned via interisotope Feshbach resonances [214], or via optical Feshbach resonances [215, 216, 217, 218, 219].

### 5.7.3   Third scenario

A third scenario is to tune the interaction between $^{171}$Yb and $^{173}$Yb to a larger value in amplitude than $a_{12}^{(\mathrm{PAS})}$, e.g., $a_{12} = 2a_{12}^{(\mathrm{PAS})}$. In this case, we find that the three-body bound state emerges at $a_{23} \approx -10.4$ nm $\approx -196.52a_0$ at threshold energy $E_{\mathrm{thr}}/h \approx 1.10$ kHz; see Fig. 5.11. Here the chosen value of $a_{12}$ is much smaller in amplitude than the value obtained in the second scenario, and the resulting value of $a_{23}$ is smaller in amplitude than the value found in the first scenario. Therefore, a three-body bound state is observed, if the interaction between two $^{171}$Yb isotopes and also the interaction between $^{171}$Yb and $^{173}$Yb are tuned simultaneously.

Finally, we notice that in all three scenarios we have observed the formation of one three-body bound state within the range of the atomic interactions. To observe the excited three-body bound states and also to verify the generalized scaling laws (5.52) and (5.53), the Fermi mixture should be chosen such that the mass ratio $m_2/m_1$ increases.

# 5.8 Summary

In this Chapter, we have determined the three-body bound states of an atom in a Fermi mixture. Compared to the corresponding Efimov spectrum in vacuum, the three-body spectrum undergoes a shift towards positive values of the *s*-wave scattering lengths, due to the Pauli blocking of states. We have demonstrated that this effect is more pronounced near unitarity. In this regime and for a noninteracting Fermi mixture, we have provided an analytical description of the spectrum. The deformation of the Efimov spectrum in the presence of Fermi seas results in breaking the translational symmetry. This implies that the Efimov scaling law governing three-body bound states in vacuum is not valid anymore. We have shown that a scaling transformation of the Fermi momentum leads to a generalized scaling law. Finally, we have proposed three scenarios to observe a three-body bound state in a cold-atom system of fermionic Yb isotopes. We have found that to detect a three-body bound state in this system, one needs to tune the isotope interactions via optical, interisotope, or orbital Feshbach resonances.

# Chapter 6

# Conclusions and outlook

In this Thesis we have studied Cooper pairs and fermion trimers in solids and cold-atom systems. We have presented an example of the strong-coupling limit of the Cooper problem for repulsive on-site interactions. We have considered a square unit cell with three sites representing the orbital configurations of copper and oxygen atoms in a copper-oxide, $CuO_2$, plane, which is considered as a main structural unit of the high-temperature cuprate superconductors. We have argued in favor of including the next-nearest-neighbor hopping as a useful parameter that provides a Fermi-surface geometry in a better agreement with experimental data extracted mostly from the angle-resolve photoemission spectroscopy (ARPES). We have shown that this parameter changes the curvature of the dispersive bands and implies a larger hole doping while preserving the desired Fermi-surface geometry. We have represented a theoretical formalism to realize the orbital symmetry of a Cooper pair in a cuprate lattice *a priori*. To solve the Cooper problem, we have constituted the Fermi-Hubbard Hamiltonian on a submanifold of the upper band for vanishing total momentum of a pair. We have considered a singlet-state wave function and have found the ground-state solution without assuming further constraints. Our results have shown that the ground state of a Cooper pair in a cuprate lattice supports the orbital symmetry of $d_{x^2-y^2}$. We have found a critical temperature corresponding to a largest absolute magnitude of the ground-state energy within the order of 100 K. We have also gone beyond the high-temperature cuprate superconductors, and have proposed an experimental signature of the $d$-wave Cooper pairs for a cold-atom system in a cuprate lattice using the techniques of time-of-flight image and noise correlations. We have predicted that the orbital $d$-wave symmetry gives rise to an enhanced density-density correlation of a Cooper pair. We note that our analysis can be generalized to Cooper pairs with nonvanishing total momentum. This might provide an insight into the so-called Umklapp scattering and pseudogap phase in high-temperature cuprate superconductors. Moreover, taking into account higher nearest-neighbor hopping parameters and also including the interband pairings might be other future studies to investigate the resulting orbital symmetry of the ground-state solution and compare it with recent measurements.

Furthermore, we have considered two spin-up and spin-down electrons subject to an inert Fermi sea in a lower band with a quadratic dispersion relation that interact attractively in momentum space, following the reasoning of the Cooper problem. As expected, the ground-state solution results in an *s*-wave Cooper pair. Next, we have expanded the Cooper problem by including a third electron in an upper empty band with quadratic dispersion relation. The effective interaction of the additional electron with the other electrons is assumed to be attractive. We have found that beyond a critical interband interaction strength, the three electrons form a bound state at the interaction strengths that are not yet sufficient to form a Cooper pair. We have referred to this new bound state as an electron trimer state. We have obtained an analytical estimate for the magnitude of the critical interband interaction which can be controlled by the ratio of the Fermi velocity, and the effective mass of the electron in the upper band and the Debye energy. We have shown that as the the interaband interaction increases in absolute magnitude, the trimer state competes with the formation of a Cooper pair. For strong enough interband interactions, we have found that a trimer state can also be formed for noninteracting intraband electrons. From the perspective of the lower band, we have interpreted this trimer state as a particle-induced bound state. In this regime and for a Debye energy comparable with the Fermi energy, if we increase the effective mass of the electrons in the lower band, we find more than one trimer state; however, the number of the trimer states remains finite. We have found BCS-like superconductors as the relevant physical systems in this regime. To realize the signature of the trimer states in conventional superconductors, we have proposed two experimental scenarios using the pump-probe technology. We have predicted that an electron trimer can be observed as a ground state, or as an excited state revealed as an in-gap resonance peak. We emphasize that our analysis can be extended to any order described by a two-fermion order parameter. Moreover, our analysis can be applied to investigate electron trimers with nonvanishing total momentum, which can be a basis to investigate the Fulde-Ferrell-Larkin-Ovchinnikov (FFLO) states of electron trimers. Also, describing a trimer state with a dynamic order parameter using Eliashberg theory would be another future study. We also emphasize that our analysis can be considered as a basis to formulate Fermi liquid of trimers and to study many-body effects of electron trimers.

We have discussed that the existence of Fermi seas is crucial for the formation of two-body and three-body bound states in a solid. On the other hand, for short-range interactions we can mention Efimov states as the three-body bound states of particles in vacuum. We have discussed that the number of the Efimov states is in principle infinite, obeying a geometric scaling law. In a final project, we have investigated the effect of Fermi seas on the Efimov spectrum of an atom in a Fermi mixture for contact interactions. We have shown that in the presence of Fermi seas, the three-body spectrum undergoes a shift towards positive values of the *s*-wave scattering lengths. As a result, the Fermi seas demand stronger attractive interactions of particles to

form a three-body bound state. We have found that this effect is more pronounced near unitarity. To analyze the spectrum quantitatively, we have constituted a system of two coupled integral equations in momentum space. To prevent Thomas collapse and ultraviolet divergences occurring due to contact interactions, we have introduced a regularization relation, by which we have defined the *s*-wave scattering lengths. For a noninteracting Fermi mixture, we have provided an analytical estimate for the deformation of the Efimov spectrum near unitarity. Here, we have calculated the onset of the lowest-energy two-body bound state at zero energy. Moreover, when the Fermi mixture is much heavier than the single atom, we have obtained the onset of a highest-energy excited three-body bound state at zero energy. This analysis exhibits the amount of the shift that the three-body spectrum undergoes near unitarity in the presence of Fermi seas. We have discussed that the deformation of the Efimov spectrum breaks the translational symmetry, invalidating the Efimov scaling law. We have found a generalized scaling law that governs the three-body bound states in the presence of Fermi seas. Finally, our theoretical analysis has enabled us to propose three experimental scenarios to realize the signature of the three-body bound states in an ultracold fermionic mixture of Yb isotopes. Here, the two species of $^{171}$Yb that are in different internal states construct the Fermi mixture, and the additional species is $^{173}$Yb. We have found that the interaction strengths measured by the two-color photoassociation spectroscopy are not strong enough to support a three-body bound state. Therefore, we have predicted the onset of a three-body bound state and the binding energy if the interactions are tuned using the optical or orbital Feshbach resonances. Our theoretical results in this project might provide a future study to investigate the three-body bound states of ultracold fermionic mixtures of Yb isotopes that are trapped in an optical lattice[1].

---

[1] Private communication with Christoph Becker and his group at Universität Hamburg.

# Chapter 7

# Supplemental material

In this Chapter, we describe the details of calculations or derivations that we have used in the Thesis. Moreover, we append our corresponding publications and manuscripts.

## 7.1 Appendices

### Appendix A. Binding energy of a Cooper pair

We start out with Eq. (2.7), describing two electrons that are subject to an inert Fermi sea and interact via the interaction model (2.3). As discussed in the text, we consider $s$-wave symmetry of the states and assume that the total momentum of the system vanishes. Without loss of generality, we also assume that $\mathbf{p} = p\mathbf{e}_z$, where $\mathbf{e}_z$ is the unit vector in the direction of the $z$-axis. Next, we solve the integral in Eq. (2.7) analytically, see Eq. (F1), and obtain

$$\frac{1}{\xi_{12}} + \frac{2}{\pi} \left\{ \lambda - k_F - \sqrt{\mathcal{E}_{12}} \left[ \operatorname{arctanh} \left( \frac{\lambda}{\sqrt{\mathcal{E}_{12}}} \right) - \operatorname{arctanh} \left( \frac{k_F}{\sqrt{\mathcal{E}_{12}}} \right) \right] \right\} = 0. \qquad \text{(A1)}$$

Afterwards, we write the two inverse hyperbolic functions in Eq. (A1) as one function, and use the identity $\operatorname{arctanh}(x) = \frac{1}{2} \ln[(1 + x)/(1 - x)]$ for $\operatorname{Re}(x) < 1$.

Recall that near the Fermi surface we can write $|\mathcal{E}_{12}| \equiv 2\mu|E_{12}|/\hbar^2 = k_F^2 - \kappa^2$, where $0 < \kappa/k_F \ll 1$. We insert this expression for energy in Eq. (A1), and arrive at Eq. (2.9). We note that the condition $0 < \kappa/k_F \ll 1$ results in $(k_F^2 - \kappa^2)^{1/2} \sim k_F - \kappa^2/2k_F + \mathcal{O}(\kappa^2)$. We insert this in (2.9), and solve for $\kappa^2$:

$$\kappa^2 \approx 4k_F^2 \frac{\lambda - k_F}{\lambda + k_F} \exp \left( \frac{\pi}{k_F \xi_{12}} \right) \exp \left( \frac{2}{k_F} (\lambda - k_F) \right). \qquad \text{(A2)}$$

Further, we use the physical property of a typical conventional superconductor that $E_D \ll E_F$. With this, the relation (2.1) results in $\lambda - k_F \ll k_F$. We use this result

and approximate the second exponential function in Eq. (A2) as $1 + 2(\lambda - k_F)/k_F$. Finally, we define the binding energy as $|\Delta| \equiv \hbar^2 \kappa^2 / 2m$, and arrive at Eq. (2.10).

## Appendix B. Efimov attraction

In this Appendix we sketch the original derivation of the Efimov attraction. As discussed in the text, Efimov considered three equal-mass bosons that interact attractively near resonant through short-range interactions. He assumed $s$-wave symmetry of the states and considered the zero total momentum. He approximated the problem by a noninteracting three-particle system, and imposed the Bethe-Peierls boundary condition (2.22) on the wave function $\psi$. He constituted the corresponding time-independent Schrödinger equation in real space and in terms of the Jacobi coordinates $\mathbf{r}_{12}$, the relative distance of a pair, and $\boldsymbol{\rho}_{12,3}$, the distance of the third particle to the center-of-mass of that pair; see Fig. 2.6. Next, he utilized the bosonic exchange symmetry of the three-particle wave function, and decomposed it into three Faddeev components; see Eq. (2.23) and Refs. [125, 200]. Efimov applied the corresponding boundary condition (2.22) on each Faddeev component, and expanded the function $\chi$ in partial $s$-waves, i.e., $\chi(\mathbf{r}_{12}, \boldsymbol{\rho}_{12,3}) = \chi_0(r_{12}, \rho_{12,3})/r_{12}\rho_{12,3}$, where $\chi_0$ is finite as $r_{12} \to 0^+$ and vanishes as $\rho_{12,3} \to 0^+$. He rewrote the Schrödinger equation in hyper-spherical coordinates, $(R, \alpha)$, subject to the boundary conditions for $\alpha = 0$ and $\alpha = \pi/2$. The resulting equation in hyper-spherical coordinates is separable in terms of $R$ and $\alpha$; i.e., $\chi_0(R, \alpha) = F(R)\varphi(\alpha)$.

The equation governing the hyper-angle reads as

$$\frac{d^2\varphi(\alpha)}{d\alpha^2} = -s_n^2\varphi(\alpha), \tag{B1}$$

whose solution is

$$\varphi_n(\alpha) = \sin[s_n(\frac{\pi}{2} - \alpha)], \tag{B2}$$

where $n = 0, 1, 2, \ldots$ is a label denoting a channel for the hyper-radial motion [73]. The boundary condition for $\alpha = 0$ results in a transcendental equation for the parameter $s_n$ as

$$\frac{8}{\sqrt{3}} \sin(\frac{\pi}{6}s_n) = s_n \cos(\frac{\pi}{2}s_n). \tag{B3}$$

Numerical analysis shows that all roots of Eq. (B3) are real, except for the channel $n = 0$ which is pure imaginary; i.e., $s_0 \approx \pm 1.00624i$, where $i \equiv \sqrt{-1}$ [73, 128].

The equation governing the hyper-radial part for vanishing angular momentum, $l = 0$, is

$$\left(-\frac{d^2}{dR^2} - \frac{1}{R}\frac{d}{dR} + \frac{s_n^2}{R^2}\right) F_n(R) = E_n F_n(R), \tag{B4}$$

where $E_n$ is the eigenenergy. We can rewrite Eq. (B4) as

$$\left(-\frac{d^2}{dR^2} + V_n(R)\right) f_n(R) = E_n f_n(R),$$

where $f_n(R) = \sqrt{R} F_n(R)$ and $V_n(R) = (s_n^2 - \frac{1}{4})/R^2$.

We recall that Efimov assumed three particles interacting attractively in the first place. This implies that the only accepted value for the parameter $s_n$ is $s_0 \approx \pm 1.00624i$. As a result, the effective potential reads as

$$V_0^{(E)}(R) = -\frac{|s_0|^2 + \frac{1}{4}}{R^2}, \tag{B5}$$

which is referred to as the Efimov attraction.

## Appendix C. Derivation of the tight-binding Hamiltonian (3.1), and analytical description of the electronic band structure of the cuprate lattice

Including the next-nearest-neighbor hopping $t_{pp}$, cf. Fig. 2.3, results in eight new tunneling terms within the tight-binding Hamiltonian in real space:

$$\begin{aligned}
\hat{H}_{\text{tb}} = \sum_{nm} \Big[ & V_d a_{nm}^\dagger a_{nm} + V_p b_{nm}^\dagger b_{nm} + V_d c_{nm}^\dagger c_{nm} + t_{pd} a_{nm}^\dagger b_{nm} + t_{pd} b_{nm}^\dagger a_{nm} \\
& - t_{pd} a_{nm}^\dagger c_{nm} - t_{pd} c_{nm}^\dagger a_{nm} - t_{pd} a_{nm}^\dagger b_{n-1,m} - t_{pd} b_{n-1,m}^\dagger a_{nm} \\
& + t_{pd} a_{nm}^\dagger c_{n,m-1} + t_{pd} c_{n,m-1}^\dagger a_{nm} - t_{pp} b_{nm}^\dagger c_{nm} - t_{pp} c_{nm}^\dagger b_{nm} \\
& + t_{pp} c_{nm}^\dagger b_{n-1,m} + t_{pp} b_{n-1,m}^\dagger c_{nm} - t_{pp} b_{n-1,m}^\dagger c_{n,m-1} - t_{pp} c_{n,m-1}^\dagger b_{n-1,m} \\
& + t_{pp} b_{n,m}^\dagger c_{n,m-1} + t_{pp} c_{n,m-1}^\dagger b_{n,m} \Big].
\end{aligned} \tag{C1}$$

We take the Fourier transform of the Hamiltonian (C1), and obtain the tight-binding Hamiltonian in momentum space:

$$\begin{aligned}
\hat{H}_{\text{tb}} = \sum_{\mathbf{k} \in 1.\text{BZ}} \Big[ & V_d a_{\mathbf{k}}^\dagger a_{\mathbf{k}} + V_p b_{\mathbf{k}}^\dagger b_{\mathbf{k}} + V_d c_{\mathbf{k}}^\dagger c_{\mathbf{k}} + t_{pd} a_{\mathbf{k}}^\dagger b_{\mathbf{k}} + t_{pd} b_{\mathbf{k}}^\dagger a_{\mathbf{k}} \\
& - t_{pd} a_{\mathbf{k}}^\dagger c_{\mathbf{k}} - t_{pd} c_{\mathbf{k}}^\dagger a_{\mathbf{k}} - t_{pd} e^{-ik_x} a_{\mathbf{k}}^\dagger b_{\mathbf{k}} - t_{pd} e^{ik_x} b_{\mathbf{k}}^\dagger a_{\mathbf{k}} \\
& + t_{pd} e^{-ik_y} a_{\mathbf{k}}^\dagger c_{\mathbf{k}} + t_{pd} e^{ik_y} c_{\mathbf{k}}^\dagger a_{\mathbf{k}} \\
& - t_{pp} \left(1 - e^{ik_x} + e^{ik_x} e^{-ik_y} - e^{-ik_y}\right) b_{\mathbf{k}}^\dagger c_{\mathbf{k}} \\
& - t_{pp} \left(1 - e^{-ik_x} + e^{-ik_x} e^{ik_y} - e^{ik_y}\right) c_{\mathbf{k}}^\dagger b_{\mathbf{k}} \Big].
\end{aligned} \tag{C2}$$

Recall that we have defined two functions $f(k_x) = t_{pd}(1 - e^{-ik_x})$ and $g(k_y) = t_{pd}(1 - e^{-ik_y})$. With this, we can rewrite the two terms inside the brackets in Eq. (C2) as

$$1 - e^{ik_x} + e^{ik_x}e^{-ik_y} - e^{-ik_y} = (1 - e^{ik_x})(1 - e^{-ik_y})$$

$$= \frac{1}{t_{pd}^2} f^*(k_x)g(k_y), \tag{C3}$$

$$1 - e^{-ik_x} + e^{-ik_x}e^{ik_y} - e^{ik_y} = (1 - e^{-ik_x})(1 - e^{ik_y})$$

$$= \frac{1}{t_{pd}^2} f(k_x)g^*(k_y). \tag{C4}$$

We insert the identities (C3) and (C4) into Eq. (C2), and arrive at the tight-binding Hamiltonian (3.1).

Next, the characteristic equation associated with the Hamiltonian (3.1) is

$$s^3 + c(k_x, k_y)s^2 + d(k_x, k_y)s + e(k_x, k_y) = 0, \tag{C5}$$

where

$$c(k_x, k_y) = -V_d - 2V_p, \tag{C6}$$

$$d(k_x, k_y) = -|f(k_x)|^2 - |g(k_y)|^2 - \tau^2|f(k_x)|^2|g(k_y)|^2 + V_p^2 + 2V_dV_p, \tag{C7}$$

$$e(k_x, k_y) = V_p|f(k_x)|^2 + V_p|g(k_y)|^2 + \tau|f(k_x)|^2|g(k_y)|^2(\tau V_d - 2) - V_dV_p^2, \tag{C8}$$

and $\tau = t_{pp}/t_{pd}^2$. We define a new variable $S = s - c(k_x, k_y)/3$, and rewrite Eq. (C5) as

$$S^3 + 3p(k_x, k_y)S + 2q(k_x, k_y) = 0, \tag{C9}$$

where

$$p(k_x, k_y) = \frac{1}{3}d(k_x, k_y) - \frac{1}{9}[c(k_x, k_y)]^2, \tag{C10}$$

$$q(k_x, k_y) = \frac{1}{27}[c(k_x, k_y)]^3 - \frac{1}{6}c(k_x, k_y)d(k_x, k_y) + \frac{1}{2}e(k_x, k_y). \tag{C11}$$

The discriminant of Eq. (C9) reads as

$$D(k_x, k_y) = [q(k_x, k_y)]^2 + [p(k_x, k_y)]^3. \tag{C12}$$

We note that if $D(k_x, k_y) < 0$, which means necessarily that $p(k_x, k_y) < 0$, then Eq. (C9) has three real roots. However, if $D(k_x, k_y) > 0$, Eq. (C9) has one real and two complex roots that are conjugates of one another; see Ref. [150]. Because the tight-binding Hamiltonian matrix is hermitian, the three corresponding eigenvalues

are real. According to mathematical formalism represented in Ref. [150], the three roots of Eq. (C9) are

$$S_1(k_x, k_y) = 2\sqrt{-p(k_x, k_y)} \cos\left(\frac{\theta(k_x, k_y)}{3}\right), \tag{C13}$$

$$S_2(k_x, k_y) = 2\sqrt{-p(k_x, k_y)} \cos\left(\frac{\theta(k_x, k_y) + 4\pi}{3}\right), \tag{C14}$$

$$S_3(k_x, k_y) = 2\sqrt{-p(k_x, k_y)} \cos\left(\frac{\theta(k_x, k_y) + 2\pi}{3}\right), \tag{C15}$$

where

$$\cos\theta(k_x, k_y) = \frac{-q(k_x, k_y)}{\sqrt{-[p(k_x, k_y)]^3}}. \tag{C16}$$

The roots of Eq. (C5), identifying the electronic band structure, are $s_i(k_x, k_y) = S_i(k_x, k_y) + c(k_x, k_y)/3$, for $i = 1, 2, 3$. The three roots (C13)-(C15) can also be represented in terms of the hypergeometric functions. For that, see Ref. [150].

## Appendix D. Derivation of the Hamiltonians (3.9)-(3.11)

Recall that the $d_{x^2-y^2}$ orbital configuration is located on A-site. For the submanifold $\mathcal{S}$, where the total momentum of a pair vanishes, we insert $\alpha_{\mathbf{k}\sigma} = a_{\mathbf{k}\sigma}$ in Eq. (3.8). Afterwards, we write the site operators $a_{\mathbf{k}\sigma}^\dagger$ and $a_{\mathbf{k}\sigma}$ in terms of the corresponding band operators following the relation (3.6):

$$
\begin{aligned}
\hat{H}_{\text{int}}^{(d)} =& \frac{U_d}{\mathcal{A}} \sum_{\mathbf{k},\mathbf{k}'\in 1.\text{BZ}} a_{\mathbf{k}'\downarrow}^\dagger a_{-\mathbf{k}'\uparrow}^\dagger a_{-\mathbf{k}\uparrow} a_{\mathbf{k}\downarrow} \\
=& \frac{U_d}{\mathcal{A}} \sum_{\mathbf{k},\mathbf{k}'\in 1.\text{BZ}} \left\{ \left[ v_{11}(\mathbf{k}')\psi_{\text{U},\mathbf{k}'\downarrow}^\dagger + v_{12}(\mathbf{k}')\psi_{\text{F},\mathbf{k}'\downarrow}^\dagger + v_{13}(\mathbf{k}')\psi_{\text{L},\mathbf{k}'\downarrow}^\dagger \right] \right. \\
& \left[ v_{11}(-\mathbf{k}')\psi_{\text{U},-\mathbf{k}'\uparrow}^\dagger + v_{12}(-\mathbf{k}')\psi_{\text{F},-\mathbf{k}'\uparrow}^\dagger + v_{13}(-\mathbf{k}')\psi_{\text{L},-\mathbf{k}'\uparrow}^\dagger \right] \\
& \left[ v_{11}^*(-\mathbf{k})\psi_{\text{U},-\mathbf{k}\uparrow} + v_{12}^*(-\mathbf{k})\psi_{\text{F},-\mathbf{k}\uparrow} + v_{13}^*(-\mathbf{k})\psi_{\text{L},-\mathbf{k}\uparrow} \right] \\
& \left. \left[ v_{11}^*(\mathbf{k})\psi_{\text{U},\mathbf{k}\downarrow} + v_{12}^*(\mathbf{k})\psi_{\text{F},\mathbf{k}\downarrow} + v_{13}^*(\mathbf{k})\psi_{\text{L},\mathbf{k}\downarrow} \right] \right\}. \tag{D1}
\end{aligned}
$$

Next, we prevent the interband pairings and restrict ourselves to the upper band. This reduces the Hamiltonian (D1) to Eq. (3.9).

For the $p_x$ orbital configuration located on B-site, we insert $\alpha_{\mathbf{k}\sigma} = b_{\mathbf{k}\sigma}$ in Eq. (3.8), and write the site operators $b_{\mathbf{k}\sigma}^\dagger$ and $b_{\mathbf{k}\sigma}$ in terms of the corresponding band

operators to obtain:

$$
\begin{aligned}
\hat{H}_{\text{int}}^{(p_x)} =& \frac{U_p}{\mathcal{A}} \sum_{\mathbf{k},\mathbf{k}'\in 1.\text{BZ}} b_{\mathbf{k}'\downarrow}^{\dagger} b_{-\mathbf{k}'\uparrow}^{\dagger} b_{-\mathbf{k}\uparrow} b_{\mathbf{k}\downarrow} \\
=& \frac{U_p}{\mathcal{A}} \sum_{\mathbf{k},\mathbf{k}'\in 1.\text{BZ}} \Bigg\{ \Big[ v_{21}(\mathbf{k}')\psi_{\text{U},\mathbf{k}'\downarrow}^{\dagger} + v_{22}(\mathbf{k}')\psi_{\text{F},\mathbf{k}'\downarrow}^{\dagger} + v_{23}(\mathbf{k}')\psi_{\text{L},\mathbf{k}'\downarrow}^{\dagger} \Big] \\
& \Big[ v_{21}(-\mathbf{k}')\psi_{\text{U},-\mathbf{k}'\uparrow}^{\dagger} + v_{22}(-\mathbf{k}')\psi_{\text{F},-\mathbf{k}'\uparrow}^{\dagger} + v_{23}(-\mathbf{k}')\psi_{\text{L},-\mathbf{k}'\uparrow}^{\dagger} \Big] \\
& \Big[ v_{21}^{*}(-\mathbf{k})\psi_{\text{U},-\mathbf{k}\uparrow} + v_{22}^{*}(-\mathbf{k})\psi_{\text{F},-\mathbf{k}\uparrow} + v_{23}^{*}(-\mathbf{k})\psi_{\text{L},-\mathbf{k}\uparrow} \Big] \\
& \Big[ v_{21}^{*}(\mathbf{k})\psi_{\text{U},\mathbf{k}\downarrow} + v_{22}^{*}(\mathbf{k})\psi_{\text{F},\mathbf{k}\downarrow} + v_{23}^{*}(\mathbf{k})\psi_{\text{L},\mathbf{k}\downarrow} \Big] \Bigg\}. \quad\quad (D2)
\end{aligned}
$$

Excluding pairings in the flat- and lower band and also neglecting interband pairings, Eq. (D2) results in the Hamiltonian (3.10).

Finally, for the $p_y$ orbital configuration located on C-site of the unit cell, we insert $\alpha_{\mathbf{k}\sigma} = c_{\mathbf{k}\sigma}$ in Eq. (3.8), and write the site operators $c_{\mathbf{k}\sigma}^{\dagger}$ and $c_{\mathbf{k}\sigma}$ in terms of the corresponding band operators:

$$
\begin{aligned}
\hat{H}_{\text{int}}^{(p_y)} =& \frac{U_p}{\mathcal{A}} \sum_{\mathbf{k},\mathbf{k}'\in 1.\text{BZ}} c_{\mathbf{k}'\downarrow}^{\dagger} c_{-\mathbf{k}'\uparrow}^{\dagger} c_{-\mathbf{k}\uparrow} c_{\mathbf{k}\downarrow} \\
=& \frac{U_p}{\mathcal{A}} \sum_{\mathbf{k},\mathbf{k}'\in 1.\text{BZ}} \Bigg\{ \Big[ v_{31}(\mathbf{k}')\psi_{\text{U},\mathbf{k}'\downarrow}^{\dagger} + v_{32}(\mathbf{k}')\psi_{\text{F},\mathbf{k}'\downarrow}^{\dagger} + v_{33}(\mathbf{k}')\psi_{\text{L},\mathbf{k}'\downarrow}^{\dagger} \Big] \\
& \Big[ v_{31}(-\mathbf{k}')\psi_{\text{U},-\mathbf{k}'\uparrow}^{\dagger} + v_{32}(-\mathbf{k}')\psi_{\text{F},-\mathbf{k}'\uparrow}^{\dagger} + v_{33}(-\mathbf{k}')\psi_{\text{L},-\mathbf{k}'\uparrow}^{\dagger} \Big] \\
& \Big[ v_{31}^{*}(-\mathbf{k})\psi_{\text{U},-\mathbf{k}\uparrow} + v_{32}^{*}(-\mathbf{k})\psi_{\text{F},-\mathbf{k}\uparrow} + v_{33}^{*}(-\mathbf{k})\psi_{\text{L},-\mathbf{k}\uparrow} \Big] \\
& \Big[ v_{31}^{*}(\mathbf{k})\psi_{\text{U},\mathbf{k}\downarrow} + v_{32}^{*}(\mathbf{k})\psi_{\text{F},\mathbf{k}\downarrow} + v_{33}^{*}(\mathbf{k})\psi_{\text{L},\mathbf{k}\downarrow} \Big] \Bigg\}. \quad\quad (D3)
\end{aligned}
$$

Similar to the interaction Hamiltonians for $d_{x^2-y^2}$ and $p_y$, we exclude pairings in the other bands and prevent the interband pairings, resulting in Eq. (3.11).

## Appendix E. Derivation of the pairing Eq. (3.26)

To derive the pairing Eq. (3.26), first we need to verify Eqs. (3.23) and (3.24). We start out with applying $\hat{H}_{\text{kin}}$ on the pairing ansatz (3.22):

$$\hat{H}_{\text{kin}} \ket{\Phi} = \sum_{\substack{\mathbf{k}\in 1.\text{BZ}\backslash\text{FS} \\ \sigma\in\{\uparrow,\downarrow\}}} \xi_{\mathbf{k}}^{(\text{U})} \psi_{\text{U},\mathbf{k}\sigma}^{\dagger} \psi_{\text{U},\mathbf{k}\sigma} \ket{\Phi}$$

$$= \sum_{\mathbf{k}\in 1.\text{BZ}\backslash\text{FS}} \xi_{\mathbf{k}}^{(\text{U})} \psi_{\text{U},\mathbf{k}\uparrow}^{\dagger} \psi_{\text{U},\mathbf{k}\uparrow} \ket{\Phi} + \sum_{\mathbf{k}\in 1.\text{BZ}\backslash\text{FS}} \xi_{\mathbf{k}}^{(\text{U})} \psi_{\text{U},\mathbf{k}\downarrow}^{\dagger} \psi_{\text{U},\mathbf{k}\downarrow} \ket{\Phi}$$

$$\equiv \hat{H}_{\text{kin}}^{(1)} \ket{\Phi} + \hat{H}_{\text{kin}}^{(2)} \ket{\Phi}. \tag{E1}$$

We apply $\hat{H}_{\text{kin}}^{(1)}$ on the pairing ansatz $\ket{\Phi}$:

$$\hat{H}_{\text{kin}}^{(1)} \ket{\Phi} = \sum_{\mathbf{k}\in 1.\text{BZ}\backslash\text{FS}} \xi_{\mathbf{k}}^{(\text{U})} \psi_{\text{U},\mathbf{k}\uparrow}^{\dagger} \psi_{\text{U},\mathbf{k}\uparrow} \sum_{\boldsymbol{\kappa}\in 1.\text{BZ}\backslash\text{FS}} \phi(\boldsymbol{\kappa}) \psi_{\text{U},\boldsymbol{\kappa}\uparrow}^{\dagger} \psi_{\text{U},-\boldsymbol{\kappa}\downarrow}^{\dagger} \ket{\text{FS}}$$

$$= \sum_{\boldsymbol{\kappa}\in 1.\text{BZ}\backslash\text{FS}} \delta_{\boldsymbol{\kappa}\mathbf{k}} \xi_{\boldsymbol{\kappa}}^{(\text{U})} \phi(\boldsymbol{\kappa}) \psi_{\text{U},\boldsymbol{\kappa}\uparrow}^{\dagger} \psi_{\text{U},-\boldsymbol{\kappa}\downarrow}^{\dagger} \ket{\text{FS}}$$

$$- \sum_{\boldsymbol{\kappa}\in 1.\text{BZ}\backslash\text{FS}} \delta_{\boldsymbol{\kappa}\mathbf{k}} \xi_{\boldsymbol{\kappa}}^{(\text{U})} \sum_{\boldsymbol{\kappa}\in 1.\text{BZ}\backslash\text{FS}} \phi(\boldsymbol{\kappa}) \psi_{\text{U},\boldsymbol{\kappa}\uparrow} \psi_{\text{U},\boldsymbol{\kappa}\uparrow}^{\dagger} \psi_{\text{U},\boldsymbol{\kappa}\uparrow}^{\dagger} \psi_{\text{U},-\boldsymbol{\kappa}\downarrow}^{\dagger} \ket{\text{FS}}$$

$$= \sum_{\boldsymbol{\kappa}\in 1.\text{BZ}\backslash\text{FS}} \delta_{\boldsymbol{\kappa}\mathbf{k}} \xi_{\mathbf{k}}^{(\text{U})} \ket{\Phi}, \tag{E2}$$

where $\delta_{\boldsymbol{\kappa}\mathbf{k}}$ denotes the Kronecker delta and $\ket{\text{FS}}$ can be in general either the noninteracting Fermi-sea state, cf. Eq. (3.19), or the interacting Fermi-sea state, cf. Eq. (3.20). To find the effect of $\hat{H}_{\text{kin}}^{(2)}$ on $\ket{\Phi}$, first we define $\boldsymbol{\kappa}' = -\boldsymbol{\kappa}$, and rewrite the asnatz (3.22) as

$$\ket{\Phi} = \sum_{\boldsymbol{\kappa}'\in 1.\text{BZ}\backslash\text{FS}} \phi(-\boldsymbol{\kappa}') \psi_{\text{U},-\boldsymbol{\kappa}'\uparrow}^{\dagger} \psi_{\text{U},\boldsymbol{\kappa}'\downarrow}^{\dagger} \ket{\text{FS}}. \tag{E3}$$

Next, we find that:

$$\hat{H}_{\text{kin}}^{(2)} \ket{\Phi} = \sum_{\mathbf{k}\in 1.\text{BZ}\backslash\text{FS}} \xi_{\mathbf{k}}^{(\text{U})} \psi_{\text{U},\mathbf{k}\downarrow}^{\dagger} \psi_{\text{U},\mathbf{k}\downarrow} \sum_{\boldsymbol{\kappa}'\in 1.\text{BZ}\backslash\text{FS}} \phi(-\boldsymbol{\kappa}') \psi_{\text{U},-\boldsymbol{\kappa}'\uparrow}^{\dagger} \psi_{\text{U},\boldsymbol{\kappa}'\downarrow}^{\dagger} \ket{\text{FS}}$$

$$= \sum_{\boldsymbol{\kappa}'\in 1.\text{BZ}\backslash\text{FS}} \delta_{\boldsymbol{\kappa}'\mathbf{k}} \xi_{\boldsymbol{\kappa}'}^{(\text{U})} \sum_{\boldsymbol{\kappa}'\in 1.\text{BZ}\backslash\text{FS}} \phi(-\boldsymbol{\kappa}') \psi_{\text{U},\boldsymbol{\kappa}'\downarrow}^{\dagger} \psi_{\text{U},\boldsymbol{\kappa}'\downarrow} \psi_{\text{U},-\boldsymbol{\kappa}'\uparrow}^{\dagger} \psi_{\text{U},\boldsymbol{\kappa}'\downarrow}^{\dagger} \ket{\text{FS}}$$

$$= \sum_{\boldsymbol{\kappa}'\in 1.\text{BZ}\backslash\text{FS}} \delta_{\boldsymbol{\kappa}'\mathbf{k}} \xi_{\boldsymbol{\kappa}'}^{(\text{U})} \ket{\Phi}. \tag{E4}$$

We insert the resulting operators (E2) and (E4) into Eq. (E1), and obtain

$$\hat{H}_{\text{kin}} \ket{\Phi} = \sum_{\mathbf{k}\in 1.\text{BZ}\backslash\text{FS}} \left( \xi_{\mathbf{k}}^{(\text{U})} + \xi_{-\mathbf{k}}^{(\text{U})} \right) \ket{\Phi}. \tag{E5}$$

Further, we calculate the effect of $\hat{H}_{\text{int}}$ on the pairing ansatz (3.22):

$$
\begin{aligned}
\hat{H}_{\text{int}} \left|\Phi\right\rangle =& \frac{1}{\mathcal{A}} \sum_{\mathbf{k},\mathbf{k}'\in 1.\text{BZ}\backslash\text{FS}} \mathcal{V}_{\mathbf{k},\mathbf{k}'} \psi^{\dagger}_{\text{U},\mathbf{k}'\downarrow}\psi^{\dagger}_{\text{U},-\mathbf{k}'\uparrow}\psi_{\text{U},-\mathbf{k}\uparrow}\psi_{\text{U},\mathbf{k}\downarrow} \left|\Phi\right\rangle \\
=& \frac{1}{\mathcal{A}} \sum_{\mathbf{k},\mathbf{k}'\in 1.\text{BZ}\backslash\text{FS}} \mathcal{V}_{\mathbf{k},\mathbf{k}'} \psi^{\dagger}_{\text{U},\mathbf{k}'\downarrow}\psi^{\dagger}_{\text{U},-\mathbf{k}'\uparrow}\psi_{\text{U},-\mathbf{k}\uparrow}\psi_{\text{U},\mathbf{k}\downarrow} \sum_{\boldsymbol{\kappa}\in 1.\text{BZ}\backslash\text{FS}} \phi(\boldsymbol{\kappa}) \\
& \times \psi^{\dagger}_{\text{U},\boldsymbol{\kappa}\uparrow}\psi^{\dagger}_{\text{U},-\boldsymbol{\kappa}\downarrow} \left|\text{FS}\right\rangle .
\end{aligned}
\tag{E6}
$$

For diagonal elements, $\mathbf{k}' = \mathbf{k}$, we have:

$$
\begin{aligned}
\hat{H}_{\text{int}}^{(\text{diag})} \left|\Phi\right\rangle =& \frac{1}{\mathcal{A}} \sum_{\mathbf{k}\in 1.\text{BZ}\backslash\text{FS}} \mathcal{V}_{\mathbf{k},\mathbf{k}} \psi^{\dagger}_{\text{U},\mathbf{k}\downarrow}\psi^{\dagger}_{\text{U},-\mathbf{k}\uparrow}\psi_{\text{U},-\mathbf{k}\uparrow}\psi_{\text{U},\mathbf{k}\downarrow} \sum_{\boldsymbol{\kappa}\in 1.\text{BZ}\backslash\text{FS}} \phi(\boldsymbol{\kappa})\psi^{\dagger}_{\text{U},\boldsymbol{\kappa}\uparrow}\psi^{\dagger}_{\text{U},-\boldsymbol{\kappa}\downarrow} \left|\text{FS}\right\rangle \\
=& \frac{-1}{\mathcal{A}} \sum_{\mathbf{k}\in 1.\text{BZ}\backslash\text{FS}} \mathcal{V}_{\mathbf{k},\mathbf{k}} \sum_{\boldsymbol{\kappa}\in 1.\text{BZ}\backslash\text{FS}} \phi(\boldsymbol{\kappa})\psi^{\dagger}_{\text{U},\mathbf{k}\downarrow}\psi^{\dagger}_{\text{U},-\mathbf{k}\uparrow}\psi_{\text{U},-\mathbf{k}\uparrow}\psi^{\dagger}_{\text{U},\boldsymbol{\kappa}\uparrow} \\
& \left(\hat{\delta}_{\mathbf{k},-\boldsymbol{\kappa}} - \psi^{\dagger}_{\text{U},-\boldsymbol{\kappa}\downarrow}\psi_{\text{U},\mathbf{k}\downarrow}\right) \left|\text{FS}\right\rangle \\
=& \frac{-1}{\mathcal{A}} \sum_{\mathbf{k}\in 1.\text{BZ}\backslash\text{FS}} \mathcal{V}_{\mathbf{k},\mathbf{k}} \sum_{\boldsymbol{\kappa}\in 1.\text{BZ}\backslash\text{FS}} \delta_{\mathbf{k},-\boldsymbol{\kappa}}\phi(\boldsymbol{\kappa}) \, \psi^{\dagger}_{\text{U},\mathbf{k}\downarrow} \left(\hat{1} - \psi_{\text{U},-\mathbf{k}\uparrow}\psi^{\dagger}_{\text{U},-\mathbf{k}\uparrow}\right)\psi^{\dagger}_{\text{U},\boldsymbol{\kappa}\uparrow} \left|\text{FS}\right\rangle \\
=& \frac{1}{\mathcal{A}} \sum_{\mathbf{k}\in 1.\text{BZ}\backslash\text{FS}} \mathcal{V}_{\mathbf{k},\mathbf{k}} \sum_{\boldsymbol{\kappa}\in 1.\text{BZ}\backslash\text{FS}} \phi(-\mathbf{k}) \, \psi^{\dagger}_{\text{U},-\mathbf{k}\uparrow}\psi^{\dagger}_{\text{U},\mathbf{k}\downarrow} \left|\text{FS}\right\rangle \\
& + \frac{1}{\mathcal{A}} \sum_{\mathbf{k}\in 1.\text{BZ}\backslash\text{FS}} \mathcal{V}_{\mathbf{k},\mathbf{k}} \sum_{\boldsymbol{\kappa}\in 1.\text{BZ}\backslash\text{FS}} \delta_{\mathbf{k},-\boldsymbol{\kappa}}\phi(\boldsymbol{\kappa})\psi^{\dagger}_{\text{U},\mathbf{k}\downarrow}\psi_{\text{U},-\mathbf{k}\uparrow}\psi^{\dagger}_{\text{U},-\mathbf{k}\uparrow}\psi^{\dagger}_{\text{U},\boldsymbol{\kappa}\uparrow} \left|\text{FS}\right\rangle \\
=& \frac{1}{\mathcal{A}} \sum_{\mathbf{k}\in 1.\text{BZ}\backslash\text{FS}} \mathcal{V}_{\mathbf{k},\mathbf{k}} \left|\Phi\right\rangle .
\end{aligned}
\tag{E7}
$$

For off-diagonal elements, $\mathbf{k}' \neq \mathbf{k}$, we have:

$$
\begin{aligned}
\hat{H}_{\text{int}}^{(\text{off-diag})} \left|\Phi\right\rangle =& \frac{1}{\mathcal{A}} \sum_{\substack{\mathbf{k},\mathbf{k}'\in 1.\text{BZ}\backslash\text{FS} \\ \mathbf{k}\neq\mathbf{k}'}} \mathcal{V}_{\mathbf{k},\mathbf{k}'} \psi^{\dagger}_{\text{U},\mathbf{k}'\downarrow}\psi^{\dagger}_{\text{U},-\mathbf{k}'\uparrow} \sum_{\boldsymbol{\kappa}\in 1.\text{BZ}\backslash\text{FS}} \phi(\boldsymbol{\kappa}) \\
& \times \psi_{\text{U},-\mathbf{k}\uparrow}\psi_{\text{U},\mathbf{k}\downarrow}\psi^{\dagger}_{\text{U},\boldsymbol{\kappa}\uparrow}\psi^{\dagger}_{\text{U},-\boldsymbol{\kappa}\downarrow} \left|\text{FS}\right\rangle \\
=& \frac{-1}{\mathcal{A}} \sum_{\substack{\mathbf{k},\mathbf{k}'\in 1.\text{BZ}\backslash\text{FS} \\ \mathbf{k}\neq\mathbf{k}'}} \mathcal{V}_{\mathbf{k},\mathbf{k}'} \psi^{\dagger}_{\text{U},\mathbf{k}'\downarrow}\psi^{\dagger}_{\text{U},-\mathbf{k}'\uparrow} \sum_{\boldsymbol{\kappa}\in 1.\text{BZ}\backslash\text{FS}} \phi(\boldsymbol{\kappa}) \\
& \times \psi_{\text{U},-\mathbf{k}\uparrow}\psi^{\dagger}_{\text{U},\boldsymbol{\kappa}\uparrow} \left(\hat{\delta}_{\mathbf{k},-\boldsymbol{\kappa}} - \psi^{\dagger}_{\text{U},-\boldsymbol{\kappa}\downarrow}\psi_{\text{U},\mathbf{k}\downarrow}\right) \left|\text{FS}\right\rangle
\end{aligned}
$$

$$
\begin{aligned}
=&\frac{-1}{\mathcal{A}} \sum_{\substack{\mathbf{k},\mathbf{k}'\in 1.\mathrm{BZ}\backslash\mathrm{FS} \\ \mathbf{k}\neq\mathbf{k}'}} \mathcal{V}_{\mathbf{k},\mathbf{k}'} \psi^{\dagger}_{\mathrm{U},\mathbf{k}'\downarrow}\psi^{\dagger}_{\mathrm{U},-\mathbf{k}'\uparrow} \sum_{\boldsymbol{\kappa}\in 1.\mathrm{BZ}\backslash\mathrm{FS}} \phi(\boldsymbol{\kappa})\psi_{\mathrm{U},\boldsymbol{\kappa}\uparrow}\psi^{\dagger}_{\mathrm{U},\boldsymbol{\kappa}\uparrow}\ket{\mathrm{FS}} \\
=&\frac{-1}{\mathcal{A}} \sum_{\substack{\mathbf{k},\mathbf{k}'\in 1.\mathrm{BZ}\backslash\mathrm{FS} \\ \mathbf{k}\neq\mathbf{k}'}} \mathcal{V}_{\mathbf{k},\mathbf{k}'} \psi^{\dagger}_{\mathrm{U},\mathbf{k}'\downarrow}\psi^{\dagger}_{\mathrm{U},-\mathbf{k}'\uparrow} \sum_{\mathbf{k}'\in 1.\mathrm{BZ}\backslash\mathrm{FS}} \phi(\mathbf{k}')\left(\hat{1}-\psi^{\dagger}_{\mathrm{U},\mathbf{k}'\uparrow}\psi_{\mathrm{U},\mathbf{k}'\uparrow}\right)\ket{\mathrm{FS}} \\
=&\frac{-1}{\mathcal{A}} \sum_{\substack{\mathbf{k},\mathbf{k}'\in 1.\mathrm{BZ}\backslash\mathrm{FS} \\ \mathbf{k}\neq\mathbf{k}'}} \mathcal{V}_{\mathbf{k},\mathbf{k}'} \sum_{\mathbf{k}'\in 1.\mathrm{BZ}\backslash\mathrm{FS}} \phi(\mathbf{k}')\psi^{\dagger}_{\mathrm{U},\mathbf{k}'\downarrow}\psi^{\dagger}_{\mathrm{U},-\mathbf{k}'\uparrow}\ket{\mathrm{FS}} \\
=&\frac{1}{\mathcal{A}} \sum_{\substack{\mathbf{k},\mathbf{k}'\in 1.\mathrm{BZ}\backslash\mathrm{FS} \\ \mathbf{k}\neq\mathbf{k}'}} \mathcal{V}_{\mathbf{k},\mathbf{k}'}\ket{\Phi}. & \text{(E8)}
\end{aligned}
$$

We insert the results of the diagonal and off-diagonal elements into Eq. (E6), and obtain

$$
\hat{H}_{\mathrm{int}}\ket{\Phi} = \frac{1}{\mathcal{A}} \sum_{\mathbf{k},\mathbf{k}'\in 1.\mathrm{BZ}\backslash\mathrm{FS}} \mathcal{V}_{\mathbf{k},\mathbf{k}'}\ket{\Phi}. \tag{E9}
$$

Finally, we insert Eqs. (E5) and (E9) into the eigenvalue problem (3.25), and arrive at the pairing Eq. (3.26).

# Appendix F. Useful integrations

For $a, b, c, d, e, f \in \mathbb{R}$ and $a, d \neq 0$ we have:

$$
\int dx\, \frac{x^2}{ax^2+b} = \frac{1}{a}\left[x - \sqrt{\frac{b}{a}}\arctan\left(\frac{x}{\sqrt{\frac{b}{a}}}\right)\right] + \mathrm{const.} \tag{F1}
$$

$$
\begin{aligned}
\int dx\, x \ln\left(\frac{ax^2+bx+c}{dx^2+ex+f}\right) =& \frac{1}{4a^2d^2}\Bigg\{-2bd^2\sqrt{b^2-4ac}\,\mathrm{arctanh}\left(\frac{2ax+b}{\sqrt{b^2-4ac}}\right) \\
& + 2ea^2\sqrt{e^2-4df}\,\mathrm{arctanh}\left(\frac{2dx+e}{\sqrt{e^2-4df}}\right) \\
& + d\Bigg[-d(b^2-2ac)\ln(ax^2+bx+c)
\end{aligned}
$$

$$+ 2ax \left( adx \ln \left( \frac{ax^2 + bx + c}{dx^2 + ex + f} \right) + bd - ae \right) \bigg]$$
$$+ a^2(e^2 - 2df) \ln(dx^2 + ex + f) \bigg\} + \text{const.} \qquad \text{(F2)}$$

## 7.2 Publications

In this Section, we append our manuscripts [S1], [S2], and [S3] that constitute the main basis of this cumulative Thesis:

- [S1] Ali Sanayei, Pascal Naidon, and Ludwig Mathey, *Electron trimer states in conventional superconductors*, Phys. Rev. Research **2**, 013341 (2020).

- [S2] Ali Sanayei and Ludwig Mathey, *Three-body bound states of an atom in a Fermi mixture*, arXiv:2007.13511v2 [submitted].

- [S3] Ali Sanayei and Ludwig Mathey, *Cooper problem in a cuprate lattice* [manuscript is ready for submission].

For more information on the statement of contributions, see page vii of the Thesis.

# Electron trimer states in conventional superconductors

Ali Sanayei,[1,2,*] Pascal Naidon,[3,†] and Ludwig Mathey[1,2,4,‡]

[1]*Zentrum für Optische Quantentechnologien, Universität Hamburg, Luruper Chaussee 149, D-22761 Hamburg, Germany*
[2]*Institut für Laserphysik, Universität Hamburg, Luruper Chaussee 149, D-22761 Hamburg, Germany*
[3]*RIKEN Nishina Center, RIKEN, Wakō 351-0198, Japan*
[4]*The Hamburg Centre for Ultrafast Imaging, Luruper Chaussee 149, D-22761 Hamburg, Germany*

We expand the Cooper problem by including a third electron in an otherwise empty band. We demonstrate the formation of a trimer state of two electrons above the Fermi sea and the third electron, for sufficiently strong interband attractive interaction. We show that the critical interaction strength is the lowest for small Fermi velocities, large masses of the additional electron, and large Debye energy. This trimer state competes with the formation of the two-electron Cooper pair, and can be created transiently via optical pumping.

## I. INTRODUCTION

In a seminal paper, Ref. [1], Cooper showed that two electrons immersed in a Fermi sea form a bound state for arbitrarily weak attractive interactions. The Cooper problem assumes the dominance of the effective interaction induced by the electron-phonon interaction over the screened Coulomb potential [2–5]. It is modeled as constant in momentum space within a narrow energy range of the order of the Debye energy for the relative kinetic energy of the electrons. This simplified model distills the key features and energy scales of the full interaction induced by electron-phonon coupling that are relevant for the formation of the bound state and its properties. The existence of this bound state indicates that the noninteracting Fermi sea is unstable against pair formation, which suggests the emergence of a superconducting state. A more extensive theory of this state was provided by BCS theory [2–11], which elaborated on the essential ingredients that are necessary for the formation of conventional superconductors, pointed out by the Cooper problem and its solution.

Furthermore, and going beyond superconductivity, a Cooper problem can be formulated for any order parameter composed of two fermionic operators. For example, the weak-coupling limit of charge-density-wave and spin-density-wave orders can be formulated as the formation of an electron-hole pair. Here, the electron is restricted to occupy states outside the Fermi sea, and the hole is restricted to states inside the Fermi sea. Given this broad applicability of the Cooper

problem, it is of fundamental importance for condensed-matter physics.

While the solution of the Cooper problem is a two-particle bound state, further down we will discuss the formation of three-particle bound states. As an example for three-body bound states, we mention Efimov trimers [12–15]. These trimers are formed of particles interacting via contact
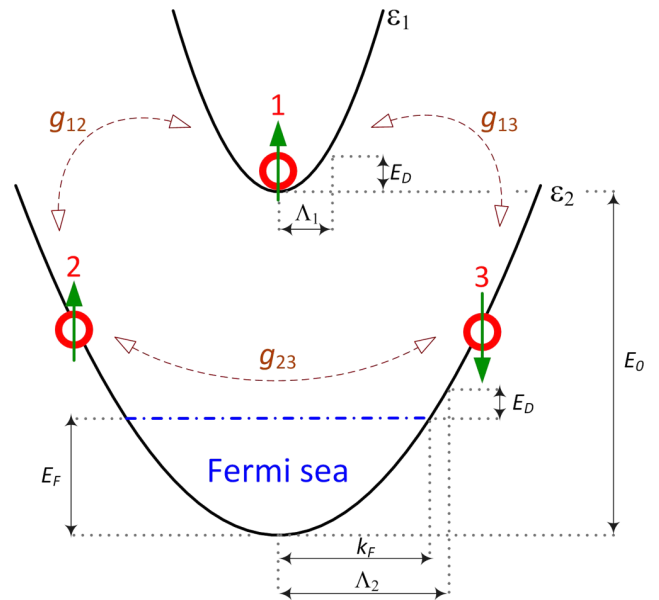


FIG. 1. The expanded Cooper problem consists of two electrons in a partially filled band with dispersion $\varepsilon_2$ and a third electron in an empty band with dispersion $\varepsilon_1$. The inert Fermi sea in the lower band has the Fermi energy $E_F$ and Fermi momentum $k_F$. The energy difference of the two bands is $E_0$. The three electrons interact attractively via the two-body interactions $g_{12}$, $g_{13}$, and $g_{23}$, with $g_{12} = g_{13}$. These interactions are cut off in momentum space by the cutoffs $\Lambda_1$ and $\Lambda_2$, whose magnitudes are chosen to fulfill $\varepsilon_1(\Lambda_1) = \varepsilon_2(\Lambda_2) - E_F = E_D$, where $E_D$ is the Debye energy.

*asanayei@physnet.uni-hamburg.de
†pascal@riken.jp
‡lmathey@physnet.uni-hamburg.de
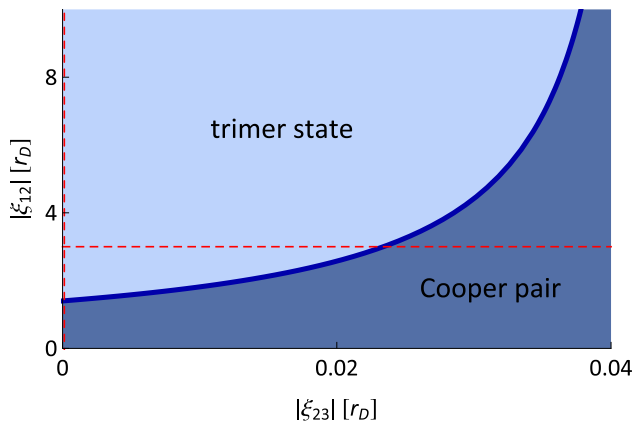
FIG. 2. Lowest energy state as a function of the interaction parameters $|\xi_{23}|$ and $|\xi_{12}|$, both in units of $r_D$. In this example, we choose $E_D/E_F = 0.02$, $m_2/m_1 = 1$, and the cutoffs $\Lambda_1$ and $\Lambda_2$ according to Eq. (1). For sufficiently strong attractive interband interaction $\xi_{12}$, the trimer state has lower energy than the Cooper pair. The horizontal red dashed line is a cut at $|\xi_{12}| = 3r_D$, see Fig. 3, and the vertical red dashed line is a cut at $|\xi_{23}| = 0$, see Fig. 4.



FIG. 3. Shifted energy $E = \mathcal{E} - E_0$ normalized by $2E_F$ vs the interaction parameter $|\xi_{23}|$, in units of $r_D$, for $E_D/E_F = 0.02$, $m_2/m_1 = 1$, and $\xi_{12} = -3r_D$, which corresponds to the horizontal red dashed line in Fig. 2. The lowest energy state for small values of $|\xi_{23}|$ is a trimer state. For sufficiently large values of $|\xi_{23}|$ the formation of Cooper pairs (dimer 23) will be dominant over a trimer state.

interactions at interaction strengths that are not sufficient to support a two-particle bound state. Furthermore, in principle infinitely many three-body bound states are formed, which obey a scaling relation. In contrast to Cooper pairs, Efimov trimers are formed in vacuum. The Efimov effect has been experimentally observed in ultracold atomic gases [16–18] and helium beams experiments [19].

In this paper, we expand the Cooper problem by including a third electron, as depicted in Fig. 1, to demonstrate the formation of electron trimers in the presence of a Fermi sea. We assume that the additional electron, labeled "1," is in an otherwise empty band with quadratic dispersion relation $\varepsilon_1$. Its spin state is arbitrarily depicted as spin-up. The two electrons "2" and "3" are restricted to be outside of an inert Fermi sea, where $k_F$ denotes the Fermi momentum and $E_F$ is the Fermi energy. For simplicity, the dispersion $\varepsilon_2$ of the lower band is assumed to be quadratic. We propose to realize this scenario by optically pumping electrons from a lower band into an unoccupied band, using current technology of pump-probe experiments [20–23]. This results in a low metastable electron density in the upper band. We assume that the effective interaction between the electrons is attractive, following the reasoning of the Cooper problem. We consider the interaction between two electrons to be a negative constant $g_{ij}$, with $i, j = 1, 2, 3$ and $i \neq j$, for the incoming and outgoing momentum of particle $i$ smaller than a cutoff $\Lambda_i$, and zero otherwise. We choose the values of $\Lambda_1$ and $\Lambda_2 = \Lambda_3$ such that

$$E_D = \frac{\hbar^2}{2m_1}\Lambda_1^2 = \frac{\hbar^2}{2m_2}(\Lambda_2^2 - k_F^2), \qquad (1)$$

where $m_i$ is the effective mass of particle $i$ and $E_D$ is the Debye energy; see Fig. 1. For clarity, we allow for three different masses $m_1$, $m_2$, and $m_3$, but are primarily interested in the case $m_3 = m_2$. A similar restriction will be placed on $g_{12}$ and $g_{13}$, which we choose to be equal throughout this paper. For a typical conventional superconductor we have $E_D \ll E_F$,

implying that $\Lambda_1 \ll k_F$ and $\Lambda_2 - k_F \ll k_F$, which we will use as small parameters further down. We define the length scale

$$r_D = (\Lambda_2 - k_F)^{-1} \approx \hbar\frac{v_F}{E_D}, \qquad (2)$$

where $v_F = \hbar k_F/m_2$ is the Fermi velocity. We note that in the following we consider three-body states with vanishing total momentum.

## II. OVERVIEW AND MAIN RESULTS

The main result of our analysis is shown in Fig. 2. We depict whether the lowest energy state is a Cooper pair state or a trimer state, as a function of the interaction parameters $\xi_{23}$ and $\xi_{12} = \xi_{13}$, where $\xi_{23} = 2\tilde{\mu}/(4\pi\hbar^2)g_{23}$ and $\xi_{12} = 2\mu/(4\pi\hbar^2)g_{12}$. The reduced masses are $1/\tilde{\mu} = 1/m_2 + 1/m_3 = 2/m_2$ and $1/\mu = 1/m_1 + 1/m_2$.

For $g_{12} = 0$ we recover the result of the Cooper problem. For any value of $g_{23} < 0$ the electrons in the lower band form a pair. As $g_{12}$ is set to a negative nonzero value, we show that the three electrons form a trimer state beyond a critical value of $g_{12}$, which increases in absolute magnitude as $|g_{23}|$ increases. This trimer formation also occurs for vanishing $g_{23}$. From the perspective of the electrons in the lower band, this can also be considered as a bound-state formation that is induced by a third electron in a higher band, i.e., a particle-induced bound state. As we show below, the magnitude of the critical value of $g_{12}$ for trimer formation is controlled by the ratio of the Fermi velocity, and the mass of the electron in the upper band and the Debye energy. If the mass of the electrons in the upper band is heavier, the critical value is reduced. Similarly, a smaller Fermi velocity and a larger Debye energy reduces the critical value. We note that for the typical parameter regime of conventional superconductors we find one trimer state only. However, we also give an example for a parameter regime in which more than one trimer state exists below.

For a pump-probe experiment, this result implies that a system that is initially either in a superconducting or a metallic

state can be transformed into a Fermi liquid of electron trimers when electrons are pumped into a higher band, and the attractive interband interaction is sufficiently strong.

## III. ELECTRON TRIMER STATES

To determine the bound states of the three-electron system we consider the Schrödinger equation in momentum space:

$$\left(\frac{\hbar^2 k_1^2}{2m_1} + E_0 + \frac{\hbar^2 k_2^2}{2m_2} + \frac{\hbar^2 k_3^2}{2m_3} + \hat{U}_{12} + \hat{U}_{13} + \hat{U}_{23} - \mathcal{E}\right)\psi = 0,$$
(3)

where $\mathbf{k}_1$, $\mathbf{k}_2$, $\mathbf{k}_3$ are the electron momenta and $\psi = \psi(\mathbf{k}_1, \mathbf{k}_2, \mathbf{k}_3)$ is the wave function. The total energy of the electron "1" is $\hbar^2 k_1^2/2m_1 + E_0$, where $E_0$ is the energy difference of the two bands; see Fig. 1. Here we define a shifted energy $E = \mathcal{E} - E_0$, where $\mathcal{E}$ is the eigenenergy [24]. The interaction $\hat{U}_{ij}$ between two electrons "$i$" and "$j$" is

$$\hat{U}_{ij}\psi = g_{ij}\theta_{\Lambda_i}(\mathbf{k}_i)\theta_{\Lambda_j}(\mathbf{k}_j)\int\frac{d^3\mathbf{q}}{(2\pi)^3}\theta_{\Lambda_i}(\mathbf{k}_i - \mathbf{q})\theta_{\Lambda_j}(\mathbf{k}_j + \mathbf{q})\psi,$$
(4)

where $g_{ij} < 0$ and $\mathbf{q}$ denotes the momentum transfer [25]; see Appendix A for the resulting operators $\hat{U}_{ij}\psi$. The cutoff function $\theta_{a,b}(\mathbf{k})$ is defined as

$$\theta_{a,b}(\mathbf{k}) = \begin{cases} 1 & \text{for } a \leqslant |\mathbf{k}| \leqslant b, \\ 0 & \text{otherwise,} \end{cases}$$
(5)

for two real numbers $0 \leqslant a < b$, and $\theta_b(\mathbf{k}) \equiv \theta_{0,b}(\mathbf{k})$. The inert Fermi sea demands the constraints $k_2 > k_F$ and $k_3 > k_F$ on the momenta of electrons "2" and "3," respectively. We consider a singlet state for the electrons "2" and "3" in the following. This system is separable, see Appendix A, which results in a system of two coupled integral equations:

$$\left[\frac{1}{g_{12}} + \int\frac{d^3\mathbf{p}_3}{(2\pi)^3}K_1(\mathbf{k}_2, \mathbf{p}_3; E)\right]F_2(\mathbf{k}_2)$$

$$= -\theta_{k_F,\Lambda_2}(\mathbf{k}_2)\left[\int\frac{d^3\mathbf{p}_3}{(2\pi)^3}K_1(\mathbf{k}_2, \mathbf{p}_3; E)F_2(\mathbf{p}_3)\right.$$

$$\left. + \int\frac{d^3\mathbf{p}_1}{(2\pi)^3}K_2(\mathbf{k}_2, \mathbf{p}_1; E)F_1(\mathbf{p}_1)\right],$$
(6)

$$\left[\frac{1}{g_{23}} + \int\frac{d^3\mathbf{p}_3}{(2\pi)^3}K_3(\mathbf{k}_1, \mathbf{p}_3; E)\right]F_1(\mathbf{k}_1)$$

$$= -2\theta_{\Lambda_1}(\mathbf{k}_1)\int\frac{d^3\mathbf{p}_3}{(2\pi)^3}K_3(\mathbf{k}_1, \mathbf{p}_3; E)F_2(\mathbf{p}_3),$$
(7)

where $\mathbf{p}_i = \mathbf{k}_i - \mathbf{q}$, for $i = 1, 2$, and $\mathbf{p}_3 = \mathbf{k}_3 + \mathbf{q}$. The three integral kernels $K_1$, $K_2$, $K_3$ and the three functions $F_1$, $F_2$, $F_3$ are derived in Appendix A. Due to the singlet symmetry for electrons "2" and "3" we consider $F_2 = F_3$. We assume $F_i(\mathbf{k}) = F_i(k)$, implying $s$-wave symmetry of the state. We notice that in the absence of a Fermi sea and for a contact interaction, Eqs. (6) and (7) will reduce to the standard Skorniakov–Ter Martirosian equation [26] leading to the Efimov effect [27].

To determine whether the lowest energy state is a two-body or a three-body bound state, we use the small parameter

$E_D/E_F$ to approximate the full integral equation with an equation that relates $\xi_{23}$, $\xi_{12}$, and $E$; see Appendix B. We solve this equation numerically for eigenenergies $\mathcal{E}$ near the threshold energy $E_{\text{thr}} = 2E_F + E_0 = \hbar^2 k_F^2/m_2 + E_0$ [28] which results in Fig. 2, depicting a region where electrons "2" and "3" form a Cooper pair, and a second region where the three electrons form a trimer state. The intraband electrons "2" and "3" can form a Cooper pair for any attractive interaction $\xi_{23}$. The trimer state is only formed when the interband interaction $\xi_{12}$ is sufficiently strong. Trimer states of zero total momentum appear as discrete energy levels, whereas dimer states appear as continuum of states.

Next, we solve the full Eqs. (6) and (7) numerically to find the full spectrum and also to validate the analytical estimates. For that, we reduce the three-dimensional integrals over momentum to one-dimensional integrals over the absolute value of each momentum. We approximate the integrals by a sum over discrete values according to the Gauss-Legendre quadrature rule [29–31]. The continuous functions $F_1$ and $F_2$ are evaluated at these discrete momentum values. We therefore approximate Eqs. (6) and (7) with a discrete eigenvalue problem; see Appendix C.

We calculate the resulting eigenenergies $\mathcal{E}$ below the threshold energy $E_{\text{thr}}$. In Fig. 3 we show the shifted energy $E = \mathcal{E} - E_0$ normalized by $2E_F$, for $E_D/E_F = 0.02$ and $\xi_{12} = -3r_D$. For small values of $|\xi_{23}|$ the lowest energy state is a trimer state which appears as a single line of solutions. For larger values the lowest energy state is a Cooper pair which appears as the lowest energy state of a two-body bound-state continuum.

To estimate the critical value of $g_{12}$ for vanishing $g_{23}$ analytically, we recall that $F_1 \propto g_{23}$ and $F_2 \propto g_{12}$; cf. Eqs. (A6) and (A7). With this, Eqs. (6) and (7) reduce to

$$\frac{4\pi\hbar^2}{2\mu g_{12}} + \frac{\tau}{\frac{\mu}{m_1}\pi k_F}\int_{k_F}^{\Lambda_2}dp_3\,p_3$$

$$\times\ln\left(\frac{\left(1 - \frac{\mu}{m_1}\right)p_3^2 + \left(1 - \frac{\mu}{m_1}\right)k_F^2 + \frac{\mu}{m_1}\Lambda_1^2 - \frac{2\mu}{\hbar^2}E}{p_3^2 - \frac{2\mu}{m_1}k_F p_3 + k_F^2 - \frac{2\mu}{\hbar^2}E}\right) \approx 0,$$
(8)

where $\tau = 1$ describes the system of three electrons and $\tau = 1/2$ corresponds to a system of two electrons, "1" and "2" (or "3"); see Appendix D. We evaluate the integral and expand to lowest order in $E_D/E_F$; see Appendices B and D. We solve for the interaction parameter $g_{12}$, then choose the threshold condition $\mathcal{E} = E_{\text{thr}}$ [28], which finally gives the critical value

$$\left|g_{12}^{(c)}\right| \sim \frac{2\pi^2\hbar^2}{m_1}r_D \approx \frac{2\pi^2\hbar^3}{m_1}\frac{v_F}{E_D},$$
(9)

where $v_F = \hbar k_F/m_2$; see Appendix D. This shows that a lower value of the critical interaction strength is achieved for heavier electrons in the upper band, for a smaller Fermi velocity, and a higher Debye energy.

An approximate analytical solution of Eq. (8), which describes both the trimer state and the lowest energy two-body bound state, is derived in Appendix D. These solutions are depicted as the red dashed and the red continuous line in Figs. 4(a)–4(c). For $m_1 \gg m_2$ and $E_D \ll E_F$ we have $|\xi_{12}^{(c)}| = 2\mu/(4\pi\hbar^2)|g_{12}^{(c)}| \to 0^+$. In this case, a second analytical
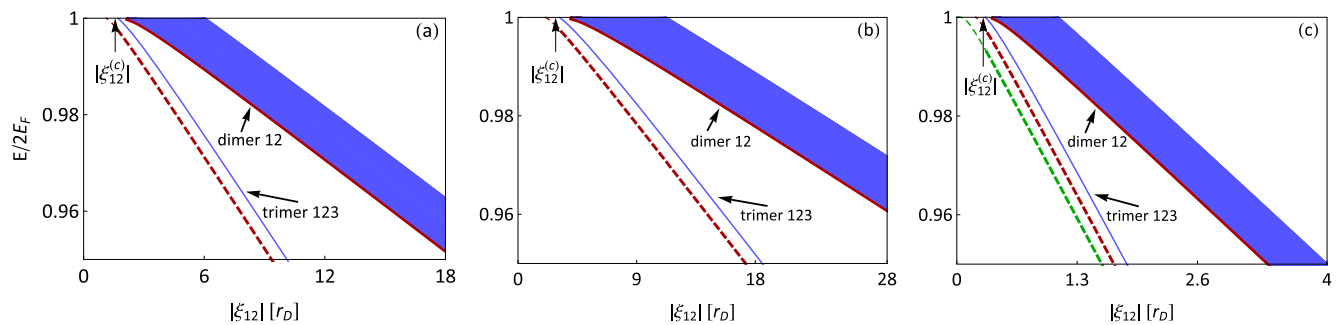
FIG. 4. Shifted energy $E = \mathcal{E} - E_0$ normalized by $2E_F$ vs the interaction parameter $|\xi_{12}|$, in units of $r_D$, with $g_{23} = 0$ and $E_D/E_F = 0.02$, for (a) $m_2/m_1 = 1$, corresponding to the vertical red dashed line in Fig. 2, (b) $m_2/m_1 = 10$, and (c) $m_2/m_1 = 1/10$. In each panel, the single blue curve is the numerical solution of the lowest energy trimer state and the red dashed curve is the analytical approximation for the trimer state; see Appendix D. As $|\xi_{12}|$ increases, the first pair (dimer 12) appears as the lowest energy state of a two-body bound state continuum (blue dense curves) [32]. The red solid curve is the analytical approximation for the lowest energy pair (dimer 12); see Appendix D. The vertical arrow locates the critical value of the interband interaction parameter given by Eq. (9). In panel (c), the green dashed curve is the second analytical approximation (10), representing a good approximation for the asymptotic of the single blue curve as long as $m_1 \gg m_2$.

approximate solution of Eq. (8) can be represented by

$$E \approx 2E_F + \frac{E_D}{1 - \exp\left(\pi \frac{\mu}{m_1} \frac{r_D}{|\xi_{12}|}\right)}; \qquad (10)$$

see Appendix D. This approximation is shown as a green dashed line in Fig. 4(c). For larger $m_1/m_2$, Eq. (10) becomes a better approximation. We compare these analytical results with the numerical results [32] for different parameter sets in Fig. 4. In Fig. 4(a) we use $m_2 = m_1$ and $E_D/E_F = 0.02$. In Fig. 4(b) we use $m_2/m_1 = 10$ and $E_D/E_F = 0.02$. In Fig. 4(c) we use $m_2/m_1 = 1/10$ and $E_D/E_F = 0.02$. We observe the formation of a trimer state, that is well approximated by the analytical approximation. In contrast to the Cooper problem where a two-body bound state originates at a vanishing coupling constant [1,5,7], here, a trimer state emerges at the critical value $\xi_{12}^{(c)}$.

Finally, for $m_2 \gg m_1$ and large values of the Debye energy that are comparable to the Fermi energy, $E_D \sim E_F$, we observe the formation of more than one trimer state. This is reminiscent of the Efimov effect, however, here the number of the trimers remains finite. Figure 5 shows the formation of two trimer states for $m_2/m_1 = 10$. Physical systems in this regime are superconductors like fullerides [33] or magnesium diboride [34].

## IV. EXPERIMENTAL SIGNATURES

The observation of trimer states in conventional superconductors can be realized in several scenarios. As a first experimental scenario, the trimer state can be detected as an excited state, as an in-gap resonance peak, $E_0 > E_F$, while the electrons in the lower band are in a superconducting state, generically. Optically probing this state, see also Refs. [35,36], will result in the observation of a resonance at the trimer binding energy below the empty band. This resonance is broadened by the three-body nature of the bound state. We also propose to realize this effect by optically pumping electrons to an otherwise empty band [20]. Here, our study applies to a long-lived metastable state created by optically pumping electrons to a higher band. For time scales below the relaxation rate from the upper band, the system will form a trimer state for

the regime indicated in Fig. 2, giving rise to a Fermi liquid of trimers; see Fig. 6 in Appendix E.

As a second scenario, for trimer binding energies exceeding the energy difference of the bands, the trimer state is the ground state of the system and destabilizes the BCS state. Here, the upper band is lowered, $E_0 \gtrsim E_F$, and touches the Fermi energy of the lower band, $E_0 \sim E_F$; see Figs. 7(a) and 7(b) in Appendix F. One can also imagine that the upper band is lowered into the Fermi sea, $E_0 \lesssim E_F$. Here, we assume that the upper band is very dilute; see Fig. 7(c) in Appendix F. Because of this, new electron pockets will appear. Our prediction is now that trimer formation is possible as the ground state, if the Fermi sea is tuned to formation of the electron pockets. For $g_{23} = 0$, the formation of a trimer liquid is achieved for any density of fermions in the upper band, if $g_{12}$ and $g_{13}$ are above the critical interaction strength. If $g_{23}$ induces a BCS state in the lower band, the energy reduction of the formation
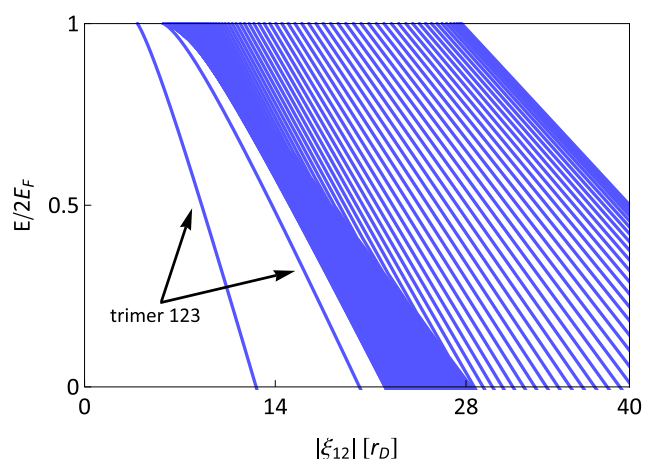


FIG. 5. The resulting three-body shifted energy $E = \mathcal{E} - E_0$ normalized by $2E_F$ vs the interaction parameter $|\xi_{12}|$, in units of $r_D$, with $g_{23} = 0$ and $E_D \sim E_F$, for $m_2/m_1 = 10$. Here, we see the formation of two trimer states that are shown by two single blue curves. The dense curves show the two-body bound-state continuum [32]. When $m_2 \gg m_1$, we can see the formation of more than one trimer state.

of a trimer liquid has to be compared to the energy of the BCS state. For sufficiently high density of electrons in the upper band, the trimer state competes with the BCS order.

Finally, to realize our prediction of forming more than one trimer state, see Fig. 5, BCS-like superconductors, e.g., fullerides or magnesium diboride, can be used, where $m_2 \gg m_1$ and the Debye energy is comparable to the Fermi energy. For high-temperature superconductors similar considerations for sufficiently strong interband attractive interactions might apply. Here, the formation of a trimer state might support pairing enhancement [37,38].

## V. CONCLUSIONS

In conclusion, we have demonstrated the formation of a trimer state of electrons in a conventional superconductor, in which an additional electron occupies a higher band. We show this by expanding the Cooper problem of two attractively interacting electrons by adding an additional electron that also interacts attractively with the other electrons. The trimer formation sets in beyond a critical interband interaction strength, for which we give an analytical estimate. This demonstrates an instability of the optically pumped BCS state. Out of the initial superconducting or metallic state, a transient state of a Fermi liquid of electron trimers can be formed.

As mentioned above, the analog of the Cooper problem can also be formulated for orders such as spin-density-wave or charge-density-wave orders, as a two-body problem of an electron and a hole. We emphasize that the analysis of this paper can be extended to any order that is described by a two-fermion order parameter, and predicts three-fermion bound states for all these orders for the corresponding parameter regimes.

## ACKNOWLEDGMENTS

## APPENDIX A: DERIVATION OF THE SYSTEM OF TWO COUPLED INTEGRAL EQUATIONS (6) AND (7)

We apply the interaction operators $\hat{U}_{ij}$, given by Eq. (4), on the wave function $\psi = \psi(\mathbf{k}_1, \mathbf{k}_2, \mathbf{k}_3)$ governing the three-electron system in momentum space, and write the

Schrödinger Eq. (3) as follows:

$$\left( \frac{\hbar^2 k_1^2}{2m_1} + \frac{\hbar^2 k_2^2}{2m_2} + \frac{\hbar^2 k_3^2}{2m_3} - E \right)\psi = -(\hat{U}_{12} + \hat{U}_{13} + \hat{U}_{23})\psi,$$
(A1)

where

$$\hat{U}_{12}\psi = g_{12}\theta_{\Lambda_1}(\mathbf{k}_1)\theta_{\Lambda_2}(\mathbf{k}_2) \int \frac{d^3\mathbf{q}}{(2\pi)^3} \theta_{\Lambda_1}(\mathbf{k}_1 - \mathbf{q})$$
$$\times \theta_{\Lambda_2}(\mathbf{k}_2 + \mathbf{q})\psi(\mathbf{k}_1 - \mathbf{q}, \mathbf{k}_2 + \mathbf{q}, \mathbf{k}_3), \quad \text{(A2)}$$

$$\hat{U}_{13}\psi = g_{13}\theta_{\Lambda_1}(\mathbf{k}_1)\theta_{\Lambda_3}(\mathbf{k}_3) \int \frac{d^3\mathbf{q}}{(2\pi)^3} \theta_{\Lambda_1}(\mathbf{k}_1 - \mathbf{q})$$
$$\times \theta_{\Lambda_3}(\mathbf{k}_3 + \mathbf{q})\psi(\mathbf{k}_1 - \mathbf{q}, \mathbf{k}_2, \mathbf{k}_3 + \mathbf{q}), \quad \text{(A3)}$$

$$\hat{U}_{23}\psi = g_{23}\theta_{\Lambda_2}(\mathbf{k}_2)\theta_{\Lambda_3}(\mathbf{k}_3) \int \frac{d^3\mathbf{q}}{(2\pi)^3} \theta_{\Lambda_2}(\mathbf{k}_2 - \mathbf{q})$$
$$\times \theta_{\Lambda_3}(\mathbf{k}_3 + \mathbf{q})\psi(\mathbf{k}_1, \mathbf{k}_2 - \mathbf{q}, \mathbf{k}_3 + \mathbf{q}). \quad \text{(A4)}$$

Here, $E = \mathcal{E} - E_0$ is the shifted energy, where $\mathcal{E}$ denotes the eigenenergy and $E_0$ is the energy difference of the two bands; see Fig. 1. The function $\theta_{a,b}(\mathbf{k})$ is defined by Eq. (5) and $\theta_b(\mathbf{k}) \equiv \theta_{0,b}(\mathbf{k})$.

Next, we introduce three variables $\tilde{\mathbf{p}}_i \equiv \mathbf{q} + \mathbf{k}_i$, with $i = 1, 2, 3$, and assume the zero total momentum of the system, $\psi(\mathbf{k}_1, \mathbf{k}_2, \mathbf{k}_3) = \psi(\mathbf{k}_2, \mathbf{k}_3)\delta^{(3)}(\mathbf{k}_1 + \mathbf{k}_2 + \mathbf{k}_3)$, where $\delta^{(3)}$ is the three-dimensional Dirac delta function. We rewrite Eq. (A1) in the following form:

$$\left( \frac{\hbar^2(\mathbf{k}_2 + \mathbf{k}_3)^2}{2m_1} + \frac{\hbar^2 k_2^2}{2m_2} + \frac{\hbar^2 k_3^2}{2m_3} - E \right)\psi(\mathbf{k}_2, \mathbf{k}_3)$$
$$= -\theta_{\Lambda_1}(-\mathbf{k}_2 - \mathbf{k}_3)\theta_{\Lambda_2}(\mathbf{k}_2)F_3(\mathbf{k}_3) - \theta_{\Lambda_1}(-\mathbf{k}_2 - \mathbf{k}_3)$$
$$\times \theta_{\Lambda_3}(\mathbf{k}_3)F_2(\mathbf{k}_2) - \theta_{\Lambda_2}(\mathbf{k}_2)\theta_{\Lambda_3}(\mathbf{k}_3)F_1(-\mathbf{k}_2 - \mathbf{k}_3), \quad \text{(A5)}$$

where the functions $F_1$, $F_2$, and $F_3$ are defined as

$$F_1(\mathbf{k}_1) = g_{23} \int \frac{d^3\tilde{\mathbf{p}}_3}{(2\pi)^3} \theta_{\Lambda_2}(-\mathbf{k}_1 - \tilde{\mathbf{p}}_3)\theta_{\Lambda_3}(\tilde{\mathbf{p}}_3)$$
$$\times \psi(-\mathbf{k}_1 - \tilde{\mathbf{p}}_3, \tilde{\mathbf{p}}_3), \quad \text{(A6)}$$

$$F_2(\mathbf{k}_2) = g_{13} \int \frac{d^3\tilde{\mathbf{p}}_3}{(2\pi)^3} \theta_{\Lambda_1}(-\mathbf{k}_2 - \tilde{\mathbf{p}}_3)\theta_{\Lambda_3}(\tilde{\mathbf{p}}_3)\psi(\mathbf{k}_2, \tilde{\mathbf{p}}_3),$$
(A7)

$$F_3(\mathbf{k}_3) = g_{12} \int \frac{d^3\tilde{\mathbf{p}}_2}{(2\pi)^3} \theta_{\Lambda_1}(-\mathbf{k}_3 - \tilde{\mathbf{p}}_2)\theta_{\Lambda_2}(\tilde{\mathbf{p}}_2)\psi(\tilde{\mathbf{p}}_2, \mathbf{k}_3).$$
(A8)

Equation (A5) provides now an ansatz for the wave function $\psi(\mathbf{k}_2, \mathbf{k}_3)$:

$$\psi(\mathbf{k}_2, \mathbf{k}_3) = -\frac{\theta_{\Lambda_1}(-\mathbf{k}_2 - \mathbf{k}_3)\theta_{\Lambda_2}(\mathbf{k}_2)F_3(\mathbf{k}_3) + \theta_{\Lambda_1}(-\mathbf{k}_2 - \mathbf{k}_3)\theta_{\Lambda_3}(\mathbf{k}_3)F_2(\mathbf{k}_2) + \theta_{\Lambda_2}(\mathbf{k}_2)\theta_{\Lambda_3}(\mathbf{k}_3)F_1(-\mathbf{k}_2 - \mathbf{k}_3)}{\frac{\hbar^2(\mathbf{k}_2 + \mathbf{k}_3)^2}{2m_1} + \frac{\hbar^2 k_2^2}{2m_2} + \frac{\hbar^2 k_3^2}{2m_3} - E}. \quad \text{(A9)}$$

If electrons "2" and "3" are in a spin singlet state and $g_{12} = g_{13}$, then $F_3 = F_2$. We also assume $m_3 = m_2$ and take

into account the Fermi sea condition by $k_2 > k_F$ and $k_3 > k_F$. Next, we introduce the variables $\mathbf{p}_1 \equiv -\mathbf{k}_2 - \tilde{\mathbf{p}}_3$ and

$\mathbf{p}_2 \equiv -\mathbf{k}_1 - \tilde{\mathbf{p}}_3$, with $\mathbf{p}_3 \equiv \tilde{\mathbf{p}}_3$. We also assume $\Lambda_3 = \Lambda_2$. The functions $F_1$ and $F_2$ now read

$$F_1(\mathbf{k}_1) = g_{23} \int \frac{d^3\mathbf{p}_3}{(2\pi)^3} \theta_{k_F,\Lambda_2}(-\mathbf{k}_1 - \mathbf{p}_3)\theta_{k_F,\Lambda_2}(\mathbf{p}_3)$$
$$\times \psi(-\mathbf{k}_1 - \mathbf{p}_3, \mathbf{p}_3), \qquad (A10)$$

$$F_2(\mathbf{k}_2) = g_{12} \int \frac{d^3\mathbf{p}_3}{(2\pi)^3} \theta_{\Lambda_1}(-\mathbf{k}_2 - \mathbf{p}_3)\theta_{k_F,\Lambda_2}(\mathbf{p}_3)\psi(\mathbf{k}_2, \mathbf{p}_3). \qquad (A11)$$

We insert the ansatz (A9) into Eqs. (A10) and (A11), and arrive at a system of two coupled integral Eqs. (6) and (7), where the three kernels $K_1$, $K_2$, and $K_3$ are

$$K_1(\mathbf{k}_2, \mathbf{p}_3; E) = \frac{\theta_{\Lambda_1}(-\mathbf{k}_2 - \mathbf{p}_3)\theta_{k_F,\Lambda_2}(\mathbf{p}_3)}{\frac{\hbar^2(\mathbf{k}_2 + \mathbf{p}_3)^2}{2m_1} + \frac{\hbar^2 k_2^2}{2m_2} + \frac{\hbar^2 p_3^2}{2m_2} - E}, \qquad (A12)$$

$$K_2(\mathbf{k}_2, \mathbf{p}_1; E) = \frac{\theta_{\Lambda_1}(\mathbf{p}_1)\theta_{k_F,\Lambda_2}(-\mathbf{p}_1 - \mathbf{k}_2)}{\frac{\hbar^2 p_1^2}{2m_1} + \frac{\hbar^2 k_2^2}{2m_2} + \frac{\hbar^2(\mathbf{p}_1 + \mathbf{k}_2)^2}{2m_2} - E}, \qquad (A13)$$

$$K_3(\mathbf{k}_1, \mathbf{p}_3; E) = \frac{\theta_{k_F,\Lambda_2}(-\mathbf{k}_1 - \mathbf{p}_3)\theta_{k_F,\Lambda_2}(\mathbf{p}_3)}{\frac{\hbar^2 k_1^2}{2m_1} + \frac{\hbar^2(\mathbf{k}_1 + \mathbf{p}_3)^2}{2m_2} + \frac{\hbar^2 p_3^2}{2m_2} - E}. \qquad (A14)$$

## APPENDIX B: OVERALL BEHAVIOR OF THE THREE-ELECTRON SYSTEM

As mentioned, we choose the values of the cutoffs $\Lambda_1$ and $\Lambda_2$ according to relation (1). For a typical conventional superconductor we have $E_D \ll E_F$, implying that $\Lambda_1 \ll k_F$ and $\Lambda_2 - k_F \ll k_F$. We recall that $0 < k_1 < \Lambda_1$ and $k_F < k_2 < \Lambda_2$. We thus make a first approximation such that $k_1 \sim 0$ and $k_2 \sim k_F$. In addition, because the integral variable $p_3$ is varying within the interval $(k_F, \Lambda_2)$, and also $\Lambda_2 - k_F \ll k_F$, we make a second approximation in this interval and assume that the two functions $F_2(k_2)$ and $F_2(p_3)$ remain constant, $F_2(k_F)$. We rewrite the system of Eqs. (6) and (7) as follows:

$$\begin{cases} \Omega_1(E, g_{12}; \tau)F_2(k_F) + \Omega_2(E)F_1(0) \approx 0, \\ \Omega_3(E)F_2(k_F) + \Omega_4(E, g_{23})F_1(0) \approx 0. \end{cases} \qquad (B1)$$

We recall that $\tau = 1$ describes the system of three electrons and $\tau = 1/2$ corresponds to a system of two electrons "1" and "2" (or "3"). We calculate the function $\Omega_1(E, g_{12}; \tau)$ to be

$$\Omega_1(E, g_{12}; \tau) = \frac{4\pi\hbar^2}{2\mu g_{12}} + \tilde{\Omega}_1(E; \tau), \qquad (B2)$$

where

$$\tilde{\Omega}_1(E; \tau) = \frac{\tau}{\frac{\mu}{m_1}\pi k_F} \int_{k_F}^{\Lambda_2} dp_3\, p_3 \ln\left(\frac{\left(1 - \frac{\mu}{m_1}\right)p_3^2 + \left(1 - \frac{\mu}{m_1}\right)k_F^2 + \frac{\mu}{m_1}\Lambda_1^2 - \frac{2\mu}{\hbar^2}E}{p_3^2 - \frac{2\mu}{m_1}k_F p_3 + k_F^2 - \frac{2\mu}{\hbar^2}E}\right)$$

$$= \frac{\tau}{\pi}(\Lambda_2 - k_F) + \frac{2\tau}{\pi}\sqrt{\eta(E)}\left[\arctan\left(\frac{\frac{\mu}{m_1}k_F - \Lambda_2}{\sqrt{\eta(E)}}\right) - \arctan\left(\frac{\left(\frac{\mu}{m_1} - 1\right)k_F}{\sqrt{\eta(E)}}\right)\right]$$

$$+ \frac{\tau\Lambda_2^2}{\frac{2\mu}{m_1}\pi k_F}\ln\left(\frac{-\rho(E) + \left(1 - \frac{\mu}{m_1}\right)\Lambda_2^2}{\chi(E)}\right) - \frac{\tau k_F}{\frac{2\mu}{m_1}\pi}\ln\left(\frac{\rho(E) + \left(\frac{\mu}{m_1} - 1\right)k_F^2}{\rho(E) + \left(\frac{\mu}{m_1} - 1\right)k_F^2 + \frac{\mu}{m_1}\Lambda_1^2}\right) + \frac{\tau\rho(E)}{\frac{2\mu}{m_1}\left(\frac{\mu}{m_1} - 1\right)\pi k_F}$$

$$\times \ln\left(\frac{\rho(E) + \left(\frac{\mu}{m_1} - 1\right)\Lambda_2^2}{\rho(E) + \left(\frac{\mu}{m_1} - 1\right)k_F^2}\right) - \frac{\tau\left[\eta(E) - \left(\frac{\mu}{m_1}\right)^2 k_F^2\right]}{\frac{2\mu}{m_1}\pi k_F}\ln\left(\frac{\chi(E)}{-\rho(E) + \left(1 - \frac{\mu}{m_1}\right)k_F^2 - \frac{\mu}{m_1}\Lambda_1^2}\right). \qquad (B3)$$

Here, $\eta(E) = [1 - (\frac{\mu}{m_1})^2]k_F^2 - \frac{2\mu}{\hbar^2}E$, $\rho(E) = (\frac{\mu}{m_1} - 1)k_F^2 - \frac{\mu}{m_1}\Lambda_1^2 + \frac{2\mu}{\hbar^2}E$, $\chi(E) = k_F^2 - \frac{2\mu}{m_1}k_F\Lambda_2 + \Lambda_2^2 - \frac{2\mu}{\hbar^2}E$, and $1/\mu = 1/m_1 + 1/m_2$. For $\Lambda_1 \ll k_F$ and $\Lambda_2 - k_F \ll k_F$, we obtain

$$\Omega_2(E) = \frac{1}{\frac{2\mu}{m_2}\pi k_F} \int_0^{\Lambda_1} dp_1\, p_1 \ln\left(\frac{p_1^2 + \frac{2\mu}{m_2}k_F p_1 + k_F^2 - \frac{2\mu}{\hbar^2}E}{p_1^2 - \frac{2\mu}{m_2}k_F p_1 + k_F^2 - \frac{2\mu}{\hbar^2}E}\right) \approx \frac{2}{3\pi}\frac{\Lambda_1^3}{k_F^2 - \frac{2\mu}{\hbar^2}E}, \qquad (B4)$$

$$\Omega_3(E) = \frac{2}{\frac{2\tilde{\mu}}{m_2}\pi k_F} \int_{k_F}^{\Lambda_2} dp_3\, \frac{p_3}{k_1} \ln\left(\frac{\frac{2\tilde{\mu}}{m_2}p_3^2 + \frac{2\tilde{\mu}}{m_2}k_1 p_3 + \frac{\tilde{\mu}}{\mu}k_1^2 - \frac{\tilde{\mu}}{\mu}\frac{2\mu}{\hbar^2}E}{\frac{2\tilde{\mu}}{m_2}p_3^2 - \frac{2\tilde{\mu}}{m_2}k_1 p_3 + \frac{\tilde{\mu}}{\mu}k_1^2 - \frac{\tilde{\mu}}{\mu}\frac{2\mu}{\hbar^2}E}\right) \sim \frac{4}{\pi} \int_{k_F}^{\Lambda_2} dp_3\, \frac{p_3^2}{p_3^2 - \frac{\tilde{\mu}}{\mu}\frac{2\mu}{\hbar^2}E}$$

$$\approx \frac{4}{\pi}\left[\Lambda_2 - k_F + \frac{k_F}{2}\ln\left(\frac{2k_F(\Lambda_2 - k_F)}{k_F^2 - \frac{\tilde{\mu}}{\mu}\frac{2\mu}{\hbar^2}E}\right)\right], \qquad (B5)$$

$$\Omega_4(E, g_{23}) = \frac{4\pi\hbar^2}{2\tilde{\mu}g_{23}} + \frac{1}{2}\Omega_3(E), \qquad (B6)$$

where $1/\tilde{\mu} = 1/m_2 + 1/m_3 = 2/m_2$.

In order that Eq. (B1) possesses nontrivial solutions, it is required that

$$\Omega_1(E, g_{12}; \tau = 1)\Omega_4(E, g_{23}) - \Omega_2(E)\Omega_3(E) = 0, \quad \text{(B7)}$$

which gives rise to a relation between $g_{12}$ and $g_{23}$ through $E$. Figure 2 shows the result for $E = \mathcal{E} - E_0 \approx 2E_F$, where $E_F = \hbar^2 k_F^2/2m_2$ is the Fermi energy and $k_F$ is the Fermi momentum.

## APPENDIX C: NUMERICAL SOLUTIONS OF THE SYSTEM OF TWO COUPLED INTEGRAL EQUATIONS (6) AND (7)

As mentioned, we assume $F_i(\mathbf{k}) = F_i(k)$, implying that we only consider the isotropic solutions of Eqs. (6) and (7). To solve Eqs. (6) and (7) numerically we therefore replace the three-dimensional integrals over momentum by one-dimensional integrals over absolute values of each momentum. We discretize each integral range such that the grid points $\{x_j\}$, $j = 1, 2, \ldots, N$, are the set of zeros of the Legendre polynomials $P_N(x)$. We approximate the integrals by a truncated sum weighted by $w_j$:

$$w_j = \frac{2}{(1 - x_j^2)[P_N'(x_j)]^2}, \quad \text{(C1)}$$

where $P_N'(x) = dP_N(x)/dx$ [30,31]. This choice, which is the so-called Gauss-Legendre quadrature rule, scales the range of integration from a given real interval $(a, b)$ to $(-1, 1)$, and has order of accuracy exactly $2N - 1$, which is the highest accuracy among the other quadrature choices [29].

We apply the Gauss-Legendre quadrature rule on each integral and construct a matrix equation analog to each integral equation. For given values of $E$ below $2E_F$ [28] we calculate the eigenvalues, which then provide the corresponding values of the interaction parameter. The functions $F_1$ and $F_2$ are also obtained as the eigenvectors of the matrix equations. We notice that, due to the truncation on each sum, the two-body continuum revealed in Figs. 3–5 has a finite range.

## APPENDIX D: DERIVATION AND SOLUTION OF EQUATION (8) AND DERIVATION OF EQUATIONS (9) AND (10)

To derive Eq. (8), recall that for vanishing $g_{23}$ we have $F_1 = 0$, and therefore Eq. (7) will have no effect anymore. As discussed in Appendix B, for a conventional superconductor we make an approximation such that $k_1 \sim 0$ and $k_2 \sim k_F$. The system of three electrons is then described by Eq. (8) for $\tau = 1$. The system of two electrons "1" and "2" (or "3") will be described by the same equation when $\tau = 1/2$.

Equation (8) for $\tau = 1$ is then solved by

$$\Omega_1(E, g_{12}; \tau = 1) = 0, \quad \text{(D1)}$$

where the function $\Omega_1(E, g_{12}; \tau)$ was calculated in Appendix B; see Eq. (B2). Equation (D1) provides now a relation between the interaction parameter $g_{12}$ and the shifted energy $E$; see red dashed curves in Fig. 4.

For the system of two electrons "1" and "2" (or "3") we set $\tau = 1/2$ and calculate the integral by the same argument. The
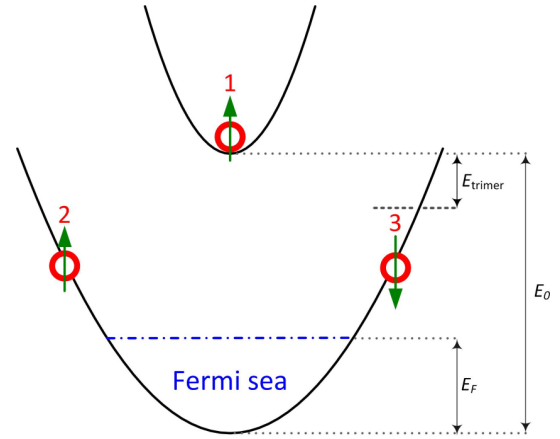


FIG. 6. Sketch of the first scenario for the experimental signature of the trimer states. The trimer state can be detected as an excited state, as an in-gap resonance peak, by either optically probing the state or optically pumping electrons from the lower band. Here, $E_0 > E_F$ and $E_{\text{trimer}}$ is the trimer binding energy.

lowest energy two-body bound state is obtained by solving

$$\Omega_1(E, g_{12}; \tau = 1/2) = 0; \quad \text{(D2)}$$

see red solid curves in Fig. 4.

To calculate the onset of the trimer state analytically, we expand Eq. (D1) for $\Lambda_2 - k_F \ll k_F$ and $\Lambda_1 \ll k_F$ at the shifted energy $E \approx 2E_F = \hbar^2 k_F^2/m_2$ [28], and solve the leading order for the interaction parameter $g_{12}^{(c)} \equiv g_{12}(E = 2E_F)$, which results in Eq. (9).

To derive Eq. (10), we notice that the onset of the trimer state for $m_1 \gg m_2$ leads to the origin, $|\xi_{12}^{(c)}| = 2\mu/(4\pi\hbar^2)|g_{12}^{(c)}| \rightarrow 0^+$. In this case, to find the asymptotic of the trimer state we solve the integral appearing in Eq. (B2) by changing a variable $X \equiv p_3/k_F$. The integral bounds will then be 1 and $\Lambda_2/k_F$. For a conventional superconductor the upper bound $\Lambda_2/k_F$ is very close to the lower bound; therefore, we calculate the integral by making the leading order of the integrand when $X \rightarrow 1$. We solve the result for $E$ and arrive at Eq. (10); see green dashed curve in Fig. 4(c) of the paper.

## APPENDIX E: VISUALIZATION OF THE FIRST SCENARIO FOR THE EXPERIMENTAL SIGNATURE

In the first experimental scenario, the electrons in the lower band are either in a superconducting ($g_{23} < 0$) or in a metallic state ($g_{23} = 0$). The energy difference of the two bands exceeds the Fermi energy, $E_0 > E_F$. Here, we predict that the trimer state can be detected as an excited state. To observe that, one can use either a probe or pump pulse. By optically probing this state one can observe the trimer state as an in-gap resonance peak at the trimer binding energy, $E_{\text{trimer}}$, below the empty band; see Fig. 6. We predict that the three-body bound state broadens the resonance peak. By optically pumping electrons from the lower band to the upper empty band, we also predict that a trimer state will be formed, if the time scales do not exceed the relaxation rate from the upper band. Figure 6 represents a visualization of the first
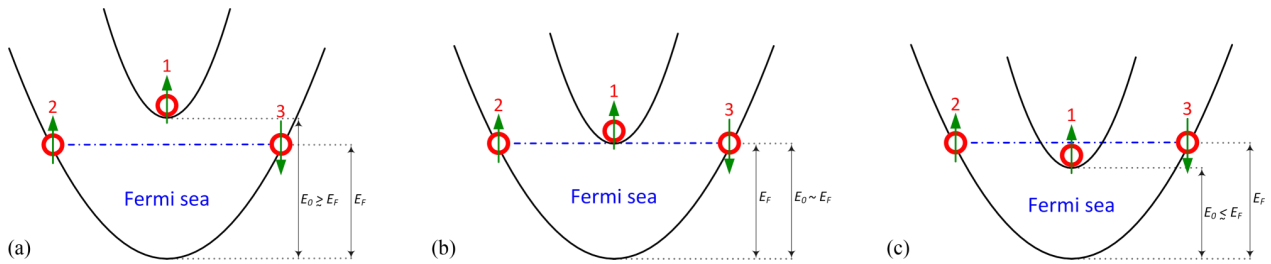
FIG. 7. Sketch of the second scenario for the experimental signature of the trimer states: (a) the upper band is lowered, $E_0 \gtrsim E_F$, (b) it touches the surface of the Fermi sea in the lower band, $E_0 \sim E_F$, (c) it is lowered into the Fermi sea, $E_0 \lesssim E_F$. In all cases we have assumed that the upper band is very dilute.

scenario for both optically probing the state and optically pumping electrons from the lower band.

## APPENDIX F: VISUALIZATION OF THE SECOND SCENARIO FOR THE EXPERIMENTAL SIGNATURE

In the second scenario, the electrons in the lower band are in a superconducting state and the trimer binding energy is larger than the energy difference of the bands, $E_{\text{trimer}} > E_0$. Here, we predict that the trimer state can be detected as the ground state of the system. The upper band is lowered, $E_0 \gtrsim E_F$, see Fig. 7(a), and touches the surface of the Fermi sea, $E_0 \sim E_F$, see Fig. 7(b). In both figures the electrons in the lower band are around the surface of the Fermi sea. The upper band can also be lowered into the Fermi sea of the lower band, $E_0 \lesssim E_F$, see Fig. 7(c), giving rise to new electron pockets. Here, we assume that the upper band is very dilute and the Fermi sea is tuned to formation of the electron pockets. In this case we also predict that the trimer state can be formed as the ground state of the system.

[1] L. N. Cooper, Phys. Rev. **104**, 1189 (1956).

[2] J. Bardeen, L. N. Cooper, and J. R. Schrieffer, Phys. Rev. **108**, 1175 (1957).

[3] A. A. Abrikosov, L. P. Gorkov, and I. E. Dzyaloshinski, *Methods of Quantum Field Theory in Statistical Physics* (Dover, New York, 1975).

[4] J. R. Schrieffer, *Theory of Superconductivity* (Westview, Boulder, Colorado, 1999).

[5] M. Tinkham, *Introduction to Superconductivity* (Dover, New York, 2004).

[6] N. W. Ashcroft and N. D. Mermin, *Solid State Physics* (Brooks/Cole, Belmont, CA, 1976).

[7] G. Baym, *Lectures on Quantum Mechanics* (CRC, New York, 1990), Chap. 8.

[8] A. L. Fetter and J. D. Walecka, *Quantum Theory of Many-Particle Systems* (Dover, New York, 2003).

[9] E. M. Lifshitz and L. P. Pitaevskii, *Statistical Physics* (Butterworth-Heinemann, Oxford, 2006), Chap. V.

[10] A. J. Leggett, *Quantum Liquids: Bose Condensation and Cooper Pairing in Condensed-Matter Systems* (Oxford University Press, New York, 2008).

[11] G. Grosso and G. P. Parravicini, *Solid State Physics* (Academic, Oxford, 2014), Chap. 18.

[12] V. Efimov, Sov. J. Nucl. Phys. **12**, 589 (1971) [Yad. Fiz. **12**, 1080 (1970)]

[13] V. Efimov, Phys. Lett. B **33**, 563 (1970).

[14] F. Ferlaino and R. Grimm, Physics **3**, 9 (2010).

[15] P. Naidon and S. Endo, Rep. Prog. Phys. **80**, 056001 (2017).

[16] B. Huang, L. A. Sidorenkov, R. Grimm, and J. M. Hutson, Phys. Rev. Lett. **112**, 190401 (2014).

[17] S.-K. Tung, K. Jiménez-García, J. Johansen, C. V. Parker, and C. Chin, Phys. Rev. Lett. **113**, 240402 (2014).

[18] R. Pires, J. Ulmanis, S. Häfner, M. Repp, A. Arias, E. D. Kuhnle, and M. Weidemüller, Phys. Rev. Lett. **112**, 250404 (2014).

[19] M. Kunitski, S. Zeller, J. Voigtsberger, A. Kalinin, L. P. H. Schmidt, M. Schöffler, A. Czasch, W. Schöllkopf, R. E. Grisenti, T. Jahnke, D. Blume, and R. Dörner, Science **348**, 551 (2015).

[20] I. Gierz, M. Mitrano, H. Bromberger, C. Cacho. R. Chapman, E. Springate, S. Link, U. Starke, B. Sachs, M. Eckstein, T. O. Wehling, M. I. Katsnelson, A. Lichtenstein, and A. Cavalleri, Phys. Rev. Lett. **114**, 125503 (2015).

[21] R. Mankowsky, M. Först, and A. Cavalleri, Rep. Prog. Phys. **79**, 064503 (2016).

[22] D. Nicoletti and A. Cavalleri, Adv. Opt. Photon. **8**, 401 (2016).

[23] J.-i. Okamoto, W. Hu, A. Cavalleri, and L. Mathey, Phys. Rev. B **96**, 144505 (2017).

[24] In this paper, momentum is measured in units of the Fermi momentum, $k_F$, and energy is measured in units of the Fermi energy, $E_F = \hbar^2 k_F^2 / 2m_2$.

[25] By "momentum transfer" we simply mean the difference of the in-state and out-state momenta of a particle; see, e.g., J. R. Taylor, *Scattering Theory: The Quantum Theory of Nonrelativistic Collisions* (Dover, New York, 2006).

[26] G. V. Skorniakov and K. A. Ter-Martirosian, Sov. Phys. JETP **4**, 648 (1957).

[27] We have formulated the problem in three dimensions. For one and two dimensions, we do not expect a qualitative change of the integral Eqs. (6) and (7).

[28] We recall that the shifted energy $E$ was defined as $E = \mathcal{E} - E_0$. Thus, for eigenenergies $\mathcal{E}$ near the threshold $E_{thr}$, we have $E \sim 2E_F$.

[29] L. N. Trefethen and D. Bau, III, *Numerical Linear Algebra* (SIAM, Philadelphia, 1997).

[30] V. I. Krylov, *Approximate Calculation of Integrals* (Dover, New York, 2005).

[31] W. H. Press, S. A. Teukolsky, W. T. Vetterling, and B. P. Flannery, *Numerical Recipes: The Art of Scientific Computing* (Cambridge University Press, New York, 2007).

[32] Notice that, due to the truncation on each sum described in Appendix C, the two-body continuum appears with finite range.

[33] O. Gunnarsson, Rev. Mod. Phys. **69**, 575 (1997).

[34] C. Buzea and T. Yamashita, Supercond. Sci. Technol. **14**, R115 (2001).

[35] M. Zachmann, M. D. Croitoru, A. Vagov, V. M. Axt, T. Papenkort, and T. Kuhn, New J. Phys. **15**, 055016 (2013).

[36] N. Tsuji and H. Aoki, Phys. Rev. B **92**, 064508 (2015).

[37] D. Fausti, R. I. Tobey, N. Dean, S. Kaiser, A. Dienst, M. C. Hoffmann, S. Pyon, T. Takayama, H. Takagi, and A. Cavalleri, Science **331**, 189 (2011).

[38] S. Kaiser, C. R. Hunt, D. Nicoletti, W. Hu, I. Gierz, H. Y. Liu, M. Le Tacon, T. Loew, D. Haug, B. Keimer, and A. Cavalleri, Phys. Rev. B **89**, 184516 (2014).

# Three-body bound states of an atom in a Fermi mixture

Ali Sanayei[1, 2, *] and Ludwig Mathey[1, 2, 3, †]

[1]*Zentrum für Optische Quantentechnologien, Universität Hamburg,*
*Luruper Chaussee 149, D-22761 Hamburg, Germany*
[2]*Institut für Laserphysik, Universität Hamburg, Luruper Chaussee 149, D-22761 Hamburg, Germany*
[3]*The Hamburg Centre for Ultrafast Imaging, Luruper Chaussee 149, D-22761 Hamburg, Germany*
(Dated: August 4, 2020)

We determine the three-body bound states of an atom in a Fermi mixture. Compared to the Efimov spectrum of three atoms in vacuum, we show that the Fermi seas deform the Efimov spectrum systematically. We demonstrate that this effect is more pronounced near unitarity, for which we give an analytical estimate. We show that in the presence of Fermi seas, the three-body bound states obey a generalized discrete scaling law. For an experimental confirmation of our prediction, we propose three signatures of three-body bound states of an ultracold Fermi mixture of Yb isotopes, and provide an estimate for the onset of the bound state and the binding energy.

## I. INTRODUCTION

In a seminal paper, Ref. [1], Efimov showed that three bosons that interact attractively in vacuum via short-range interactions form three-body bound states at interaction strengths that are not yet sufficient to support two-body bound states. He also showed that the number of the three-body bound states is in principle infinite, and that there is a geometric scaling law that governs the bound states [2–7]. Technical advances in the trapping and cooling of atoms [8, 9] as well as in the Feshbach resonances [10, 11] have led to the observation of the Efimov effect in ultracold atomic gases [12–17] and helium beams experiments [18, 19]. Excited three-body bound states were observed [14, 20], and the Efimov scaling law was confirmed. The Efimov effect was also generalized to more than three particles [5, 21]. It was shown that for a critical mass ratio three fermions and a lighter particle form a four-body bound state [22]. The four-body bound states of two heavy and two light bosons for different mass ratios was investigated in Ref. [23]. The formation of a five-body bound state in fermionic mixtures was discussed in Ref. [24].

Recently, we demonstrated the formation of three-electron bound states in conventional superconductors, and showed that the trimer state competes with the formation of the two-electron Cooper pair [25]. For that, we modeled the interaction between two particles "$i$" and "$j$" as a negative constant $g_{ij}$ in momentum space for an incoming and outgoing momentum of a particle smaller than a cutoff $\Lambda_i$, following the reasoning of the Cooper problem [26]. We fixed the cutoffs by a typical value of the Debye energy in a conventional superconductor [25]. In this paper we determine the three-body bound states of an atom in a Fermi mixture for contact interactions. To describe contact interactions we take the limit of the cutoffs $\Lambda_i$ to infinity. We show that this model is sep-

arable [27], leading to a system of two coupled integral equations. This model enables us to calculate the three-body bound-state spectrum in the presence of Fermi seas.

In this work, we consider a cold-atom system of Fermi mixtures. We assume a density of the species, labeled "2", that interacts attractively with another species of the same density, labeled "3". We assume that the two species "2" and "3" are in different internal states. Next, we include an additional atom, labeled "1", that interacts attractively with the other atoms via contact interactions; see Fig. 1. In general, the three masses $m_1$, $m_2$, and $m_3$ can be different, but we are primarily interested in the case $m_3 = m_2$. We assume that atom "1" is a fermion. A similar analysis can be applied when it is a boson. The species "2" and "3" define the Fermi seas with the Fermi momentum $k_F$. This imposes the constraints $k_2 > k_F$ and $k_3 > k_F$ on the momentum of atoms "2" and "3", respectively. We also assume that the interatomic distances, proportional to $1/k_F$, are much larger than the range of the atomic interactions. With this, we neglect the many-body effects on the formation of a three-body bound state within the interatomic distances. For contact interactions we introduce the $s$-wave scattering lengths as it relates to the contact interaction in its regularized form. We also define a three-body parameter, $\Lambda$, in order to regularize the range of the three-body interactions and to prevent Thomas collapse [28]. This parameter defines a length scale of the range of the atomic interactions using the van der Waals length [5, 29, 30].

We calculate the three-body bound states for different mass ratios. We provide an analytical description of the lowest-energy two-body bound states and the two-body continuum, and find the three-body bound-state solutions numerically. For a noninteracting mixture, $g_{23} = 0$, we provide an analytical formula for the onset of the lowest-energy two-body bound state at zero energy. For a high mass ratio $m_2/m_1$, where the excited three-body bound states appear, we also find an analytical estimate for the onset of a highest-energy excited three-body bound state at zero energy. With this, we can estimate the amount of the shift that the spectrum undergoes near unitarity due to the Fermi seas. Further, for our system

* asanayei@physnet.uni-hamburg.de
† lmathey@physnet.uni-hamburg.de
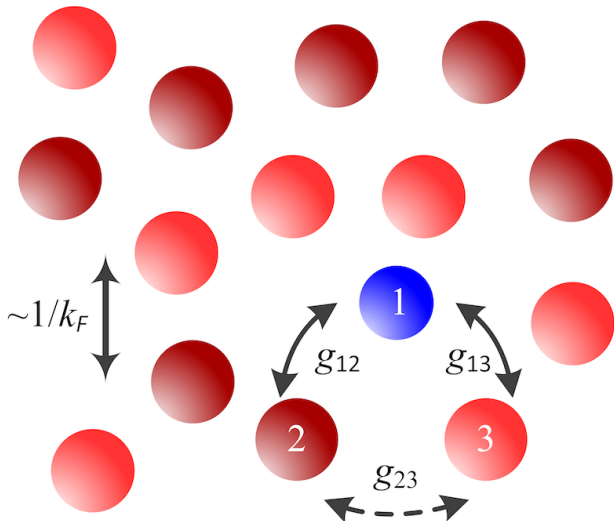
Figure 1. Sketch of an atom in a Fermi mixture. All species interact attractively via contact interactions. Species "2" and "3" are a Fermi mixture, and atom "1" can in general be a boson or fermion. The interaction strengths are shown by three negative constants $g_{12}$, $g_{13}$, and $g_{23}$. The species "2" and "3" are assumed to be in different internal states and $m_3 = m_2$. The density of each species "2" and "3" is $n_{\text{tot}}/2$, defining an inert Fermi sea with the Fermi momentum $k_F = (3\pi^2 n_{\text{tot}})^{1/3}$. The interatomic distances are proportional to $1/k_F$.

and interaction model we demonstrate that a generalized scaling law governs the three-body bound states in the presence of Fermi seas. Finally, we propose three experimental scenarios in an ultracold system of fermionic mixtures of Yb isotopes to observe three-body bound states in the presence of Fermi seas. Here the $^{171}$Yb isotopes, that are in two different internal states, constitute the Fermi seas, and interact attractively with $^{173}$Yb. We predict the onset of the three-body bound states and provide an estimate for the threshold energy.

This paper is organized as follows. In Sec. II we provide the main formulation of the problem for contact interactions, and derive a system of two coupled integral equations describing an atom in a Fermi mixture. In Sec. III we represent our results for two- and three interacting pairs in the presence of Fermi seas, and demonstrate a generalized scaling law governing the three-body bound states. Here we also derive an analytical estimate to describe the effect of the Fermi seas near unitarity. In Sec. IV we present three experimental signatures of a three-body bound state in an ultracold Fermi mixture of Yb isotopes. Finally, in Sec. V we present our concluding remarks.

## II. FORMULATION OF THE PROBLEM

The Schrödinger equation for a system of three atoms in momentum space is

$$\left( \frac{\hbar^2 k_1^2}{2m_1} + \frac{\hbar^2 k_2^2}{2m_2} + \frac{\hbar^2 k_3^2}{2m_3} + \hat{U}_{12} + \hat{U}_{13} + \hat{U}_{23} - E \right)\psi = 0,$$

(1)

where $\hbar$ is the reduced Planck's constant, $m_i$ and $\mathbf{k}_i$ is the atom mass and momentum, respectively, $E$ is the energy, and $\psi = \psi(\mathbf{k}_1, \mathbf{k}_2, \mathbf{k}_3)$ is the wave function. We consider the interaction $\hat{U}_{ij}$ between the atom "$i$" and "$j$", $i,j = 1,2,3$ and $i \neq j$, as

$$\hat{U}_{ij}\psi = g_{ij}\theta_{\Lambda_i}(\mathbf{k}_i)\theta_{\Lambda_j}(\mathbf{k}_j)\int \frac{d^3\mathbf{q}}{(2\pi)^3}\theta_{\Lambda_i}(\mathbf{k}_i{-}\mathbf{q})\theta_{\Lambda_j}(\mathbf{k}_j{+}\mathbf{q})\psi,$$

(2)

where $\mathbf{q}$ is the momentum transfer [31] and $g_{ij} < 0$ is the interaction strength; see Ref. [25]. The resulting operators $\hat{U}_{ij}\psi$ are given in Appendix B. The cutoff function $\theta_{a,b}(\mathbf{k})$ for two real numbers $0 \leqslant a < b$ is defined as

$$\theta_{a,b}(\mathbf{k}) = \begin{cases} 1 & \text{for } a \leqslant |\mathbf{k}| \leqslant b, \\ 0 & \text{otherwise}, \end{cases}$$

(3)

and $\theta_b(\mathbf{k}) \equiv \theta_{0,b}(\mathbf{k})$. Here we consider three-body bound states with vanishing total momentum. We also consider a singlet state for the species "2" and "3" in the following. The Fermi seas demand the constraints $k_2 > k_F$ and $k_3 > k_F$ on the momentum of the atoms "2" and "3", respectively. The threshold energy of the bound states is

$$E_{\text{thr}} = \frac{\hbar^2}{m_2}k_F^2 = 2E_F,$$

(4)

where $E_F$ denotes the Fermi energy and $m_3 = m_2$. To describe contact interactions we take the limit of the cutoffs $\Lambda_i$ and $\Lambda_j$ to infinity. We introduce the $s$-wave scattering length, $a_{ij}$, using the following regularization identity:

$$\frac{2\pi\hbar^2}{\mu_{ij}}\frac{1}{g_{ij}} + \frac{2}{\pi}\Lambda_j \equiv \frac{1}{a_{ij}} \text{ as } \Lambda_j \to \infty,$$

(5)

for $i,j = 1,2,3$ and $i \neq j$; see Appendix A. Here, $\mu_{ij}$ is a reduced mass, $1/\mu_{ij} = 1/m_i + 1/m_j$, $m_3 = m_2$, and $\Lambda_i \sim \Lambda_j$. Next, we define $\Lambda$ as the three-body parameter that fixes the range of the atomic interactions and regularizes the three-body bound states [5, 29, 30]. We also define a length scale, $r_D$, as

$$r_D = \frac{1}{\Lambda}.$$

(6)

The value of $\Lambda$ is chosen such that $\Lambda \gg k_F$, implying that $r_D \ll 1/k_F$. With this, we neglect the many-body effects on the formation of a three-body bound state. We determine $r_D$ as the range of the atomic interactions, which we take as the van der Waals length,
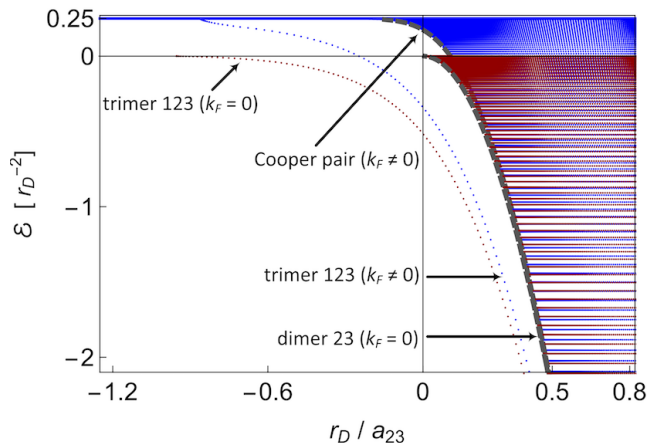
Figure 2. Energy $\mathcal{E} = 2\mu_{12}E/\hbar^2$ in units of $r_D^{-2}$ vs $r_D/a_{23}$ for three interacting pairs, where $m_2/m_1 = 1$ and $a_{12} \approx -36r_D$. The red curves show the solution in vacuum, $k_F = 0$. The blue curves show the result in the presence of Fermi seas, $k_F r_D \approx 0.17$. The single blue curve is the three-body bound-state solution for $k_F \neq 0$. The gray dashed curves are the lowest-energy two-body bound-state solutions of the two-body continuum in vacuum, cf. Eq. (A11), and in the presence of Fermi seas; cf. Eq. (15). The onset of the two-body bound-state continuum is shifted towards negative values of $a_{23}$. The onset of the three-body bound state is pushed towards positive values of $a_{23}$. The dependence of the trimer energy on $a_{23}$ is modified noticeably.

$\ell_{ij}^{(\mathrm{vdW})} = \frac{1}{2}(2\mu_{ij}C_6/\hbar^2)^{1/4}$, where $C_6$ is a dispersive coefficient associated with the polarizability of the electronic cloud of the atoms [5, 11, 32–35]. We also assume that the range of the interactions is much larger than the Compton wave length of the particles, $r_D \gg \lambda_C$, implying that relativistic corrections to the three-body bound-state spectrum can be neglected. In what follows, we refer to a two-body bound state of atoms "$i$" and "$j$" as a dimer-$ij$, and to a three-body bound state of atoms "$i$", "$j$" and "$l$" as a trimer-$ijl$. We also refer to a two-body bound state of species "2" and "3" as a Cooper pair for $k_F \neq 0$, and as a dimer-23 for $k_F = 0$.

We note that the interaction model (2) is separable, as shown in Appendix B. This constitutes a system of the two coupled integral equations of the functions $F_1$ and $F_2$:

$$\Omega_{12}(g_{12}, \mathbf{k}_2; k_F, E)F_2(\mathbf{k}_2) = \xi_1(\mathbf{k}_2; F_2) + \xi_2(\mathbf{k}_2; F_1), \quad (7)$$
$$\Omega_{23}(g_{23}, \mathbf{k}_1; k_F, E)F_1(\mathbf{k}_1) = \xi_3(\mathbf{k}_1; F_2). \quad (8)$$

The two functions $\Omega_{12}$ and $\Omega_{23}$ describe the two-body bound state continuum, dimers-12 and dimers-23, respectively:

$$\Omega_{12}(g_{12}, \mathbf{k}_2; k_F, E) = \frac{1}{g_{12}} + \int \frac{d^3\mathbf{p}_3}{(2\pi)^3} K_1(\mathbf{k}_2, \mathbf{p}_3; E), \quad (9)$$
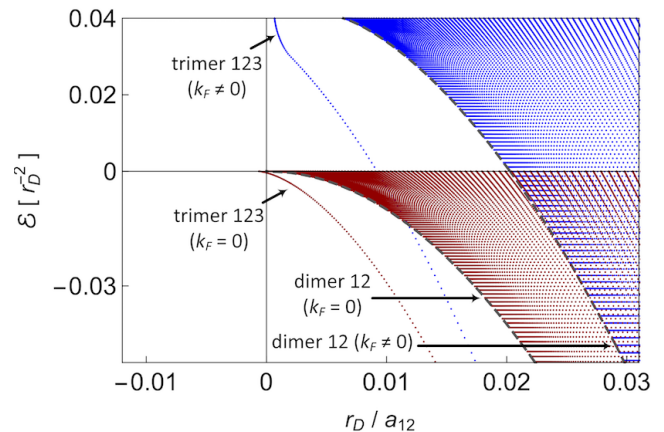


Figure 3. Energy $\mathcal{E} = 2\mu_{12}E/\hbar^2$ in units of $r_D^{-2}$ vs $r_D/a_{12}$ for $g_{23} = 0$ and $m_2/m_1 = 1$. The single red curve is the three-body bound-state solution for $k_F = 0$, and the single blue curve is the solution for $k_F r_D \approx 0.02$. The gray dashed curves are the lowest-energy two-body bound states of the two-body continuum in vacuum, cf. Eq. (A11), and in the presence of Fermi seas; cf. Eq. (17). The Fermi seas push the onset of the two-body bound-state continuum as well as the onset of the three-body bound state to positive values of $a_{12}$.

$$\Omega_{23}(g_{23}, \mathbf{k}_1; k_F, E) = \frac{1}{g_{23}} + \int \frac{d^3\mathbf{p}_3}{(2\pi)^3} K_3(\mathbf{k}_1, \mathbf{p}_3; E), \quad (10)$$

where for contact interactions we use the regularization relation (5) to introduce the $s$-wave scattering lengths. The three functions $\xi_1$, $\xi_2$, and $\xi_3$ describe the coupling of a pair to the third atom within the range of the length scale $r_D$ that is introduced by the three-body parameter $\Lambda$:

$$\xi_1(\mathbf{k}_2; F_2) = -\int \frac{d^3\tilde{\mathbf{p}}_3}{(2\pi)^3} \tilde{K}_1(\mathbf{k}_2, \tilde{\mathbf{p}}_3; E)F_2(\tilde{\mathbf{p}}_3), \quad (11)$$

$$\xi_2(\mathbf{k}_2; F_1) = -\int \frac{d^3\tilde{\mathbf{p}}_1}{(2\pi)^3} \tilde{K}_2(\mathbf{k}_2, \tilde{\mathbf{p}}_1; E)F_1(\tilde{\mathbf{p}}_1), \quad (12)$$

$$\xi_3(\mathbf{k}_1; F_2) = -2\int \frac{d^3\tilde{\mathbf{p}}_3}{(2\pi)^3} \tilde{K}_3(\mathbf{k}_1, \tilde{\mathbf{p}}_3; E)F_2(\tilde{\mathbf{p}}_3); \quad (13)$$

see Appendix B. The integral kernels $K_i$ and $\tilde{K}_i$, $i = 1, 2, 3$, and also the functions $F_1$ and $F_2$ are represented in Appendix B. We assume that $F_i(\mathbf{k}) = F_i(k)$, implying $s$-wave symmetry of the states. We notice that the system of the integral Eqs. (7) and (8) can be interpreted as the Skorniakov–Ter-Martirosian equation for the zero-range limit of the interaction model (2); cf. Ref. [36].
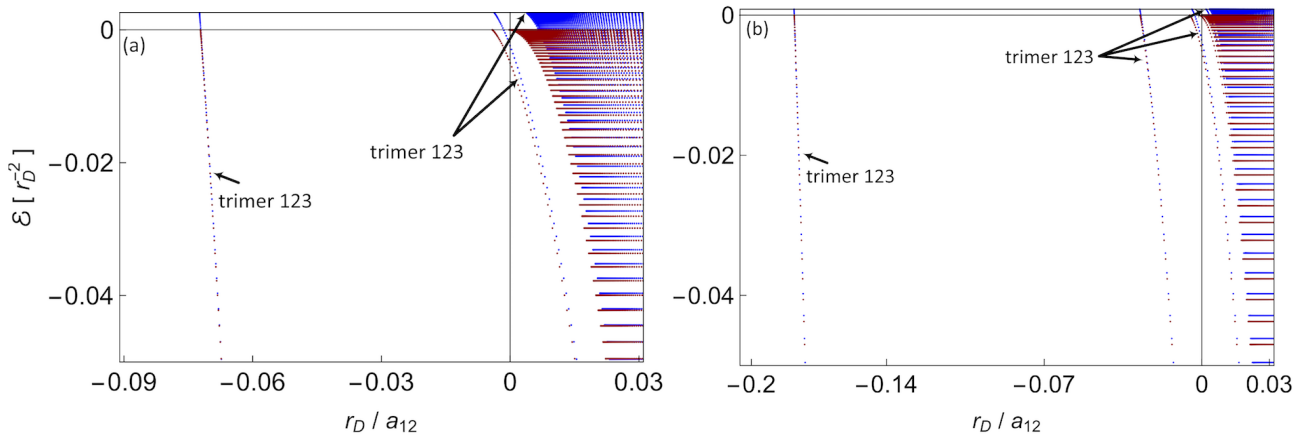
Figure 4. Energy $\mathcal{E} = 2\mu_{12}E/\hbar^2$ in units of $r_D^{-2}$ vs $r_D/a_{12}$ for $g_{23} = 0$. Red curves correspond to Efimov states, $k_F = 0$, and blue curves are the results for $k_F r_D \approx 0.01$: (a) $m_2/m_1 \approx 6.64$, (b) $m_2/m_1 \approx 22.26$. As the mass ratio $m_2/m_1$ increases, excited three-body bound states appear. A zoom on the region where a highest-energy excited three-body bound state emerges is depicted in Fig. 5.

## III. RESULTS

The coupled integral equations (7) and (8) describe three interacting pairs. For contact interactions and $s$-wave symmetry of the states we calculate the two functions $\Omega_{23}$ and $\Omega_{12}$ analytically; see Appendices C and D. These functions describe the lowest-energy two-body bound states and the two-body continuum, dimers-23 and dimers-12, respectively. Next, for a given value of the three-body parameter $\Lambda \gg k_F$ we evaluate the functions $\xi_1$, $\xi_2$, and $\xi_3$ numerically, and solve the system of the integral Eqs. (7) and (8) in order to find the three-body bound-state solutions. For that, we discretize the interval $(k_F, \Lambda)$, and evaluate each integral as a truncated sum following the Gauss-Legendre quadrature rule [37–40]. We construct the corresponding matrix equation and calculate the eigenvalues for different values of energy $E \leqslant E_{\text{thr}}$, resulting in the $s$-wave scattering lengths $a_{23}$ and $a_{12}$. We find the values of the functions $F_1$ and $F_2$ at the grid points as the corresponding eigenvectors; see Appendix E. We note that the two-body bound states appear as continuum states, whereas the three-body bound states appear at discrete energy levels.

For three interacting pairs and for a fixed value of $a_{12}$, Fig. 2 shows the energy as a function of the inverse $s$-wave scattering length $1/a_{23}$ for $m_2/m_1 = 1$, and comparison with the result for $k_F = 0$. It reveals a deformation of the Efimov spectrum in the presence of Fermi seas. We notice that for vanishing $k_F$, the two-body bound-state continuum emerges at unitarity, $a_{23} \to \pm\infty$, whereas the presence of Fermi seas expands the region of the two-body bound states to negative values of $a_{23}$. The single red and blue curves show the three-body bound-state solution for $k_F = 0$ and $k_F \neq 0$, respectively. For $k_F \neq 0$ the three-body bound state emerges at a larger value of $|a_{23}|$ at $E = E_{\text{thr}}$, and converges asymptotically to the three-body bound-state solution in vacuum. As

a general tendency, the effect of the Fermi seas is more pronounced as we approach unitarity. Our results are consistent with Refs. [41–45], which explore different, but related scenarios.

To find an analytical solution of the lowest-energy two-body bound state, Cooper pair-23, we note that for $g_{12}, g_{13} = 0$ the system of the integral Eqs. (7) and (8) reduces to

$$\frac{1}{g_{23}} + \lim_{\Lambda_2 \to \infty} \int \frac{d^3\mathbf{p}_3}{(2\pi)^3} \frac{\theta_{k_F,\Lambda_2}(\mathbf{p}_3)}{\frac{\hbar^2}{m_2}p_3^2 - E_{23}} = 0, \qquad (14)$$

where $E_{23} < 0$ is the bound-state energy of the Cooper pair. We use the regularization relation (5) and solve Eq. (14) for $s$-wave symmetry of the states, resulting in

$$\frac{1}{a_{23}} = \frac{2}{\pi}k_F + \frac{2}{\pi}\sqrt{-\mathcal{E}_{23}} \arctan\left(\frac{\sqrt{-\mathcal{E}_{23}}}{k_F}\right), \qquad (15)$$

where $\mathcal{E}_{23} = 2\mu_{23}E_{23}/\hbar^2$ and $\mu_{23}$ is a reduced mass, $1/\mu_{23} = 1/m_2 + 1/m_3 = 2/m_2$; see gray dashed curves in Fig. 2. Far from the resonance, the Cooper-pair solution for $k_F \neq 0$ converges asymptotically to the lowest-energy two-body bound state in vacuum, $1/a_{23} = \sqrt{-\mathcal{E}_{23}}$, described by Eq. (15) as $k_F \to 0$.

For a noninteracting mixture, $g_{23} = 0$, Eq. (8) has no effect anymore. For $s$-wave symmetry of the states the integral Eq. (7) reduces to

$$\Omega_{12}F_2(k_2) = -\frac{1}{2\pi\frac{\mu_{12}}{m_1}k_2}\int_{k_F}^{\Lambda} d\tilde{p}_3\,\tilde{p}_3$$
$$\times \ln\left(\frac{\tilde{p}_3^2 + \frac{2\mu_{12}}{m_1}k_2\tilde{p}_3 + k_2^2 - \mathcal{E}}{\tilde{p}_3^2 - \frac{2\mu_{12}}{m_1}k_2\tilde{p}_3 + k_2^2 - \mathcal{E}}\right)F_2(\tilde{p}_3),$$
$$(16)$$
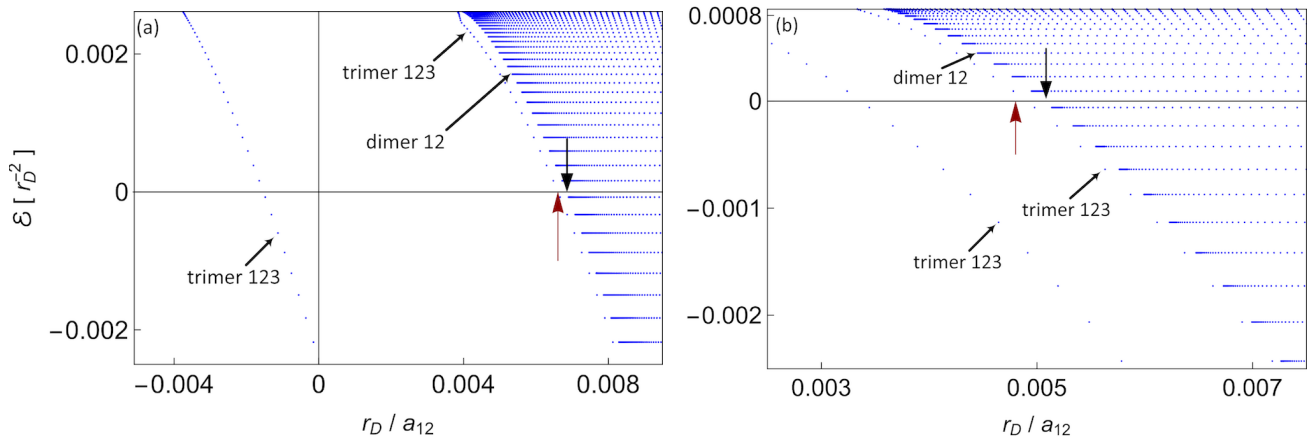
Figure 5. A zoom on the plot of energy $\mathcal{E} = 2\mu_{12}E/\hbar^2$ in units of $r_D^{-2}$ vs $r_D/a_{12}$ for (a) $m_2/m_1 \approx 6.64$ corresponding to Fig. 4(a), and (b) $m_2/m_1 \approx 22.26$ corresponding to Fig. 4(b). Both panels show the region where a highest-energy excited three-body bound state emerges. The red vertical arrow locates the onset of a highest-energy excited three-body bound state at zero energy, given by Eq. (19). The black vertical arrow locates the onset of the lowest-energy two-body bound state at zero energy, given by Eq. (18).

where $\mathcal{E} = 2\mu_{12}E/\hbar^2$, $E$ is the energy of the three-body bound state, and $\mu_{12}$ is a reduced mass, $1/\mu_{12} = 1/m_1 + 1/m_2$; see Appendix D. The analytical calculation of the function $\Omega_{12}$ is given by Eq. (D4). We solve the integral Eq. (16) numerically, using the Gauss-Legendre quadrature rule; see Appendix E. Figure 3 shows the result for vanishing and nonvanishing $k_F$, where $m_2/m_1 = 1$. In the presence of the Fermi seas, the onset of the three-body bound state is pushed to positive values of $a_{12}$, and the three-body bound-state solution converges asymptotically to the corresponding Efimov state in vacuum.

We note that for a given value of $k_F$, as we increase the mass ratio $m_2/m_1$, excited three-body bound states appear [46]. Figure 4(a) shows the result for $m_2/m_1 \approx 6.64$, where two excited additional three-body bound states are visible. In Fig. 4(b) we increase the mass ratio to $m_2/m_1 \approx 22.26$, and obtain three excited three-body bound states. The red curves in Fig. 4(a) and Fig. 4(b) show the result in vacuum, which are the Efimov states. The blue curves show the result in the presence of Fermi seas. Near unitarity the Fermi seas have a noticeable influence on the spectrum. Far from the resonance and for low energies, the effect of the Fermi seas is negligible. In the presence of the Fermi seas the translational invariance is broken, and the Efimov scaling law in vacuum does not hold anymore, which we discuss in the following.

For $g_{23} = 0$ we describe the two-body bound-state continuum, dimers-12, by solving

$$\Omega_{12}(a_{12}, k_2; k_F, \mathcal{E}_{12}) = 0, \qquad (17)$$

where $\Omega_{12}$ is given by Eq. (D4), $\mathcal{E}_{12} = 2\mu_{12}E_{12}/\hbar^2$, and $E_{12}$ is the energy of the dimers-12. For the lowest-energy dimer-12 we solve Eq. (17) as $k_2 \to k_F$. The result converges asymptotically to the lowest-energy two-body bound-state solution in vacuum; see gray dashed curves

in Fig. 3 for $m_2/m_1 = 1$. At zero energy we find an analytical estimate for the onset of the the lowest-energy two-body bound state. For that, we solve Eq. (17) as $k_2 \to k_F$ and $\mathcal{E}_{12} \to 0$, resulting in a critical $s$-wave scattering length, $a_{12,\text{dimer}}^{(c)} \equiv a_{12}(E_{12} = 0)$:

$$\frac{1}{a_{12,\text{dimer}}^{(c)}} = \frac{k_F}{\pi} \left[ 1 + \frac{1 + \frac{2m_2}{m_1}}{\frac{2m_2}{m_1}\left(1 + \frac{m_2}{m_1}\right)} \ln\left(1 + \frac{2m_2}{m_1}\right) \right.$$
$$\left. + \frac{\pi}{2} \frac{1}{1 + \frac{m_2}{m_1}} \sqrt{1 + \frac{2m_2}{m_1}} \right]. \qquad (18)$$

Equation (18) gives an estimate of the shift to the repulsive region of $a_{12}$ that the lowest-energy two-body bound state undergoes at zero energy in the presence of Fermi seas; see black vertical arrows in Fig. 5(a) and 5(b). For $m_2 \gg m_1$ this amount approaches $k_F/\pi$.

Moreover, for $g_{23} = 0$ and a high mass ratio $m_2/m_1 \gg 1$, we find an analytical estimate for the onset of a highest-energy excited three-body bound state at zero energy. For that, we note that near the Fermi surface we can approximate the momentum of the species "2" and "3" to be around $k_F$ but in opposite directions, $\mathbf{k}_2 \sim -\mathbf{k}_3$. Because we have assumed that the total momentum of the three-body bound state is zero, this results in the vanishing momentum of the atom "1", $\mathbf{k}_1 \sim \mathbf{0}$. Next, we consider the pair-12, where $m_2/m_1 \gg 1$ and $k_1 \sim 0$. With these assumption, the relative momentum of the pair-12, defined as $\mathbf{p}_{12} \equiv [m_2/(m_1 + m_2)]\mathbf{k}_1 - [m_1/(m_1 + m_2)]\mathbf{k}_2$, approaches zero. We note that the Fermi surface, $k_2 \sim k_F$, can be described in terms of the relative momentum, $\mathbf{p}_{12}$, and total momentum, $\mathbf{P}_{12}$, of the pair-12 as $|(\mu_{12}/m_1)\mathbf{P}_{12} - \mathbf{p}_{12}| \sim k_F$, where $\mathbf{P}_{12} \equiv \mathbf{k}_1 + \mathbf{k}_2$; see Appendix F. This implies that for $m_2/m_1 \gg 1$ and $k_1 \sim 0$ we can approximate the total momentum of
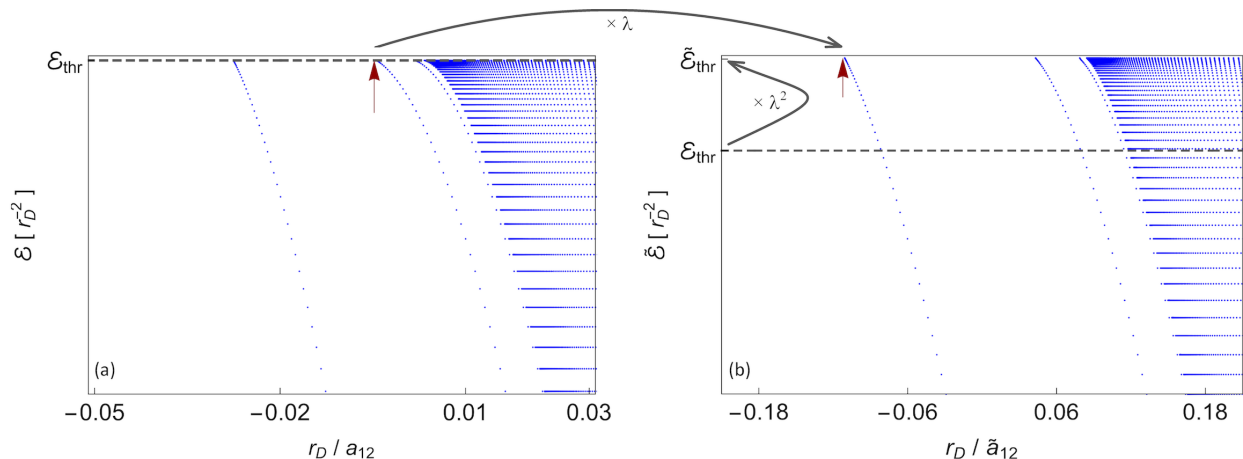
Figure 6. Demonstration of the generalized scaling law (20) and (21) for $g_{23} = 0$ and $m_2/m_1 \approx 22.26$: (a) energy $\mathcal{E} = 2\mu_{12}E/\hbar^2$ in units of $r_D^{-2}$ vs $r_D/a_{12}$ for $k_F r_D \approx 0.01$, (b) rescaled energy $\tilde{\mathcal{E}} = 2\mu_{12}\tilde{E}/\hbar^2$ in units of $r_D^{-2}$ vs rescaled $r_D/\tilde{a}_{12}$, for $k_i \mapsto \lambda k_i$, $i = 1, 2, 3$, $k_F \mapsto \lambda k_F$, $a_{12} \mapsto \lambda^{-1}a_{12}$, $E \mapsto \lambda^2 E$, where $\lambda = \exp(\pi/|s_0|) \approx 4.84998$. The red vertical arrow in panel (a) locates the onset of the $(n+1)$-th excited three-body bound state at $\mathcal{E}_{\text{thr}} = 2\mu_{12}E_{\text{thr}}/\hbar^2$. The red vertical arrow in (b) locates the onset of the $n$-th excited three-body bound state of the rescaled spectrum at $\tilde{\mathcal{E}}_{\text{thr}} = \lambda^2 \mathcal{E}_{\text{thr}}$. The gray dashed lines in both panels show the value of $\mathcal{E}_{\text{thr}}$.

the pair-12 to be $P_{12} \sim (\mu_{12}/m_1)^{-1}k_F$. We also note that for large mass ratios $m_2/m_1$, the threshold energy of the three-body bound state, $\mathcal{E}_{\text{thr}} = 2\mu_{12}E_{\text{thr}}/\hbar^2 = 2(1 - \mu_{12}/m_1)k_F^2$, approaches the threshold energy of the pair-12, $\mathcal{E}_{\text{thr}}^{(12)} = \mathcal{E}_{\text{thr}}/2$. To find the onset of a highest-energy excited three-body bound state at $E = 0$, we calculate the onset of the lowest-energy pair-12 for total momentum $P_{12} \sim (\mu_{12}/m_1)^{-1}k_F$ and $E_{12} \sim 0$. To do this, we use the interaction model (2), and write the Schrödinger equation describing the pair-12 for a contact interaction in terms of the relative and total momenta; see Appendix F. The solution for $P_{12} \to (\mu_{12}/m_1)^{-1}k_F$ and $E_{12} \to 0$ results in an estimate for the critical $s$-wave scattering length, $a_{12,\text{trimer}}^{(c)} \equiv a_{12}(E \approx 0)$:

$$\frac{1}{a_{12,\text{trimer}}^{(c)}} \approx \frac{k_F}{\pi}\left[1 + \frac{1}{4}\frac{1}{1 + \frac{m_2}{m_1}}\ln\left(4(1 + \frac{m_2}{m_1})\right)\right.$$
$$\left. -\frac{\pi}{2}\frac{1}{\sqrt{1 + \frac{m_2}{m_1}}} + \frac{1}{2}\frac{1}{1 + \frac{m_2}{m_1}}\right] \text{ for } \frac{m_2}{m_1} \gg 1;$$

(19)

see Appendix F. For a high mass ratio $m_2/m_1 \gg 1$, Eq. (19) gives an estimate for the amount of the shift to the repulsive region of $a_{12}$ that a highest-energy excited three-body bound state undergoes at zero energy in the presence of Fermi seas. Figure 5 reveals a zoom on the region where a highest-energy three-body bound state emerges for $m_2/m_1 = 6.64$ and $m_2/m_1 \approx 22.26$. The red vertical arrows locate the critical value (19). For a very large mass ratio $m_2/m_1$, the critical value (19) eventually approaches $k_F/\pi$, converging to the lowest-energy two-body bound state at zero energy. Equations

(18) and (19) provide a quantitative analysis for the effect of the Fermi seas on the near-resonant spectrum.

Finally, we elaborate on the observation that the Fermi seas deform the Efimov spectrum. This effect is more pronounced as we approach unitarity. As a result, the Efimov scaling factor that governs the three-body bound states in vacuum does not hold anymore. Here we show that a scaling transformation $k_F \mapsto \lambda k_F$, where $\lambda$ is the Efimov scaling factor, gives rise to a generalized scaling law for our system and interaction model (2). To this end, we notice that $k_F \mapsto \lambda k_F$ implies a scaling transformation of all momenta as $k_i \mapsto \lambda k_i$, for $i = 1, 2, 3$. It also rescales the threshold energy as $E_{\text{thr}} \mapsto \lambda^2 E_{\text{thr}}$, cf. Eq. (4), implying a general scaling transformation of energy as $E \mapsto \lambda^2 E$. To ensure that the system of the coupled integral Eqs. (7) and (8) remains valid, it requires a scaling transformation of the $s$-wave scattering length as $a \mapsto \lambda^{-1}a$; see Eqs. (C6), (C9), and (D4). This results in a discrete scaling law for the three-body bound states in the presence of Fermi seas:

$$\frac{\lambda}{a_{n+1}(k_F)} = \frac{1}{a_n(\lambda k_F)}, \tag{20}$$
$$\lambda^2 E_{n+1}(k_F, 1/a) = E_n(\lambda k_F, \lambda/a), \tag{21}$$

where $n \in \mathbb{N}$ is an index labeling the three-body bound state, $\lambda = \exp(\pi/|s_0|)$, and the parameter $s_0$, that depends on the mass ratio $m_2/m_1$, is determined in Appendix G. Our finding is in agreement with the result of Ref. [47]. Figure 6 demonstrates the generalized scaling law (20) and (21) for an atomic system of three fermions with a noninteracting mixture, $g_{23} = 0$, and $m_2/m_1 \approx 22.26$.
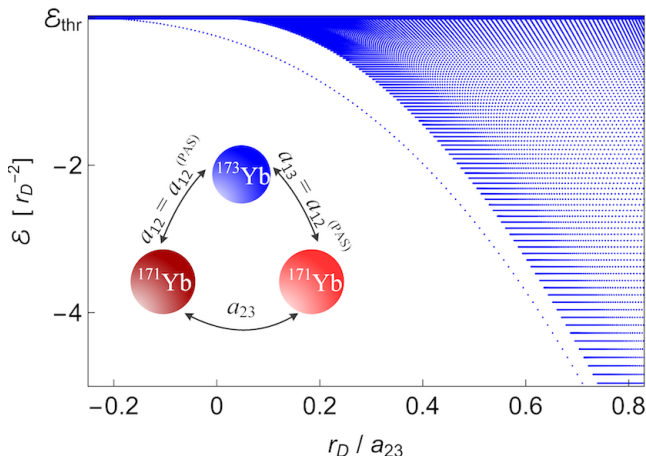
Figure 7. Visualization of the first scenario for the experimental signature of a three-body bound state in an ultracold fermionic mixture of Yb isotopes. The plot shows the energy $\mathcal{E} = 2\mu^{(\mathrm{Yb})}E/\hbar^2$ in units of $r_D^{-2}$ vs $r_D/a_{23}$, where $r_D \equiv \ell_{23}^{(\mathrm{vdW})} \approx 4.145$ nm. The $s$-wave scattering length of $^{171}$Yb and $^{173}$Yb is fixed as the value measured via photoassociation spectroscopy (PAS), $a_{12} = a_{13} = a_{12}^{(\mathrm{PAS})} \approx -30.6$ nm. The three-body bound state emerges at $a_{23} \approx -20.7$ nm at the threshold energy $E_{\mathrm{thr}} \approx 1.10$ kHz.

## IV. EXPERIMENTAL SIGNATURES

We propose three scenarios to observe three-body bound states in mixtures of Yb isotopes, in particular a mixture of $^{171}$Yb and $^{173}$Yb. In the terminology that is illustrated in Fig. 1, $^{173}$Yb plays the role of species "1", and species "2" and "3" are two internal states of $^{171}$Yb. The density of each of the $^{171}$Yb species is $n_{\mathrm{tot}}/2$, whereas the density of $^{173}$Yb is much smaller. We denote the $s$-wave scattering lengths of $^{171}$Yb and $^{173}$Yb by $a_{12}$ and $a_{13}$, and the $s$-wave scattering length of two $^{171}$Yb isotopes by $a_{23}$. We also assume that $a_{13} = a_{12}$.

As measured via two-color photoassociation spectroscopy (PAS), see Ref. [33], $^{171}$Yb isotopes are almost noninteracting, while the $s$-wave scattering length between $^{171}$Yb and $^{173}$Yb atoms is $a_{12}^{(\mathrm{PAS})} \approx -30.6$ nm $\approx -578.23a_0$, where $a_0$ denotes the Bohr radius [48]. We note that $^{171}$Yb and $^{173}$Yb have almost the same atomic mass, where the reduced mass is $\mu_{12} \approx 85.9657$ u [49]. The reduced mass of two $^{171}$Yb isotopes is $\mu_{23} \approx 85.4682$ u [49]. The van der Waals dispersive coefficient, $C_6^{(\mathrm{Yb})}$, that determines the atomic interaction in a Yb$_2$ molecule is given by Refs. [33, 50]. We calculate the van der Waals lengths to be $\ell_{12}^{(\mathrm{vdW})} = \frac{1}{2}[2\mu_{12}C_6^{(\mathrm{Yb})}/\hbar^2]^{1/4} \approx 4.151$ nm $\approx 78.44a_0$ and $\ell_{23}^{(\mathrm{vdW})} = \frac{1}{2}[2\mu_{23}C_6^{(\mathrm{Yb})}/\hbar^2]^{1/4} \approx 4.145$ nm $\approx 78.33a_0$. These values fix the corresponding length scales $r_D$. Next, for each internal state we assume that the density of $^{171}$Yb species is $n_{\mathrm{tot}}/2 = \frac{1}{2} \times 10^{17}$ m$^{-3}$. We calculate the value of the Fermi momentum as $k_F = (3\pi^2 n_{\mathrm{tot}})^{1/3}$; cf. Ref. [9].
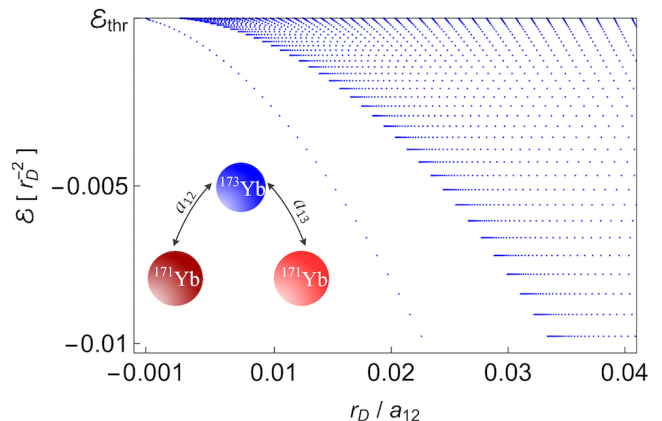


Figure 8. Visualization of the second scenario in which $^{171}$Yb and $^{173}$Yb are interact attractively, while the two $^{171}$Yb species are noninteracting. The plot shows the energy $\mathcal{E} = 2\mu^{(\mathrm{Yb})}E/\hbar^2$ in units of $r_D^{-2}$ vs $r_D/a_{12}$, where $r_D \equiv \ell_{12}^{(\mathrm{vdW})} \approx 4.151$ nm and $a_{13} = a_{12}$. The onset of the three-body bound state is at $a_{12} \approx -3193$ nm with the threshold energy $E_{\mathrm{thr}} \approx 1.09$ kHz.

We adopt the $s$-wave scattering length of $^{171}$Yb and $^{173}$Yb as reported in Ref. [33], i.e., $a_{12} = a_{12}^{(\mathrm{PAS})}$, and calculate the three-body bound-state solution for three interacting pairs [51]. Figure 7 shows the three-body bound-state energy as a function of $1/a_{23}$. We find that the onset of the three-body bound state is $a_{23} \approx -20.7$ nm $\approx -391.16a_0$, emerging at the threshold energy $E_{\mathrm{thr}} \approx 1.10$ kHz. As a first experimental scenario, we propose to tune the interaction between two $^{171}$Yb isotopes via optical Feshbach resonances [52–56], across the onset of the three-body bound state, which should result in increased atomic losses.

As a second scenario we consider two noninteracting $^{171}$Yb isotopes, and calculate the three-body bound-state solution for two interacting pairs $^{171}$Yb - $^{173}$Yb. Figure 8 shows the energy of the three-body bound state as a function of $1/a_{12}$. It reveals that the three-body bound state emerges at $a_{12} \approx -3193$ nm $\approx -60336.40a_0$ at the threshold energy $E_{\mathrm{thr}} \approx 1.09$ kHz. Here the $s$-wave scattering length $a_{12}$ is much larger in amplitude than $a_{12}^{(\mathrm{PAS})}$, and the threshold energy is smaller than the value obtained in the first scenario. A three-body bound state is observed, if the interaction between two $^{171}$Yb and $^{173}$Yb is tuned via interisotope Feshbach resonances [57], or via orbital Feshbach resonances [58, 59].

As a third scenario, if the interaction between two $^{171}$Yb and $^{173}$Yb isotopes is tuned to a larger value in amplitude than $a_{12}^{(\mathrm{PAS})}$, e.g., $a_{12} = 2a_{12}^{(\mathrm{PAS})}$, we find that the three-body bound state emerges at $a_{23} \approx -10.4$ nm $\approx -196.52a_0$ with the same threshold energy of the first scenario; see Fig. 9. Here the value of $a_{12}$ is much smaller in amplitude than the value obtained in the second scenario. Also, the value of $a_{23}$ is smaller in amplitude than the value found in the first scenario. A three-body
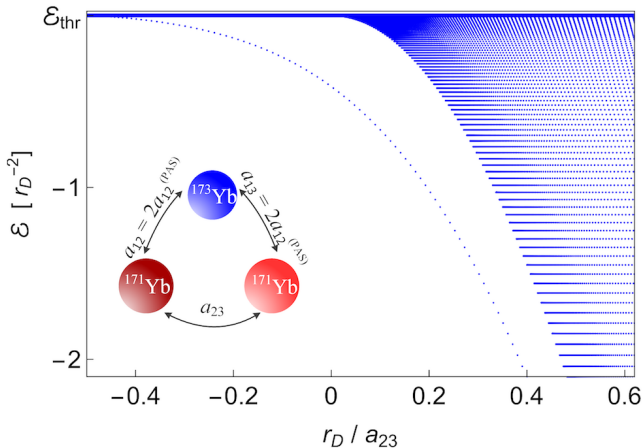
Figure 9. Visualization of the third scenario. The plot shows the energy $\mathcal{E} = 2\mu^{(\mathrm{Yb})}E/\hbar^2$ in units of $r_D^{-2}$ vs $r_D/a_{23}$, where $r_D \equiv \ell_{23}^{(\mathrm{vdW})} \approx 4.145$ nm. The $s$-wave scattering length of $^{171}$Yb and $^{173}$Yb is fixed to be $a_{12} = a_{13} = 2a_{12}^{(\mathrm{PAS})} \approx -2 \times 30.6$ nm. The three-body bound state emerges at $a_{23} \approx -10.4$ nm at the threshold energy $E_{\mathrm{thr}} \approx 1.10$ kHz.

bound state is observed, if the interaction between two $^{171}$Yb isotopes and also the interaction between $^{171}$Yb and $^{173}$Yb are tuned simultaneously.

We note that in all scenarios we have assumed that the interatomic distances are much larger than the range of the atomic interactions, $1/k_F \gg r_D$. The onset of the three-body bound states might slightly deviate if this criterion is not met. Here there will be a competition of $^{171}$Yb isotopes to form a three-body bound state with $^{173}$Yb.

## V. CONCLUSIONS

In conclusion, we have demonstrated and characterized three-body bound states of a single fermionic atom interacting with a Fermi mixture of two fermionic species. For this purpose, we have expanded and elaborated on a model previously used to determine trimer states in conventional superconductors, Ref. [25]. We have shown that the expanded interaction model is separable, leading to a system of integral equations in momentum space. Based on these equations we have presented their full numerical solution, as well as analytical solutions of limiting cases. Compared to three atoms interacting in vacuum, the presence of the Fermi seas renormalizes the eigenstates and eigenenergies, in particular near unitarity. Compared the Efimov scaling law of three atoms in vacuum, we have shown that our system and interaction model obeys a generalized discrete scaling law. We have also proposed three scenarios to obtain experimental signatures of the modified Efimov effect in an ultracold Fermi system of Yb isotopes.

## APPENDIX A. INTRODUCING THE $s$-WAVE SCATTERING LENGTHS

We consider the Schrödinger equation in momentum space governing two atoms "A" and "B" in vacuum:

$$\left( \frac{\hbar^2 k_{\mathrm{A}}^2}{2m_{\mathrm{A}}} + \frac{\hbar^2 k_{\mathrm{B}}^2}{2m_{\mathrm{B}}} + \hat{U}_{\mathrm{AB}} - E_{\mathrm{AB}} \right) \phi = 0, \qquad (\mathrm{A1})$$

where $m_i$ and $\mathbf{k}_i$, $i \in \{\mathrm{A}, \mathrm{B}\}$, is the atom mass and momentum, respectively, $E_{\mathrm{AB}}$ is the energy, and $\phi = \phi(\mathbf{k}_{\mathrm{A}}, \mathbf{k}_{\mathrm{B}})$ is the wave function. The interaction $\hat{U}_{\mathrm{AB}}$ between the atoms "A" and "B" follows from the interaction model (2). The resulting operator $\hat{U}_{\mathrm{AB}}\phi$ reads:

$$\hat{U}_{\mathrm{AB}}\phi = g_{\mathrm{AB}} \theta_{\Lambda_{\mathrm{A}}}(\mathbf{k}_{\mathrm{A}}) \theta_{\Lambda_{\mathrm{B}}}(\mathbf{k}_{\mathrm{B}}) \int \frac{d^3\mathbf{q}}{(2\pi)^3} \theta_{\Lambda_{\mathrm{A}}}(\mathbf{k}_{\mathrm{A}} - \mathbf{q})$$
$$\times \theta_{\Lambda_{\mathrm{B}}}(\mathbf{k}_{\mathrm{B}} + \mathbf{q}) \phi(\mathbf{k}_{\mathrm{A}} - \mathbf{q}, \mathbf{k}_{\mathrm{B}} + \mathbf{q}), \qquad (\mathrm{A2})$$

where $g_{\mathrm{AB}} < 0$ and $\mathbf{q}$ is the momentum transfer [31]. We assume the zero total momentum, $\mathbf{k}_{\mathrm{A}} + \mathbf{k}_{\mathrm{B}} = \mathbf{0}$, and $\Lambda_{\mathrm{B}} = \Lambda_{\mathrm{A}}$. Next, we define the variables $\boldsymbol{\kappa}_i \equiv \mathbf{q} + \mathbf{k}_i$, $i \in \{\mathrm{A}, \mathrm{B}\}$, and write the Schrödinger Eq. (A1) as

$$\left( \frac{\hbar^2 k_{\mathrm{A}}^2}{2\mu_{\mathrm{AB}}} - E_{\mathrm{AB}} \right) \phi(\mathbf{k}_{\mathrm{A}}) = -g_{\mathrm{AB}} \theta_{\Lambda_{\mathrm{A}}}(\mathbf{k}_{\mathrm{A}}) \int \frac{d^3\boldsymbol{\kappa}_{\mathrm{B}}}{(2\pi)^3}$$
$$\times \theta_{\Lambda_{\mathrm{A}}}(\boldsymbol{\kappa}_{\mathrm{B}}) \phi(\boldsymbol{\kappa}_{\mathrm{B}}), \qquad (\mathrm{A3})$$

where $\mu_{\mathrm{AB}}$ is a reduced mass, $1/\mu_{\mathrm{AB}} = 1/m_{\mathrm{A}} + 1/m_{\mathrm{B}}$. We define

$$\mathcal{F} \equiv -4\pi \left( \frac{2\mu_{\mathrm{AB}}}{4\pi\hbar^2} g_{\mathrm{AB}} \right) \theta_{\Lambda_{\mathrm{A}}}(\mathbf{k}_{\mathrm{A}}) \int \frac{d^3\mathbf{k}_{\mathrm{A}}}{(2\pi)^3} \theta_{\Lambda_{\mathrm{A}}}(\mathbf{k}_{\mathrm{A}}) \phi(\mathbf{k}_{\mathrm{A}}), \qquad (\mathrm{A4})$$

and rewrite Eq. (A3) as

$$(k_{\mathrm{A}}^2 - \mathcal{E}_{\mathrm{AB}}) \phi(\mathbf{k}_{\mathrm{A}}) = \mathcal{F}, \qquad (\mathrm{A5})$$

where $\mathcal{E}_{\mathrm{AB}} = 2\mu_{\mathrm{AB}} E_{\mathrm{AB}}/\hbar^2$.

For $\mathcal{E}_{\mathrm{AB}} > 0$ the solution of Eq. (A5) is

$$\phi(\mathbf{k}_{\mathrm{A}}) = (2\pi)^3 \delta^{(3)}(\mathbf{k}_{\mathrm{A}} - \mathbf{K}) + \frac{\mathcal{F}}{k_{\mathrm{A}}^2 - \mathcal{E}_{\mathrm{AB}} + i\varepsilon}, \qquad (\mathrm{A6})$$

where $0 < \varepsilon \ll 1$, $|\mathbf{K}|^2 = \mathcal{E}_{\mathrm{AB}}$, and $\delta^{(3)}$ denotes the three-dimensional Dirac delta function. We insert the ansazt (A6) into Eq. (A4):

$$\frac{\mathcal{F}}{4\pi \left(\frac{2\mu_{\mathrm{AB}}}{4\pi\hbar^2} g_{\mathrm{AB}}\right)} = -\theta_{\Lambda_{\mathrm{A}}}(\mathbf{k}_{\mathrm{A}}) \int \frac{d^3\mathbf{k}_{\mathrm{A}}}{(2\pi)^3} \theta_{\Lambda_{\mathrm{A}}}(\mathbf{k}_{\mathrm{A}}) \Big[(2\pi)^3$$
$$\times \delta^{(3)}(\mathbf{k}_{\mathrm{A}} - \mathbf{K}) + \frac{\mathcal{F}}{k_{\mathrm{A}}^2 - \mathcal{E}_{\mathrm{AB}} + i\varepsilon}\Big]. \tag{A7}$$

We note that in the zero-energy limit, $\mathcal{E}_{\mathrm{AB}} \to 0^+$, we have $\mathcal{F} = -4\pi a_{\mathrm{AB}}$, where $a_{\mathrm{AB}}$ is the $s$-wave scattering length; see Ref. [60]. Next, for contact interactions and $s$-wave symmetry of the states, we evaluate Eq. (A7) by taking the limit of $\Lambda_{\mathrm{A}}$ to infinity:

$$\frac{4\pi\hbar^2}{2\mu_{\mathrm{AB}} g_{\mathrm{AB}}} + \frac{2}{\pi} \lim_{\Lambda_{\mathrm{A}} \to \infty} \int_0^{\Lambda_{\mathrm{A}}} dk_{\mathrm{A}} \frac{k_{\mathrm{A}}^2}{k_{\mathrm{A}}^2 + i\varepsilon} = \frac{1}{a_{\mathrm{AB}}}, \quad \text{(A8)}$$

which yields

$$\frac{2\pi\hbar^2}{\mu_{\mathrm{AB}}} \frac{1}{g_{\mathrm{AB}}} + \frac{2}{\pi}\Lambda_{\mathrm{A}} = \frac{1}{a_{\mathrm{AB}}} \text{ as } \Lambda_{\mathrm{A}} \to \infty. \tag{A9}$$

In this paper, we use Eq. (A9) as a regularization relation to introduce the $s$-wave scattering length. With this, we can eliminate the ultraviolet divergences due to contact interactions.

We also notice that for the bound states, $\mathcal{E}_{\mathrm{AB}} < 0$, the solution of Eq. (A5) is

$$\phi(\mathbf{k}_{\mathrm{A}}) = \frac{\mathcal{F}}{k_{\mathrm{A}}^2 - \mathcal{E}_{\mathrm{AB}}}. \tag{A10}$$

We insert the ansatz (A10) into Eq. (A4), take the limit $\Lambda_{\mathrm{A}} \to \infty$, and use Eq. (A9). This results in

$$\frac{1}{a_{\mathrm{AB}}} = \sqrt{-\mathcal{E}_{\mathrm{AB}}}; \tag{A11}$$

cf. Fig. 10. Equation (A11) shows that for contact interactions the lowest-energy two-body bound state in vacuum emerges at unitarity, $a_{\mathrm{AB}} \to \pm\infty$, where $|\mathcal{E}_{\mathrm{AB}}| \to 0^+$; cf. Figs. 2 and 3.

## APPENDIX B. SEPARABLE INTERACTION MODEL (2) AND DERIVATION OF THE SYSTEM OF TWO COUPLED INTEGRAL EQS. (7) AND (8)

We apply the interaction operators $\hat{U}_{ij}$, given by Eq. (2), on the wave function $\psi = \psi(\mathbf{k}_1, \mathbf{k}_2, \mathbf{k}_3)$, and write the Schrödinger Eq. (1) as follows:

$$\left(\frac{\hbar^2 k_1^2}{2m_1} + \frac{\hbar^2 k_2^2}{2m_2} + \frac{\hbar^2 k_3^2}{2m_3} - E\right)\psi = -(\hat{U}_{12} + \hat{U}_{13} + \hat{U}_{23})\psi, \tag{B1}$$

where

$$\hat{U}_{12}\psi = g_{12}\theta_{\Lambda_1}(\mathbf{k}_1)\theta_{\Lambda_2}(\mathbf{k}_2) \int \frac{d^3\mathbf{q}}{(2\pi)^3} \theta_{\Lambda_1}(\mathbf{k}_1 - \mathbf{q})$$
$$\times \theta_{\Lambda_2}(\mathbf{k}_2 + \mathbf{q})\psi(\mathbf{k}_1 - \mathbf{q}, \mathbf{k}_2 + \mathbf{q}, \mathbf{k}_3), \tag{B2}$$

$$\hat{U}_{13}\psi = g_{13}\theta_{\Lambda_1}(\mathbf{k}_1)\theta_{\Lambda_3}(\mathbf{k}_3) \int \frac{d^3\mathbf{q}}{(2\pi)^3} \theta_{\Lambda_1}(\mathbf{k}_1 - \mathbf{q})$$
$$\times \theta_{\Lambda_3}(\mathbf{k}_3 + \mathbf{q})\psi(\mathbf{k}_1 - \mathbf{q}, \mathbf{k}_2, \mathbf{k}_3 + \mathbf{q}), \tag{B3}$$

$$\hat{U}_{23}\psi = g_{23}\theta_{\Lambda_2}(\mathbf{k}_2)\theta_{\Lambda_3}(\mathbf{k}_3) \int \frac{d^3\mathbf{q}}{(2\pi)^3} \theta_{\Lambda_2}(\mathbf{k}_2 - \mathbf{q})$$
$$\times \theta_{\Lambda_3}(\mathbf{k}_3 + \mathbf{q})\psi(\mathbf{k}_1, \mathbf{k}_2 - \mathbf{q}, \mathbf{k}_3 + \mathbf{q}), \tag{B4}$$

and the cutoff function $\theta$ is defined by Eq. (3). The resulting operators (B2)-(B4) reveal that the interaction operator $\hat{U}$ is separable [27]. Next, we define the variables $\boldsymbol{\kappa}_i \equiv \mathbf{q} + \mathbf{k}_i$, for $i = 1, 2, 3$, and also assume $m_3 = m_2$ and $\Lambda_1 \sim \Lambda_2 = \Lambda_3$. We consider the zero total momentum of the three-body bound states, $\psi(\mathbf{k}_1, \mathbf{k}_2, \mathbf{k}_3) = \psi(\mathbf{k}_2, \mathbf{k}_3)\delta^{(3)}(\mathbf{k}_1 + \mathbf{k}_2 + \mathbf{k}_3)$, where $\delta^{(3)}$ denotes the three-dimensional Dirac delta function. We also define three functions $F_1$, $F_2$, and $F_3$ as

$$F_1(\mathbf{k}_1) = g_{23} \int \frac{d^3\boldsymbol{\kappa}_3}{(2\pi)^3} \theta_{\Lambda_2}(-\mathbf{k}_1 - \boldsymbol{\kappa}_3)\theta_{\Lambda_3}(\boldsymbol{\kappa}_3)$$
$$\times \psi(-\mathbf{k}_1 - \boldsymbol{\kappa}_3, \boldsymbol{\kappa}_3), \tag{B5}$$

$$F_2(\mathbf{k}_2) = g_{13} \int \frac{d^3\boldsymbol{\kappa}_3}{(2\pi)^3} \theta_{\Lambda_1}(-\mathbf{k}_2 - \boldsymbol{\kappa}_3)\theta_{\Lambda_3}(\boldsymbol{\kappa}_3)\psi(\mathbf{k}_2, \boldsymbol{\kappa}_3), \tag{B6}$$

$$F_3(\mathbf{k}_3) = g_{12} \int \frac{d^3\boldsymbol{\kappa}_2}{(2\pi)^3} \theta_{\Lambda_1}(-\mathbf{k}_3 - \boldsymbol{\kappa}_2)\theta_{\Lambda_2}(\boldsymbol{\kappa}_2)\psi(\boldsymbol{\kappa}_2, \mathbf{k}_3). \tag{B7}$$

We use Eqs. (B5)-(B7) and rewrite Eq. (B1) as follows:

$$\left(\frac{\hbar^2(\mathbf{k}_2 + \mathbf{k}_3)^2}{2m_1} + \frac{\hbar^2 k_2^2}{2m_2} + \frac{\hbar^2 k_3^2}{2m_3} - E\right)\psi(\mathbf{k}_2, \mathbf{k}_3)$$
$$= -\theta_{\Lambda_2}(\mathbf{k}_2)\theta_{\Lambda_2}(\mathbf{k}_3)F_1(-\mathbf{k}_2 - \mathbf{k}_3) - \theta_{\Lambda_1}(-\mathbf{k}_2 - \mathbf{k}_3)$$
$$\times \theta_{\Lambda_3}(\mathbf{k}_3)F_2(\mathbf{k}_2) - \theta_{\Lambda_1}(-\mathbf{k}_2 - \mathbf{k}_3)\theta_{\Lambda_2}(\mathbf{k}_2)F_3(\mathbf{k}_3). \tag{B8}$$

Equation (B8) provides an ansatz for the wave function:

$$\psi(\mathbf{k}_2,\mathbf{k}_3) = -\frac{\theta_{\Lambda_2}(\mathbf{k}_2)\theta_{\Lambda_2}(\mathbf{k}_3)F_1(-\mathbf{k}_2-\mathbf{k}_3) + \theta_{\Lambda_1}(-\mathbf{k}_2-\mathbf{k}_3)\theta_{\Lambda_3}(\mathbf{k}_3)F_2(\mathbf{k}_2) + \theta_{\Lambda_1}(-\mathbf{k}_2-\mathbf{k}_3)\theta_{\Lambda_2}(\mathbf{k}_2)F_3(\mathbf{k}_3)}{\frac{\hbar^2(\mathbf{k}_2+\mathbf{k}_3)^2}{2m_1} + \frac{\hbar^2 k_2^2}{2m_2} + \frac{\hbar^2 k_3^2}{2m_3} - E}. \quad \text{(B9)}$$

We take into account the Fermi sea constraints by $k_2 > k_F$ and $k_3 > k_F$. We also assume $g_{13} = g_{12}$. If the species "2" and "3" are in a singlet state, then $F_3 = F_2$. Now we define $\mathbf{p}_1 \equiv -\mathbf{k}_2 - \boldsymbol{\kappa}_3$, $\mathbf{p}_2 \equiv -\mathbf{k}_1 - \boldsymbol{\kappa}_3$, $\mathbf{p}_3 \equiv \boldsymbol{\kappa}_3$, and rewrite the unknown functions $F_1$ and $F_2$ as follows:

$$F_1(\mathbf{k}_1) = g_{23} \int \frac{d^3\mathbf{p}_3}{(2\pi)^3} \theta_{k_F,\Lambda_2}(-\mathbf{k}_1 - \mathbf{p}_3)\theta_{k_F,\Lambda_2}(\mathbf{p}_3)$$
$$\times \psi(-\mathbf{k}_1 - \mathbf{p}_3, \mathbf{p}_3), \quad \text{(B10)}$$

$$F_2(\mathbf{k}_2) = g_{12} \int \frac{d^3\mathbf{p}_3}{(2\pi)^3} \theta_{\Lambda_1}(-\mathbf{k}_2 - \mathbf{p}_3)\theta_{k_F,\Lambda_2}(\mathbf{p}_3)\psi(\mathbf{k}_2, \mathbf{p}_3). \quad \text{(B11)}$$

Finally, we choose a three-body parameter $\Lambda \gg k_F$ to fix the range of the interactions and to regularize the three-body bound-state solutions. We insert the ansatz (B9) into Eqs. (B10) and (B11), and arrive at the system of two coupled integral Eqs. (7) and (8), where the integral kernels $K_i$ and $\tilde{K}_i$, $i = 1, 2, 3$, are:

$$K_1(\mathbf{k}_2, \mathbf{p}_3; E) = \frac{\theta_{\Lambda_1}(-\mathbf{k}_2 - \mathbf{p}_3)\theta_{k_F,\Lambda_2}(\mathbf{p}_3)}{\frac{\hbar^2(\mathbf{k}_2+\mathbf{p}_3)^2}{2m_1} + \frac{\hbar^2 k_2^2}{2m_2} + \frac{\hbar^2 p_3^2}{2m_2} - E}, \quad \text{(B12)}$$

$$K_2(\mathbf{k}_2, \mathbf{p}_1; E) = \frac{\theta_{\Lambda_1}(\mathbf{p}_1)\theta_{k_F,\Lambda_2}(-\mathbf{p}_1 - \mathbf{k}_2)}{\frac{\hbar^2 p_1^2}{2m_1} + \frac{\hbar^2 k_2^2}{2m_2} + \frac{\hbar^2(\mathbf{p}_1+\mathbf{k}_2)^2}{2m_2} - E}, \quad \text{(B13)}$$

$$K_3(\mathbf{k}_1, \mathbf{p}_3; E) = \frac{\theta_{k_F,\Lambda_2}(-\mathbf{k}_1 - \mathbf{p}_3)\theta_{k_F,\Lambda_2}(\mathbf{p}_3)}{\frac{\hbar^2 k_1^2}{2m_1} + \frac{\hbar^2(\mathbf{k}_1+\mathbf{p}_3)^2}{2m_2} + \frac{\hbar^2 p_3^2}{2m_2} - E}, \quad \text{(B14)}$$

$$\tilde{K}_1(\mathbf{k}_2, \tilde{\mathbf{p}}_3; E) = \frac{\theta_{\Lambda}(-\mathbf{k}_2 - \tilde{\mathbf{p}}_3)\theta_{k_F,\Lambda}(\mathbf{k}_2)\theta_{k_F,\Lambda}(\tilde{\mathbf{p}}_3)}{\frac{\hbar^2(\mathbf{k}_2+\tilde{\mathbf{p}}_3)^2}{2m_1} + \frac{\hbar^2 k_2^2}{2m_2} + \frac{\hbar^2 \tilde{p}_3^2}{2m_2} - E}, \quad \text{(B15)}$$

$$\tilde{K}_2(\mathbf{k}_2, \tilde{\mathbf{p}}_1; E) = \frac{\theta_{\Lambda}(\tilde{\mathbf{p}}_1)\theta_{k_F,\Lambda}(\mathbf{k}_2)\theta_{k_F,\Lambda}(-\tilde{\mathbf{p}}_1 - \mathbf{k}_2)}{\frac{\hbar^2 \tilde{p}_1^2}{2m_1} + \frac{\hbar^2 k_2^2}{2m_2} + \frac{\hbar^2(\tilde{\mathbf{p}}_1+\mathbf{k}_2)^2}{2m_2} - E}, \quad \text{(B16)}$$

$$\tilde{K}_3(\mathbf{k}_1, \tilde{\mathbf{p}}_3; E) = \frac{\theta_{k_F,\Lambda}(-\mathbf{k}_1 - \tilde{\mathbf{p}}_3)\theta_{\Lambda}(\mathbf{k}_1)\theta_{k_F,\Lambda}(\tilde{\mathbf{p}}_3)}{\frac{\hbar^2 k_1^2}{2m_1} + \frac{\hbar^2(\mathbf{k}_1+\tilde{\mathbf{p}}_3)^2}{2m_2} + \frac{\hbar^2 \tilde{p}_3^2}{2m_2} - E}. \quad \text{(B17)}$$

## APPENDIX C. CALCULATION OF THE FUNCTION $\Omega_{23}$

For $s$-wave symmetry of the states we write the integral kernel $K_3(\mathbf{k}_1, \mathbf{p}_3; \mathcal{E})$ as

$$\mathcal{K}_3(k_1, p_3; \mathcal{E}) = p_3 \ln\left(\frac{p_3^2 + k_1 p_3 v_{\max} + \frac{\mu_{23}}{\mu_{12}}k_1^2 - \frac{\mu_{23}}{\mu_{12}}\mathcal{E}}{p_3^2 + k_1 p_3 v_{\min} + \frac{\mu_{23}}{\mu_{12}}k_1^2 - \frac{\mu_{23}}{\mu_{12}}\mathcal{E}}\right), \quad \text{(C1)}$$

where $\mathcal{E} = 2\mu_{12}E/\hbar^2$, $E$ is the energy of the three-body system, $v_{\max}$ and $v_{\min}$ denote the upper- and lower bound of $v \equiv \cos\vartheta_{\mathbf{p}_3, \mathbf{k}_1}$, respectively, and $\mu_{23}$ is a reduced mass, $1/\mu_{23} = 1/m_2 + 1/m_3 = 2/m_2$. For contact interactions we have:

$$v_{\max} = \min_{p_3}\left(1, \frac{\Lambda_2^2 - k_1^2 - p_3^2}{2k_1 p_3}\right) \to 1 \text{ as } \Lambda_2 \to \infty, \quad \text{(C2)}$$

$$v_{\min} = \max_{p_3}\left(-1, \frac{k_F^2 - k_1^2 - p_3^2}{2k_1 p_3}\right)$$
$$= \begin{cases} -1, & \text{for } k_F < p_3 < k_1 - k_F \\ & \quad \text{or } p_3 > k_1 + k_F, \\ \frac{k_F^2 - k_1^2 - p_3^2}{2k_1 p_3}, & \text{for } k_1 - k_F < p_3 < k_1 + k_F. \end{cases} \quad \text{(C3)}$$

Next, without loss of generality we assume that $\mathbf{p}_3 = p_3\mathbf{e}_z$, where $\mathbf{e}_z$ is the unit vector in the direction of the $z$-axis, and calculate the function $\Omega_{23}$ for contact interactions:

$$\Omega_{23} \equiv \Omega_{23}(a_{23}, k_1; k_F, \mathcal{E})$$
$$\equiv \frac{4\pi\hbar^2}{2\mu_{23}g_{23}} + \frac{1}{\frac{2\mu_{23}}{m_2}\pi k_1} \lim_{\Lambda_2 \to \infty} \int_{k_F}^{\Lambda_2} dp_3$$
$$\times p_3 \ln\left(\frac{p_3^2 + k_1 p_3 v_{\max} + \frac{\mu_{23}}{\mu_{12}}k_1^2 - \frac{\mu_{23}}{\mu_{12}}\mathcal{E}}{p_3^2 + k_1 p_3 v_{\min} + \frac{\mu_{23}}{\mu_{12}}k_1^2 - \frac{\mu_{23}}{\mu_{12}}\mathcal{E}}\right). \quad \text{(C4)}$$

To calculate Eq. (C4) we consider two cases. For $0 < k_1 \leqslant 2k_F$ we have:

$$\Omega_{23} = \frac{4\pi\hbar^2}{2\mu_{23}g_{23}} + \frac{1}{\pi k_1} \int_{k_F}^{k_1+k_F} dp_3\, p_3$$
$$\times \ln\left(\frac{p_3^2 + k_1 p_3 + \frac{\mu_{23}}{\mu_{12}}k_1^2 - \frac{\mu_{23}}{\mu_{12}}\mathcal{E}}{\frac{1}{2}p_3^2 + (\frac{\mu_{23}}{\mu_{12}} - \frac{1}{2})k_1^2 + \frac{1}{2}k_F^2 - \frac{\mu_{23}}{\mu_{12}}\mathcal{E}}\right)$$
$$+ \frac{1}{\pi k_1} \lim_{\Lambda_2 \to \infty} \int_{k_1+k_F}^{\Lambda_2} dp_3\, p_3$$
$$\times \ln\left(\frac{p_3^2 + k_1 p_3 + \frac{\mu_{23}}{\mu_{12}}k_1^2 - \frac{\mu_{23}}{\mu_{12}}\mathcal{E}}{p_3^2 - k_1 p_3 + \frac{\mu_{23}}{\mu_{12}}k_1^2 - \frac{\mu_{23}}{\mu_{12}}\mathcal{E}}\right). \quad \text{(C5)}$$

We calculate each integral and use Eq. (5). The result is

$$
\begin{aligned}
\Omega_{23} =& \frac{1}{a_{23}} - \frac{k_1}{2\pi} - \frac{k_F}{\pi} + \frac{2\sqrt{\kappa}}{\pi}\left[\arctan\left(\frac{\frac{1}{2}k_1 + k_F}{\sqrt{\kappa}}\right) - \frac{\pi}{2}\right] \\
&+ \frac{1}{\pi k_1}\left((\frac{\mu_{23}}{\mu_{12}} - \frac{1}{2})k_1^2 + k_F^2 - \frac{\mu_{23}}{\mu_{12}}\mathcal{E}\right) \\
&\times \ln\left(\frac{(\frac{\mu_{23}}{\mu_{12}} - \frac{1}{2})k_1^2 + k_F^2 - \frac{\mu_{23}}{\mu_{12}}\mathcal{E}}{\frac{\mu_{23}}{\mu_{12}}k_1^2 + k_F k_1 + k_F^2 - \frac{\mu_{23}}{\mu_{12}}\mathcal{E}}\right),
\end{aligned} \quad \text{(C6)}
$$

where $\kappa \equiv (\frac{\mu_{23}}{\mu_{12}} - \frac{1}{4})k_1^2 - \frac{\mu_{23}}{\mu_{12}}\mathcal{E}$. The lowest-energy two-body bound state, Cooper pair-23, is described by

$$
\Omega_{23}(a_{23}, k_1 \to 0; k_F, \mathcal{E} \to \mathcal{E}_{23}) = 0, \quad \text{(C7)}
$$

resulting in Eq. (15); cf. Fig. 2.

For $k_1 \geqslant 2k_F$ we have:

$$
\begin{aligned}
\Omega_{23} =& \frac{4\pi\hbar^2}{2\mu_{23}g_{23}} + \frac{1}{\pi k_1}\int_{k_F}^{k_1 - k_F} dp_3\, p_3 \\
&\times \ln\left(\frac{p_3^2 + k_1 p_3 + \frac{\mu_{23}}{\mu_{12}}k_1^2 - \frac{\mu_{23}}{\mu_{12}}\mathcal{E}}{p_3^2 - k_1 p_3 + \frac{\mu_{23}}{\mu_{12}}k_1^2 - \frac{\mu_{23}}{\mu_{12}}\mathcal{E}}\right) \\
&+ \frac{1}{\pi k_1}\int_{k_1 - k_F}^{k_1 + k_F} dp_3\, p_3 \\
&\times \ln\left(\frac{p_3^2 + k_1 p_3 + \frac{\mu_{23}}{\mu_{12}}k_1^2 - \frac{\mu_{23}}{\mu_{12}}\mathcal{E}}{\frac{1}{2}p_3^2 + (\frac{\mu_{23}}{\mu_{12}} - \frac{1}{2})k_1^2 + \frac{1}{2}k_F^2 - \frac{\mu_{23}}{\mu_{12}}\mathcal{E}}\right) \\
&+ \frac{1}{\pi k_1}\lim_{\Lambda_2 \to \infty}\int_{k_1 + k_F}^{\Lambda_2} dp_3\, p_3 \\
&\times \ln\left(\frac{p_3^2 + k_1 p_3 + \frac{\mu_{23}}{\mu_{12}}k_1^2 - \frac{\mu_{23}}{\mu_{12}}\mathcal{E}}{p_3^2 - k_1 p_3 + \frac{\mu_{23}}{\mu_{12}}k_1^2 - \frac{\mu_{23}}{\mu_{12}}\mathcal{E}}\right).
\end{aligned} \quad \text{(C8)}
$$

We calculate each integral and use Eq. (5), which results in

$$
\begin{aligned}
\Omega_{23} =& \frac{1}{a_{23}} - \frac{2k_F}{\pi} - \frac{2\sqrt{\kappa}}{\pi}\left[\arctan\left(\frac{\frac{1}{2}k_1 - k_F}{\sqrt{\kappa}}\right) + \right. \\
&\left. - \arctan\left(\frac{\frac{1}{2}k_1 + k_F}{\sqrt{\kappa}}\right) + \frac{\pi}{2}\right] + \\
&+ \frac{1}{\pi k_1}\left((\frac{\mu_{23}}{\mu_{12}} - \frac{1}{2})k_1^2 + k_F^2 - \frac{\mu_{23}}{\mu_{12}}\mathcal{E}\right) \\
&\times \ln\left(\frac{\frac{\mu_{23}}{\mu_{12}}k_1^2 + k_F k_1 + k_F^2 - \frac{\mu_{23}}{\mu_{12}}\mathcal{E}}{\frac{\mu_{23}}{\mu_{12}}k_1^2 - k_F k_1 + k_F^2 - \frac{\mu_{23}}{\mu_{12}}\mathcal{E}}\right).
\end{aligned} \quad \text{(C9)}
$$

## APPENDIX D. CALCULATION OF THE FUNCTION $\Omega_{12}$

For a noninteracting mixture, $g_{23} = 0$, the system of the integral Eqs. (7) and (8) reduces to

$$
\begin{aligned}
&\left[\frac{1}{g_{12}} + \int \frac{d^3\mathbf{p}_3}{(2\pi)^3}K_1(\mathbf{k}_2, \mathbf{p}_3; E)\right]F_2(\mathbf{k}_2) \\
&= -\int \frac{d^3\tilde{\mathbf{p}}_3}{(2\pi)^3}\tilde{K}_1(\mathbf{k}_2, \tilde{\mathbf{p}}_3; E)F_2(\tilde{\mathbf{p}}_3), \quad \text{(D1)}
\end{aligned}
$$

where the integral kernels $K_1$ and $\tilde{K}_1$ are given by Eqs. (B12) and (B15), respectively. The cutoff function $\theta_{\Lambda_1}(-\mathbf{k}_2 - \mathbf{p}_3)$, which appears in $K_1$, imposes an upper bound, $u_{\max}$, on the angle between the two momenta $\mathbf{k}_2$ and $\mathbf{p}_3$, $u \equiv \cos\vartheta_{\mathbf{p}_3, \mathbf{k}_2}$:

$$
u_{\max} = \min_{p_3}\left(1, \frac{\Lambda_1^2 - k_2^2 - p_3^2}{2k_2 p_3}\right) \to 1 \text{ as } \Lambda_1 \to \infty. \quad \text{(D2)}
$$

Next, without loss of generality we assume that $\mathbf{p}_3 = p_3\mathbf{e}_z$, where $\mathbf{e}_z$ is the unit vector in the direction of the $z$-axis. For contact interactions and $s$-wave symmetry of the states we write Eq. (D1) as Eq. (16), where

$$
\begin{aligned}
\Omega_{12} \equiv& \Omega_{12}(a_{12}, k_2; k_F, \mathcal{E}) \\
\equiv& \frac{4\pi\hbar^2}{2\mu_{12}g_{12}} + \frac{1}{2\pi\frac{\mu_{12}}{m_1}k_2}\lim_{\Lambda_2 \to \infty}\int_{k_F}^{\Lambda_2} dp_3 \\
&\times p_3 \ln\left(\frac{p_3^2 + \frac{2\mu_{12}}{m_1}k_2 p_3 + k_2^2 - \mathcal{E}}{p_3^2 - \frac{2\mu_{12}}{m_1}k_2 p_3 + k_2^2 - \mathcal{E}}\right).
\end{aligned} \quad \text{(D3)}
$$

Here, $\mathcal{E} = 2\mu_{12}E/\hbar^2$ and $E$ is the energy of the three-body system. We calculate the integral (D3), and use Eq. (5) to obtain:

$$
\begin{aligned}
\Omega_{12} =& \frac{1}{a_{12}} - \frac{k_F}{\pi} + \frac{\sqrt{\eta}}{\pi}\left[\arctan\left(\frac{\frac{\mu_{12}}{m_1}k_2 + k_F}{\sqrt{\eta}}\right)\right. \\
&\left. - \arctan\left(\frac{\frac{\mu_{12}}{m_1}k_2 - k_F}{\sqrt{\eta}}\right) - \pi\right] + \frac{1}{4\pi\frac{\mu_{12}}{m_1}k_2} \\
&\times \left[\left(2(\frac{\mu_{12}}{m_1})^2 - 1\right)k_2^2 - k_F^2 + \mathcal{E}\right] \\
&\times \ln\left(\frac{k_2^2 + \frac{2\mu_{12}}{m_1}k_F k_2 + k_F^2 - \mathcal{E}}{k_2^2 - \frac{2\mu_{12}}{m_1}k_F k_2 + k_F^2 - \mathcal{E}}\right),
\end{aligned} \quad \text{(D4)}
$$

where $\eta \equiv [1 - (\mu/m_1)^2]k_2^2 - \mathcal{E}$.

## APPENDIX E. NUMERICAL SOLUTION OF THE SYSTEM OF INTEGRAL EQS. (7) AND (8)

Recall that we only consider the isotropic solutions of Eqs. (7) and (8), i.e., $F_i(\mathbf{k}) = F_i(k)$. To solve the system of the two coupled integral Eqs. (7) and (8) we replace the three-dimensional integrals over momentum by the absolute value of each momentum. Next, we calculate the

two functions $\Omega_{23}$ and $\Omega_{12}$ analytically; see Appendices C and D. The analytical results reveal the lowest-energy dimer state and the two-body bound-state continuum. We solve the coupled Eqs. (7) and (8) for a given three-body parameter $\Lambda \gg k_F$. For that, we discretize the integral ranges on the grid points $\{x_j^{(N)}\}$, $j = 1, 2, \ldots, N$, that are the sets of zeros of the Legendre polynomials $P_N(x)$. We approximate each integral by a truncated sum that is weighted by $w_j^{(N)}$:

$$w_j^{(N)} = \frac{2}{1 - [x_j^{(N)}]^2} \frac{1}{[P_N'(x_j^{(N)})]^2}, \qquad \text{(E1)}$$

where $P_N'(x) = dP_N(x)/dx$ [37, 38]. This choice is the so-called Gauss-Legendre quadrature rule, supporting the highest order of accuracy among the other quadrature rules [37].

We apply the Gauss-Legendre quadrature rule on each integral and construct a matrix equation analog to an integral equation. For given values of $E$ below the threshold energy (4), we calculate the eigenvalues resulting in the corresponding values of the $s$-wave scattering lengths. The unknown functions $F_1$ and $F_2$ will be obtained as the eigenvectors of the matrix equations.

## APPENDIX F. DERIVATION OF EQ. (19)

The atoms "1" and "2" interact attractively via contact interactions according to Eq. (2). We follow Appendix B and rewrite the Schrödinger equation describing the pair-12 in terms of the relative momentum, $\mathbf{p}_{12} \equiv (\mu_{12}/m_1)\mathbf{k}_1 - (1 - \mu_{12}/m_1)\mathbf{k}_2$, and the total momentum, $\mathbf{P}_{12} \equiv \mathbf{k}_1 + \mathbf{k}_2$, as

$$\frac{4\pi\hbar^2}{2\mu_{12}g_{12}} = -4\pi \int \frac{d^3\mathbf{p}_{12}}{(2\pi)^3} \frac{1}{p_{12}^2 + \frac{\mu_{12}}{m_1}(1 - \frac{\mu_{12}}{m_1})P_{12}^2 - \mathcal{E}_{12}},$$
$$\text{(F1)}$$

where $\mathcal{E}_{12} = 2\mu_{12}E_{12}/\hbar^2$, $E_{12}$ is the energy of the pair-12, and $\mu_{12}$ is a reduced mass, $1/\mu_{12} = 1/m_1 + 1/m_2$. The Fermi sea demands a constraint on the momentum of the atom "2", $k_2 > k_F$, which in terms of the relative and total momenta reads $|\frac{\mu_{12}}{m_1}\mathbf{P}_{12} - \mathbf{p}_{12}| > k_F$. This constraint imposes an upper bound on $\cos\vartheta_{\mathbf{p}_{12},\mathbf{P}_{12}}$. Without loss of generality we assume that $\mathbf{P}_{12} = P_{12}\mathbf{e}_z$, where $\mathbf{e}_z$ is the unit vector in the direction of the $z$-axis.

To solve Eq. (F1) analytically, we assume $s$-wave symmetry of the states and consider two cases. For $P_{12} \leqslant (\mu_{12}/m_1)^{-1}k_F$ we have:

$$\frac{4\pi\hbar^2}{2\mu_{12}g_{12}} = \frac{-1}{\frac{2\mu_{12}}{m_1}\pi P_{12}} \int_{k_F - \frac{\mu_{12}}{m_1}P_{12}}^{k_F + \frac{\mu_{12}}{m_1}P_{12}} dp_{12}\, p_{12}$$
$$\times \frac{p_{12}^2 + (\frac{\mu_{12}}{m_1})^2 P_{12}^2 - k_F^2}{p_{12}^2 + \frac{\mu_{12}}{m_1}(1 - \frac{\mu_{12}}{m_1})P_{12}^2 - \mathcal{E}_{12}}$$
$$- \frac{1}{\pi} \int_{k_F - \frac{\mu_{12}}{m_1}P_{12}}^{k_F + \frac{\mu_{12}}{m_1}P_{12}} dp_{12}\, p_{12}^2$$
$$\times \frac{1}{p_{12}^2 + \frac{\mu_{12}}{m_1}(1 - \frac{\mu_{12}}{m_1})P_{12}^2 - \mathcal{E}_{12}}$$
$$- \frac{2}{\pi} \int_{k_F + \frac{\mu_{12}}{m_1}P_{12}}^{\Lambda_2} dp_{12}\, p_{12}^2$$
$$\times \frac{1}{p_{12}^2 + \frac{\mu_{12}}{m_1}(1 - \frac{\mu_{12}}{m_1})P_{12}^2 - \mathcal{E}_{12}}. \qquad \text{(F2)}$$

We calculate each integral, take the limit $\Lambda_2 \to \infty$, and use Eq. (5). The result is
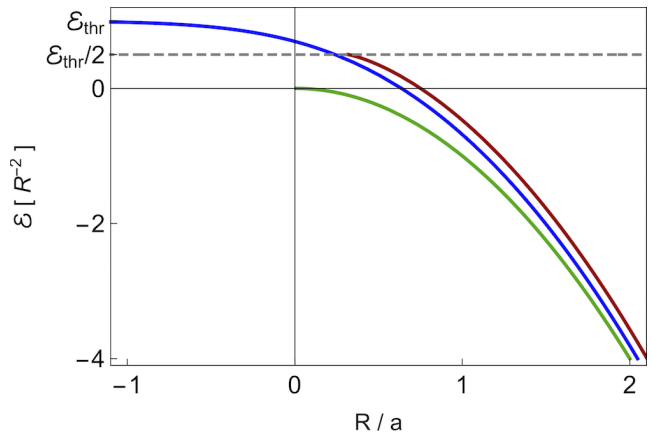


Figure 10. Energy $\mathcal{E} = 2\mu E/\hbar^2$ in units of $R^{-2}$ vs $R/a$ for two equal-mass atoms with a reduced mass $\mu$ and the $s$-wave scattering length $a$, where $R$ denotes an arbitrary length scale. The green curve is the result in vacuum, $k_F = 0$, given by Eq. (A11). The blue curve shows the result of a Cooper pair with vanishing total momentum described by Eq. (15), where both atoms are immersed in an inert Fermi sea with the Fermi momentum $k_F R = 1$. The red curve is the result for a pair with the total momentum $k_F$, where one atom is in vacuum and the other is subject to an inert Fermi sea with the Fermi momentum $k_F R = 1$; cf. Eqs. (F3) and (F5). The gray dashed lines show $\mathcal{E}_{\text{thr}}$ and $\mathcal{E}_{\text{thr}}/2$, where $\mathcal{E}_{\text{thr}} = 2\mu E_{\text{thr}}/\hbar^2 = k_F^2$.

$$\frac{1}{a_{12}} = \frac{k_F}{\pi} - \frac{1}{\pi}\sqrt{\varrho}\left[\arctan\left(\frac{k_F - \frac{\mu_{12}}{m_1}P_{12}}{\sqrt{\varrho}}\right)\right.$$
$$\left. + \arctan\left(\frac{k_F + \frac{\mu_{12}}{m_1}P_{12}}{\sqrt{\varrho}}\right) - \pi\right] + \frac{1}{4\pi\frac{\mu_{12}}{m_1}P_{12}}$$
$$\times\left(\frac{\mu_{12}}{m_1}(\frac{2\mu_{12}}{m_1} - 1)P_{12}^2 - k_F^2 + \mathcal{E}_{12}\right)$$
$$\times\ln\left(\frac{\frac{\mu_{12}}{m_1}P_{12}^2 - \frac{2\mu_{12}}{m_1}k_FP_{12} + k_F^2 - \mathcal{E}_{12}}{\frac{\mu_{12}}{m_1}P_{12}^2 + \frac{2\mu_{12}}{m_1}k_FP_{12} + k_F^2 - \mathcal{E}_{12}}\right), \quad \text{(F3)}$$

where $\varrho \equiv \frac{\mu_{12}}{m_1}(1 - \frac{\mu_{12}}{m_1})P_{12}^2 - \mathcal{E}_{12}$ .

For $P_{12} \geqslant (\mu_{12}/m_1)^{-1}k_F$ we have:

$$\frac{4\pi\hbar^2}{2\mu_{12}g_{12}} = -\frac{2}{\pi}\int_0^{\frac{\mu_{12}}{m_1}P_{12}-k_F} dp_{12}\, p_{12}^2$$
$$\times \frac{1}{p_{12}^2 + \frac{\mu_{12}}{m_1}(1 - \frac{\mu_{12}}{m_1})P_{12}^2 - \mathcal{E}_{12}}$$
$$- \frac{1}{\frac{2\mu_{12}}{m_1}\pi P_{12}}\int_{\frac{\mu_{12}}{m_1}P_{12}-k_F}^{\frac{\mu_{12}}{m_1}P_{12}+k_F} dp_{12}\, p_{12}$$
$$\times \frac{p_{12}^2 + (\frac{\mu_{12}}{m_1})^2P_{12}^2 - k_F^2}{p_{12}^2 + \frac{\mu}{m_1}(1 - \frac{\mu}{m_1})P_{12}^2 - \mathcal{E}_{12}}$$
$$- \frac{1}{\pi}\int_{\frac{\mu_{12}}{m_1}P_{12}-k_F}^{\frac{\mu_{12}}{m_1}P_{12}+k_F} dp_{12}\, p_{12}^2$$
$$\times \frac{1}{p_{12}^2 + \frac{\mu_{12}}{m_1}(1 - \frac{\mu_{12}}{m_1})P_{12}^2 - \mathcal{E}_{12}}$$
$$- \frac{2}{\pi}\int_{\frac{\mu_{12}}{m_1}P_{12}+k_F}^{\Lambda_2} dp_{12}\, p_{12}^2$$
$$\times \frac{1}{p_{12}^2 + \frac{\mu_{12}}{m_1}(1 - \frac{\mu_{12}}{m_1})P_{12}^2 - \mathcal{E}_{12}}. \quad \text{(F4)}$$

We calculate each integral, take the limit $\Lambda_2 \to \infty$, use Eq. (5), and arrive at:

$$\frac{1}{a_{12}} = \frac{k_F}{\pi} + \frac{1}{\pi}\sqrt{\varrho}\left[\arctan\left(\frac{\frac{\mu_{12}}{m_1}P_{12} - k_F}{\sqrt{\varrho}}\right)\right.$$
$$\left. - \arctan\left(\frac{\frac{\mu_{12}}{m_1}P_{12} + k_F}{\sqrt{\varrho}}\right) + \pi\right] + \frac{1}{4\pi\frac{\mu_{12}}{m_1}P_{12}}$$
$$\times\left(\frac{\mu_{12}}{m_1}(\frac{2\mu_{12}}{m_1} - 1)P_{12}^2 - k_F^2 + \mathcal{E}_{12}\right)$$
$$\times\ln\left(\frac{\frac{\mu_{12}}{m_1}P_{12}^2 - \frac{2\mu_{12}}{m_1}k_FP_{12} + k_F^2 - \mathcal{E}_{12}}{\frac{\mu_{12}}{m_1}P_{12}^2 + \frac{2\mu_{12}}{m_1}k_FP_{12} + k_F^2 - \mathcal{E}_{12}}\right); \quad \text{(F5)}$$

see Fig. 10.

As discussed in the text, for $m_2/m_1 \gg 1$ we estimate the onset of a highest-energy excited three-body bound state at zero energy by calculating the onset of the lowest-energy pair-12. To do that, we expand Eq. (F3) or Eq. (F5) for $m_2/m_1 \gg 1$, as $\mathcal{E}_{12} \to 0$ and $P_{12} \to (\frac{\mu_{12}}{m_1})^{-1}k_F$, which results in Eq. (19).

## APPENDIX G. CALCULATION OF THE PARAMETER $s_0$

The Efimov scaling factor is $\lambda = \exp(\pi/|s_0|)$, where the effect of the mass ratio $m_2/m_1$ is described by the parameter $s_0$. For s-wave symmetry of the states, if we have a system of three species only with two-resonantly interacting pairs, then $s_0$ is the purely imaginary root of the transcendental equation

$$\cos\left(\frac{\pi}{2}s_0\right) = \frac{2}{\sin 2\vartheta}\frac{\sin(\vartheta s_0)}{s_0}, \quad \text{(G1)}$$

where $\vartheta = \arcsin[(m_2/m_1)/(1 + m_2/m_1)]$, $\vartheta \in [0, \pi/2]$. If all three species are resonantly interacting, we obtain $s_0$ as the purely imaginary root of the equation

$$\left[\cos\left(\frac{\pi}{2}s_0\right) - \frac{2}{\sin 2\vartheta}\frac{\sin(\vartheta s_0)}{s_0}\right]\cos\left(\frac{\pi}{2}s_0\right)$$
$$= \frac{8}{\sin^2 2\gamma}\frac{\sin^2(\gamma s_0)}{s_0^2}, \quad \text{(G2)}$$

where $\gamma = \arcsin\{\sqrt{(m_1/m_2)/[2(1 + m_2/m_1)]}\}$, $\gamma \in [0, \pi/4]$. For a proof, see Ref. [5].

[1] V. Efimov, Sov. J. Nucl. Phys. **12**, 589 (1971) [V. Efimov, Yad. Fiz. **12**, 1080 (1970)].

[2] V. Efimov, Phys. Lett. B **33**, 563 (1970).

[3] E. Braaten and H-. W. Hammer, Phys. Rep. **428**, 259 (2006).

[4] F. Ferlaino and R. Grimm, Physics **3**, 9 (2010).

[5] P. Naidon and S. Endo, Rep. Prog. Phys. **80**, 056001 (2017).

[6] C. H. Greene, P. Giannakeas, and J. P-. Ríos, Rev. Mod. Phys. **89**, 035006 (2017).

[7] J. P. D'Incao, J. Phys. B **51** 043001 (2018).

[8] J. Fortágh and C. Zimmermann, Rev. Mod. Phys. **79**, 235 (2007).

[9] C. J. Pethick and H. Smith, *Bose–Einstein Condensation in Dilute Gases* (Cambridge University Press, New York, 2008).

[10] I. Bloch, J. Dalibard, and W. Zwerger, Rev. Mod. Phys. **80**, 885 (2008).

[11] C. Chin, R. Grimm, P. Julienne, and E. Tiesinga, Rev. Mod. Phys. **82**, 1225 (2010).

[12] T. Kraemer, M. Mark, P. Waldburger, J. G. Danzl, C. Chin, B. Engeser, A. D. Lange, K. Pilch, A. Jaakkola, H. -C. Nägerl, and R. Grimm, Nature **440**, 315 (2006).

[13] M. Jag, M. Zaccanti, M. Cetina, R. S. Lous, F. Schreck, R. Grimm, D. S. Petrov, and J. Levinsen, Phys. Rev. Lett. **112**, 075302 (2014).

[14] B. Huang, L. A. Sidorenkov, R. Grimm, and J. M. Hutson, Phys. Rev. Lett. **112**, 190401 (2014).

[15] R. Pires, J. Ulmanis, S. Hälfner, M. Repp, A. Arias, E. D. Kuhnle, and M. Weidemüller, Phys. Rev. Lett. **112**, 250404 (2014).

[16] S-. K. Tung, K. Jiménez-García, J. Johansen, C. V. Parker, and C. Chin, Phys. Rev. Lett. **113**, 240402 (2014).

[17] R. Grimm, Few-Body Syst. **60**, 23 (2019).

[18] J. Voigtsberger, S. Zeller, J. Becht, N. Neumann, F. Sturm, H. -K. Kim, M. Waitz, F. Trinter, M. Kunitski, A. Kalinin, J. Wu, W. Schoöllkopf, D. Bressanini, A. Czasch, J. B. Williams, K. Ullmann-Pfleger, L. Ph H. Schmidt, M. S. Schöffler, R. E. Grisenti, T. Jahnke, and R. Dörner, Nat. Commun. **5**, 5765 (2014).

[19] M. Kunitski, S. Zeller, J. Voigtsberger, A. Kalinin, L. P. H. Schmidt, M. Schöffler, A. Czasch, W. Schöllkopf, R. E. Grisenti, T. Jahnke, D. Blume, and R. Dörner, Science **348**, 551 (2015).

[20] J. Ulmanis, S. Häfner, R. Pires, E. D. Kuhnle, Y. Wang, C. H. Greene, and M. Weidemüller, Phys. Rev. Lett. **117**, 153201 (2016).

[21] F. Ferlaino, A. Zenesini, M. Berninger, B. Huang, H-. C. Nägerl, and R. Grimm, Few-Body Syst. **51**, 113 (2011).

[22] Y. Castin, C. Mora, and L. Pricoupenko, Phys. Rev. Lett. **105**, 223201 (2010).

[23] P. Naidon, Few-Body Syst. **59**, 64 (2018).

[24] B. Bazak and D. S. Petrov, Phys. Rev. Lett. **118**, 083002 (2017).

[25] A. Sanayei, P. Naidon, and L. Mathey, Phys. Rev. Research **2**, 013341 (2020).

[26] L. N. Cooper, Phys. Rev. **104**, 1189 (1956).

[27] An interaction operator $\hat{U}$ which is a projector onto a state $|\varphi\rangle$ is called separable, and can be represented as $\hat{U} = g |\varphi\rangle \langle\varphi|$, where $g$ is the strength of the interaction; see, e.g., Y. Yamaguchi, Phys. Rev. **95**, 1628 (1954); L. D. Faddeev, *Mathematical Aspects of the Three-Body Problem in the Quantum Scattering Theory* (Sivan, Jerusalem, 1965); L. D. Faddeev and S. P. Merkuriev, *Quantum Scattering Theory for Several Par-*

*ticle Systems* (Kluwers Academic, Dordrecht, 1993).

[28] L. H. Thomas, Phys. Rev. **47**, 903 (1935).

[29] P. Naidon, S. Endo, and M. Ueda, Phys. Rev. Lett. **112**, 105301 (2014).

[30] P. Naidon, S. Endo, and M. Ueda, Phys. Rev. A **90**, 022106 (2014).

[31] By "momentum transfer" we mean the difference of the in-state and out-state momenta of a particle; see, e.g., Ref. [60].

[32] A. Derevianko, J. F. Babb, and A. Dalgarno, Phys. Rev. A **63**, 052704 (2001).

[33] M. Kitagawa, K. Enomoto, K. Kasa, Y. Takahashi, R. Ciuryło, P. Naidon, and P. S. Julienne, Phys. Rev. **A** 77, 012719 (2008).

[34] J. Tao, J. P. Perdew, and A. Ruzsinszky, PNAS **109**, 18 (2012).

[35] T. Gould and T. Buckǒ, J. Chem. Theory Comput. **12**, 3603 (2016).

[36] G. V. Skorniakov and K. A. Ter-Martirosian, Sov. Phys. JETP **4**, 648 (1957).

[37] L. N. Trefethen and D. Bau, III, *Numerical Linear Algebra* (SIAM, Philadelphia, 1997).

[38] V. I. Krylov, *Approximate Calculation of Integrals* (Dover, New York, 2005).

[39] W. H. Press, S. A. Teukolsky, W. T. Vetterling, and B. P. Flannery, *Numerical Recipes: The Art of Scientific Computing* (Cambridge University Press, New York, 2007).

[40] P. O. J. Scherer, *Computational Physics: Simulation of Classical and Quantum Systems* (Springer, Heidelberg, 2013).

[41] D. J. MacNeil and F. Zhou, Phys. Rev. Lett. **106**, 145301 (2011).

[42] P. Niemann and H. -W. Hammer, Phys. Rev. A **86**, 013628 (2012).

[43] N. T. Zinner, Few-Body Syst. **55**, 599 (2014).

[44] N. G. Nygaard and N. T. Zinner, New J. Phys. **16**, 023026 (2014).

[45] H. Tajima and P. Naidon, New J. Phys. **21**, 073051 (2019).

[46] For Efimov states in vacuum, $k_F = 0$, by increasing the mass ratio $m_2/m_1$, the Efimov scaling factor $\exp(\pi/|s_0|)$ decreases; cf. Appendix G. This implies that for a given value of $\Lambda$, increasing $m_2/m_1$ leads to more excited Efimov states. For $k_F \neq 0$ the Efimov spectrum is deformed near unitarity and the Efimov scaling factor does not hold anymore; nevertheless, as we increase $m_2/m_1$, excited three-body bound states appear.

[47] M. Sun and X. Cui, Phys. Rev. A **99**, 060701 (R) (2019).

[48] The Bohr radius is $a_0 = \frac{\hbar^2}{m_e} \frac{4\pi\varepsilon_0}{|e|} \approx 0.05292$ nm.

[49] Atomic Data for Ytterbium (Yb), *NIST Handbook of Basic Atomic Spectroscopic Data*.

[50] M. S. Safronova, S. G. Porsev, and C. W. Clark, Phys. Rev. Lett. **109**, 230802 (2012).

[51] An estimation of the numerical error occurred in our calculations is discussed in Appendix E.

[52] M. Theis, G. Thalhammer, K. Winkler, M. Hellwig, G. Ruff, R. Grimm, and J. H. Denschlag, Phys. Rev. Lett. **93**, 123001 (2004).

[53] G. Thalhammer, M. Theis, K. Winkler, R. Grimm, and J. H. Denschlag, Phys. Rev. A **71**, 033403 (2005).

[54] K. Enomoto, K. Kasa, M. Kitagawa, and Y. Takahashi, Phys. Rev. Lett. **101**, 203201 (2008).

[55] K. Ono, J. Kobayashi, Y. Amano, K. Sato, and Y. Takahashi, Phys. Rev. A **99**, 032707 (2019).

[56] O. Bettermann, N. D. Oppong, G. Pasqualetti, L. Riegger, I. Bloch, and S. Fölling, arXiv:2003.10599v1.

[57] E. G. M. v. Kempen, B. Marcelis, and S. J. J. M. F. Kokkelmans, Phys. Rev. A **70**, 050701(R) (2004).

[58] R. Zhang, Y. Cheng, H. Zhai, and P. Zhang, Phys. Rev. Lett **115**, 135301 (2015).

[59] M. Höfer, L. Riegger, F. Scazza, C. Hofrichter, D. R. Fernandes, M. M. Parish, J. Levinsen, I. Bloch, and S. Fölling, Phys. Rev. Lett **115**, 265302 (2015).

[60] J. R. Taylor, *Scattering Theory: The Quantum Theory of Nonrelativistic Collisions* (Dover, New York, 2006).

# Cooper problem in a cuprate lattice

Ali Sanayei[1, 2, *] and Ludwig Mathey[1, 2, 3, †]

[1]*Zentrum für Optische Quantentechnologien, Universität Hamburg,*
*Luruper Chaussee 149, D-22761 Hamburg, Germany*
[2]*Institut für Laserphysik, Universität Hamburg, Luruper Chaussee 149, D-22761 Hamburg, Germany*
[3]*The Hamburg Centre for Ultrafast Imaging, Luruper Chaussee 149, D-22761 Hamburg, Germany*
(Dated: August 3, 2020)

We solve the Cooper problem in a cuprate lattice. We determine the ground state of a Cooper pair for strongly repulsive on-site interactions, and demonstrate *a priori* that the corresponding wave function supports an orbital symmetry of $d_{x^2-y^2}$. We also show that the next-nearest-neighbor hopping changes the curvature of the dispersive bands, resulting in a Fermi-surface geometry that is in better agreement with experiments. We also propose a scenario to observe an experimental signature of the $d$-wave Cooper pairs for a cold-atom system in a cuprate lattice.

## I. INTRODUCTION

A cuprate lattice is a two-dimensional Lieb lattice that is characterized by a square unit cell with three sites and a sufficiently large charge-transfer energy [1–4]; see Fig. 1. The single-particle energy spectrum of the lattice reveals two dispersive bands and one flat band in between. A large charge-transfer energy provides a gap between the dispersive upper band and the other two bands; see Figs. 2(a) and 2(c). Technical advances in the cooling and trapping of atoms [5, 6] have led to engineer the square lattice via optical lattices [7–9], photonics [10], and cold atoms [11, 12]. The material realization of the lattice has also been proposed in a covalent-organic framework [13, 14]. These experimental realizations provide useful platforms to study and examine the phenomena occurring in a flat band or in a three-band structure [15–22]. An important application of the cuprate lattice is to describe the atomic configuration of a copper-oxide, $CuO_2$, plane. It is a layer of Cu and O atoms that are arranged in a square unit cell, where the three sites include one $d_{x^2-y^2}$ orbital configuration representing the Cu, and two $p_x$ and $p_y$ orbitals representing two oxygens; see Fig. 1.

The $CuO_2$ plane is also the basic structural unit of the high-temperature cuprate superconductors [4]. It is accepted that superconductivity in cuprates is due to the Cooper pairs that occur independently in different $CuO_2$ planes [23–26]. However, the main mechanism of the pairing is still under debates. There are arguments in favor of the electron-phonon interactions as the main pairing mechanism [27–31]. On the contrary, the orbital $d$-wave symmetry of the order parameter supports the counterarguments in favor of the antiferromagnetic magnons [32, 33] or plasmons [34–37].

The Cooper problem and its solution assume an effective electron-electron attraction due to the dominance of the electron-phonon interaction over the screened

Coulomb repulsion, leading to a Cooper pair with an orbital $s$-wave symmetry [4, 38–42]. However, in high-temperature cuprate superconductors the order parameter supports an orbital $d$-wave symmetry, originating mostly from the strong electron-electron repulsion; see, e.g., Refs. [43–45].

Experimental data reveal that cuprates at exact stoichiometry is almost not a superconductor. The superconducting regime is achieved by doping the system, i.e., by injecting holes into a $CuO_2$ plane [3, 4]. Extracted data from the angle-resolved photoemission spectroscopy (ARPES) show that the geometry of the Fermi surface for a $CuO_2$ plane is dependent on the doping. By changing the hole doping the Fermi surface can be deformed from being quite rounded to the form of a square near the half-filling with vanishing hole doping. The desired geometry of the Fermi surface in high-temperature cuprate superconductors consists of four Fermi arcs, revealing nodal and antinodal regions [3, 4, 44, 46–51]; see Fig. 2(b) and 2(d). Following P. W. Anderson, this can be realized to a first approximation by an effectively single-band two-dimensional Fermi-Hubbard model; see, e.g., Refs. [25, 52]. This implies that the Fermi surface not only depends on the hole doping, but it also varies slightly if the on-site Coulomb interaction strength, $U_C$, changes. Here the notion of the interacting- and noninteracting Fermi sea corresponds to $U_C = 0$ and $U_C \neq 0$, respectively.

The ground state of a Cooper pair in a $CuO_2$ plane has been considered by different approaches. The ground-state solution of the Fermi-Hubbard, $t$-$J$, $t$-$J$-$U$, and Hatsugai-Kohmoto model was found by variational calculations [45, 53–55]. The other approaches are, for example, based on the density matrix embedding theory [56, 57], constrained path auxiliary field Monte Carlo [58], the tensor network wave function ansatz [59], density matrix renormalization group method [60], and dynamical mean-field theory combined with the fluctuation exchange approximation [61]. We notice that in many calculations, an orbital $d$-wave symmetry of the order parameter has been considered *a posteriori* to follow the experiments.

In this paper we solve the Cooper problem in a cuprate

* asanayei@physnet.uni-hamburg.de
† lmathey@physnet.uni-hamburg.de
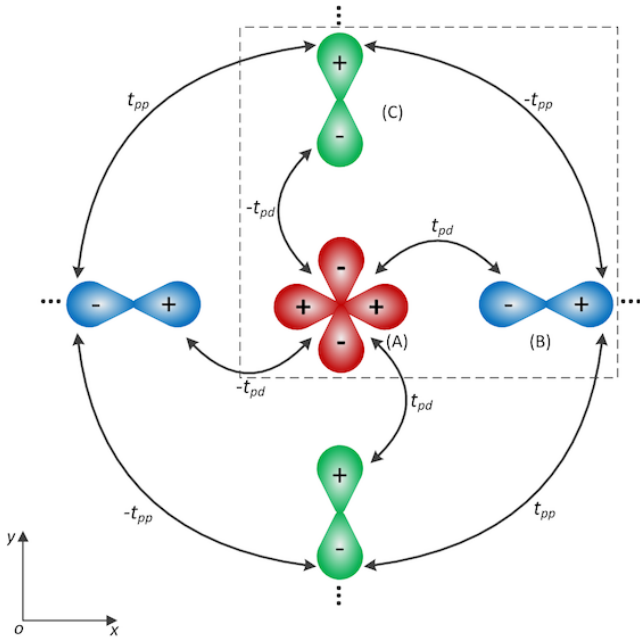
Figure 1. Sketch of the two-dimensional cuprate lattice in real space. The unit cell is shown by a dashed square, including a $d_{x^2-y^2}$ orbital configuration on A-site, a $p_x$ orbital on B-site, and a $p_y$ orbital on C-site. The nearest-neighbor hopping is shown by $t_{pd}$ and the next-nearest-neighbor hopping is shown by $t_{pp}$.

lattice. While the Cooper problem is usually considered as a weak-coupling limit to describe an electron pair, here we present an example that includes the repulsive strong-coupling regime. We determine the ground-state solution and the orbital symmetry of a Cooper pair *a priori*. To do this, first we consider the Fermi-Hubbard Hamiltonian in a single upper band of the cuprate lattice; cf. Figs. 1 and 2. We show that the next-nearest-neighbor hopping, $t_{pp}$, provides a better agreement of the Fermi-surface geometry with the extracted data from ARPES. We demonstrate that with $t_{pp} \neq 0$ we can vary the curvature of the Fermi arcs, and capture the desired Fermi-surface geometry for a larger hole doping [62]. Next, we consider the singlet Cooper-pair wave function on a submanifold $\mathcal{S}$, where the total momentum of a pair is vanishing. We do not consider further constraints, and do not assume any feature of the orbital $d$-wave symmetry on the ground-state solution. We constitute an eigenequation describing a Cooper pair, and solve it numerically. We demonstrate that the ground-state solution supports an orbital symmetry of $d_{x^2-y^2}$. We find a largest absolute value of the ground-state energy of a Cooper pair corresponding to a critical temperature within the order of 100 K. Finally, we discuss an experimental signature of the $d$-wave Cooper pairs for a cold-atom system in a cuprate lattice using the techniques of time-of-flight image and noise correlations.

This paper is organized as follows. In Sec. II we calcu-

late the electronic band structure of the cuprate lattice for $t_{pp} \neq 0$. We define the interacting Fermi sea, and demonstrate the effect of $t_{pp}$ on the Fermi-surface geometry. In Sec. III we consider the Cooper problem, and derive an eigenequation describing a Cooper pair on the submanifold $\mathcal{S}$ of the upper band. In Sec. IV we calculate the ground-state energy and wave function, and determine its orbital symmetry. In Sec. V we propose a signature of the $d$-wave Cooper pairs for a cold-atom system in a cuprate lattice. Finally, in Sec. VI we present the concluding remarks.

## II. ELECTRONIC BAND STRUCTURE AND FERMI-HUBBARD MODEL

For our lattice configuration with three sites A, B, and C in the square unit cell, see Fig. 1, we assume the on-site energies to be $V_A \equiv V_d$ and $V_B = V_C \equiv V_p$. We also define three sets of creation and annihilation operators $\{a_{nm}^\dagger, a_{nm}\}$, $\{b_{nm}^\dagger, b_{nm}\}$, $\{c_{nm}^\dagger, c_{nm}\}$ corresponding to the A-, B-, and C-site, respectively, where the indices $n$ and $m$ refer to the $x$- and $y$ direction in real space. These operators fulfill the fermionic algebra, and we refer to them further as site operators.

The spinless tight-binding Hamiltonian in momentum space is

$$\hat{H}_{\text{tb}} = \sum_{\mathbf{k} \in 1.\text{BZ}} \begin{pmatrix} a_{\mathbf{k}}^\dagger & b_{\mathbf{k}}^\dagger & c_{\mathbf{k}}^\dagger \end{pmatrix} \text{h}_{\text{tb}} \begin{pmatrix} a_{\mathbf{k}} \\ b_{\mathbf{k}} \\ c_{\mathbf{k}} \end{pmatrix}, \qquad (1)$$

for all momentum points $\mathbf{k} = (k_x, k_y)$ within the first Brillouin zone (1.BZ), where $k_x, k_y \in [-\pi/a, \pi/a)$ and $a$ denotes the lattice constant. The matrix $\text{h}_{\text{tb}}$ is

$$\text{h}_{\text{tb}} = \begin{pmatrix} V_d & f(k_x) & -g(k_y) \\ f^*(k_x) & V_p & -\tau f^*(k_x) g(k_y) \\ -g^*(k_y) & -\tau f(k_x) g^*(k_y) & V_p \end{pmatrix},$$
$$(2)$$

where $f(k_x) = t_{pd}(1 - e^{-ik_x})$, $g(k_y) = t_{pd}(1 - e^{-ik_y})$, and $\tau = t_{pp}/t_{pd}^2$. The parameters $t_{pd}$ and $t_{pp}$ show the nearest-neighbor and next-nearest-neighbor hopping, respectively. The functions $f^*$ and $g^*$ denote the complex conjugate of $f$ and $g$, respectively; see Appendix A.

The characteristic equation of the matrix $\text{h}_{\text{tb}}$ is cubic with three solutions $E_{\mathbf{k}}^{(U)}$, $E_{\mathbf{k}}^{(F)}$, and $E_{\mathbf{k}}^{(L)}$, that exhibit the electronic band structure of the lattice; see Appendix B for analytical solutions. Here the index U, F, and L stands for the upper-, flat-, and lower band, respectively. Figures 2(a) and 2(c) show the band structure for vanishing and nonvanishing $t_{pp}$, respectively. For both cases there are two dispersive bands $E_{\mathbf{k}}^{(U)}$ and $E_{\mathbf{k}}^{(L)}$. For $t_{pp} = 0$ there is a completely flat band, $E_{\mathbf{k}}^{(F)} = V_p$, between $E_{\mathbf{k}}^{(U)}$ and $E_{\mathbf{k}}^{(L)}$. However, for $t_{pp} \neq 0$ we find that the flat band is deformed, and the curvature of the dispersive bands is changed.
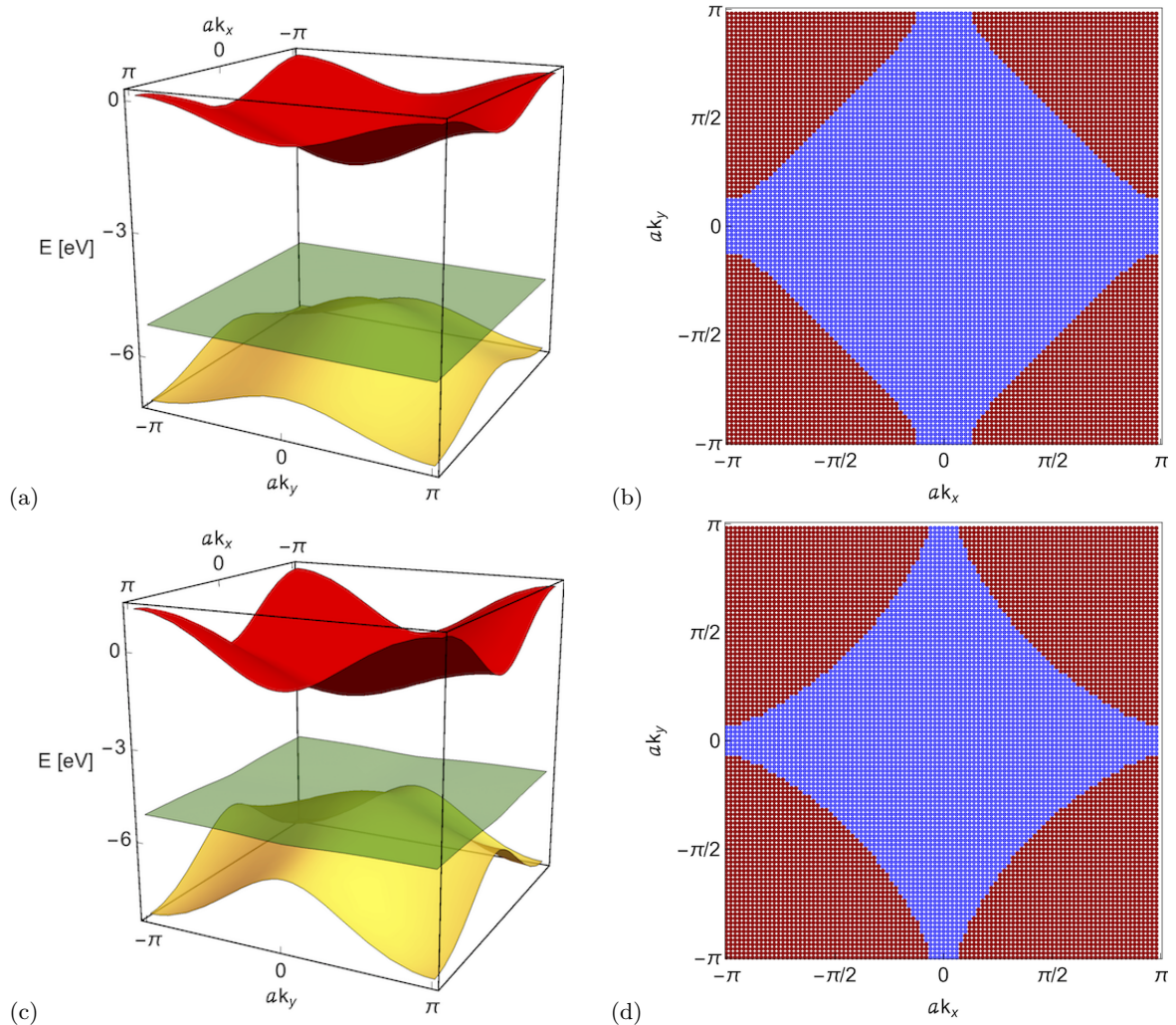
Figure 2. Electronic band structure and Fermi surface of a cuprate lattice in the first Brillouin zone for $V_{dp} = 3.45$ eV and $t_{pd} = 1.13$ eV: (a) Band structure for $t_{pp} = 0$; (b) the corresponding Fermi surface for $\mu \approx -0.679$ eV; (c) band structure for $t_{pp} = 0.8$ eV; and (d) the corresponding Fermi surface for $\mu \approx -0.679$ eV. For $t_{pp} \neq 0$ the flat band is deformed, and the curvature of the dispersive bands is changed. Blue and red dots in panels (b) and (d) correspond to the occupied and unoccupied states, respectively.

To constitute the Fermi-Hubbard Hamiltonian for a CuO$_2$ plane on a single upper band, first we note that here we are primarily interested in a submanifold $\mathcal{S}$, where the total momentum of an electron-pair vanishes. To find the interacting part of the Fermi-Hubbard model, we define three sets of creation and annihilation operators corresponding to each band as $\{\psi^\dagger_{\mathrm{U},\mathbf{k}\sigma}, \psi_{\mathrm{U},\mathbf{k}\sigma}\}$, $\{\psi^\dagger_{\mathrm{F},\mathbf{k}\sigma}, \psi_{\mathrm{F},\mathbf{k}\sigma}\}$, and $\{\psi^\dagger_{\mathrm{L},\mathbf{k}\sigma}, \psi_{\mathrm{L},\mathbf{k}\sigma}\}$, where $\sigma \in \{\uparrow, \downarrow\}$ is a spin index. These operators fulfill the fermionic algebra, and create or annihilate an electron in the the upper-, flat-, and lower band, respectively. In the following we refer to them as band operators. The band operators can be related to the site operators using the components of the eigenvectors of the matrix $h_{\mathrm{tb}}$; see Appendix C. We assume that the charge-transfer energy, $V_{dp} \equiv V_d - V_p$, is sufficiently large so that we neglect the interband pair-

ings; cf. Figs. 2(a) and 2(c). We find the interaction Hamiltonian on the submanifold $\mathcal{S}$ of the upper band to be

$$\hat{H}_{\mathrm{int}} = \frac{1}{\mathcal{A}} \sum_{\mathbf{k},\mathbf{k}' \in 1.\mathrm{BZ}} \mathcal{V}_{\mathbf{k},\mathbf{k}'} \psi^\dagger_{\mathrm{U},\mathbf{k}'\downarrow} \psi^\dagger_{\mathrm{U},-\mathbf{k}'\uparrow} \psi_{\mathrm{U},-\mathbf{k}\uparrow} \psi_{\mathrm{U},\mathbf{k}\downarrow}; \quad (3)$$

see Appendix C for derivation. Here, $\mathcal{A}$ denotes the area of the first Brillouin zone and the interaction function $\mathcal{V}_{\mathbf{k},\mathbf{k}'}$ is

$$\mathcal{V}_{\mathbf{k},\mathbf{k}'} = U_d \mathcal{V}^{(d)}_{\mathbf{k},\mathbf{k}'} + U_p \left( \mathcal{V}^{(p_x)}_{\mathbf{k},\mathbf{k}'} + \mathcal{V}^{(p_y)}_{\mathbf{k},\mathbf{k}'} \right), \quad (4)$$

where the functions $\mathcal{V}^{(d)}_{\mathbf{k},\mathbf{k}'}$, $\mathcal{V}^{(p_x)}_{\mathbf{k},\mathbf{k}'}$, and $\mathcal{V}^{(p_y)}_{\mathbf{k},\mathbf{k}'}$ are derived in Appendix C. The on-site Coulomb interaction strength
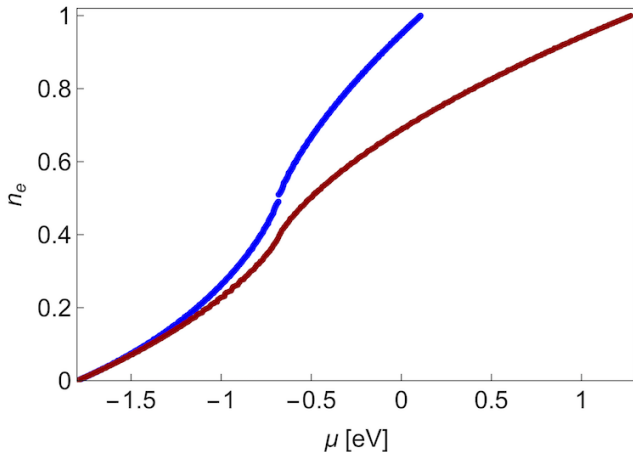
Figure 3. Electron density, $n_e$, vs chemical potential, $\mu$, in units of eV, for a single upper band of the cuprate lattice, where $V_{dp} = 3.45$ eV and $t_{pd} = 1.13$ eV. The blue curve corresponds to $t_{pp} = 0$, and the red curve corresponds to $t_{pp} = 0.8$ eV. For a given value of $\mu$, we have $n_e(t_{pp} \neq 0) \leqslant n_e(t_{pp} = 0)$.

for $d_{x^2-y^2}$ orbital configuration is $U_d$, and for both $p_x$ and $p_y$ is $U_p$.

Next, we define the Fermi sea by introducing a chemical potential, $\mu$. We define the interacting Fermi sea, $\mathrm{FS_{int}}$, as the momentum space occupied by electrons:

$$\mathrm{FS_{int}} = \left\{ \mathbf{k} \in 1.\mathrm{BZ} : 2E_{\mathbf{k}}^{(\mathrm{U})} + \frac{1}{\mathcal{A}} \mathcal{V}_{\mathbf{k},\mathbf{k}} < 2\mu \right\}, \quad (5)$$

where the interaction function $\mathcal{V}_{\mathbf{k},\mathbf{k}}$ is obtained as Eq. (4) for $\mathbf{k}' = \mathbf{k}$. The unoccupied region where an electron-pair can form is defined as the first Brillouin zone where the Fermi sea has been excluded; i.e., $\mathbf{k} \in 1.\mathrm{BZ} \backslash \mathrm{FS_{int}}$. Figures 2(b) and 2(d) show the interacting Fermi surface for $t_{pp} = 0$ and $t_{pp} \neq 0$, respectively. The nonvanishing $t_{pp}$ changes the curvature of the dispersive bands, resulting in a Fermi-surface geometry that is in better agreement with the experimental data extracted from ARPES [3, 4, 44, 46–51]. Moreover, we vary $\mu$ and calculate the corresponding electron density, $n_e$, for both $t_{pp} = 0$ and $t_{pp} \neq 0$, resulting in Fig. 3. For a given value of $\mu$ we find that $n_e(t_{pp} \neq 0) \leqslant n_e(t_{pp} = 0)$. As a result, while the desired geometry of the Fermi surface is preserved, we can increase the hole doping for $t_{pp} \neq 0$ [62].

Finally, we take into account the interacting Fermi sea and obtain the total Fermi-Hubbard Hamiltonian to be

$$\hat{H}_{\mathrm{tot}} = \sum_{\substack{\mathbf{k} \in 1.\mathrm{BZ} \backslash \mathrm{FS_{int}} \\ \sigma \in \{\uparrow, \downarrow\}}} \xi_{\mathbf{k}}^{(\mathrm{U})} \psi_{\mathrm{U},\mathbf{k}\sigma}^{\dagger} \psi_{\mathrm{U},\mathbf{k}\sigma} + \frac{1}{\mathcal{A}}$$
$$\times \sum_{\mathbf{k},\mathbf{k}' \in 1.\mathrm{BZ} \backslash \mathrm{FS_{int}}} \mathcal{V}_{\mathbf{k},\mathbf{k}'} \psi_{\mathrm{U},\mathbf{k}'\downarrow}^{\dagger} \psi_{\mathrm{U},-\mathbf{k}'\uparrow}^{\dagger} \psi_{\mathrm{U},-\mathbf{k}\uparrow} \psi_{\mathrm{U},\mathbf{k}\downarrow},$$
$$(6)$$

where $\xi_{\mathbf{k}}^{(\mathrm{U})} = E_{\mathbf{k}}^{(\mathrm{U})} - \mu$ and $\mathcal{V}_{\mathbf{k},\mathbf{k}'}$ is given by Eq. (4); see Appendix C.

## III. COOPER PROBLEM AND PAIRING EQUATION

The original Cooper problem and its solution show that two electrons that are immersed in an inert Fermi sea form a bound state with an orbital $s$-wave symmetry for an arbitrarily weak attractive interaction [4, 38–42]. The effective attraction is due to the electron-phonon interaction that is dominant over the screened Coulomb repulsion. The interaction is modeled as a negative coupling constant in momentum space for the relative kinetic energy of the electrons smaller than the Debye energy. The Cooper problem is usually considered as a weak-coupling limit of an electron pairing. However, experimental data as well as various theoretical results reveal that the Cooper pairing in a cuprate lattice is mainly due to the strongly repulsive electron-electron interactions; see, e.g. Refs. [43–45]. Our objective is to show an example of the Cooper problem that includes the strong-coupling limit of the repulsive on-site interactions for the single-band Fermi-Hubbard model (6). To this end, we follow the Cooper problem, cf. e.g., Refs. [38, 41, 42], and consider a singlet-state Cooper pair as

$$|\Phi\rangle = \sum_{\boldsymbol{\kappa} \in 1.\mathrm{BZ} \backslash \mathrm{FS_{int}}} \phi(\boldsymbol{\kappa}) \psi_{\mathrm{U},\boldsymbol{\kappa}\uparrow}^{\dagger} \psi_{\mathrm{U},-\boldsymbol{\kappa}\downarrow}^{\dagger} |\mathrm{FS_{int}}\rangle, \quad (7)$$

where $\phi(\boldsymbol{\kappa})$ is the wave function of the Cooper pair in momentum space and $|\mathrm{FS_{int}}\rangle$ denotes the interacting Fermi-sea state; cf. Eq. (5).

To find the ground-state energy and wave function, we constitute the eigenvalue problem

$$\hat{H}_{\mathrm{tot}} |\Phi\rangle = \mathcal{E} |\Phi\rangle, \quad (8)$$

where $\mathcal{E}$ is the eigenenergy. We calculate the resulting operator $\hat{H}_{\mathrm{tot}} |\Phi\rangle$, see Appendix D, and obtain an eigenequation describing the Cooper pair:

$$\left( \xi_{\mathbf{k}}^{(\mathrm{U})} + \xi_{-\mathbf{k}}^{(\mathrm{U})} + \frac{1}{\mathcal{A}} \mathcal{V}_{\mathbf{k},\mathbf{k}} - \mathcal{E} \right) \phi(\mathbf{k})$$
$$= -\frac{1}{\mathcal{A}} \sum_{\substack{\mathbf{k},\mathbf{k}' \in 1.\mathrm{BZ} \backslash \mathrm{FS_{int}} \\ \mathbf{k}' \neq \mathbf{k}}} \mathcal{V}_{\mathbf{k},\mathbf{k}'} \phi(\mathbf{k}'); \quad (9)$$

see Appendix D. In what fallows we solve Eq. (9) numerically, and determine the ground-state energy, $E_{\mathrm{G}} < 0$.

## IV. GROUND-STATE ENERGY AND WAVE FUNCTION

To solve Eq. (9) numerically, first we discretize the first Brillouin zone as $\mathbf{k}_j = (k_x^{(j)}, k_y^{(j)})$, where
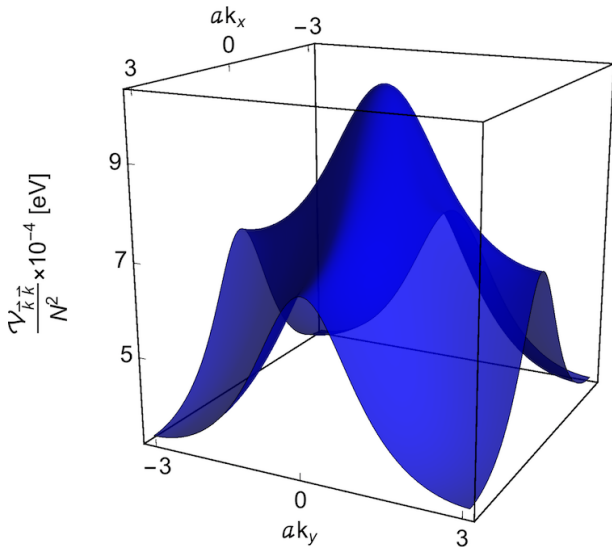
Figure 4. Interaction function $\mathcal{V}_{\mathbf{k},\mathbf{k}}/N^2$ in units of eV, cf. Eq. (4), for the strong-coupling limit of the Fermi-Hubbard model (6) and repulsive on-site interactions, where $N = 100$, $V_{dp} = 3.45$ eV, $t_{pd} = 1.13$ eV, $t_{pp} = 0.8$ eV, $U_d = 10.3$ eV, and $U_p = 4.1$ eV.



Figure 5. Ground-state wave function, $\phi(ak_x, ak_y)$, of a Cooper pair for $N = 100$, $V_{dp} = 3.45$ eV, $t_{pd} = 1.13$ eV, $t_{pp} = 0.8$ eV, $U_d = 10.3$ eV, $U_p = 4.1$ eV, and the hole doping $\delta_h \approx 0.104$, where $a$ denotes the lattice constant. The nodal points are visible along the Fermi arcs. The Blue color corresponds to the values with zero phase, and the red color corresponds to the values with the phase $\pi$. The orbital symmetry of the wave function is $d_{x^2-y^2}$.

$$k_x^{(j)}, k_y^{(j)} = \frac{1}{a}\left[-\pi + \frac{2\pi}{N}(j-1)\right] \ \ \text{for } j = 1, 2, \ldots, N. \ (10)$$

Here, $a$ denotes the lattice constant and $N \in \mathbb{N}$ is the number of the grid points in $x$- and $y$ direction, i.e., $N_x = N_y = N$. With this, we calculate the electronic band structure numerically, and find the interaction function $\mathcal{V}_{\mathbf{k},\mathbf{k}'}$ at each grid point using Eq. (4). Next, for a given value of $\mu$ we determine the Fermi surface following the relation (5). We note that the number of the grid points within the first Brillouin zone is proportional to $N_x N_y = N^2$. The size of the matrix associated with $\hat{H}_{\text{tot}}$ is proportional to $N^4$, cf. Eq. (6), that increases drastically by increasing the number of the grid points. In order to stabilize the numerical calculation, the number of the grid points should be sufficiently large. For that, we calculate the Fermi surface numerically, and exclude it from the first Brillouin zone. We constitute $\hat{H}_{\text{tot}}$ on the reduced momentum space that corresponds to the unoccupied states; see Appendix E.

As expected, we find that the ground-state solution for the attractive regime, $U_d, U_p < 0$, tends to a Cooper pair supporting an orbital $s$-wave symmetry; see Appendix F.

For strongly repulsive on-site interactions, $U_d, U_p > 0$, $U_d/t_{pd} \gg 1$, the interaction function $\mathcal{V}_{\mathbf{k},\mathbf{k}}$, cf. Eq. (4), has a concave structure; see Fig. 4. Here, the two electrons repel each other strongly and there is no tendency for the kinetic energy of the pair to be minimized. If the two electrons form a bound state, the geometry of the Fermi surface does not support an isotropic ground-state solution, preventing an orbital $s$-wave symmetry of the

wave function. For the lattice parameters $V_{dp} = 3.45$ eV, $t_{pd} = 1.13$ eV, and $t_{pp} = 0.8$ eV that follow approximately the values given by Ref. [45], Fig. 5 shows the ground-state wave function for the strongly repulsive regime. We find that the wave function of the Cooper pair reveals nodal points along the Fermi arcs. Here a nodal point partitions a Fermi arc into two regions with a phase shift of $\pi$. As a result, we find that the wave function supports an orbital symmetry of $d_{x^2-y^2}$.

Finally, we vary the hole doping, $\delta_h$, by changing the chemical potential, $\mu$ [62]. We calculate the corresponding ground-state energy, $E_{\text{G}}$, resulting in Fig. 6. It reveals that a largest absolute magnitude of the ground-state energy, $|E_{\text{G}}^{(\text{max})}| \sim 0.01$ eV, occurs near the hole doping $\delta_h \sim 0.35$. We also find that the critical temperature corresponding to $|E_{\text{G}}^{(\text{max})}|$ is within the order of 100 K. The behavior of the ground-state energy captures Ref. [45] qualitatively.

## V. EXPERIMENTAL SIGNATURE IN A COLD-ATOM SYSTEM

Going beyond high-temperature cuprate superconductors, we propose an experimental signature of the $d$-wave Cooper pairs for a cold fermion in a cuprate lattice. Here, a first step is to engineer the cuprate lattice using the optical lattices; cf., e.g., Refs. [7–9]. Next, the desired Fermi-surface geometry that includes Fermi arcs should
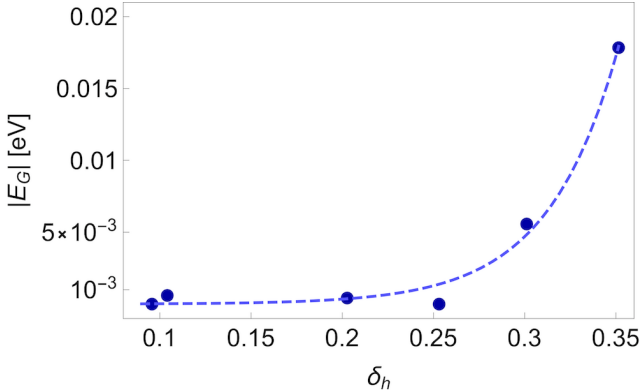
Figure 6. Ground-state energy $|E_\mathrm{G}|$ of a Cooper pair in units of eV vs hole doping, $\delta_h$ [62], where $N = 100$, $V_{dp} = 3.45$ eV, $t_{pd} = 1.13$ eV, $t_{pp} = 0.8$ eV, $U_d = 10.3$ eV, and $U_p = 4.1$ eV. A largest value of $|E_\mathrm{G}|$ corresponding to a critical temperature of the order of 100 K is obtained near the hole doping of 0.35.

be constructed using the techniques of time-of-flight image and noise correlations; see, e.g., Refs. [63–66]. Following the reasoning of the Cooper problem, for an atom with the momentum $\mathbf{k}$ and spin $\sigma$ in the ground state, there is another atom with the momentum $-\mathbf{k}$ and spin $-\sigma$, for which we consider the corresponding density operators $\hat{n}(\mathbf{k}, \sigma)$ and $\hat{n}(-\mathbf{k}, -\sigma)$. The time-of-flight image of a cold-atom system is performed when the optical trap is turned off and the atoms fall freely in gravity for a certain time, if the system is dilute and the interactions are far from the resonance. After a sufficiently long time of flight, this provides a single realization of the momentum density $\langle\hat{n}(\mathbf{k}, \sigma)\rangle$ and $\langle\hat{n}(-\mathbf{k}, -\sigma)\rangle$. As a result, to construct the interacting Fermi sea and to determine the orbital symmetry of a Cooper pair, a time-of-flight image is not merely adequate. For that, the density-density correlation $\langle\hat{n}(\mathbf{k}, \sigma)\hat{n}(-\mathbf{k}, -\sigma)\rangle$ can be measured at a temperature $T > 0$ around the Fermi surface using the technique of noise correlations, resulting in an enhanced correlation for a Cooper pair. The behavior of the enhanced correlation can be considered as a probe of the regime where a Cooper pair is formed [65], leading to an estimate of the binding energy. Detecting higher angular harmonics in the correlation measurement will be the signature of a higher angular symmetry of the Cooper pair.

## VI.   CONCLUSIONS

In conclusion, we have solved the Cooper problem in a cuprate lattice for strongly repulsive on-site interactions. We have derived an equation describing a Cooper pair in a single-band Fermi-Hubbard model, and have calculated the ground-state solution *a priori*. We have demonstrated that the ground-state wave function reveals nodal points along the Fermi arcs, supporting an orbital symmetry of $d_{x^2-y^2}$. We have shown that the next-nearest-

neighbor hopping, $t_{pp}$, deforms the flat band and changes the curvature of the dispersive bands. As a result, we have found that the geometry of the Fermi surface for $t_{pp} \neq 0$ is in better agreement with experimental data. This implies that we can achieve a larger hole doping while the desired Fermi-surface geometry is preserved. We have also calculated the ground-state energy for different values of the hole doping, and have found that a largest absolute value of the energy corresponds to a critical temperature of the order of 100 K. Furthermore, and going beyond high-temperature cuprate superconductors, we have proposed an experimental signature of the $d$-wave Cooper pairs for a cold fermion in a cuprate lattice using the techniques of time-of-flight image and noise correlations.

## APPENDIX A. DERIVATION OF THE TIGHT-BINDING HAMILTONIAN (1)

We consider the cuprate lattice, see Fig. 1, and write the spinless tight-binding Hamiltonian in terms of the site operators in real space:

$$
\begin{aligned}
\hat{H}_\mathrm{tb} = \sum_{nm} \Big[ & V_d a^\dagger_{nm} a_{nm} + V_p b^\dagger_{nm} b_{nm} + V_d c^\dagger_{nm} c_{nm} \\
& + t_{pd} a^\dagger_{nm} b_{nm} + t_{pd} b^\dagger_{nm} a_{nm} - t_{pd} a^\dagger_{nm} c_{nm} \\
& - t_{pd} c^\dagger_{nm} a_{nm} - t_{pd} a^\dagger_{nm} b_{n-1,m} - t_{pd} b^\dagger_{n-1,m} a_{nm} \\
& + t_{pd} a^\dagger_{nm} c_{n,m-1} + t_{pd} c^\dagger_{n,m-1} a_{nm} - t_{pp} b^\dagger_{nm} c_{nm} \\
& - t_{pp} c^\dagger_{nm} b_{nm} + t_{pp} c^\dagger_{nm} b_{n-1,m} + t_{pp} b^\dagger_{n-1,m} c_{nm} \\
& - t_{pp} b^\dagger_{n-1,m} c_{n,m-1} - t_{pp} c^\dagger_{n,m-1} b_{n-1,m} \\
& + t_{pp} b^\dagger_{n,m} c_{n,m-1} + t_{pp} c^\dagger_{n,m-1} b_{n,m} \Big],
\end{aligned} \tag{A1}
$$

where $n$ and $m$ are two indices for the $x$- and $y$ direction, respectively. Next, we take the Fourier transform of each operator, and obtain the tight-binding Hamiltonian in momentum space:

$$\hat{H}_{\mathrm{tb}} = \sum_{\mathbf{k} \in 1.\mathrm{BZ}} \Big[ V_d a_{\mathbf{k}}^{\dagger} a_{\mathbf{k}} + V_p b_{\mathbf{k}}^{\dagger} b_{\mathbf{k}} + V_d c_{\mathbf{k}}^{\dagger} c_{\mathbf{k}}$$
$$+ t_{pd} a_{\mathbf{k}}^{\dagger} b_{\mathbf{k}} + t_{pd} b_{\mathbf{k}}^{\dagger} a_{\mathbf{k}} - t_{pd} a_{\mathbf{k}}^{\dagger} c_{\mathbf{k}}$$
$$- t_{pd} c_{\mathbf{k}}^{\dagger} a_{\mathbf{k}} - t_{pd} e^{-ik_x} a_{\mathbf{k}}^{\dagger} b_{\mathbf{k}} - t_{pd} e^{ik_x} b_{\mathbf{k}}^{\dagger} a_{\mathbf{k}}$$
$$+ t_{pd} e^{-ik_y} a_{\mathbf{k}}^{\dagger} c_{\mathbf{k}} + t_{pd} e^{ik_y} c_{\mathbf{k}}^{\dagger} a_{\mathbf{k}}$$
$$- t_{pp} \left( 1 - e^{ik_x} + e^{ik_x} e^{-ik_y} - e^{-ik_y} \right) b_{\mathbf{k}}^{\dagger} c_{\mathbf{k}}$$
$$- t_{pp} \left( 1 - e^{-ik_x} + e^{-ik_x} e^{ik_y} - e^{ik_y} \right) c_{\mathbf{k}}^{\dagger} b_{\mathbf{k}} \Big].$$
$$(\mathrm{A2})$$

Finally, we define $f(k_x) = t_{pd}(1 - e^{-ik_x})$, $g(k_y) = t_{pd}(1 - e^{-ik_y})$, and $\tau = t_{pp}/t_{pd}^2$, and arrive at Eq. (1).

## APPENDIX B. ANALYTICAL DESCRIPTION OF THE BAND STRUCTURE OF THE CUPRATE LATTICE

The characteristic equation associated with Eq. (2) reads as

$$s^3 + c(k_x, k_y) s^2 + d(k_x, k_y) s + e(k_x, k_y) = 0, \quad (\mathrm{B1})$$

where

$$c(k_x, k_y) = - V_d - 2V_p, \quad (\mathrm{B2})$$

$$d(k_x, k_y) = - |f(k_x)|^2 - |g(k_y)|^2 - \tau^2 |f(k_x)|^2 |g(k_y)|^2 + V_p^2 + 2V_d V_p, \quad (\mathrm{B3})$$

$$e(k_x, k_y) = V_p |f(k_x)|^2 + V_p |g(k_y)|^2 + \tau(\tau V_d - 2) \times |f(k_x)|^2 |g(k_y)|^2 - V_d V_p^2, \quad (\mathrm{B4})$$

and $\tau = t_{pp}/t_{pd}^2$. Next, we define a variable $S = s - c(k_x, k_y)/3$, and rewrite Eq. (B1) as

$$S^3 + 3p(k_x, k_y) S + 2q(k_x, k_y) = 0, \quad (\mathrm{B5})$$

where

$$p(k_x, k_y) = \frac{1}{3} d(k_x, k_y) - \frac{1}{9} [c(k_x, k_y)]^2, \quad (\mathrm{B6})$$

$$q(k_x, k_y) = \frac{1}{27} [c(k_x, k_y)]^3 - \frac{1}{6} c(k_x, k_y) d(k_x, k_y) + \frac{1}{2} e(k_x, k_y). \quad (\mathrm{B7})$$

Following the mathematical formalism represented in Ref. [67], we calculate the three roots of Eq. (B1), revealing the band structure of the cuprate lattice:

$$E_{\mathbf{k}}^{(\mathrm{U})} = 2\sqrt{-p(k_x, k_y)} \cos\left( \frac{\theta(k_x, k_y)}{3} \right) - \frac{c(k_x, k_y)}{3}, \quad (\mathrm{B8})$$

$$E_{\mathbf{k}}^{(\mathrm{F})} = 2\sqrt{-p(k_x, k_y)} \cos\left( \frac{\theta(k_x, k_y) + 4\pi}{3} \right) - \frac{c(k_x, k_y)}{3}, \quad (\mathrm{B9})$$

$$E_{\mathbf{k}}^{(\mathrm{L})} = 2\sqrt{-p(k_x, k_y)} \cos\left( \frac{\theta(k_x, k_y) + 2\pi}{3} \right) - \frac{c(k_x, k_y)}{3}, \quad (\mathrm{B10})$$

where $\cos\theta(k_x, k_y) = -q(k_x, k_y)/\sqrt{-[p(k_x, k_y)]^3}$; see Fig. 2(c). We note that for $t_{pp} = 0$, the three solutions (B8)-(B10) reduce to:

$$\tilde{E}_{\mathbf{k}}^{(\mathrm{U})} = \frac{V_d + V_p}{2} + 2t_{pd} \sqrt{\sin^2(\frac{k_x}{2}) + \sin^2(\frac{k_y}{2}) + \left( \frac{V_{dp}}{4t_{pd}} \right)^2}, \quad (\mathrm{B11})$$

$$\tilde{E}_{\mathbf{k}}^{(\mathrm{F})} = V_p, \quad (\mathrm{B12})$$

$$\tilde{E}_{\mathbf{k}}^{(\mathrm{L})} = \frac{V_d + V_p}{2} - 2t_{pd} \sqrt{\sin^2(\frac{k_x}{2}) + \sin^2(\frac{k_y}{2}) + \left( \frac{V_{dp}}{4t_{pd}} \right)^2}, \quad (\mathrm{B13})$$

respectively; see Fig. 2(a). By comparing Eqs. (B8)-(B13) we find that the next-nearest-neighbor hopping, $t_{pp}$, deforms the flat band $E_{\mathbf{k}}^{(\mathrm{F})}$, and changes the curvature of the dispersive bands $E_{\mathbf{k}}^{(\mathrm{U})}$ and $E_{\mathbf{k}}^{(\mathrm{L})}$.

## APPENDIX C. DERIVATION OF THE HAMILTONIANS (3) AND (6)

For the cuprate lattice, see Fig. 1, the interaction Hamiltonian of the Fermi-Hubbard model reads in general as

$$\hat{\tilde{H}}_{\mathrm{int}} = \frac{U_{\mathrm{C}}}{\mathcal{A}} \sum_{\mathbf{k}, \mathbf{p}, \mathbf{q} \in 1.\mathrm{BZ}} \alpha_{\mathbf{k}+\mathbf{q},\downarrow}^{\dagger} \alpha_{\mathbf{p}-\mathbf{q},\uparrow}^{\dagger} \alpha_{\mathbf{p},\uparrow} \alpha_{\mathbf{k}\downarrow}, \quad (\mathrm{C1})$$

where $\alpha^{\dagger} \in \{a^{\dagger}, b^{\dagger}, c^{\dagger}\}$ and $\alpha \in \{a, b, c\}$ denote the creation and annihilation site operators, respectively, $\mathbf{q}$ is the momentum transfer [68], and $U_{\mathrm{C}}$ is an on-site Coulomb interaction strength. We notice that for each

eigenvalue of $h_{tb}$, cf. Eq. (2), there exists a corresponding normalized eigenvector, which we denote as $\mathbf{v}_{\mathbf{k}}^{(U)} = (v_{\mathbf{k}}^{(1;U)}, v_{\mathbf{k}}^{(2;U)}, v_{\mathbf{k}}^{(3;U)})$, $\mathbf{v}_{\mathbf{k}}^{(F)} = (v_{\mathbf{k}}^{(1;F)}, v_{\mathbf{k}}^{(2;F)}, v_{\mathbf{k}}^{(3;F)})$, and $\mathbf{v}_{\mathbf{k}}^{(L)} = (v_{\mathbf{k}}^{(1;L)}, v_{\mathbf{k}}^{(2;L)}, v_{\mathbf{k}}^{(3;L)})$. The index U, F, and L corresponds to the upper-, flat-, and lower band, respectively. The site operators can be related to the band operators using the following relation:

$$
\begin{pmatrix} a_{\mathbf{k}\sigma}^{\dagger} \\ b_{\mathbf{k}\sigma}^{\dagger} \\ c_{\mathbf{k}\sigma}^{\dagger} \end{pmatrix} = \begin{pmatrix} v_{\mathbf{k}}^{(1;U)} & v_{\mathbf{k}}^{(2;U)} & v_{\mathbf{k}}^{(3;U)} \\ v_{\mathbf{k}}^{(1;F)} & v_{\mathbf{k}}^{(2;F)} & v_{\mathbf{k}}^{(3;F)} \\ v_{\mathbf{k}}^{(1;L)} & v_{\mathbf{k}}^{(2;L)} & v_{\mathbf{k}}^{(3;L)} \end{pmatrix}^{-1} \begin{pmatrix} \psi_{U,\mathbf{k}\sigma}^{\dagger} \\ \psi_{F,\mathbf{k}\sigma}^{\dagger} \\ \psi_{L,\mathbf{k}\sigma}^{\dagger} \end{pmatrix}
$$

$$
\equiv \begin{pmatrix} v_{11}(\mathbf{k}) & v_{12}(\mathbf{k}) & v_{13}(\mathbf{k}) \\ v_{21}(\mathbf{k}) & v_{22}(\mathbf{k}) & v_{23}(\mathbf{k}) \\ v_{31}(\mathbf{k}) & v_{32}(\mathbf{k}) & v_{33}(\mathbf{k}) \end{pmatrix} \begin{pmatrix} \psi_{U,\mathbf{k}\sigma}^{\dagger} \\ \psi_{F,\mathbf{k}\sigma}^{\dagger} \\ \psi_{L,\mathbf{k}\sigma}^{\dagger} \end{pmatrix}.
$$

$$(C2)$$

We can rewrite the interaction Hamiltonian (C1) corresponding to three sites A, B, and C in terms of the band operators using the relation (C2). We recall that here we are primarily interested in a submanifold $\mathcal{S}$, where the total momentum of an electron-pair is vanishing. Because we are interested in the effective Fermi-Hubbard model constituted in the upper band, we prevent the interband pairings as well as the pairings in the flat- and lower band. We write the three interaction Hamiltonians corresponding to $d_{x^2-y^2}$, $p_x$, and $p_y$ orbital configurations on the submanifold $\mathcal{S}$ of the upper band in terms of the band operators:

$$
\hat{H}_{int}^{(\Omega)} = \frac{U_{\Omega}}{\mathcal{A}} \sum_{\mathbf{k},\mathbf{k}' \in 1.BZ} \mathcal{V}_{\mathbf{k},\mathbf{k}'}^{(\Omega)} \psi_{U,\mathbf{k}\downarrow}^{\dagger} \psi_{U,-\mathbf{k}'\uparrow}^{\dagger} \psi_{U,-\mathbf{k}\uparrow} \psi_{U,\mathbf{k}\downarrow},
$$

$$(C3)$$

where the label $\Omega$ denotes an orbital configuration which can be $d \equiv d_{x^2-y^2}$, $p_x$, and $p_y$. The on-site Coulomb interaction strengths for $d_{x^2-y^2}$ and $p_x$ ($p_y$) orbitals are assumed to be $U_d$ and $U_p$, respectively, and the interaction functions are

$$
\mathcal{V}_{\mathbf{k},\mathbf{k}'}^{(d)} = v_{11}(\mathbf{k}') v_{11}(-\mathbf{k}') v_{11}^*(-\mathbf{k}) v_{11}^*(\mathbf{k}), \qquad (C4)
$$

$$
\mathcal{V}_{\mathbf{k},\mathbf{k}'}^{(p_x)} = v_{21}(\mathbf{k}') v_{21}(-\mathbf{k}') v_{21}^*(-\mathbf{k}) v_{21}^*(\mathbf{k}), \qquad (C5)
$$

$$
\mathcal{V}_{\mathbf{k},\mathbf{k}'}^{(p_y)} = v_{31}(\mathbf{k}') v_{31}(-\mathbf{k}') v_{31}^*(-\mathbf{k}) v_{31}^*(\mathbf{k}). \qquad (C6)
$$

The functions $v_{ij}$ have been introduced in Eq. (C2), and $v_{ij}^*$ denotes the complex conjugate of $v_{ij}$. The interaction Hamiltonian (3) is obtained as $\hat{H}_{int} = \hat{H}_{int}^{(d)} + \hat{H}_{int}^{(p_x)} + \hat{H}_{int}^{(p_y)}$, where $\mathcal{V}_{\mathbf{k},\mathbf{k}'} = \mathcal{V}_{\mathbf{k},\mathbf{k}'}^{(d)} + \mathcal{V}_{\mathbf{k},\mathbf{k}'}^{(p_x)} + \mathcal{V}_{\mathbf{k},\mathbf{k}'}^{(p_x)}$ and the Fermi sea has been excluded from the first Brillouin zone.

We note that the tight-binding Hamiltonian (1) in the basis spanned by the band operators is diagonal. For the submanifold $\mathcal{S}$ of the upper band, we find the kinetic energy to be

$$
\hat{H}_{kin} = \sum_{\substack{\mathbf{k} \in 1.BZ \\ \sigma \in \{\uparrow,\downarrow\}}} E_{\mathbf{k}}^{(U)} \psi_{U,\mathbf{k}\sigma}^{\dagger} \psi_{U,\mathbf{k}\sigma}, \qquad (C7)
$$

where the Fermi sea will be excluded from the first Brillouin zone by introducing a chemical potential, $\mu$. Finally, the total Hamiltonian (6) is obtained as $\hat{H}_{tot} = \hat{H}_{kin} + \hat{H}_{int}$.

## APPENDIX D. DERIVATION OF THE EIGENEQUATION (9)

To derive the pairing equation we calculate the resulting operator $\hat{H}_{tot} |\Phi\rangle$, where $\hat{H}_{tot} = \hat{H}_{kin} + \hat{H}_{int}$ subject to the interacting Fermi sea. For that, first we apply $\hat{H}_{kin}$ on $|\Phi\rangle$. The part corresponding to spin-up, $\hat{H}_{kin}^{(\uparrow)}$, is obtained to be

$$
\hat{H}_{kin}^{(\uparrow)} |\Phi\rangle = \sum_{\mathbf{k} \in 1.BZ \backslash FS_{int}} \xi_{\mathbf{k}}^{(U)} \psi_{U,\mathbf{k}\uparrow}^{\dagger} \psi_{U,\mathbf{k}\uparrow} \sum_{\boldsymbol{\kappa} \in 1.BZ \backslash FS} \phi(\boldsymbol{\kappa})
$$

$$
\times \psi_{U,\boldsymbol{\kappa}\uparrow}^{\dagger} \psi_{U,-\boldsymbol{\kappa}\downarrow}^{\dagger} |FS_{int}\rangle
$$

$$
= \sum_{\boldsymbol{\kappa} \in 1.BZ \backslash FS_{int}} \delta_{\boldsymbol{\kappa}\mathbf{k}} \xi_{\mathbf{k}}^{(U)} |\Phi\rangle, \qquad (D1)
$$

where $\delta_{\boldsymbol{\kappa}\mathbf{k}}$ denotes the Kronecker delta. To find the effect of the spin-down part, $\hat{H}_{kin}^{(\downarrow)}$, we define $\boldsymbol{\kappa}' \equiv -\boldsymbol{\kappa}$, and rewrite the singlet-state Cooper pair (7) in terms of $\boldsymbol{\kappa}'$. We obtain that

$$
\hat{H}_{kin}^{(\downarrow)} |\Phi\rangle = \sum_{\boldsymbol{\kappa}' \in 1.BZ \backslash FS_{int}} \delta_{\boldsymbol{\kappa}'\mathbf{k}} \xi_{\boldsymbol{\kappa}'}^{(U)} |\Phi\rangle. \qquad (D2)
$$

Equations (D1) and (D2) result in:

$$
\hat{H}_{kin} |\Phi\rangle = \sum_{\mathbf{k} \in 1.BZ \backslash FS_{int}} \left( \xi_{\mathbf{k}}^{(U)} + \xi_{-\mathbf{k}}^{(U)} \right) |\Phi\rangle. \qquad (D3)
$$

Next, we apply $\hat{H}_{int}$ on $|\Phi\rangle$. Here we split up the interaction Hamiltonian to the diagonal and off-diagonal parts. For the diagonal part we obtain:

$$\begin{aligned}
\hat{H}_{\mathrm{int}}^{(\mathrm{diag})}\left|\Phi\right\rangle =&\frac{1}{\mathcal{A}}\sum_{\mathbf{k}\in1.\mathrm{BZ}\backslash\mathrm{FS}_{\mathrm{int}}}\mathcal{V}_{\mathbf{k},\mathbf{k}}\psi_{\mathrm{U},\mathbf{k}\downarrow}^{\dagger}\psi_{\mathrm{U},-\mathbf{k}\uparrow}^{\dagger}\psi_{\mathrm{U},-\mathbf{k}\uparrow}\psi_{\mathrm{U},\mathbf{k}\downarrow}\sum_{\boldsymbol{\kappa}\in1.\mathrm{BZ}\backslash\mathrm{FS}_{\mathrm{int}}}\phi(\boldsymbol{\kappa})\psi_{\mathrm{U},\boldsymbol{\kappa}\uparrow}^{\dagger}\psi_{\mathrm{U},-\boldsymbol{\kappa}\downarrow}^{\dagger}\left|\mathrm{FS}_{\mathrm{int}}\right\rangle \\
=&\frac{1}{\mathcal{A}}\sum_{\mathbf{k}\in1.\mathrm{BZ}\backslash\mathrm{FS}_{\mathrm{int}}}\mathcal{V}_{\mathbf{k},\mathbf{k}}\sum_{\boldsymbol{\kappa}\in1.\mathrm{BZ}\backslash\mathrm{FS}_{\mathrm{int}}}\phi(-\mathbf{k})\psi_{\mathrm{U},-\mathbf{k}\uparrow}^{\dagger}\psi_{\mathrm{U},\mathbf{k}\downarrow}^{\dagger}\left|\mathrm{FS}_{\mathrm{int}}\right\rangle \\
&+\frac{1}{\mathcal{A}}\sum_{\mathbf{k}\in1.\mathrm{BZ}\backslash\mathrm{FS}_{\mathrm{int}}}\mathcal{V}_{\mathbf{k},\mathbf{k}}\sum_{\boldsymbol{\kappa}\in1.\mathrm{BZ}\backslash\mathrm{FS}_{\mathrm{int}}}\delta_{\mathbf{k},-\boldsymbol{\kappa}}\phi(\boldsymbol{\kappa})\psi_{\mathrm{U},\mathbf{k}\downarrow}^{\dagger}\psi_{\mathrm{U},-\mathbf{k}\uparrow}\psi_{\mathrm{U},-\mathbf{k}\uparrow}^{\dagger}\psi_{\mathrm{U},\boldsymbol{\kappa}\uparrow}^{\dagger}\left|\mathrm{FS}_{\mathrm{int}}\right\rangle \\
=&\frac{1}{\mathcal{A}}\sum_{\mathbf{k}\in1.\mathrm{BZ}\backslash\mathrm{FS}_{\mathrm{int}}}\mathcal{V}_{\mathbf{k},\mathbf{k}}\left|\Phi\right\rangle ,
\end{aligned}\tag{D4}$$

where $\mathcal{A}$ denotes the area of the first Brillouin zone. For the off-diagonal part we obtain:

$$\begin{aligned}
\hat{H}_{\mathrm{int}}^{(\mathrm{off\text{-}diag})}\left|\Phi\right\rangle =&\frac{1}{\mathcal{A}}\sum_{\substack{\mathbf{k},\mathbf{k}'\in1.\mathrm{BZ}\backslash\mathrm{FS}_{\mathrm{int}}\\\mathbf{k}\neq\mathbf{k}'}}\mathcal{V}_{\mathbf{k},\mathbf{k}'}\psi_{\mathrm{U},\mathbf{k}'\downarrow}^{\dagger}\psi_{\mathrm{U},-\mathbf{k}'\uparrow}^{\dagger}\sum_{\boldsymbol{\kappa}\in1.\mathrm{BZ}\backslash\mathrm{FS}}\phi(\boldsymbol{\kappa})\psi_{\mathrm{U},-\mathbf{k}\uparrow}\psi_{\mathrm{U},\mathbf{k}\downarrow}\psi_{\mathrm{U},\boldsymbol{\kappa}\uparrow}^{\dagger}\psi_{\mathrm{U},-\boldsymbol{\kappa}\downarrow}^{\dagger}\left|\mathrm{FS}_{\mathrm{int}}\right\rangle \\
=&\frac{-1}{\mathcal{A}}\sum_{\substack{\mathbf{k},\mathbf{k}'\in1.\mathrm{BZ}\backslash\mathrm{FS}_{\mathrm{int}}\\\mathbf{k}\neq\mathbf{k}'}}\mathcal{V}_{\mathbf{k},\mathbf{k}'}\psi_{\mathrm{U},\mathbf{k}'\downarrow}^{\dagger}\psi_{\mathrm{U},-\mathbf{k}'\uparrow}^{\dagger}\sum_{\mathbf{k}'\in1.\mathrm{BZ}\backslash\mathrm{FS}_{\mathrm{int}}}\phi(\mathbf{k}')\left(\hat{1}-\psi_{\mathrm{U},\mathbf{k}'\uparrow}^{\dagger}\psi_{\mathrm{U},\mathbf{k}'\uparrow}\right)\left|\mathrm{FS}_{\mathrm{int}}\right\rangle \\
=&\frac{1}{\mathcal{A}}\sum_{\substack{\mathbf{k},\mathbf{k}'\in1.\mathrm{BZ}\backslash\mathrm{FS}_{\mathrm{int}}\\\mathbf{k}\neq\mathbf{k}'}}\mathcal{V}_{\mathbf{k},\mathbf{k}'}\left|\Phi\right\rangle .
\end{aligned}\tag{D5}$$

Equations (D4) and (D5) result in

$$\hat{H}_{\mathrm{int}}\left|\Phi\right\rangle =\frac{1}{\mathcal{A}}\sum_{\mathbf{k},\mathbf{k}'\in1.\mathrm{BZ}\backslash\mathrm{FS}_{\mathrm{int}}}\mathcal{V}_{\mathbf{k},\mathbf{k}'}\left|\Phi\right\rangle .\tag{D6}$$

Finally, we insert Eqs. (D3) and (D6) into the eigenvalue problem (8), and arrive at the pairing equation (9).

### APPENDIX E. NUMERICAL CALCULATION OF EQ. (9)

As discussed in the text, to solve Eq. (9) numerically we discretize the first Brillouin zone equidistantly following the relation (10). In order to increase the number of the grid points in each direction and to achieve the numerical stability, first we calculate the interacting Fermi surface using the relation

$$\mathrm{FS}_{\mathrm{int}}=\left\{\mathbf{k}^{(j)}\in1.\mathrm{BZ}:2E_{\mathbf{k}^{(j)}}^{(\mathrm{U})}+\frac{1}{N^{2}}\mathcal{V}_{\mathbf{k}^{(j)},\mathbf{k}^{(j)}}<2\mu\right\},\tag{E1}$$

and exclude it from the first Brillouin zone. Next, we constitute the pairing equation (9) on the reduced momentum space as

$$\begin{aligned}
&\left(\xi_{\mathbf{k}_{j}}^{(\mathrm{U})}+\xi_{-\mathbf{k}_{j}}^{(\mathrm{U})}+\frac{1}{N^{2}}\mathcal{V}_{\mathbf{k}_{j},\mathbf{k}_{j}}\right)\phi(\mathbf{k}_{j})\\
&+\frac{1}{N^{2}}\sum_{\substack{\mathbf{k}_{j},\mathbf{k}_{j}'\in1.\mathrm{BZ}\backslash\mathrm{FS}_{\mathrm{int}}\\\mathbf{k}_{j}'\neq\mathbf{k}_{j}}}\mathcal{V}_{\mathbf{k}_{j},\mathbf{k}_{j}'}\phi(\mathbf{k}_{j}')=\mathcal{E}_{j}\phi(\mathbf{k}_{j}),\quad\text{(E2)}
\end{aligned}$$

for $j=1,2,\ldots,N$. Finally, we diagonalize Eq. (E2), and obtain the eigenenergies $\mathcal{E}_{j}$. Among $\mathcal{E}_{j}$, the desired ground-state energy, $E_{\mathrm{G}}$, is the one which is negative and has the largest absolute value.

Finally, we notice that the behavior of the desired eigenvalues as a function of the chemical potential, $\mu$, might display a zigzag effect due to the finite discretization of the momentum space. To prevent this behavior, for the noninteracting regime, we calculate the smallest value of the eigenenergy, $E_0$, of Eq. (E2) for the occupied states. Next, for the interacting regime, we add $E_0$ within the first bracket of Eq. (E2), and calculate the ground-state energy for the unoccupied states.

## APPENDIX F. GROUND-STATE SOLUTION FOR THE ATTRACTIVE REGIME

As expected, for the attractive regime, $U_d, U_p < 0$, the ground-state solution supports an orbital $s$-wave symmetry. Figure 7 shows the wave function for $U_d = -2$ eV and $U_p = -1$ eV.
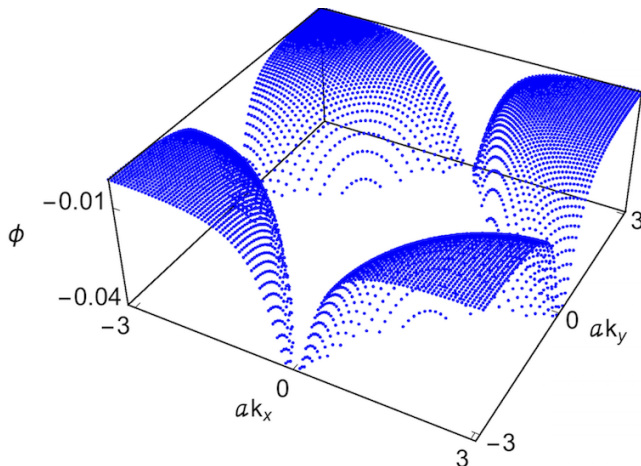


Figure 7. Ground-state wave function of the Cooper pair in the attractive regime of the Fermi-Hubbard model (6), where $N = 100$, $V_{dp} = 3.45$ eV, $t_{pd} = 1.13$ eV, $t_{pp} = 0.8$ eV, $\mu \approx -0.679$ eV, $U_d = -2$ eV, and $U_p = -1$ eV. The wave function supports an orbital $s$-wave symmetry.

[1] E. H. Lieb, Phys. Rev. Lett. **62**, 1201 (1989).

[2] M. Niţă, B. Ostahie, and A. Aldea, Phys. Rev. B **87**, 125428 (2013).

[3] N. Plakida, *High-Temperature Cuprate Superconductors: Experiment, Theory, and Applications* (Springer, Berlin, 2010), Chaps. 2 and 3.

[4] A. J. Leggett, *Quantum Liquids* (Oxford University Press, New York, 2006), Chaps. 5 and 7.

[5] C. J. Pethick and H. Smith, *Bose–Einstein Condensation in Dilute Gases* (Cambridge University Press, New York, 2008), Chap. 5.

[6] J. Fortágh and C. Zimmermann, Rev. Mod. Phys. **79**, 235 (2007).

[7] R. Shen, L. B. Shao, B. Wang, and D. Y. Xing, Phys. Rev. B **81**, 041410(R) (2010).

[8] V. Apaja, M. Hyrkäs, and M. Manninen, Phys. Rev. A **82**, 041402(R) (2010).

[9] S. Taie, H. Ozawa, T. Ichinose, T. Nishio, S. Nakajima, and Y. Takahashi, Sci. Adv. **1**, e1500854 (2015).

[10] S. Mukherjee, A. Spracklen, D. Choudhury, N. Goldman, P. Öhberg, E. Andersson, and R. R. Thomson, Phys. Rev. Lett. **114**, 245504 (2015).

[11] M. R. Slot, T. S. Gardenier, P. H. Jacobse, G. C. P. van Miert, S. N. Kempkes, S. J. M. Zevenhuizen, C. M. Smith, D. Vanmaekelbergh, and I. Swart, Nat. Phys. **13**, 672 (2017).

[12] R. Drost, T. Ojanen, A. Harju, and P. Liljeroth, Nat. Phys. **13**, 668 (2017).

[13] W. Jiang, H. Huang, and F. Liu, Nat. Comm. **10**, 2207 (2019).

[14] B. Cui, X. Zheng, J. Wang, D. Liu, S. Xie, and B. Huang, Nat. Comm. **11**, 66 (2020).

[15] J. D. Bodyfelt, D. Leykam, C. Danieli, X. Yu, and S. Flach, Phys. Rev. Lett. **113**, 236403 (2014).

[16] D. Leykam, A. Andreanov, and S. Flach, Adv. Phys. X **3**, 1473052 (2018).

[17] N. B. Kopnin, T. T. Heikkilä, and G. E. Volovik, Phys. Rev. B **83**, 220503(R) (2011).

[18] V. I. Iglovikov, F. Hébert, B. Grémaud, G. G. Batrouni, and R. T. Scalettar, Phys. Rev. B **90**, 094506 (2014).

[19] S. Peotta and P. Törmä, Nat. Comm. **6**, 8944 (2014).

[20] A. Julku, S. Peotta, T. I. Vanhala, D. -H. Kim, and P. Törmä, Phys. Rev. Lett. **117**, 045303 (2016).

[21] K. Kobayashi, M. Okumura, S. Yamada, M. Machida, and H. Aoki, Phys. Rev. B **94**, 214501 (2016).

[22] M. Tovmasyan, S. Peotta, P. Törmä, and S. D. Huber, Phys. Rev. B **94**, 245149 (2016).

[23] J. R. Schrieffer and J. S. Brooks (eds.), *Handbook of High-Temperature Superconductivity: Theory and Experiment* (Springer, New York, 2007), Chap. 1.

[24] J. W. Lynn (ed.), *High-Temperature Superconductivity* (Springer, New York, 1990), Chap. 5.

[25] P. W. Anderson, *The Theory of Superconductivity in the High-T$_c$ Cuprates* (Princeton University Press, Princeton, New Hersey, 1997), Chap. 1.

[26] S. Uchida, *High Temperature Superconductivity: The Road to Higher Critical Temperature* (Springer, Tokyo, 2015), Chap. 3.

[27] A. A. Abrikosov, Int. J. Mod. Phys. **13**, 3405 (1999).

[28] S. R. Park, D. J. Song, C. S. Leem, C. Kim, C. Kim, B. J. Kim, and H. Eisaki, Phys. Rev. Lett. **101**, 117006 (2008).

[29] S. Johnston, F. Vernay, B. Moritz, Z. -X. Shen, N. Nagaosa, J. Zaanen, and T. P. Devereaux, Phys. Rev. B **82**, 064513 (2010).

[30] P. J. Carbotte, T. Timusk, and J. Hwang, Rep. Prog. Phys. **74**, 066501 (2011).

[31] A. S. Alexandrov, J. H. Samson, and G. Sica, Europhys. Lett. **100**, 17011 (2012).

[32] P. Monthoux, A. V. Balatsky, and D. Pines, Phys. Rev. Lett. **67**, 3448 (1991).

[33] V. M. Krasnov, S. -O. Katterwe, and A. Rydh, Nat. Comm. **4**, 2970 (2013).

[34] H. Rietschel and L. J. Sham, Phys. Rev. B **28**, 5100 (1983).

[35] A. Bill, H. Morawitz, and V. Z. Kresin, Phys. Rev. B **68**, 144519 (2003).

[36] G. S. Atwal and N. W. Ashcroft, Phys. Rev. B **70**, 104513 (2004).

[37] E. A. Pashitskii and V. I. Pentegov, Low Temp. Phys. **34**, 113 (2008).

[38] L. N. Cooper, Phys. Rev. **104**, 1189 (1956).

[39] D. L. Goodstein, *States of Matter* (Dover, New York, 1985), Chap. 5.

[40] A. A. Abrikosov, *Fundamentals of the Theory of Metals* (Dover, New York, 2017), Chap. 16.

[41] M. Tinkham, *Introduction to Superconductivity* (Dover, New York, 2004), Chap. 3.

[42] N. W. Ashcroft and N. D. Mermin, *Solid State Physics* (Brooks/Cole, Belmont, CA, 1976), Chaps. 26 and 34.

[43] A. S. Alexandrov and V. V. Kabanov, Phys. Rev. Lett. **106**, 136403 (2011).

[44] A. S. Alexandrov, *Strong-Coupling Theory of High-Temperature Superconductivity* (Cambridge University Press, Cambridge, 2013), Chaps. 6 and 8.

[45] M. Zegrodnik, A. Biborski, M. Fidrysiak, and J. Spałek, Phys. Rev. B **99**, 104511 (2019).

[46] A. Damascelli, Z. Hussain, and Z. -X. Shen, Rev. Mod. Phys. **75**, 473 (2003).

[47] D. Koralek, J. F. Douglas, N. C. Plumb, Z. Sun, A. V. Fedorov, M. M. Murnane, H. C. Kapteyn, S. T. Cundiff, Y. Aiura, K. Oka, H. Eisaki, and D. S. Dessau, Phys. Rev. Lett. **96**, 017005 (2006).

[48] J. D. Koralek, J. F. Douglas, N. C. Plumb, J. D. Griffith, S. T. Cundiff, H. C. Kapeteyn, M. M. Murnane, and D. S. Dessau, Rev. Sci. Instrum. **78**, 053905 (2007).

[49] G. Liu, G. Wang, Y. Zhu, H. Zhang, G. Zhang, X. Wang, Y. Zhou, W. Zhang, H. Liu, L. Zhao, J. Meng, X. Dong, C. Chen, Z. Xu, and X. J. Zhou, Rev. Sci. Instrum. **79**, 023105 (2008).

[50] H. Li, X. Zhou, S. Parham, T. J. Reber, H. Berger, G. B. Arnold, and D. S. Dessau, Nat. Comm. **9**, 26 (2018).

[51] H. Li, X. Zhou, S. Parham, K. N. Gordon, R. D. Zhong, J. Schneeloch, G. D. Gu, Y. Huang, H. Berger, G. B. Arnold, and D. S. Dessau, arXiv:1809.02194v2.

[52] P. W. Anderson, Phys. Scripta. **T102**, 10 (2002).

[53] J. Kaczmarczyk, J. Bünemann, and J. Spałek, New J. Phys. **16**, 073018 (2014).

[54] J. Spałek, M. Zegrodnik, and J. Kaczmarczyk, Phys. Rev. B **95**, 024506 (2017).

[55] P. W. Phillips, L. Yeo, and E. W. Huang, arXiv:1912.01008.

[56] G. Knizia and G. K. -L. Chan, Phys. Rev. Lett. **109**, 186404 (2012).

[57] T. I. Vanhala and P. Törmä, Phys. Rev. B **97**, 075112 (2018).

[58] S. Zhang, J. Carlson, and J. E. Gubernatis, Phys. Rev. Lett. **74**, 3652 (1995).

[59] J. Jordan, R. Orús, G. Vidal, F. Verstraete, and J. I. Cirac, Phys. Rev. Lett. **101**, 250602 (2008).

[60] E. M. Stoudenmire and S. R. White, Annu. Rev. Condens. Matter Phys. **3**, 111 (2012).

[61] M. Kitatani, N. Tsuji, and H. Aoki, Phys. Rev. B **95**, 075109 (2017).

[62] To define the hole doping, $\delta_h$, here we follow this convention: At the half-filling the electron density $n_e = 1/2$, and the hole doping is vanishing, $\delta_h = 0$. As we decrease $n_e$, we inject more holes into the desired momentum space, which increases $\delta_h$. Here the hole doping is obtained as $\delta_h = 1/2 - n_e$, for $0 \leqslant n_e \leqslant 1/2$.

[63] M. Lewenstein, A. Sanpera, and V. Ahufinger, *Ultracold Atoms in Optical Lattices: Simulating Quantum Many-Body Systems* (Oxford University Press, 2012), Chap. 14.

[64] M. Inguscio and L. Fallani, *Atomic Physics: Precise Measurements & Ultracold Matter* (Oxford University Press, Oxford, 2013), Chap. 6.

[65] E. Altman, E. Demler, and M. D. Lukin , Phys. Rev. A **70**, 013603 (2004).

[66] L. Mathey, A. Vishwanath, and E. Altman, Phys. Rev. A **79**, 013609 (2009).

[67] I. J. Zucker, Math. Gazet. **92**, 264 (2008).

[68] By "momentum transfer" we mean the difference of the in-state and out-state momenta of a particle; see, e.g., J. R. Taylor, *Scattering Theory: The Quantum Theory of Nonrelativistic Collisions* (Dover, New York, 2006).

# Bibliography

[1] L. N. Cooper, Bound electron pairs in a degenerate Fermi gas, Phys. Rev. **104**, 1189 (1956).

[2] A. J. Leggett, *Quantum Liquids* (Oxford University Press, New York, 2006), Chap. 5.

[3] D. L. Goodstein, *States of Matter* (Dover, New York, 1985), Chap. 5.

[4] A. A. Abrikosov, *Fundamentals of the Theory of Metals* (Dover, New York, 2017), Chap. 16.

[5] M. Tinkham, *Introduction to Superconductivity* (Dover, New York, 2004), Chap. 3.

[6] N. W. Ashcroft and N. D. Mermin, *Solid State Physics* (Brooks/Cole, Belmont, CA, 1976), Chaps. 26 and 34.

[7] E. Maxwell, Isotope effect in the superconductivity of mercury, Phys. Rev. **78**, 477 (1950).

[8] C. A. Reynolds, B. Serin, W. H. Wright, and L. B. Nesbitt, Superconductivity of isotopes of mercury, Phys. Rev. **78**, 487 (1950).

[9] A. B. Migdal, Interaction between electrons and lattice vibrations in a normal metal, Sov. Phys. JETP **34**, 996 (1958).

[10] T. Jarlborg and A. Bianconi, Breakdown of the Migdal approximation at Lifshitz transitions with giant zero-point motion in the $H_3S$ superconductor, Sci. Rep. **6**, 24816 (2016).

[11] G. M. Eliashberg, Interactions between electrons and lattice vibrations in a superconductor, Sov. Phys. JETP **11**, 696 (1960).

[12] G. M. Eliashberg, Temperature Green's function for electrons in a superconductor, Sov. Phys. JETP **12**, 1000 (1961).

[13] F. Marsiglio, Eliashberg theory in the weak-coupling limit, Phys. Rev. B **98**, 024523 (2018).

[14] S. Mirabi, R. Boyack, and F. Marsiglio, Eliashberg theory in the weak-coupling limit: Results on the real frequency axis, Phys. Rev. B **101**, 064506 (2020).

[15] F. Marsiglio, Eliashberg theory: A short review, Ann. Phys. **417**, 168102 (2020).

[16] J. Bardeen, L. N. Cooper, and J. R. Schrieffer, Theory of superconductivity, Phys. Rev. **108**, 1175 (1957).

[17] A. A. Abrikosov, L. P. Gorkov, and I. E. Dzyaloshinski, *Methods of Quantum Field Theory in Statistical Physics* (Dover, New York, 1975), Chap. 7.

[18] J. R. Schrieffer, *Theory of Superconductivity* (Westview, Boulder, Colorado, 1999), Chap. 2.

[19] G. Baym, *Lectures on Quantum Mechanics* (CRC, New York, 1990), Chap. 8.

[20] A. L. Fetter and J. D. Walecka, *Quantum Theory of Many-Particle Systems* (Dover, New York, 2003), Chaps. 12 and 13.

[21] E. M. Lifshitz and L. P. Pitaevskii, *Statistical Physics* (Butterworth-Heinemann, Oxford, 2006), Chap. V.

[22] G. Grosso and G. P. Parravicini, *Solid State Physics* (Academic, Oxford, 2014), Chap. 18.

[23] G. Grüner, The dynamics of charge-density waves, Rev. Mod. Phys. **60**, 1129 (1988).

[24] G. Grüner, *Density Waves in Solids* (CRC, NW, 2018), Chaps 3 and 4.

[25] E. H. Lieb, Two theorems on the Hubbard model, Phys. Rev. Lett. **62**, 1201 (1989).

[26] M. Niţă, B. Ostahie, and A. Aldea, Spectral and transport properties of the two-dimensional Lieb lattice, Phys. Rev. B **87**, 125428 (2013).

[27] R. Shen, L. B. Shao, B. Wang, and D. Y. Xing, Single Dirac cone with a flat band touching on line-centered-square optical lattices, Phys. Rev. B **81**, 041410(R) (2010).

[28] V. Apaja, M. Hyrkäs, and M. Manninen, Flat bands, Dirac cones, and atom dynamics in an optical lattice, Phys. Rev. A **82**, 041402(R) (2010).

[29] S. Taie, H. Ozawa, T. Ichinose, T. Nishio, S. Nakajima, and Y. Takahashi, Coherent driving and freezing of bosonic matter wave in an optical Lieb lattice, Sci. Adv. **1**, e1500854 (2015).

[30] S. Mukherjee, A. Spracklen, D. Choudhury, N. Goldman, P. Öhberg, E. Andersson, and R. R. Thomson, Observation of a localized flat-band state in a photonic Lieb lattice, Phys. Rev. Lett. **114**, 245504 (2015).

[31] M. R. Slot, T. S. Gardenier, P. H. Jacobse, G. C. P. van Miert, S. N. Kempkes, S. J. M. Zevenhuizen, C. M. Smith, D. Vanmaekelbergh, and I. Swart, Experimental realization and characterization of an electronic Lieb lattice. Nat. Phys. **13**, 672 (2017).

[32] R. Drost, T. Ojanen, A. Harju, and P. Liljeroth, Topological states in engineered atomic lattices, Nat. Phys. **13**, 668 (2017).

[33] W. Jiang, H. Huang, and F. Liu, A Lieb-like lattice in a covalent-organic framework and its Stoner ferromagnetism, Nat. Comm. **10**, 2207 (2019).

[34] B. Cui, X. Zheng, J. Wang, D. Liu, S. Xie, and B. Huang, Realization of Lieb lattice in covalent-organic frameworks with tunable topology and magnetism, Nat. Comm. **11**, 66 (2020).

[35] J. D. Bodyfelt, D. Leykam, C. Danieli, X. Yu, and S. Flach, Flatbands under correlated perturbations, Phys. Rev. Lett. **113**, 236403 (2014).

[36] D. Leykam, A. Andreanov, and S. Flach, Artificial flat band systems: from lattice models to experiments, Adv. Phys. X **3**, 1473052 (2018).

[37] N. B. Kopnin, T. T. Heikkilä, and G. E. Volovik, High-temperature surface superconductivity in topological flat-band systems, Phys. Rev. B **83**, 220503(R) (2011).

[38] V. I. Iglovikov, F. Hébert, B. Grémaud, G. G. Batrouni, and R. T. Scalettar, Superconducting transitions in flat-band systems, Phys. Rev. B **90**, 094506 (2014).

[39] S. Peotta and P. Törmä, Superfluidity in topologically nontrivial flat bands, Nat. Comm. **6**, 8944 (2014).

[40] A. Julku, S. Peotta, T. I. Vanhala, D. -H. Kim, and P. Törmä, Geometric origin of superfluidity in the Lieb-lattice flat band, Phys. Rev. Lett. **117**, 045303 (2016).

[41] K. Kobayashi, M. Okumura, S. Yamada, M. Machida, and H. Aoki, Superconductivity in repulsively interacting fermions on a diamond chain: Flat-band-induced pairing, Phys. Rev. B **94**, 214501 (2016).

[42] M. Tovmasyan, S. Peotta, P. Törmä, and S. D. Huber, Effective theory and emergent SU(2) symmetry in the flat bands of attractive Hubbard models, Phys. Rev. B **94**, 245149 (2016).

[43] N. Plakida, *High-Temperature Cuprate Superconductors: Experiment, Theory, and Applications* (Springer, Berlin, 2010), Chaps. 2 and 3.

[44] A. J. Leggett, *Quantum Liquids* (Oxford University Press, New York, 2006), Chap. 7.

[45] J. R. Schrieffer and J. S. Brooks (eds.), *Handbook of High-Temperature Superconductivity: Theory and Experiment* (Springer, New York, 2007), Chap. 1.

[46] J. W. Lynn (ed.), *High-Temperature Superconductivity* (Springer, New York, 1990), Chap. 5.

[47] P. W. Anderson, *The Theory of Superconductivity in the High-$T_c$ Cuprates* (Princeton University Press, Princeton, New Jersey, 1997), Chap. 1.

[48] S. Uchida, *High Temperature Superconductivity: The Road to Higher Critical Temperature* (Springer, Tokyo, 2015), Chap. 3.

[49] A. A. Abrikosov, Theory of high-$T_c$ superconducting cuprates based on experimental evidence, Int. J. Mod. Phys. **13**, 3405 (1999).

[50] S. R. Park, D. J. Song, C. S. Leem, C. Kim, C. Kim, B. J. Kim, and H. Eisaki, Angle-resolved photoemission spectroscopy of electron-doped cuprate superconductors: Isotropic electron-phonon coupling, Phys. Rev. Lett. **101**, 117006 (2008).

[51] S. Johnston, F. Vernay, B. Moritz, Z. -X. Shen, N. Nagaosa, J. Zaanen, and T. P. Devereaux, Systematic study of electron-phonon coupling to oxygen modes across the cuprates. Phys. Rev. B **82**, 064513 (2010).

[52] P. J. Carbotte, T. Timusk, and J. Hwang, Bosons in high-temperature superconductors: an experimental survey, Rep. Prog. Phys. **74**, 066501 (2011).

[53] A. S. Alexandrov, J. H. Samson, and G. Sica, High-temperature superconductivity from realistic Coulomb and Fröhlich interactions, Europhys. Lett. **100**, 17011 (2012).

[54] P. Monthoux, A. V. Balatsky, and D. Pines, Toward a theory of high-temperature superconductivity in the antiferromagnetically correlated cuprate oxides, Phys. Rev. Lett. **67**, 3448 (1991).

[55] V. M. Krasnov, S. -O. Katterwe1, and A. Rydh, Signatures of the electronic nature of pairing in high-$T_c$ superconductors obtained by non-equilibrium boson spectroscopy, Nat. Comm. **4**, 2970 (2013).

[56] H. Rietschel and L. J. Sham, Role of electron Coulomb interaction in super-conductivity, Phys. Rev. B **28**, 5100 (1983).

[57] A. Bill, H. Morawitz, and V. Z. Kresin, Electronic collective modes and superconductivity in layered conductors, Phys. Rev. B **68**, 144519 (2003).

[58] G. S. Atwal and N. W. Ashcroft, Polarization waves and superconducting instabilities in electron systems, Phys. Rev. B **70**, 104513 (2004).

[59] E. A. Pashitskii and V. I. Pentegov, On the plasmon mechanism of high-$T_c$ superconductivity in layered crystals and two dimensional systems, Low Temp. Phys. **34**, 113 (2008).

[60] M. Zegrodnik, A. Biborski, M. Fidrysiak, and J. Spałek, Superconductivity in the three-band model of cuprates: Variational wave function study and relation to the single-band case, Phys. Rev. B **99**, 104511 (2019).

[61] J. Kaczmarczyk, J. Bünemann, and J. Spałek, High-temperature superconductivity in the two-dimensional $t$–$J$ model: Gutzwiller wavefunction solution, New J. Phys. **16**, 073018 (2014).

[62] J. Spałek, M. Zegrodnik, and J. Kaczmarczyk, Universal properties of high-temperature superconductors from real-space pairing: $t-J-U$ model and its quantitative comparison with experiment, Phys. Rev. B **95**, 024506 (2017).

[63] Y. Hatsugai, and M. Kohmoto, Exactly solvable model of correlated lattice electrons in any dimensions, J. Phys. Soc. Jpn **61**, 2056 (1992).

[64] P. W. Phillips, L. Yeo, and W. Huang, Exact theory for superconductivity in a doped Mott insulator, arXiv:1912.01008.

[65] G. Knizia and G. K. -L. Chan, Density matrix embedding: A simple alternative to dynamical mean-field theory, Phys. Rev. Lett. **109**, 186404 (2012).

[66] T. I. Vanhala and P. Törmä, Dynamical mean-field theory study of stripe order and $d$-wave superconductivity in the two-dimensional Hubbard model, Phys. Rev. B **97**, 075112 (2018).

[67] S. Zhang, J. Carlson, and J. E. Gubernatis, Constrained path quantum Monte Carlo method for fermion ground states, Phys. Rev. Lett. **74**, 3652 (1995).

[68] J. Jordan, R. Orús, G. Vidal, F. Verstraete, and J. I. Cirac, Classical simulation of infinite-size quantum lattice systems in two spatial dimensions, Phys. Rev. Lett. **101**, 250602 (2008).

[69] E. M. Stoudenmire and S. R. White, Studying two-dimensional systems with the density matrix renormalization group, Annu. Rev. Condens. Matter Phys. **3**, 111 (2012).

[70] M. Kitatani, N. Tsuji, and H. Aoki, Interplay of Pomeranchuk instability and superconductivity in the two-dimensional repulsive Hubbard model, Phys. Rev. B **95**, 075109 (2017).

[71] V. Efimov, Weakly-bound states of three resonantly-interacting particles, Sov. J. Nucl. Phys. **12**, 589 (1971) [V. Efimov, Yad. Fiz. **12**, 1080 (1970)].

[72] E. Nielsen, D. V. Fedorov, A. S. Jensen, and E. Garrido, The three-body problem with short-range interactions, Phys. Rep. **347**, 373 (2001).

[73] P. Naidon and S. Endo, Efimov physics: a review, Prog. Phys. **80**, 056001 (2017).

[74] C. H. Greene, P. Giannakeas, and J. P-. Ríos, Universal few-body physics and cluster formation, Rev. Mod. Phys. **89**, 035006 (2017).

[75] J. P. D'Incao, Few-body physics in resonantly interacting ultracold quantum gases, J. Phys. B **51** 043001 (2018).

[76] T. Kraemer, M. Mark, P. Waldburger, J. G. Danzl, C. Chin, B. Engeser, A. D. Lange, K. Pilch, A. Jaakkola, H. -C. Nägerl, and R. Grimm, Evidence for Efimov quantum states in an ultracold gas of caesium atoms, Nature **440**, 315 (2006).

[77] M. Jag, M. Zaccanti, M. Cetina, R. S. Lous, F. Schreck, R. Grimm, D. S. Petrov, and J. Levinsen, Observation of a strong atom-dimer attraction in a mass-imbalanced Fermi-Fermi mixture, Phys. Rev. Lett. **112**, 075302 (2014).

[78] R. Pires, J. Ulmanis, S. Hälfner, M. Repp, A. Arias, E. D. Kuhnle, and M. Weidemüller, Observation of Efimov resonances in a mixture with extreme mass imbalance, Phys. Rev. Lett. **112**, 250404 (2014).

[79] S. -K. Tung, K. Jiménez-García, J. Johansen, C. V. Parker, and C. Chin, Geometric scaling of Efimov states in a $^6$Li-$^{133}$Cs mixture, Phys. Rev. Lett. **113**, 240402 (2014).

[80] J. Voigtsberger, S. Zeller, J. Becht, N. Neumann, F. Sturm, H. -K. Kim, M. Waitz, F. Trinter, M. Kunitski, A. Kalinin, J. Wu, W. Schoöllkopf, D. Bressanini, A. Czasch, J. B. Williams, K. U-. Pfleger, L. Ph H. Schmidt, M. S. Schöffler, R. E. Grisenti, T. Jahnke, and R. Dörner, Imaging the structure of the trimer systems $^4$He$_3$ and $^3$He$^4$He$_2$, Nat. Comm. **5**, 5765 (2014).

[81] M. Kunitski, S. Zeller, J. Voigtsberger, A. Kalinin, L. P. H. Schmidt, M. Schöffler, A. Czasch, W. Schöllkopf, R. E. Grisenti, T. Jahnke, D. Blume, and R. Dörner, Observation of the Efimov state of the helium trimer, Science **348**, 551 (2015).

[82] N. N. Bogoliubov, A new method in the theory of superconductivity, Sov. Phys. JETP **34**, 41 (1958).

[83] H. Fröhlich, Interaction of electrons with lattice vibrations, Proc. Roy. Soc. A **215**, 291 (1952).

[84] J. Bardeen and D. Pines, Electron-phonon interaction in metals, Phys. Rev. **99**, 1140 (1955).

[85] N. W. Ashcroft and N. D. Mermin, *Solid State Physics* (Brooks/Cole, Belmont, CA, 1976), Chap. 22.

[86] A. H. Dayem and J. J. Wiegand, Emitted phonon spectrum and its influence on the detected signal in superconducting Sn diodes, Phys. Rev. B **5**, 4390 (1972).

[87] W. Eisenmenger and A. H. Dayem, Quantum generation and detection of incoherent phonons in superconductors, Phys. Rev. Lett. **18**, 125 (1967).

[88] A. H. Dayem, B. I. Miller, and J. J. Wiegand, Phonon generation and detection in superconducting lead diodes, Phys. Rev. B **3**, 2949 (1971).

[89] J. R. Taylor, *Scattering Theory: The Quantum Theory of Nonrelativistic Collisions* (Dover, New York, 2006).

[90] W. Nolting, *Fundamentals of Many-Body Physics: Principles and Methods* (Springer, Berlin, 2009), Chaps. 1 and 2.

[91] M. Combescot and S-. Y. Shiau, *Excitons and Cooper Pairs: Two Composite Bosons in Many-Body Physics* (Oxford University Press, Oxford, 2016), Chap. 7.

[92] A. S. Alexandrov, Breakdown of the Migdal-Eliashberg theory in the strong-coupling adiabatic regime, Eur. Phys. Lett. **56**, 92 (2001).

[93] M. Mekata, Kagome: The story of the basketweave lattice, Phys. Today **56**, 12 (2003).

[94] K-. E. Huhtinen, M. Tylutki, P. Kumar, T. I. Vanhala, S. Peotta, and P. Törmä, Spin-imbalanced pairing and Fermi surface deformation in flat bands, Phys. Rev. B **97**, 214503 (2018).

[95] C. J. Pethick and H. Smith, *Bose–Einstein Condensation in Dilute Gases* (Cambridge University Press, New York, 2008) Chap. 5.

[96] J. Fortágh and C. Zimmermann, Magnetic microtraps for ultracold atoms, Rev. Mod. Phys. **79**, 235 (2007).

[97] A. J. Leggett, What do we know about high $T_c$?, Nat. Phys. **2**, 134 (2006).

[98] N. W. Ashcroft and N. D. Mermin, *Solid State Physics* (Brooks/Cole, Belmont, CA, 1976), Chaps. 8 and 10.

[99] F. H. L. Essler. H. Frahm, F. Göhmann, A. Klümper, and V. E. Korepin, *The One-Dimensional Hubbard Model* (Cambridge University Press, Cambridge, 2005), Chaps. 1 and 2.

[100] P. Fazekas, *Lecture Notes on Electron Correlation and Magnetism* (World Scientific, Singapore, 1999), Chap. 4.

[101] W. Nolting and A. Ramakanth, *Quantum Theory of Magnetism* (Springer, Berlin, 2009), Chap. 8.

[102] T. Esslinger, Fermi-Hubbard physics with atoms in an optical lattice, Annu. Rev. Condens. Matter Phys. **1**, 129 (2010).

[103] R. T. Scalettar, "An Introduction to the Hubbard Hamiltonian," *Quantum Materials: Experiments and Theory Modeling and Simulation*, (Forschungszentrum Jülich, 2016), Chap. 4.

[104] M. C. Gutzwiller, Effect of correlation on the ferromagnetism of transition metals, Phys. Rev. Lett. **10**, 159 (1963).

[105] J. Kanamori, Electron correlation and ferromagnetism of transition metals, Prog. Theor. Phys. **30**, 275 (1963).

[106] J. Hubbard, Electron correlations in narrow energy bands, Proc. R. Soc. A **276**, 238 (1963).

[107] J. Hubbard, Electron correlations in narrow energy bands II. The degenerate band case, Proc. R. Soc. A **277**, 237 (1964).

[108] J. Hubbard, Electron correlations in narrow energy bands III. An improved solution, Proc. R. Soc. A **281**, 401 (1964).

[109] L. Arrachea and A. A. Aligia, d-Wave superconductivity in the effective extended Hubbard model for cuprates, Physica C **408**, 224 (2004).

[110] A. P. Kądzielawa, J. Spałek, J. Kurzyk, and W. W'ojcik, Extended Hubbard model with renormalized Wannier wave functions in the correlated state III, Eur. Phys. J. B **86**, 252 (2013).

[111] A. Zouhair, S. Harir, M. Bennai, A. M-. Zalas, Y. Boughaleb, Local magnetic properties of $L \times L$ square lattice with an extended Hubbard model, Opt. Quant. Electron **47**, 523 (2015).

[112] O. Dutta, M. Gajda, P. Hauke, M. Lewenstein, D-. S. Lühmann, B. A. Malomed, T. Sowiński, and J. Zakrzewski, Non-standard Hubbard models in optical lattices: a review, Rep. Prog. Phys. **78**, 066001 (2015).

[113] O. Jürgensen, *Extended Hubbard Models for Ultracold Atoms in Optical Lattices*, PhD Dissertation, Universität Hamburg, 2015.

[114] A. Dhar, J. J. Kinnunen, and P. Törmä, Population imbalance in the extended Fermi-Hubbard model, Phys. Rev. B **94**, 075116 (2016).

[115] A. S. Alexandrov, *Strong-Coupling Theory of High-Temperature Superconductivity* (Cambridge University Press, Cambridge, 2013), Chap. 6.

[116] P. W. Anderson, Superconductivity in high-$T_c$ cuprates: the cause is no longer a mystery, Phys. Scripta. **T102**, 10 (2002).

[117] J. R. Schrieffer and J. S. Brooks (eds.), *Handbook of High-Temperature Superconductivity: Theory and Experiment* (Springer, New York, 2007), Chap. 13.

[118] D. J. Scalapino, A common thread: The pairing interaction for unconventional superconductors, Rev. Mod. Phys. **84**, 1383 (2012).

[119] T. I. Vanhala and P. Törmä, Dynamical mean-field theory study of stripe order and $d$-wave superconductivity in the two-dimensional Hubbard model, Phys. Rev. B **97**, 075112 (2018).

[120] N. J. Robinson, P. D. Johnson, T. M. Rice, and A. M. Tsvelik, Anomalies in the pseudogap phase of the cuprates: competing ground states and the role of umklapp scattering, Rep. Prog. Phys. **82**, 126501 (2019).

[121] L. H. Thomas, The interaction between a neutron and a proton and the structure of H$^3$, Phys. Rev. **47**, 903 (1935).

[122] G. V. Skorniakov and K. A. Ter-Martirosian, Three body problem for short range forces: Scattering of low energy neutrons by deuterons, Sov. Phys. JETP **4**, 648 (1957).

[123] M. E. Peskin and D. V. Schroeder, *An Introduction to Quantum Field Theory* (Westview, Boulder, Colorado, 1995), Chap. 4.

[124] H. Bethe and R. Peierls, Quantum theory of the diplon, Proc. Roy. Soc. A **148**, 146 (1935).

[125] L. D. Faddeev, *Mathematical Aspects of the Three-Body Problem in the Quantum Scattering Theory* (Sivan, Jerusalem, 1965).

[126] D. V. Fedorov and A. S. Jensen, Efimov effect in coordinate space Faddeev equations, Phys. Rev. Lett. **71**, 4103 (1993).

[127] M. T. Yamashita, Dimensional effects in Efimov physics, Few-Body Syst. **60**, 22 (2019).

[128] G. S. Danilov, On the three-body problem with short-range forces, JETP **40**, 498 (1961).

[129] V. F. Kharchenko, Solution of the Skornyakov–Ter-Martirosyan equations for three nucleons with cutoff at large momenta, Yad. Fiz. **16**, 310 (1972).

[130] P. Naidon, S. Endo, and M. Ueda, Phys. Rev. Lett. 112, 105301 (2014).

[131] P. Naidon, S. Endo, and M. Ueda, Phys. Rev. A 90, 022106 (2014).

[132] I. Bloch, J. Dalibard, and W. Zwerger, Many-body physics with ultracold gases, Rev. Mod. Phys. **80**, 885 (2008).

[133] C. Chin, R. Grimm, P. Julienne, and E. Tiesinga, Feshbach resonances in ultracold gases, Rev. Mod. Phys. **82**, 1225 (2010).

[134] R. Grimm, Efimov states in an ultracold gas: How it happened in the laboratory, Few-Body Syst. **60**, 23 (2019).

[135] B. Huang, L. Sidorenkov, R. Grimm, J. M. Hutson, Observation of the second triatomic resonance in Efimov's scenario, Phys. Rev. Lett. **112**, 190401 (2014).

[136] J. Ulmanis, S. Häfner, R. Pires, E. D. Kuhnle, Y. Wang, C. H. Greene, and M. Weidemüller, Heteronuclear Efimov scenario with positive intraspecies scattering length, Phys. Rev. Lett. **117**, 153201 (2016).

[137] M. J. Gullans, S. Diehl, S. T. Rittenhouse, B. P. Ruzi, J. P. D'Incao, P. Julienne, A. V. Gorshkov, and J. M. Taylor, Efimov states of strongly interacting photons, Phys. Rev. Lett. **119**, 2336101 (2017).

[138] Q. -Y. Liang, A. V. Venkatramani, S. H. Cantu, T. L. Nicholson, M. J. Gullans, A. V. Gorshkov, J. D. Thompson, C. Chin, M. D. Lukin, V. Vuletić, Observation of three-photon bound states in a quantum nonlinear medium, Science **359**, 783 (2018).

[139] C. Kittel, *Quantum Theory of Solids* (John Wiley & Sons, New York, 1963), Chap. 4.

[140] N. W. Ashcroft and N. D. Mermin, *Solid State Physics* (Brooks/Cole, Belmont, CA, 1976), Chap. 33.

[141] M. Combescot and S-. Y. Shiau, *Excitons and Cooper Pairs: Two Composite Bosons in Many-Body Physics* (Oxford University Press, Oxford, 2016), Chap. 2.

[142] Y. Nishida, Y. Kato, and C. D. Batista, Efimov effect in quantum magnets, Nat. Phys. **9**, 93 (2013).

[143] Y. Nishida, Electron spin resonance in a dilute magnon gas as a probe of magnon scattering resonances, Phys. Rev. B **88**, 224402 (2013).

[144] H. Watanabe and H. Murayama, Unified description of Nambu-Goldstone bosons without Lorentz invariance, Phys. Rev. Lett. **108**, 251602 (2012).

[145] J. Omachi, T. Suzuki, K. Kato, N. Naka, K. Yoshioka, and M. K. Gonokami, Observation of excitonic *N*-body bound states: Polyexcitons in diamond, Phys. Rev. Lett. **111**, 026402 (2013).

[146] F. Ferlaino, A. Zenesini, M. Berninger, B. Huang, H.-C. Nägerl, and R. Grimm, Efimov resonances in ultracold quantum gases, Few-Body Syst. **51**, 113 (2011).

[147] Y. Castin, C. Mora, and L. Pricoupenko, Four-body Efimov effect for three fermions and a lighter particle, Phys. Rev. Lett. **105**, 223201 (2010).

[148] P. Naidon, Tetramers of two heavy and two light bosons, Few-Body Syst. **59**, 64 (2018).

[149] B. Bazak and D. S. Petrov, Five-body Efimov effect and universal pentamer in fermionic mixtures, Phys. Rev. Lett. **118**, 083002 (2017).

[150] I. J. Zucker, The cubic equation – a new look at the irreducible case, Math. Gazet. **92**, 264 (2008).

[151] G. Ehlers, J. Sólyom, Ö. Legeza, and R. M. Noack, Entanglement structure of the Hubbard model in momentum space, Phys. Rev. B **92**, 235116 (2015).

[152] N. Plakida, *High-Temperature Cuprate Superconductors: Experiment, Theory, and Applications* (Springer, Berlin, 2010), Chap. 5.

[153] T. Timusk and B. Statt, The pseudogapp in high-temperature superconductors: an experimental survey, Rep. Prog. Phys. **62**, 61 (1999).

[154] A. Damascelli, Z. Hussain, and Z. -X. Shen, Angle-resolved photoemission studies of the cuprate superconductors, Rev. Mod. Phys. **75**, 473 (2003).

[155] D. Koralek, J. F. Douglas, N. C. Plumb, Z. Sun, A. V. Fedorov, M. M. Murnane, H. C. Kapteyn, S. T. Cundiff, Y. Aiura, K. Oka, H. Eisaki, and D. S. Dessau, Laser based angle-resolved photoemission, the sudden approximation, and quasiparticle-like spectral peaks in $Bi_2Sr_2CaCu_2O_{8+\delta}$, Phys. Rev. Lett. **96**, 017005 (2006).

[156] J. D. Koralek, J. F. Douglas, N. C. Plumb, J. D. Griffith, S. T. Cundiff, H. C. Kapeteyn, M. M. Murnane, and D. S. Dessau, Experimental setup for low-energy laser-based angle resolved photoemission spectroscopy, Rev. Sci. Instrum. **78**, 053905 (2007).

[157] G. Liu, G. Wang, Y. Zhu, H. Zhang, G. Zhang, X. Wang, Y. Zhou, W. Zhang, H. Liu, L. Zhao, J. Meng, X. Dong, C. Chen, Z. Xu, and X. J. Zhou, Development of a vacuum ultraviolet laser-based angle-resolved photoemission system with a superhigh energy resolution better than 1 meV, Rev. Sci. Instrum. **79**, 023105 (2008).

[158] H. Li, X. Zhou, S. Parham, T. J. Reber, H. Berger, G. B. Arnold, and D. S. Dessau, Coherent organization of electronic correlations as a mechanism to enhance and stabilize high-$T_c$ cuprate superconductivity, Nat. Comm. **9**, 26 (2018).

[159] H. Hertz, Ueber einen Einfluss des ultravioletten Lichtes auf die electrische Entladung, Ann. Phys. (Leipzig) **17**, 983 (1887).

[160] A. Einstein, Über einen die Erzeugung und Verwandlung des Lichtes betreffenden heuristischen Gesichtspunkt, Ann. Phys. (Leipzig) **31**, 132 (1905).

[161] A. A. Kordyuk, S. V. Borisenko, M. S. Golden, S. Legner, K. A. Nenkov, M. Knupfer, J. Fink, H. Berger, L. Forró, and R. Follath, Doping dependence of the Fermi surface in $(Bi, Pb)_2Sr_2CaCu_2O_{8+\delta}$, Phys. Rev. B **66**, 014502 (2002).

[162] M. Platé, J. D. F. Mottershead, I. S. Elfimov, D. C. Peets, R. Liang, D. A. Bonn, W. N. Hardy, S. Chiuzbaian, M. Falub, M. Shi, L. Patthey, and A. Damascelli, Fermi surface and quasiparticle excitations of overdoped $Tl_2Ba_2CuO_{6+\delta}$, Phys. Rev. Lett. **95**, 077001 (2005).

[163] J. R. Schrieffer and J. S. Brooks (eds.), *Handbook of High-Temperature Su-perconductivity: Theory and Experiment* (Springer, New York, 2007), Chap. 3.

[164] K. Fujita, C. K. Kim, I. Lee, J. Lee, M. H. Hamidian, I. A. Firmo, S. Mukhopadhyay, H. Eisaki, S. Uchida, M. J. Lawler, E. -A. Kim, J. C. Davis, Simultaneous transitions in cuprate momentum-space topology and electronic symmetry breaking, Science **344**, 612 (2014).

[165] H. Li, X. Zhou, S. Parham, K. N. Gordon, R. D. Zhong, J. Schneeloch, G. D. Gu, Y. Huang, H. Berger, G. B. Arnold, and D. S. Dessau, Four-legged starfish-shaped Cooper pairs with ultrashort antinodal length scales in cuprate superconductors, arXiv:1809.02194.

[166] D. Duffy and A. Moreo, Influence of next-nearest-neighbor electron hopping on the static and dynamical properties of the two-dimensional Hubbard model, Phys. Rev. B **52**, 15607 (1995).

[167] Y. Gao and F. Han, Effects of the neat-nearest-neighbor hopping in optical lattices, Mod. Phys. Lett. B **22**, 33 (2008).

[168] T. A. Zaleski and T. K. Kopeć, Effect of next-nearest-neighbour hopping on Bose-Einstein condensation in optical lattices, J. Phys. B **43**, 085303 (2010).

[169] V. H. Dao and R. Frésard, Effect of the next-nearest-neighbor hopping on the charge collective modes in the paramagnetic phase of the Hubbard model, Eur. Phys. Lett. **120**, 17004 (2017).

[170] R. Micnas, J. Ranninger, and S. Robaszkiewicz, Superconductivity in narrow-band systems with local nonretarded attractive interactions, Rev. Mod. Phys. **62**, 113 (1990).

[171] A. Neumayr and W. Metzner, Renormalized perturbation theory for Fermi sys-tems: Fermi surface deformation and superconductivity in the two-dimensional Hubbard model, Phys. Rev. B **67**, 035112 (2003).

[172] A. S. Alexandrov and V. V. Kabanov, Unconventional high-temperature super-conductivity from repulsive interactions: theoretical constraints, Phys. Rev. Lett. **106**, 136403 (2011).

[173] M. S. Hybertsen, M. Schlüter, and N. E. Christensen, Calculation of Coulomb-interaction parameters for $La_2CuO_4$ using a constrained-density-functional ap-proach, Phys. Rev. B **39**, 9028 (1989).

[174] A. K. McMahan, J. F. Annett, and R. M. Martin, Cuprate parameters from numerical Wannier functions, Phys. Rev. B **42**, 6268 (1990).

[175] M. Hirayama, Y. Yamaji, T. Misawa, and M. Imada, *Ab initio* effective Hamiltonians for cuprate superconductors, Phys. Rev. B **98**, 134501 (2018).

[176] M. Lewenstein, A. Sanpera, and V. Ahufinger, *Ultracold Atoms in Optical Lattices: Simulating Quantum Many-Body Systems* (Oxford University Press, Oxford, 2012), Chap. 14.

[177] M. Inguscio and L. Fallani, *Atomic Physics: Precise Measurements & Ultracold Matter* (Oxford University Press, Oxford, 2013), Chap. 6.

[178] V. P. Singh and L. Mathey, Noise correlations of two-dimensional Bose gases, Phys. Rev. A **89**, 053612 (2014).

[179] E. Altman, E. Demler, and M. D. Lukin , Probing many-body states of ultracold atoms via noise correlations, Phys. Rev. A **70**, 013603 (2004).

[180] L. Mathey, E. Altman, and A. Vishwanath, Noise Correlations in one-dimensional systems of ultracold fermions, Phys. Rev. Lett. 100, 240401 (2008).

[181] L. Mathey, A. Vishwanath, and E. Altman, Noise correlations in low-dimensional systems of ultracold atoms, Phys. Rev. A **79**, 013609 (2009).

[182] Y. Yamaguchi , Two-nucleon problem when the potential is nonlocal but separable. I, Phys. Rev. **95**, 1628 (1954).

[183] L. D. Faddeev, *Mathematical Aspects of the Three-Body Problem in the Quantum Scattering Theory* (Sivan, Jerusalem, 1965).

[184] L. D. Faddeev and S. P. Merkuriev, *Quantum Scattering Theory for Several Particle Systems* (Kluwers Academic, Dordrecht, 1993).

[185] L. N. Trefethen and D. Bau, III, *Numerical Linear Algebra* (SIAM, Philadelphia, 1997), Chaps. IV and V.

[186] V. I. Krylov, *Approximate Calculation of Integrals* (Dover, New York, 2005), Chaps. 5 and 6.

[187] W. H. Press, S. A. Teukolsky, W. T. Vetterling, and B. P. Flannery, *Numerical Recipes: The Art of Scientific Computing* (Cambridge University Press, New York, 2007).

[188] O. Gunnarsson, Superconductivity in fullerides, Rev. Mod. Phys. **69**, 575 (1997).

[189] C. Buzea and T. Yamashita, Review of the superconducting properties of $MgB_2$, Supercond. Sci. Technol. **14**, R115 (2001).

[190] M. Zachmann, M. D. Croitoru, A. Vagov, V. M. Axt, T. Papenkort, and T. Kuhn, Ultrafast terahertz-field-induced dynamics of superconducting bulk and quasi-1D samples, New. J. Phys. **15**, 055016 (2013).

[191] N. Tsuji and H. Aoki, Theory of Anderson pseudospin resonance with Higgs mode in superconductors, Phys. Rev. B **92**, 064508 (2015).

[192] I. Gierz, M. Mitrano, H. Bromberger, C. Cacho. R. Chapman, E. Springate, S. Link, U. Starke, B. Sachs, M. Eckstein, T. O. Wehling, M. I. Katsnelson, A. Lichtenstein, and A. Cavalleri, Phonon-pump extreme-ultraviolet-photoemission probe in graphene: Anomalous heating of Dirac carriers by lattice deformation, Phys. Rev. Lett. **114**, 125503 (2015).

[193] A. Derevianko, J. F. Babb, and A. Dalgarno, High-precision calculations of van der Waals coefficients for heteronuclear alkali-metal dimers, Phys. Rev. A **63**, 052704 (2001).

[194] M. Kitagawa, K. Enomoto, K. Kasa, Y. Takahashi, R. Ciuryło, P. Naidon, and P. S. Julienne, Two-color photoassociation spectroscopy of ytterbium atoms and the precise determinations of $s$-wave scattering lengths, Phys. Rev. **A** 77, 012719 (2008).

[195] J. Tao, J. P. Perdew, and A. Ruzsinszky, Accurate van der Waals coefficients from density functional theory, PNAS **109**, 18 (2012).

[196] D. J. MacNeil and F. Zhou, Pauli blocking effect on Efimov states near a Feshbach resonance, Phys. Rev. Lett. **106**, 145301 (2011).

[197] P. Niemann and H.-W. Hammer, Pauli-blocking effects and Cooper triples in three-component Fermi gases, Phys. Rev. A **86**, 013628 (2012).

[198] N. T. Zinner, Few-body physics in a many-body world, Few-Body Syst. **55**, 599 (2014).

[199] N. G. Nygaard and N. T. Zinner, Efimov three-body states on top of a Fermi sea, New J. Phys. **16**, 023026 (2014).

[200] L. D. Faddeev and S. P. Merkuriev, *Quantum Scattering Theory for Several Particle Systems* (Kluwers Academic, Dordrecht, 1993).

[201] H. Tajima and P. Naidon, Quantum chromodynamics (QCD)-like phase diagram with Efimov trimers and Cooper pairs in resonantly interacting SU(3) Fermi gases, New J. Phys. **21**, 073051 (2019).

[202] M. Sun and X. Cui, Efimov physics in the presence of a Fermi sea, Efimov physics in the presence of a Fermi sea, Phys. Rev. A **99**, 060701 (R) (2019).

[203] K. Beloy, N. Hinkley, N. B. Phillips, J. A. Sherman, M. Schioppo, J. Lehman, A. Feldman, L. M. Hanssen, C. W. Oates, and A. D. Ludlow, Atomic clock with $1 \times 10^{-18}$ room-temperature blackbody Stark uncertainty, Phys. Rev. Lett. **113**, 260801 (2014).

[204] A. D. Ludlow, M. M. Boyd, J. Ye, E. Peik, and P. O. Schmidt, Optical atomic clocks, Rev. Mod. Phys. **87**, 637 (2015).

[205] M. Yasuda, T. Tanabe, T. Kobayashi, D. Akamatsu, T. Sato, and A. Hatakeyama, Laser-controlled cold ytterbium atom source for transportable optical clocks, J. Phys. Soc. Jpn. **86**, 125001 (2017).

[206] M. S. Safronova, S. G. Porsev, C. Sanner, and J. Ye, Two clock transitions in neutral Yb for the highest sensitivity to variations of the fine-structure constant, Phys. Rev, Lett. **120**, 173001 (2018).

[207] K. Sponselee, L. Freystatzky, B. Abeln, M. Diem, B. Hundt, A. Kochanke, T. Ponath, B. Santra, L. Mathey, and K. Sengstock, Dynamics of ultracold quantum gases in the dissipative Fermi–Hubbard model, Quantum Sci. Technol. **4**, 014002 (2018).

[208] S. Saskin,1 J. T. Wilson, B. Grinkemeyer, and J. D. Thompson, Narrow-line cooling and imaging of ytterbium atoms in an optical tweezer array, Phys. Rev. Lett. **122**, 143002 (2019).

[209] B. Braverman, A. Kawasaki, E. Pedrozo-Peñafiel, S. Colombo, C. Shu, Z. Li, E. Mendez, M. Yamoah, L. Salvi, D. Akamatsu, Y. Xiao, and V. Vuletić, Near-unitary spin squeezing in $^{171}$Yb, Phys. Rev, Lett. **122**, 223203 (2019).

[210] *NIST Handbook of Basic Atomic Spectroscopic Data* [https://physics.nist.gov/PhysRefData/Handbook/Tables/ytterbiumtable1.htm].

[211] M. S. Safronova, S. G. Porsev, and C. W. Clark, Ytterbium in quantum gases and atomic clocks: van der Waals interactions and blackbody shifts, Phys. Rev. Lett. **109**, 230802 (2012).

[212] R. Zhang, Y. Cheng, H. Zhai, and P. Zhang, Orbital Feshbach resonance in alkali-earth atoms, Phys. Rev. Lett **115**, 135301 (2015).

[213] M. Höfer, L. Riegger, F. Scazza, C. Hofrichter, D. R. Fernandes, M. M. Parish, J. Levinsen, I. Bloch, and S. Fölling, Observation of an orbital interaction-induced Feshbach resonance in $^{173}$Yb, Phys. Rev. Lett **115**, 265302 (2015).

[214] E. G. M. v. Kempen, B. Marcelis, and S. J. J. M. F. Kokkelmans, Formation of fermionic molecules via interisotope Feshbach resonances, Phys. Rev. A **70**, 050701(R) (2004).

[215] M. Theis, G. Thalhammer, K. Winkler, M. Hellwig, G. Ruff, R. Grimm, and J. H. Denschlag, Tuning the scattering length with an optically induced Feshbach resonance, Phys. Rev. Lett. **93**, 123001 (2004).

[216] G. Thalhammer, M. Theis, K. Winkler, R. Grimm, and J. H. Denschlag, Inducing an optical Feshbach resonance via stimulated Raman coupling, Phys. Rev. A **71**, 033403 (2005).

[217] K. Enomoto, K. Kasa, M. Kitagawa, and Y. Takahashi, Optical Feshbach resonance using the intercombination transition, Phys. Rev. Lett. **101**, 203201 (2008).

[218] K. Ono, J. Kobayashi, Y. Amano, K. Sato, and Y. Takahashi, Antiferromagnetic interorbital spin-exchange interaction of $^{171}$Yb, Phys. Rev. A **99**, 032707 (2019).

[219] O. Bettermann, N. D. Oppong, G. Pasqualetti, L. Riegger, I. Bloch, and S. Fölling, Clock-line photoassociation of strongly bound dimers in a magic-wavelength lattice, arXiv:2003.10599v1.

# Eidesstattliche Versicherung

Hiermit versichere ich an Eides statt, die vorliegende Dissertationsschrift selbst verfasst und keine anderen als die angegebenen Hilfsmittel und Quellen benutzt zu haben.

Die eingereichte schriftliche Fassung entspricht der auf dem elektronischen Speichermedium.

Die Dissertation wurde in der vorgelegten oder einer ähnlichen Form nicht schon einmal in einem früheren Promotionsverfahren angenommen oder als ungenügend beurteilt.

Hamburg, den 26.10.2020

Ali Sanayei